



UNIVERSIDADE ESTADUAL DE
CAMPINAS

Instituto de Matemática, Estatística e
Computação Científica

ARTHUR MIRANDA DO ESPIRITO SANTO

**Conservative numerical formulations for
approximating hyperbolic models with source
terms and related transport models**

**Formulações numéricas conservativas para
aproximação de modelos hiperbólicos com
termos de fonte e problemas de transporte
relacionados**

Campinas

2017

Arthur Miranda do Espirito Santo

**Conservative numerical formulations for approximating
hyperbolic models with source terms and related
transport models**

**Formulações numéricas conservativas para aproximação
de modelos hiperbólicos com termos de fonte e
problemas de transporte relacionados**

Tese apresentada ao Instituto de Matemática,
Estatística e Computação Científica da Uni-
versidade Estadual de Campinas como parte
dos requisitos exigidos para a obtenção do
título de Doutor em Matemática Aplicada.

e

Thesis presented to the Institute of Mathe-
matics, Statistics and Scientific Computing
of the University of Campinas in partial ful-
fillment of the requirements for the degree of
Doctor in Applied Mathematics.

Orientador: Eduardo Cardoso de Abreu

Este exemplar corresponde à versão
final da Tese defendida pelo aluno
Arthur Miranda do Espirito Santo e
orientada pelo Prof. Dr. Eduardo Car-
doso de Abreu.

Campinas

2017

Agência(s) de fomento e nº(s) de processo(s): CNPq, 165564/2014-8; CAPES

Ficha catalográfica
Universidade Estadual de Campinas
Biblioteca do Instituto de Matemática, Estatística e Computação Científica
Ana Regina Machado - CRB 8/5467

Es65c Espirito Santo, Arthur Miranda do, 1989-
Conservative numerical formulations for approximating hyperbolic models
with source terms and related transport models / Arthur Miranda do Espirito
Santo. – Campinas, SP : [s.n.], 2017.

Orientador: Eduardo Cardoso de Abreu.
Tese (doutorado) – Universidade Estadual de Campinas, Instituto de
Matemática, Estatística e Computação Científica.

1. Equações diferenciais hiperbólicas. 2. Método dos volumes finitos. 3.
Método dos elementos finitos. 4. Mecânica dos fluidos. I. Abreu, Eduardo
Cardoso de, 1974-. II. Universidade Estadual de Campinas. Instituto de
Matemática, Estatística e Computação Científica. III. Título.

Informações para Biblioteca Digital

Título em outro idioma: Formulações numéricas conservativas para aproximação de
modelos hiperbólicos com termos de fonte e problemas de transporte relacionados

Palavras-chave em inglês:

Hyperbolic differential equations

Finite volume method

Finite element method

Fluid mechanics

Área de concentração: Matemática Aplicada

Titulação: Doutor em Matemática Aplicada

Banca examinadora:

Eduardo Cardoso de Abreu [Orientador]

José Luiz Boldrini

Lucas Catão de Freitas Ferreira

Wanderson José Lambert

Grigori Chapiro

Data de defesa: 26-07-2017

Programa de Pós-Graduação: Matemática Aplicada

**Tese de Doutorado defendida em 26 de julho de 2017 e aprovada
pela banca examinadora composta pelos Profs. Drs.**

Prof(a). Dr(a). EDUARDO CARDOSO DE ABREU

Prof(a). Dr(a). JOSÉ LUIZ BOLDRINI

Prof(a). Dr(a). LUCAS CATAO DE FREITAS FERREIRA

Prof(a). Dr(a). WANDERSON JOSÉ LAMBERT

Prof(a). Dr(a). GRIGORI CHAPIRO

As respectivas assinaturas dos membros encontram-se na Ata de defesa

Dedico esse trabalho à minha mãe Hilde e ao meu pai Adelson.

Agradecimentos

Agradeço a Coordenadoria de Assistência de Pessoal de Nível Superior (CAPES) e ao Conselho Nacional de Desenvolvimento Científico e Tecnológico (CNPq) pelo apoio via uma bolsa de doutorado institucional para realização deste trabalho, sob número de processo 165564/2014-8 no período de 03/2014 até 07/2017.

Agradeço primariamente ao meu orientador Eduardo Cardoso de Abreu pelo apoio e dedicação incondicional, tanto no âmbito profissional e acadêmico, quanto no âmbito pessoal. Também agradeço primariamente ao meu núcleo familiar, minha mãe Hilde e meu pai Adelson que desde sempre investiram consideráveis recursos materiais e imateriais pra que minha educação fosse a melhor possível. Agradeço também a minha irmã Alice e meus primos Rosa e Francisco por toda a paciência na convivência.

Essa tese não seria possível também sem a colaboração muito importante de John Alexander, que é meu co-autor de artigos, de trabalhos apresentados e de palestras dadas, além de parceiro de muita discussão pelos corredores do IMECC e agora por videoconferência. Acima de tudo um grande amigo, a ele meu mais sincero obrigado. Também agradeço o apoio dos colegas do grupo de pesquisa, Paola, Jardel, Abel, Juan, Jean, Ciro e Luis, sempre pautado na colaboração, na ética e no crescimento conjunto.

Por fim, gostaria de agradecer aos meus amigos que também são importantíssimos no processo de engrandecimento pessoal. Digo sempre que existe uma relação direta entre ser meu amigo e ter estudado matemática comigo em algum momento da vida. Aos melhores amigos que carrego sempre comigo no coração, Bárbara e Bernard. Ao primo-amigo que também me acompanha desde criança, o Filipe. As minhas queridas e fieis escudeiras Gabi e Ari. Aos amigos do Cotuca, que são amigos até hoje e para sempre, o Rafa, o Akira, o Eizo e o Lyan, a Rafaela e o André, o Felipe, a Milene, a Michele e o Rafa, a Dani e o Allan, a Karina e o Gary. Aos amigos de São Paulo Brufis, Thiago, Rodrigo e Rafa, que ainda que distantes estão sempre por perto. Todo o amor e carinho que estes amigos me dão e me deram foram também parte fundamental do desenvolvimento do trabalho.

A resposta certa, não importa nada: o essencial é que as perguntas estejam certas.

Mário Quintana

Resumo

O objetivo desta tese é desenvolver, pelo menos no aspecto formal, algoritmos construtivos e bem-balanceados para a aproximação de classes específicas de modelos diferenciais. Nossas principais aplicações consistem em equações de água rasa e problemas de convecção-difusão no contexto de fenômenos de transporte, relacionados a problemas de pressão capilar descontínua em meios porosos. O foco principal é desenvolver sob o framework Lagrangian-Euleriano um esquema simples e eficiente para, em nível discreto, levar em conta o delicado equilíbrio entre as aproximações numéricas não lineares do fluxo hiperbólico e o termo fonte, e entre o fluxo hiperbólico e o operador difusivo. Os esquemas numéricos são propostos para ser independentes de estruturas particulares das funções de fluxo. Apresentamos diferentes abordagens que selecionam a solução entrópica qualitativamente correta, amparados por um grande conjunto de experimentos numéricos representativos.

Palavras-chave: Leis de Conservação Hiperbólicas. Leis de Balanço. Modelos de Transporte. Formulação Lagrangiana-Euleriana de volumes finitos. Método de elementos finitos mistos e híbridos.

Abstract

The purpose of this thesis is to develop, at least formally by construction, conservative methods for approximating specific classes of differential models. Our major applications consist in shallow water equations and nonstandard convection-diffusion problems in the context of transport phenomena, related to discontinuous capillary pressure problems in porous media. The main focus in this work is to develop under the Lagrangian-Eulerian framework a simple and efficient scheme to, on the discrete level, account for the delicate nonlinear balance between the numerical approximations of the hyperbolic flux and source term, and between the hyperbolic flux and the diffusion operator. The proposed numerical schemes are aimed to be independent of particular structures of the flux functions. We present different approaches that select the qualitatively correct entropy solution, supported by a large set of representative numerical experiments.

Keywords: Hyperbolic Conservation Laws. Balance laws. Transport Models. Lagrangian-Eulerian Finite Volume. Hybrid and mixed finite element methods.

List of Figures

Figure 1	– Illustration of the integral tubes D_j^n . On the top picture, we illustrate the nonlinear evolution via the integral curves σ linked to D_j^n in (2.6). A first order approximation is performed to the construction of the local Lagrangian-Eulerian space-time control-volume, and it is shown on the bottom picture. We notice that higher order approximations are naturally permissible as well.	29
Figure 2	– The reconstruction step. The cell $[x_{j-\frac{1}{2}}^{n+1}, x_{j+\frac{1}{2}}^{n+1}]$ conserves information both from U_j and U_{j-1}	30
Figure 3	– Illustration of the conservation relations (2.5) and (2.12). The evolution step guarantees conservation due to the no-flow conditions on the integral curves.	31
Figure 4	– The projection step. The cell $[x_{j-\frac{1}{2}}^{n+1}, x_{j+\frac{1}{2}}^{n+1}]$ collect information both from \bar{U}_j and \bar{U}_{j-1} , guided by the projection coefficients c_{0j} and c_{1j} given by (2.15).	33
Figure 5	– On the top picture (resp. bottom) we show an illustration of the continuous (resp. discrete) local space-time integral tube domains $D_{s,j}^n$, for each $s = u, v, w$	39
Figure 6	– The integral tube in 3D. We illustrate the challenge of uniquely define the tangent vector. Since here there is a tangent plane, the <i>integral surfaces</i> as well as <i>integral curves</i> coming from $[u \ f(u) \ g(u)]^T \cdot \vec{n} = 0$ seem to be at first glance not straightforward to construct.	42
Figure 7	– Mesh refinement study for a non-convex flux function. The finest mesh in this case is a solution with 1024 grid cells.	47
Figure 8	– Inviscid nonlinear Burgers' problem: post-shock solution for smooth initial data (top), Riemann problem with shock wave (middle), Riemann problem with rarefaction fan (bottom).	49
Figure 9	– Top: Classical one-dimensional Buckley-Leverett two-phase problem computed by scheme (2.19)-(2.20). Bottom: A non-convex flux function.	50
Figure 10	– Oil, water and gas saturation profiles are shown as a function of distance. RP_1 on the top and RP_2 on the bottom.	53
Figure 11	– Mesh refinement study for mesh values 256, 512 and 1024 against a reference solution of 2048 mesh points. Oil saturations are shown as a function of distance. RP_1 on the left and RP_2 on the right.	54

Figure 12 – Transcritical without shock test case. The steady-state has been already reached (exhibited time is $t = 600$ sec.). Left: $h + Z$ solutions with 200, 600 and 1000 mesh grid points. Right: discharge M with 200, 600 and 1000 mesh grid points.	60
Figure 13 – Transcritical with shock test case. The steady-state has been already reached (exhibited time is $t = 600$ sec.). Left: $h + Z$ solutions with 200, 600 and 1000 mesh grid points. Right: discharge M with 200, 600 and 1000 mesh grid points	61
Figure 14 – Subcritical test case. The steady-state has been already reached (exhibited time is $t = 600$ sec.). Left: $h + Z$ solutions with 200, 600 and 1000 mesh grid points. Right: discharge M with 200, 600 and 1000 mesh grid points	62
Figure 15 – Supercritical test case at initial time (top), $t = 1.0$ sec. (middle), and steady state at $t = 100$ sec. (bottom).	64
Figure 16 – Subcritical test case at initial time (top), $t = 0.5$ sec. (middle), and steady state at $t = 100$ sec. (bottom).	65
Figure 17 – Larger slope topography test case at initial time (top), $t = 0.05$ sec. (middle), and steady state at $t = 100$ sec. (bottom).	66
Figure 18 – Steady-state solution for the problem modeled by equation 2.73 with different topographies. The solution for both cases is approximated with 200 mesh grid cells at time $t = 100$	68
Figure 19 – Numerical solutions for the Buckley-Leveret equation. Left the solution with 512 grid points approximated with the Lagrangian-Eulerian framework. Center: The Strang splitting approach with Nessyahu-Tadmor numerical scheme with 512 points. Right: The difference error between the two approximations.	69
Figure 20 – Numerical solutions for the “fingering test”. Left the solution with 512 grid points approximated with the Lagrangian-Eulerian framework. Center: The Strang splitting approach with Nessyahu-Tadmor numerical scheme with 512 points. Right: The difference error between the two approximations.	69
Figure 21 – Numerical solutions with nontrivial spatial-discontinuous source term $g(x, u) = z'(x)u$. We present a grid refinement study for u and $u + z$ with 128, 256 and 512 mesh grid points.	71
Figure 22 – Numerical solutions with source term $g(x, u)$. 512 cells (left), 1024 cells (right).	72
Figure 23 – Numerical approximations of the scalar balance law. The solution is shown with 256 cells (left) and 512 cells (right).	72

Figure 24 – Log-log plots for norms L^1 (left), L^2 (middle) and L^∞ (right) of the error versus the cell sizes, for the the linear problem $u_t + u_x = 0$ at time $T = 1.0$ with smooth initial condition $u(x, 0) = e^{-x^2}$; we can see first-order behavior of accuracy in the numerical solutions.	73
Figure 25 – Log-log plots for norms L^1 (left), L^2 (middle) and L^∞ (right) of the error versus the cell sizes, for the situation with a source term $g(x, u)$ discontinuous in x ; we can see first-order behavior of accuracy in the numerical solutions.	74
Figure 26 – An illustration of the local space-time nonstaggered integral tube for the continuous (left) and discrete (right).	77
Figure 27 – A 2D mesh grid and its evolution in time by the integral curves. Darker cells represent the evolution in time of the previous mesh, guided by the dotted lines representing integral curves on the vertices. In this example, for the central cell, all vertices are moving inwards.	80
Figure 28 – Even within CFL-like stability conditions, finding projection coefficients in this approach would be a challenging problem, since the control volume may unpredictably change. In this example, each vertex travels no further than 0.4 of the grid width/height.	81
Figure 29 – Evolution of midpoints generates at most nine rectangles in which local mass conservation is preserved. In this example, for the central cell, all midpoints are moving inwards, but whenever a midpoint travel outwards, the respective adjacent cell will treat it as inward information.	82
Figure 30 – Left: Shu’s linear test, with spatial-dependent advection coefficient $a(x, t)$. Middle: Test case with $a(x, t) = \sin(x)$, the velocity is variable in space. Right: Test case with $a(x, t) = \sin(t)$, the velocity is variable in time.	83
Figure 31 – Nonlinear tests for Burgers’ flux function without reconstruction. Left: shock wave, initial condition $u(x, 0) = 1, x < 0$ and $u(x, 0) = 0, x > 0$, end time $t = 0.5$. Right: rarefaction wave, $u(x, 0) = -1, x < 0$ and $u(x, 0) = 1, x > 0$, end time $t = 1.0$	83
Figure 32 – Nonlinear tests with reconstruction. Left: Burgers’ flux function, shock wave solution with initial condition $u(x, 0) = 1, x < 0$ and $u(x, 0) = 0, x > 0$, end time $t = 0.5$. Middle: Burgers’ flux function, rarefaction wave with initial condition $u(x, 0) = -1, x < 0$ and $u(x, 0) = 1, x > 0$, end time $t = 1.0$. Right: Buckley-Leverett flux function ($H(u) = u^2/(u^2 + 0.5(1 - u)^2)$) with initial condition $u(x, 0) = 1, x < 0$ and $u(x, 0) = 0, x > 0$	83

Figure 33 – Buckley-Leverett flux function with initial condition $u(x, 0) = 1$, $-1 < x < 1$ and $u(x, 0) = 0$, otherwise. Snapshots at $t = 0$, $t = 0.4$ and $t = 1$, respectively.	84
Figure 34 – Numerical solutions of model problem 3.24 with smooth source term $g(x, t) = x^3 + 6tx^2$ at times $t = 0$, $t = 1.5$ and $t = 3.0$	84
Figure 35 – Convergence of error in L^1 , L^2 and L^∞ norms with uniform mesh refinement for the smooth source term test. Second-order convergence is observed in this example.	85
Figure 36 – Numerical solutions of model problem 3.25 with discontinuous source term $g(x, u)$. Grid refinement study with meshgrids 128, 256 and 512.	86
Figure 37 – Numerical solutions to shallow water system (3.26) with 128, 256 and 512 cells (top to bottom), h (height) on the left and v (velocity) on the right.	87
Figure 38 – Numerical solutions of a two-dimensional problem with nonconvex (trigonometric) flux functions in a grid refinement study ($n \times n = 128 \times 128, 256 \times 256, 512 \times 512, 1024 \times 1024$).	91
Figure 39 – Solutions of model problem (3.29) at times $t = 0.06, 0.12, 0.18, 0.24$, and 0.3 for the set of entry pressures $P^L = 0$ and $P^R = 0.5$. Here $r = 0.01$ and the mollification width is $\gamma = 0.85$. We have only one wave profile traveling left. Left: $n = 240$, right: $n = 480$	92
Figure 40 – Solutions of model problem (3.29) at times $t = 0.06, 0.12, 0.18, 0.24$, and 0.3 for the set of entry pressures $P^L = 0$ and $P^R = 2.0$. Here $r = 0.006$ and the mollification width is $\gamma = 0.85$. We have only a wave profile traveling left and a slower wave traveling right. Left: $n = 240$, right: $n = 480$	93
Figure 41 – From top to bottom: first, second and third rows depicts the solutions of linear advection problems (on the left column) with the usual (\mathbf{w}), weakened ($\tilde{\mathbf{w}}$) and corrected weakened ($\tilde{\mathbf{w}}_c$) fluxes (on the right column). We show on the bottom row the solutions combined in order to explicit the difference of the scales (we omit the corrected weakened for the sake of presentation).	119
Figure 42 – From top to bottom: first, second and third rows depicts the solutions of Burgers' viscid equation solution with exponential pulse as initial condition (on the left column) with the usual (\mathbf{w}), weakened ($\tilde{\mathbf{w}}$) and corrected weakened ($\tilde{\mathbf{w}}_c$) fluxes (on the right column). We show on the bottom row the solutions combined in order to explicit the difference of the scales (we omit the corrected weakened for the sake of presentation).	120

Figure 43 – From top to bottom: first, second and third rows depicts the solutions of Burgers’ viscid equation solution with sine wave as initial condition (on the left column) with the usual (\mathbf{w}), weakened ($\tilde{\mathbf{w}}$) and corrected weakened ($\tilde{\mathbf{w}}_c$) fluxes (on the right column). We show on the bottom row the solutions combined in order to explicit the difference of the scales (we omit the corrected weakened for the sake of presentation). 121

Figure 44 – The first picture represents the numerical solution of Model problem (3.29) with the constant initial condition $u \equiv 0.5$ and capillary pressure functions $P^{R,L} = \log(1 - u)$ and the following pictures are the classical (\mathbf{w}) and weakened ($\tilde{\mathbf{w}}$) fluxes. 122

List of Tables

Table 1 – Corresponding errors between the numerical approximations (U) and exact solutions (u) for the scalar advection problem.	73
Table 2 – Corresponding errors between the numerical approximations (U) and exact solutions (u) for the balance law with discontinuous source term. .	74

Contents

1	INTRODUCTION	18
1.1	Motivation and significance of the research work	18
1.2	Aims and objectives of the thesis proposal	19
1.3	Preliminary Results and Ongoing Work	20
1.4	Organization of the thesis proposal	22
I	THE LAGRANGIAN-EULERIAN FRAMEWORK	23
2	LAGRANGIAN-EULERIAN NUMERICAL SCHEMES	24
2.1	A Lagrangian-Eulerian constructive approximation scheme for non-linear hyperbolic conservation laws	27
2.2	The Lagrangian-Eulerian scheme for hyperbolic balance laws	35
2.3	Systems of hyperbolic conservation laws and balance laws	38
2.4	Two-dimensional hyperbolic conservation laws	42
2.5	Numerical experiment studies with applications	46
2.5.1	Convex and non-convex flux functions for conservation laws	46
2.5.2	Porous Media Flow Problems	48
2.5.3	Shallow Water Equations	55
2.5.3.1	Zero velocity and steady-state solutions	67
2.5.4	Two-dimensional simulations of nonlinear scalar conservation laws	68
2.5.5	Sources with space-discontinuous functions and nontrivial topography	69
2.5.6	A hard test case with exponential growth of the source term	70
2.5.7	Error analysis	73
3	FURTHER DEVELOPMENTS IN THE LAGRANGIAN-EULERIAN FRAMEWORK	75
3.1	The nonstaggered Lagrangian-Eulerian conservative finite volume method	75
3.1.1	Extension to balance law problems	78
3.1.2	Two-dimensional Hyperbolic Conservation Laws	79
3.1.3	Numerical Experiments	81
3.2	An Algorithm for Convection Dominated Flow Problems with a Diffusive Correction Step	88
3.2.1	The Two-phase Buckley-Leverett Problem with Gravity and Discontinuous Capillary Pressure	88

3.2.2	The correction diffusive step procedure	89
II	MIXED HYBRID FINITE ELEMENT METHODS FOR MULTIPHASE FLOW PROBLEMS	94
4	CONSERVATIVE MIXED HYBRID FINITE ELEMENT AND FI- NITE VOLUME METHODS WITH A NEW COUPLING CONDI- TION FOR SOLVING MULTIPHASE FLOW PROBLEMS	95
4.1	Multiphase Flow Transport Problems without Spatially-Dependent Diffusion Terms	97
4.1.1	Two-phase flow problems	97
4.1.1.1	Mixed formulation	98
4.1.2	Three-phase flow problems	103
4.2	Multiphase Flow Transport Problems with Spatially-Dependent Dif- fusion Terms	110
4.2.1	Two-phase flow problems	111
4.2.1.1	Extension to three-phase flow problems	112
4.3	A Fully-Coupled Finite Volume/Hybrid Mixed Finite Elements Ap- proach for Multiphase Flow Problems	113
4.3.1	Two-phase flow problem	113
4.3.1.1	Mixed formulation for the transport equation	114
4.3.1.2	Weak form of the transport system	114
4.3.1.3	Hybridized mixed finite element approximation	115
4.3.1.4	Weakening of Robin coupling conditions	115
4.3.1.5	Discrete equations and iterative procedure	117
4.3.2	Numerical Experiments	118
5	CONCLUDING REMARKS AND OUTLOOK FOR FUTURE WORK	123
5.1	Preliminary advances and achievements	123
5.2	Perspectives for future work and some final considerations	125
	Bibliography	128
	APPENDIX	138

1 Introduction

The purpose of this thesis is to develop conservative methods, at least formally by construction, for approximating specific classes of differential models. Our major applications are in balance laws systems with stiff source terms modeling shallow water equations and nonstandard convection-diffusion problems in the context of transport phenomena, related to discontinuous capillary pressure problems in porous media. Based on a finite volume Lagrangian-Eulerian framework we developed and implemented new numerical schemes for solving balance laws with nonlinear source terms, also linked to the hyperbolic scalar conservation laws. Our main focus in this work is to develop a simple and efficient scheme to, on the discrete level, account for the delicate nonlinear balance between the numerical approximations of the hyperbolic flux and (possibly stiff) source term. We present different approaches that select the qualitatively correct entropy solution, supported by a large set of representative numerical experiments.

1.1 Motivation and significance of the research work

In the past decades, there has been large interest in researching accurate and robust numerical methods for the solutions of shallow water equations due to their large scientific and engineering applications. Two types of difficulties are often encountered in the simulation of the shallow water equations, coming from the good approximation of steady state solutions (related to the treatment of the source terms) and the preservation of water height positivity (related to the appearance of dry regions in many engineering applications). An essential part for the shallow water equations and other conservation laws with source terms is that they often admit steady-state solutions in which the flux gradients are exactly balanced by the source terms [99]. Well-balanced schemes are designed to preserve exactly these steady-state solutions with relatively coarse meshes, and therefore it is desirable to design numerical methods which have the well-balanced property. Typical applications include the dam break problem, flood waves and run-up phenomena at a coast with tsunamis being the most impressive example. Special attention needs to be paid near the dry/wet front to preserve the water height positivity, otherwise they may produce non-physical negative water height, which becomes problematic when calculating the eigenvalues and renders the system not hyperbolic and not well-posed.

There are several applications for free surface flows, such as in ocean, environmental, hydraulic engineering and atmospheric modeling, with wide examples that include the dam break and flooding problem, tidal flows in coastal water region, nearshore wave propagation with complex bathymetry structure, tsunami wave propagation and ocean

model [25, 42, 58, 78, 93, 95]. These equations play a critical role in the modeling and simulation of free surface flows in rivers and coastal areas, and can predict tides, storm surge levels and coastline changes from hurricanes and ocean currents. Shallow water equations also arise in atmospheric flows, debris flows, and certain hydraulic structures like open channels and sedimentation tanks. The modeling take the form of non-homogeneous hyperbolic conservation laws with source terms encompassing the effects of bathymetry and viscous friction on the bottom. The variation of the bottom may be considered as the only source term, but other terms, such as a friction term or variations of the channel width, could also be added.

Transport of fluids in porous media is important both in scientific and technological areas, such as chemical, civil, agricultural, environmental, petroleum and mechanic engineering. Many difficulties and challenges arise on the mathematical formulation of the physical processes that govern multiphase flow in heterogeneous reservoirs, mainly due to their inherent multi-scale nature. We highlight the lack of analytical solutions in three-phase flow models and well-understanding of the underlying theory. Moreover, geological properties of the medium like permeability or porosity may present heterogeneities and are modeled in the PDE system as discontinuous coefficients with abrupt gradients [54]. In this way, the development and numerical analysis of accurate and efficient algorithms constitute an alternative to the mathematical understanding of nonlinear dynamics of these PDEs.

1.2 Aims and objectives of the thesis proposal

In this thesis, the author aspires to contribute to a novel approach for the numerical computing of convection-diffusion and balance law problems.

The objectives of this thesis are highlighted as follows:

- We will explore the use of the integrated local space-time finite control volume in a Lagrangian-Eulerian framework developed in the context of parabolic convection-diffusion equation to design a locally conservative scheme for balance laws to account the balance between numerical approximations of the hyperbolic flux function and the source term linked to steady solutions (see Chapter 2). Our Lagrangian-Eulerian scheme is aimed to be not dependent on a particular structure of the source term. The designed scheme is independent of Riemann problem solutions, but if available for a particular problem it is somewhat natural to incorporate such information into the procedure and thus yielding flexibility to the development of distinct numerical strategies upon the specific model under consideration. A set of representative numerical experiments for nonlinear problems cited in the literature of hyperbolic conservation laws and balance laws are presented to illustrate the performance of the

new method. The numerical results are compared with accuracy to the approximate solutions or exact solutions whenever possible.

- We present further developments on various branches of the Lagrangian-Eulerian framework, such as nonstaggered formulations and applications, weak asymptotic solutions theory making way to sketch a convergence proof and applications to convection-diffusion problems with spatial discontinuities modeling two- and three-phase flow problems.
- The development and implementation of a hybrid and mixed finite element formalism with a novel reinterpretation of Robin coupling conditions and a set of numerical studies with the few examples available in the literature (see Chapter 4).

1.3 Preliminary Results and Ongoing Work

The main scientific works generated by the current thesis are listed as follows:

Papers

- A significant result of this work is the article published under the title of “**A new finite volume approach for transport models and related applications with balancing source terms**” [6], in the journal *Mathematics and Computers in Simulation*. In this work, we expanded the new finite volume scheme for numerically solving transport models associated with hyperbolic problems and also balance laws. The approach was applied to several nontrivial examples to show evidence that we are calculating the correct qualitatively good solutions with an accurate resolution of small perturbations around the stationary solution. We discussed applications of the new method to classical and nonclassical nonlinear hyperbolic conservation and balance laws such as the classical inviscid Burgers equation, two-phase and three-phase flow problems in porous media as well as numerical experiments for nonlinear shallow water equations with friction terms. A discussion on the source term as a discontinuous function in x was included. We also extended the Lagrangian-Eulerian framework to the two-dimensional scalar conservation law, along with pertinent numerical experiments to show the performance of the new method.

Talks

- We gave an oral presentation at the *International Conference on Approximation Methods and Numerical Modelling in Environment and Natural Resources MAMERN VI (2015)*, in Pau, France. We constructed a simple numerical scheme based on a

reformulation of the hyperbolic conservation law in terms of an equivalent locally conservative space-time in divergence form. Such reformulation is exact in the sense that it respects the same fundamental weak form principle for conservation laws and that it comes with a natural interpretation linked to the classical finite volume framework. The novel approach was applied to classical and nonclassical nonlinear hyperbolic conservation laws (scalar and systems), to two- and three-phase Buckley-Leverett problems, to the classical inviscid Burgers equation and to the classical 2 by 2 system of nonlinear shallow water equations.

- We have also presented the work titled **“Solving hyperbolic conservation laws by using Lagrangian-Eulerian approach”** at the *XXXVI Congresso Nacional de Matemática Aplicada e Computacional* in September, 2016, in which we discussed a nonstaggered procedure for numerically solving nonlinear hyperbolic conservation law problems by means of a Lagrangian-Eulerian framework with enhanced resolution and accuracy of the approximations, making use of polynomial reconstruction.
- Two other works were presented at the *2nd IMPA-InterPore Conference on Porous Media: Conservation Laws, Numerics and Applications* in October, 2016. The first one is titled **“A numerical scheme based in a conservative formulation for solving hyperbolic conservation laws”** and was a poster presentation, in which we implemented the ideas of the Lagrangian-Eulerian framework for solving nonlinear conservation law problems, reformulating the conservation law into a divergence form, locally conservative in space-time. The second one was titled **“An approximation to hyperbolic conservation laws using a Lagrangian-Eulerian approach”** and was a poster presentation.
- We have presented the work titled **“A Conservative Lagrangian-Eulerian Finite Volume Approximation Method for Balance Law Problems”**, as an oral presentation at the *2017 SIAM Annual Meeting* in July, 2017, in which we presented further developments of the Lagrangian-Eulerian framework for numerically solving nonlinear balance law problems.
- Finally, we had a work at the *XXXVII Congresso Nacional de Matemática Aplicada e Computacional* in September, 2017, accepted for an oral presentation in which we discussed a numerical method based on a nonstaggered Lagrangian-Eulerian framework for approximate solutions of nonlinear balance law problems, which can be considered a further development of [9], but now for balance laws.

Conference Papers

- The results of the talk on the *International Conference on Approximation Methods and Numerical Modelling in Environment and Natural Resources MAMERN VI*

(2015), in Pau, France were published in the *Proceedings of the 6th International Conference on Approximation Methods and Numerical Modelling in Environment and Natural Resources*, under the title of “**A Lagrangian-Eulerian algorithm for solving hyperbolic conservation laws with applications**” [5].

- We also published in the *Proceeding Series of the Brazilian Society of Computational and Applied Mathematics*, under the title of “**A Lagrangian-Eulerian algorithm for solving hyperbolic conservation laws with applications**” [9].

1.4 Organization of the thesis proposal

This work is organized in the following manner: First, in Chapter 2, we present the Lagrangean-Eulerian framework, now with reconstruction and predictor-corrector techniques, in order to obtain a robust numerical scheme. We present the development of the method for hyperbolic conservation laws, for balance laws, the extension to systems and an unconventional two-dimensional approach for conservation laws. The chapter ends with various numerical simulations for each numerical scheme developed so far. We highlight the difficulty of approximating various shallow water equations problems and two- and three-phase flow problems. Chapter 3 then presents a follow-up on the many branches of developments within this framework. We first present a nonstaggered version of the Lagrangian-Eulerian framework for the classes of problems discussed before: hyperbolic conservation laws (both scalar and systems), balance law problems and a two-dimensional extension. Next, we present some advances towards a proof of convergence via the weak asymptotic solutions theory. The chapter ends with a very difficult problem of flow in porous media with discontinuous coefficients in the diffusive operator. This approach will comprise a correction step for the diffusive operator and because we can use any hyperbolic numerical method for the convection operator we chose the Lagrangian-Eulerian numerical scheme, in a more classical form. Finally, Chapter 4 presents several approaches for solving spatially-independent and spatially-dependent two- and three-phase flow problems, by means of a hybrid mixed finite element method. We present our approach for solving two-phase one-dimensional problems that overcomes the difficulties encountered by the previous approaches, and we expect to extend such ideas to three-phase problems. Chapter 5 presents our final remarks about these subjects and our perspectives for future works.

Part I

The Lagrangian-Eulerian Framework

2 Lagrangian-Eulerian Numerical Schemes

The development of Lagrangian methods for numerically solving convection-diffusion problems started with the seminal work by Russel [86], in which a numerical method based on the classical characteristic method was developed (the so-called “Modified Method of Characteristics”). The main advantage of such method compared to other existing procedures is that, for convection-dominated diffusive transport problems, a CFL-like condition to restrict the timestep size does not exist, and longer timesteps can be used. This is important for simulating oil reservoirs, in which numerical simulations with industrial interest must make predictions of oil production for several decades. The proposed method in [86], however, had a serious issue: the fluid mass was not conserved. This difficulty motivated the development of several new methods that had such property of fluid mass conservation. A group of researchers developed a class of methods called ELLAM (“Eulerian Lagrangian Localized Adjoint Methods”; see, for example, [32]), and another group developed methods known as “Mixed-Characteristics” [16]. In both classes of numerical methods, the local conservation of fluid masses was obtained by approximating the solution in time through tubes in space-time built as a union of characteristic curves. The development of computational codes for these methods was extremely complicated, because the union set of characteristic curves does not lead to impervious surfaces in fluid flow. The inherent difficulties of the aforementioned method lead to the development to a new class of locally conservative methods that make use of new curves on space-time that follow impervious surfaces in fluid flow. Douglas Jr. et al. [48] identified the region in the space-time domain where the mass conservation takes place, but linked to a scalar convection-dominated nonlinear parabolic problem, which models the immiscible incompressible two-phase flow in a porous medium. The key ingredient to finding this conservative region was the use of a Lagrangian-Eulerian framework; see [15] for related works with applications to radionuclide transport problems. Thus, locally conservative Lagrangean methods with very simple implementation were developed for nonlinear convection-diffusion problems. Within recent developments on these topics, the work by Perez [84] has studied purely hyperbolic problems from the Lagrangean point of view. This work extended the study for both conservation laws and balance laws. It presented new Lagrangian-Eulerian finite difference methods, as well as convergence proofs, and also a new class of methods for multidimensional problems in the same framework. In particular, a convergence proof for the unique entropy solution was established for the case of a Lagrangian-Eulerian monotone finite difference scheme related to a scalar hyperbolic conservation law. We refer to [10] for recent developments on this subject.

It is well known that many well-balanced schemes have been proposed since the

milestone work of Greenberg and LeRoux [61]. The focus of many such works was to handle shallow water equations over non-trivial topographies. The key issue is the construction of well-balanced nonlinear schemes that recover the time-asymptotic behavior of the underlying nonlinear balance law. There are relevant studies for approximation methods and numerical analysis devoted to balance law and hyperbolic law problems. Naturally, all methods exhibit advantages and disadvantages, since the underlying differential equations lead to very hard problems with a lack of general theory (see, e.g., [24, 26, 27, 31, 43, 50, 57, 60, 61, 66, 74, 77, 84]). See also [12, 56] for surveys on analytical and numerical aspects of one-dimensional hyperbolic balance laws and [55] for a good discussion of two-dimensional balance law problems along with an up-to-date and comprehensive list of references. The work [55] also includes relevant theoretical aspects of scalar conservation laws in several spatial dimensions in a more flexible Godunov framework to handle local nonlinear wave patterns to account for the flux computations. These schemes evolved following the natural understanding of fundamental concepts from the theory of nonlinear hyperbolic conservation laws concerning the properties of the characteristic surfaces, such as existence, uniqueness, and solution of the Riemann problems. Also, for a scalar balance law, the solution might depend strongly on certain properties inherent to the source term (see, e.g., [15, 56, 57, 61, 63, 74]).

The situation of balance laws $u_t + f_x(u) = g(u, x)$, with $g(u, x)$ discontinuous in x is another challenging problem encountered for such class of differential equations from both a theoretical and a numerical point of view. A kinetic scheme, with convergence proof for the scalar related problem, was introduced in [26]. Essentially, the authors propose a kinetic interpretation of upwinding techniques, taking into account the source terms to develop an equilibrium scheme as a result. Another approach was introduced in [66] (see also [27]). Without the use of upwinding solvers, this method uses the interface value rather than the cell averages for the source terms that balance the nonlinear convection at the cell interface, allowing the numerical capturing of the steady state with a formal high order accuracy. A successful alternative to accounting for the balance between the nonlinear flux and the source terms with $g(u, x)$ discontinuous in x is the use of a central differencing scheme as discussed in [7] for gas dynamics Euler equations with stiff relaxation source terms; see also [27]. A distinct numerical framework, based on Riemann solvers using local characteristic decompositions, can be found in [50]. In paper [52], the authors were concerned with the Riemann problem of the Burgers equation with a discontinuous source term, motivated by the study of propagation of singular waves in radiation hydrodynamics. Moreover, they were able to construct the global entropy solution to the related Riemann problem linked to this model. It turns out that the discontinuity of the source term has clear influences on the shock or rarefaction waves generated by the initial Riemann data. It is worth mentioning that other related problems were also described in the literature supported by numerical experiments. The interested reader is referred to the papers [7, 12,

26, 27, 50, 52, 56, 66] and papers cited therein for further details.

In this chapter we develop a numerical scheme for solving nonlinear hyperbolic conservation and balance law problems using a Lagrangian-Eulerian approach [15, 48, 63, 74]. Recently in [84], such ideas were extended to nonlinear purely hyperbolic conservation and balance laws – scalar case and systems of equations. We will explore the above mentioned innovative ideas to give a formal construction of accurate Lagrangian-Eulerian schemes for transport models and related applications with balancing source terms. As features of the novel algorithm, we highlight: we verified through numerical experiments that the new scheme seems to be locally conservative in balancing the flux and source term gradients and preserves a component-wise structure at the discrete level for systems of equations. Besides, we also discuss a set of numerical experiments to nonlinear scalar two-dimensional problems with non-symmetric and nonconvex flux function for systems of balance laws. This novel approach is applied to several nontrivial examples to show evidence that we are calculating the correct qualitatively good solutions with the accurate resolution of small perturbations around the stationary solution. We discuss applications of the new method to nonlinear hyperbolic conservation and balance laws such as the classical inviscid Burgers equation, two-phase and three-phase flow problems in porous media as well as numerical experiments for nonlinear shallow water equations with friction terms. Furthermore, our new Lagrangian-Eulerian framework is aimed to be independent of a particular structure of the flux function as well as of the source terms. We were able to reproduce several models indistinctly within the same formalism, and this indicates that our method is general to some extent. It is also important to notice that our scheme does not depend on exact or approximate solutions to Riemann problems.

2.1 A Lagrangian-Eulerian constructive approximation scheme for nonlinear hyperbolic conservation laws

We provide a formal development of the analogue Lagrangian-Eulerian scheme [84] – see also [15, 48] – for solving numerically first-order scalar hyperbolic equations $x \in \mathbb{R}$, $t > 0$, $u : (\mathbb{R}, \mathbb{R}^+) \rightarrow \mathbb{R}$, $H : \mathbb{R} \rightarrow \mathbb{R}$:

$$\frac{\partial u}{\partial t} + \frac{\partial H(u)}{\partial x} = 0, \quad x \in \mathbb{R}, t > 0 \quad u(x, 0) = \eta(x), \quad x \in \mathbb{R}. \quad (2.1)$$

Although our primary interest is to give a formal construction of the new Lagrangian-Eulerian method, the relevant issue of rigorous convergence proof to the corresponding weak entropy solution must be further addressed. As in the Lagrangian-Eulerian schemes [15, 48], local conservation is obtained by integrating the conservation law over the region in the space-time domain where the conservation of the mass flux takes place. For that, we consider the Lagrangian-Eulerian finite-volume cell centers,

$$D_j^n = \{(t, x) / t^n \leq t \leq t^{n+1}, \sigma_j^n(t) \leq x \leq \sigma_{j+1}^n(t)\}, \quad (2.2)$$

where $\sigma_j^n(t)$ is the parameterized integral curve such that $\sigma_j^n(t^n) = x_j^n$ and the conservation relation 2.4 that will result in equations 2.6. These curves are the lateral boundaries of the domain D_j^n in (2.2) and we define $\bar{x}_{j-\frac{1}{2}}^{n+1} := \sigma_j^n(t^{n+1})$ and $\bar{x}_{j+\frac{1}{2}}^{n+1} := \sigma_{j+1}^n(t^{n+1})$ as their endpoints in time t^{n+1} . Due to the inherent nature of conservation laws, the numerical scheme is expected to satisfy some type of mass conservation from time t^n in the space domain $[x_j^n, x_{j+1}^n]$ to time t^{n+1} in the space domain $[\bar{x}_{j-\frac{1}{2}}^{n+1}, \bar{x}_{j+\frac{1}{2}}^{n+1}]$. With this, the flux through curves $\sigma_j^n(t)$ must be zero. By defining the parametrized curve $(t, \sigma_j^n(t))$ and its tangent vector $(1, \sigma_j'^n(t))$, the normal vector must be $\vec{n} = (\sigma_j'^n(t), -1)$. Figure 1 presents an illustration of such objects, and different configurations of forward and backward curves will be normally handled by the CFL stability condition. We consider the equation (2.1) written in locally conservative space-time generalized divergence form (along $u(x, 0) = \eta(x)$, for $x \in \mathbb{R}$):

$$\nabla_{t,x} \cdot \begin{bmatrix} u \\ H(u) \end{bmatrix} = 0, \quad t > 0, \quad x \in \mathbb{R}. \quad (2.3)$$

We apply the divergence theorem on (2.3) over the integral tube D_j^n ,

$$\iint_{D_j^n} \nabla_{t,x} \cdot \begin{bmatrix} u \\ H(u) \end{bmatrix} dV = 0 \Leftrightarrow \oint_{\partial D_j^n} \begin{bmatrix} u \\ H(u) \end{bmatrix} \cdot \vec{n} ds = 0 \quad (2.4)$$

and then, by using the fact that the line integrals over curves $\sigma_j^n(t)$ vanish, we get the local conservation relation

$$\int_{\bar{x}_{j-\frac{1}{2}}^{n+1}}^{\bar{x}_{j+\frac{1}{2}}^{n+1}} u(x, t^{n+1}) dx = \int_{x_j^n}^{x_{j+1}^n} u(x, t^n) dx. \quad (2.5)$$

We essentially mimic the procedures of [15, 84]. In general, the curves $\sigma_j^n(t)$ are not straight lines, but rather solutions of the set of nonlinear (local) differential system of equations (by the definition of the normal vector and equation (2.4)):

$$\frac{d\sigma_j^n(t)}{dt} = \frac{H(u)}{u}, \quad \text{for } t^n < t \leq t^{n+1}, \quad (2.6)$$

with the initial condition $\sigma_j^n(t^n) = x_j^n$, assuming $u \neq 0$ (see Remark 2.1).

The extension of this construction follows naturally from the finite volume formulation of the linear Lagrangian-Eulerian scheme as building block to construct *local* approximations such as $f_j^n = \frac{H(U_j^n)}{U_j^n} \approx \frac{H(u)}{u}$ with the initial condition $\sigma_j^n(t^n) = x_j^n$.

Indeed, distinct and high-order approximations are also acceptable for $\frac{d\sigma_j^n(t)}{dt}$ and can be viewed as free ingredients to improve accuracy of the new family of Lagrangian-Eulerian. Equation (2.5) defines conservation of mass but in a different mesh cell-centered in points $\bar{x}_{j+\frac{1}{2}}$. We will later address how to project these volumes back to the original mesh. We introduce a reconstruction from a piecewise constant numerical data to a piecewise linear approximation (but high-order reconstructions are acceptable), through the use of MUSCL-type interpolants [76]:

$$L_j(x) = U_j^n + (x - x_j) \frac{1}{\Delta x} U_j'. \quad (2.7)$$

Here, $\frac{1}{\Delta x} U_j'$ is a numerical approximation of the derivative, and we shall discuss a few examples of slope limiters, which will retain the desired properties of consistency of the numerical flux function. There are several choices of slope limiters (in [76] there is a good compilation of many options). A priori choice of such slope limiters is quite hard, but they are chosen upon the underlying model problem under investigation. Here we make use of the following three options. The first is,

$$U_j' = MM \left\{ \Delta U_{j+\frac{1}{2}}^n, \Delta U_{j-\frac{1}{2}}^n \right\}, \quad (2.8)$$

where MM stands for the usual MinMod limiter [76], with $\Delta U_{j+\frac{1}{2}}^n = U_{j+1}^n - U_j^n$,

$$MM\{\sigma, \tau\} = \frac{1}{2} [sgn(\sigma) + sgn(\tau)] \min\{|\sigma|, |\tau|\}. \quad (2.9)$$

A second choice for the slope limiter can be

$$U_j' = MM \left\{ \alpha \Delta U_{j+\frac{1}{2}}^n, \frac{1}{2}(U_{j+1}^n - U_{j-1}^n), \alpha \Delta U_{j-\frac{1}{2}}^n \right\}, \quad (2.10)$$

and this choice for slope limiter allows steeper slopes near discontinuities and retain accuracy in smooth regions. Here, we must extend definition (2.9) for three variables as $MM_3\{\sigma, \tau, \rho\} = MM\{\sigma, MM\{\tau, \rho\}\}$. The range of the parameter α is typically guided

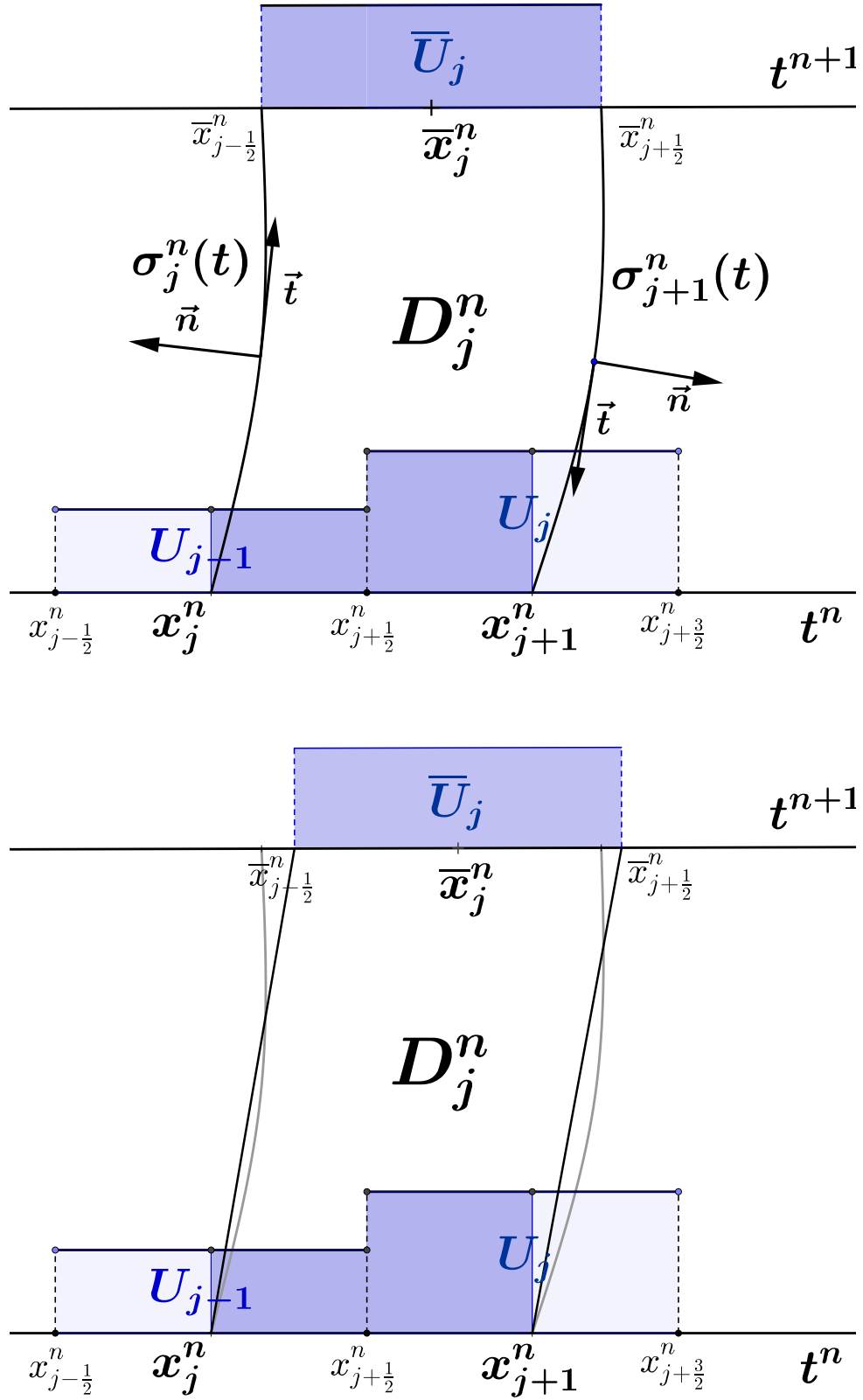


Figure 1 – Illustration of the integral tubes D_j^n . On the top picture, we illustrate the nonlinear evolution via the integral curves σ linked to D_j^n in (2.6). A first order approximation is performed to the construction of the local Lagrangian-Eulerian space-time control-volume, and it is shown on the bottom picture. We notice that higher order approximations are naturally permissible as well.

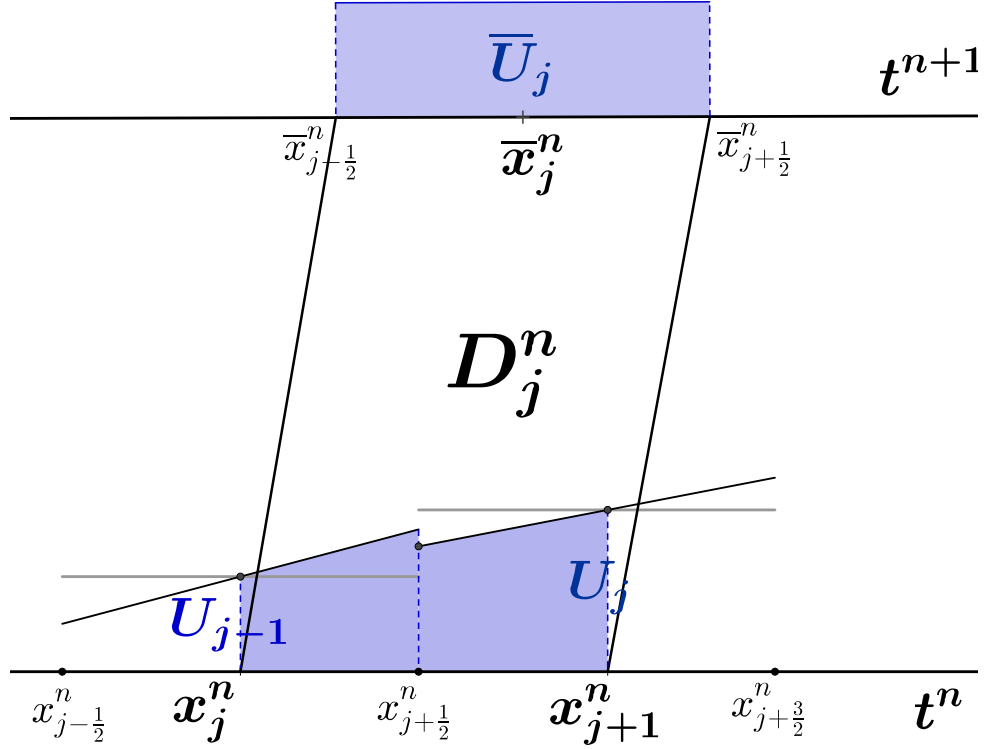


Figure 2 – The reconstruction step. The cell $[x_{j-\frac{1}{2}}^{n+1}, x_{j+\frac{1}{2}}^{n+1}]$ conserves information both from U_j and U_{j-1} .

by the CFL condition (see, e.g., [76]). In this work we also make use of the following high order slope limiter, namely, the UNO choice (where $\Delta^2 U_j^n = U_{j+1}^n - 2U_j^n + U_{j-1}^n$),

$$U_j' = MM \left\{ \Delta U_{j-\frac{1}{2}}^n + \delta^2(U_{j-1}^n, u_j), \Delta U_{j+\frac{1}{2}}^n + \delta^2(U_j^n, U_{j+1}^n) \right\}, \quad (2.11)$$

where $\delta^2(U_j^n, U_{j+1}^n) = \frac{1}{2} MM (\Delta^2 U_j^n, \Delta^2 U_{j+1}^n)$. Preliminary experiments discussed in Section 2.5 have shown that the UNO option has resulted in more satisfactory approximations for our test cases.

We notice that the integral curves may define a new mesh width in the x variable, say h_j^{n+1} . This will be addressed later in the projection step, in which we normalize the new mesh grid at time t^{n+1} into the usual grid from time t^n . In the linear advection case, however, this width is constant. The discrete version of equation (2.5), using the

approximation above, is

$$\begin{aligned}
 \bar{U}_j^{n+1} &= \frac{1}{h_j^{n+1}} \int_{\bar{x}_j^{n+1}-\frac{1}{2}}^{\bar{x}_j^{n+1}+\frac{1}{2}} u(x, t^{n+1}) dx = \frac{1}{h_j^{n+1}} \int_{x_j^n}^{x_{j+1}^n} u(x, t^n) dx \\
 &= \frac{h}{h_j^{n+1}} \left(\frac{1}{h} \int_{x_j^n}^{x_{j+\frac{1}{2}}^n} u(x, t^n) dx + \frac{1}{h} \int_{x_{j+\frac{1}{2}}^n}^{x_{j+1}^n} u(x, t^n) dx \right) \\
 &= \frac{h}{h_j^{n+1}} \frac{1}{2} (U_j^n + U_{j+1}^n) + \frac{1}{h_j^{n+1}} \frac{1}{16} h (U_j'^n - U_{j+1}'^n),
 \end{aligned} \tag{2.12}$$

where we use $\bar{U}_j^{n+1} := \frac{1}{h_j^{n+1}} \int_{\bar{x}_j^{n+1}-\frac{1}{2}}^{\bar{x}_j^{n+1}+\frac{1}{2}} u(x, t^{n+1}) dx$ and $U_j^n := \frac{1}{h} \int_{x_j^n}^{x_{j+1}^n} u(x, t^n) dx$.

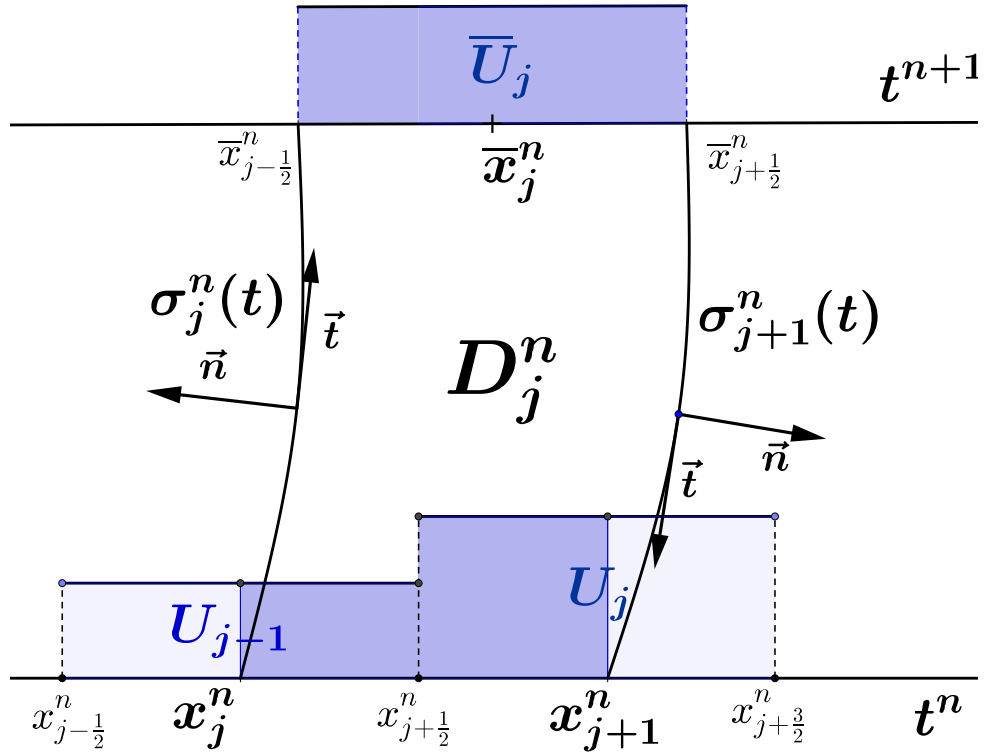


Figure 3 – Illustration of the conservation relations (2.5) and (2.12). The evolution step guarantees conservation due to the no-flow conditions on the integral curves.

We also introduce a predictor-corrector approximation by evaluating $f_j^{n+\frac{1}{2}}$, instead of f_j^n using Taylor expansion and the conservation law, and it reads,

$$U_j^{n+\frac{1}{2}} := u(x_j, t + \frac{\Delta t}{2}) = u_j(t) - \frac{1}{2} \frac{\Delta t}{\Delta x} H_j', \tag{2.13}$$

so that $f_j^{n+\frac{1}{2}} = \frac{H(U_j^{n+\frac{1}{2}})}{U_j^{n+\frac{1}{2}}}$. Now, the solutions $\sigma_j^n(t)$ of the differential system equations are (local) straight lines, but they are not parallel as in the linear case, but subject to a CFL stability condition of the form (see [84]),

$$\max_j \left| \frac{f_j^n \Delta t^n}{h} \right| \leq \frac{\sqrt{2}}{2} \quad \text{and} \quad k^n = \min_n \Delta t^n. \quad (2.14)$$

Next, we obtain the resulting projection formula as follows

$$U_j^{n+1} = \frac{1}{h} c_0 \bar{U}_{j-1} + \frac{1}{h} c_1 \bar{U}_j, \quad \text{where } c_{0j} = \frac{h}{2} + f_j^{n+\frac{1}{2}} k^n \text{ and } c_{1j} = \frac{h}{2} - f_j^{n+\frac{1}{2}} k^n. \quad (2.15)$$

Here c_{0j} and c_{1j} are the projection coefficients [84]. Combining (2.15) with the discrete version of local conservation (2.12) reads,

$$\begin{aligned} U_j^{n+1} = & \left[\frac{c_0}{2h_j^{n+1}} (U_{j-1}^n + U_j^n) + \frac{c_0}{16h_j^{n+1}} (U_{j-1}'^n - U_j'^n) \right] \\ & + \left[\frac{c_1}{2h_j^{n+1}} (U_j^n + U_{j+1}^n) + \frac{c_1}{16h_j^{n+1}} (U_j'^n - U_{j+1}'^n) \right]. \end{aligned} \quad (2.16)$$

Notice that for each $j \in \mathbb{Z}$, $h_j^{n+1} = \bar{x}_{j+\frac{1}{2}}^{n+1} - \bar{x}_{j-\frac{1}{2}}^{n+1} = h + (f_{j+1}^{n+\frac{1}{2}} - f_j^{n+\frac{1}{2}})k^n$, and, also that: $h_j^{n+1} = c_{0j+1} + c_{1j}$. Thus,

$$c_{0j} = h_{j-1}^{n+1} - c_{1j-1} \quad \text{and} \quad c_{1j} = h_j^{n+1} - c_{0j+1}, \quad \text{with} \quad (2.17)$$

$$c_{1j-1} = \frac{1}{2}(h_{j-1}^{n+1} - f_{j-1}^{n+\frac{1}{2}}k^n - f_j^{n+\frac{1}{2}}k^n), \quad c_{0j+1} = \frac{1}{2}(h_j^{n+1} + f_j^{n+\frac{1}{2}}k^n + f_{j+1}^{n+\frac{1}{2}}k^n).$$

Finally, plugging (2.17) into (2.16), we obtain the discrete equation for the Lagrangian-Eulerian finite volume scheme with reconstruction,

$$\begin{aligned} U_j^{n+1} = & \frac{U_{j-1}^n + 2U_j^n + U_{j+1}^n}{4} + \frac{U_{j-1}'^n - U_{j+1}'^n}{32} \\ & + \frac{k^n}{4} \left(\frac{f_{j-1}^{n+\frac{1}{2}} + f_j^{n+\frac{1}{2}}}{h_{j-1}^{n+1}} [U_{j-1}^n + U_j^n] - \frac{f_j^{n+\frac{1}{2}} + f_{j+1}^{n+\frac{1}{2}}}{h_j^{n+1}} [U_j^n + U_{j+1}^n] \right) \\ & + \frac{k^n}{32} \left(\frac{f_{j-1}^{n+\frac{1}{2}} + f_j^{n+\frac{1}{2}}}{h_{j-1}^{n+1}} [U_{j-1}'^n - U_j'^n] - \frac{f_j^{n+\frac{1}{2}} + f_{j+1}^{n+\frac{1}{2}}}{h_j^{n+1}} [U_j'^n - U_{j+1}'^n] \right). \end{aligned} \quad (2.18)$$

The analogue finite difference scheme (2.18) is a Lagrangian-Eulerian scheme for the nonlinear problem (2.1). The obtained scheme (2.18) can also be written in a conservative form (a novelty result for such schemes):

$$U_j^{n+1} = U_j^n - \frac{k^n}{h} [F(U_j, U_{j+1}^n) - F(U_{j-1}^n, U_j^n)], \quad (2.19)$$

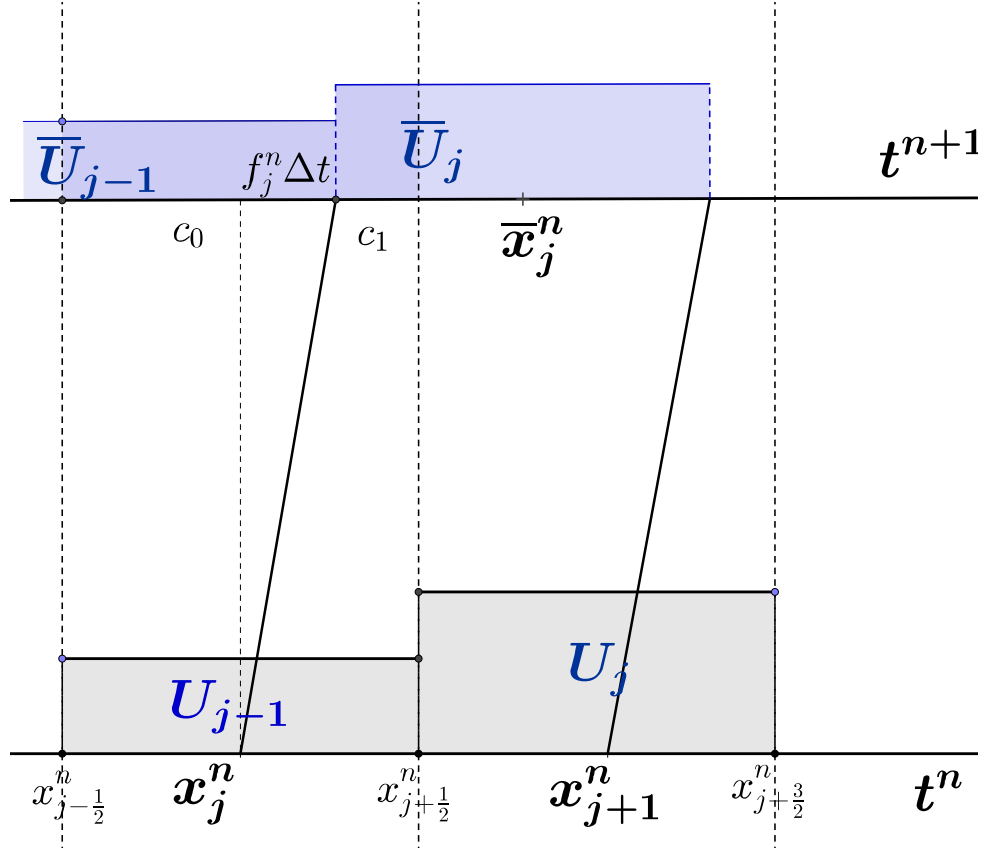


Figure 4 – The projection step. The cell $[x_{j-\frac{1}{2}}^{n+1}, x_{j+\frac{1}{2}}^{n+1}]$ collect information both from \bar{U}_j and \bar{U}_{j-1} , guided by the projection coefficients c_{0j} and c_{1j} given by (2.15).

with the Lagrangian-Eulerian numerical flux function defined by

$$F(U_j^n, U_{j+1}^n) = \frac{1}{4} \left(\frac{h}{k^n} (U_j^n - U_{j+1}^n) + \frac{h}{h_j^{n+1}} (f_j^{n+\frac{1}{2}} + f_{j+1}^{n+\frac{1}{2}}) (U_j^n + U_{j+1}^n) + \frac{h}{4k^n} (U_j^m + U_{j+1}^m) + \frac{h}{4h_j^{n+1}} (f_j^{n+\frac{1}{2}} + f_{j+1}^{n+\frac{1}{2}}) (U_j^m - U_{j+1}^m) \right). \quad (2.20)$$

Next, we will show in what follows that the Lagrangian-Eulerian numerical flux function (2.20) satisfy a form of Lipschitz continuous consistency, which in turn is a nice property for conservative numerical methods for nonlinear conservation law problems. Indeed, to show that the Lagrangian-Eulerian numerical flux satisfies a Lipschitz condition, we need (see [84]):

Lemma 2.1. *The numerical flux function defined by (2.20) is consistent with the differential equation (2.1).*

Proof. Immediate, i.e., $F(\bar{u}, \bar{u}) = H(\bar{u})$. Notice that for any choice of slope limiters, we have from (2.9) that (2.20) satisfy the consistency condition, the MinMod limiter in this case will be zero. The Lipschitz condition can also be proved by a straightforward argument and it is omitted. \square

Remark 2.1. *For the sake of simplicity of presentation we suppose $u \neq 0$ (this assumption can be suppressed by introducing some extra notation in the analysis to define the endpoints $[\bar{x}_{j-\frac{1}{2}}^{n+1}, \bar{x}_{j+\frac{1}{2}}^{n+1}]$ by analytical straight lines), when considering f_j in the case of $U_j = 0$. This means that for the resulting numerical scheme, pertinent to the Lagrangian-Eulerian framework at hand, that the projection step is not necessary anymore since the argument of the flux function (also for the numerical flux function) is now known along the vertical curves associated for the integral tubes, that are defined at the cell centers (see eqs. (2.2)-(2.6) and Figure 1).*

2.2 The Lagrangian-Eulerian scheme for hyperbolic balance laws

One may find, in a variety of physical problems, source terms that are balanced by internal forces and this balance supports multiple steady-state solutions that are stable. We are interested in designing well-balanced conceptually simple schemes, which have a well balanced property for static and moving equilibrium, applicable to a wide class of systems with source terms. The well-balance property can be formally enunciated as follows. For the system of balance laws,

$$\frac{\partial u}{\partial t} + \frac{\partial(H(u))}{\partial x} = G(u), \quad (2.21)$$

we denote u^e the stationary solution, which satisfies the equation,

$$\frac{\partial(H(u^e))}{\partial x} = G(u^e). \quad (2.22)$$

A numerical scheme is said to be *well-balanced*, if it fully satisfies a discrete version of the equilibrium equation (2.22). If a method is not well-balanced, the truncation error of solutions near the equilibrium state may be larger than $u(x, t) - u^e(x)$. Numerical experiments for solving balance laws have shown strong numerical evidence that such well-balanced property is satisfied when we applied the Lagrangian-Eulerian scheme for several models of balance laws [84].

Consider the scalar balance law problem,

$$\frac{\partial u}{\partial t} + \frac{\partial H(u)}{\partial x} = G(u), \quad t > 0, \quad x \in \mathbb{R}, \quad u(x, 0) = \eta(x) \quad x \in \mathbb{R}, \quad (2.23)$$

under the assumption $\iint_{D_j^n} G(u) \, dx \, dt < \infty$.

Now, write (2.23) as follows,

$$\nabla_{t,x} \cdot \begin{bmatrix} u \\ H(u) \end{bmatrix} = G(u) \quad t > 0, \quad x \in \mathbb{R}, \quad u(x, 0) = \eta(x) \quad x \in \mathbb{R}. \quad (2.24)$$

Now, let us integrate (2.24) over the local space-time integral tube D_j^n ,

$$\iint_{D_j^n} \nabla_{t,x} \cdot \begin{bmatrix} u \\ H(u) \end{bmatrix} \, dx \, dt = \iint_{D_j^n} G(u) \, dx \, dt. \quad (2.25)$$

Following the same arguments as in Section 2.1, we apply first the divergence theorem in (2.25) and, by means of the impervious boundaries given by $\sigma_j^n(t)$, reads:

$$\int_{\bar{x}_{j-\frac{1}{2}}^{n+1}}^{\bar{x}_{j+\frac{1}{2}}^{n+1}} u(x, t^{n+1}) \, dx = \int_{x_j^n}^{x_{j+1}^n} u(x, t^n) \, dx + \iint_{D_j^n} G(u) \, dx \, dt. \quad (2.26)$$

This equation can be viewed as the local space-time Lagrangian-Eulerian conservation relation for the balance law (2.26). Finally, we use (2.26) then to define,

$$\bar{U}_j^{n+1} = \frac{1}{h_j^{n+1}} \int_{\bar{x}_{j-\frac{1}{2}}^{n+1}}^{\bar{x}_{j+\frac{1}{2}}^{n+1}} u(x, t^{n+1}) dx = \frac{1}{h_j^{n+1}} \left[\int_{x_j^n}^{x_{j+1}^n} u(x, t^n) dx + \iint_{D_j^n} G(u) dx dt \right], \quad (2.27)$$

and its associated projection step over the original mesh grid, with $f_j^{n+\frac{1}{2}}$ defined as before,

$$U_j^{n+1} = \frac{1}{h} \left[\left(\frac{h}{2} + f_j^{n+\frac{1}{2}} k \right) \bar{U}_{j-1}^{n+1} + \left(\frac{h}{2} - f_j^{n+\frac{1}{2}} k \right) \bar{U}_j^{n+1} \right]. \quad (2.28)$$

The Lagrangian-Eulerian scheme for balance law is fully defined by combining equations (2.27) and (2.28). The key point here is how to design a discretization in a manner that an accurate balance between the gradients of the flux function and the source term is retained. Thus, let us now first extend the proposed scheme for linear hyperbolic conservation laws designed in the previous section to the case of balance laws in order to describe the features of the Lagrangian-Eulerian procedure.

Thus, combining equations (2.27)-(2.28), we obtain the Lagrangian-Eulerian scheme for nonlinear balance laws:

$$\begin{aligned} U_j^{n+1} &= \frac{U_{j-1}^n + 2U_j^n + U_{j+1}^n}{4} + \frac{U'_{j-1}{}^n - U'_{j+1}{}^n}{32} \\ &+ \frac{k^n}{4} \left(\frac{f_{j-1}^{n+\frac{1}{2}} + f_j^{n+\frac{1}{2}}}{h_{j-1}^{n+1}} [U_{j-1}^n + U_j^n] - \frac{f_j^{n+\frac{1}{2}} + f_{j+1}^{n+\frac{1}{2}}}{h_j^{n+1}} [U_j^n + U_{j+1}^n] \right) \\ &+ \frac{k^n}{32} \left(\frac{f_{j-1}^{n+\frac{1}{2}} + f_j^{n+\frac{1}{2}}}{h_{j-1}^{n+1}} [U'_{j-1}{}^n - U_j^n] - \frac{f_j^{n+\frac{1}{2}} + f_{j+1}^{n+\frac{1}{2}}}{h_j^{n+1}} [U_j^n - U'_{j+1}{}^n] \right) \\ &+ \frac{1}{h_j^{n+1}} \left[\frac{1}{h_j^{n+1}} \left(\frac{h_j^{n+1}}{2} + f_j^{n+\frac{1}{2}} k^n \right) \iint_{D_{j-1}^n} G(u(x, t)) dx dt \right. \\ &\left. + \frac{1}{h_j^{n+1}} \left(\frac{h_j^{n+1}}{2} - f_j^{n+\frac{1}{2}} k^n \right) \iint_{D_j^n} G(u(x, t)) dx dt \right]. \end{aligned} \quad (2.29)$$

Here, we use the same approximations as before with respect to (2.29), namely, $f_j^{n+\frac{1}{2}} = \frac{H(U_j^{n+\frac{1}{2}})}{U_j^{n+\frac{1}{2}}}$ and $f_j^n = \frac{H(U_j^n)}{U_j^n} \approx \frac{H(u)}{u}$. Notice that the quantities $\left(\frac{h_j^{n+1}}{2} + f_j^{n+\frac{1}{2}} k^n \right)$ and $\left(\frac{h_j^{n+1}}{2} - f_j^{n+\frac{1}{2}} k^n \right)$ are not the characteristic curves associated to the quasilinear form of the homogeneous counterpart of the balance law but rather they are precisely an approximation of the conservative integral tubes that are naturally extracted from the conservative integral form of the nonlinear balance law given by (2.23), which in turn dictates the dynamics of the local space-time control volume D_j^n and the position $\sigma_j^n(t)$

to any quadrature rule of the source term $G(u)$ of the RHS of (2.23). In addition, the balance problem is then solved by forward tracking the boundary of grid cells along the so-called integral tubes. This is a distinct feature of the proposed Lagrangian-Eulerian approach. The similar Lagrangian-Eulerian schemes in [63] are designed to handle trace-back integration related to purely hyperbolic problems rather than balance laws. Several quadrature rules can be used to such aim, based on the above framework [84]. We present a predictor-corrector type of approximation, but midpoint and trapezoidal rules have also been studied in the work [84].

We make use of $U_j^{n+\frac{1}{2}}$ as the known predictor value for $u(x, t)$ at space-time point (x_j, t^n) defined in 2.13. Thus, write the source term approximation as,

$$\iint_{D_j^n} G(u(x, t)) dx dt \approx \iint_{D_j^n} G(U_j^{n+\frac{1}{2}}) dx dt = G(U_j^{n+\frac{1}{2}}) \iint_{D_j^n} dx dt = G(U_j^{n+\frac{1}{2}}) \mathcal{A}(D_j^n),$$

where

$$\mathcal{A}(D_j^n) = \int_{t^n}^{t^{n+1}} \int_{\sigma_j^n(t)}^{\sigma_{j+1}^n(t)} dx dt = \int_{t^n}^{t^{n+1}} (\sigma_{j+1}^n(t) - \sigma_j^n(t)) dt. \quad (2.30)$$

Since $\sigma_{j+1}^n(t) - \sigma_j^n(t) = (t - t^n)f_{j+1}^{n+\frac{1}{2}} + x_{j+1}^n - (t - t^n)f_j^{n+\frac{1}{2}} - x_j^n = (t - t^n)(f_{j+1}^{n+\frac{1}{2}} - f_j^{n+\frac{1}{2}}) + h$, we recast (2.30) as,

$$\mathcal{A}(D_j^n) = k \left[\frac{k}{2}(f_{j+1}^{n+\frac{1}{2}} - f_j^{n+\frac{1}{2}}) + h \right].$$

Now, in view of the balance law $u_t + H_x(u) = G(u)$ we might write $u_t = G(u) - H_x(u)$ and thus reads,

$$G(u_j^{n+\frac{1}{2}}) \approx G(u(x_j^n, t^n) + \frac{k}{2}u_t(x_j^n, t^n)) = G \left[u_j^n + \frac{k}{2}(G(u_j^n) - (H(u))_x)_j^n \right]. \quad (2.31)$$

Here again the quantity $H_x(u(x, t))_j^n$ denotes the numerical derivative of function $H(u)$ with respect to space variable x evaluated at point (x_j, t^n) , and a family of slope limiters can be used here. Finally, from equations (2.30) and (2.31), we might write,

$$\iint_{D_j^n} G(u(x, t)) dx dt \approx k^n G \left[U_j^n + \frac{k^n}{2}(G(U_j^n) - H_x(u)_j^{n+\frac{1}{2}}) \right] \left[\frac{k^n}{2}(f_{j+1}^{n+\frac{1}{2}} - f_j^{n+\frac{1}{2}}) + h_j^{n+1} \right]. \quad (2.32)$$

2.3 Systems of hyperbolic conservation laws and balance laws

We now turn our attention to describing how to extend the scalar Lagrangian-Eulerian procedure to one-dimensional systems of balance laws $u_t + f_x(u) = G(u)$, where now $u(x, t)$ can be viewed as the unknown n -vector of the form $u = (u_1(x, t), \dots, u_n(x, t))^T$, and $f(u)$ is the flux vector function such that $f(u) = (f_1(u), f_2(u), \dots, f_n(u))^T$. We will see that the analogue Lagrangian-Eulerian scheme in the case of systems of balance laws is a straightforward application of the scalar framework and that retains all the simplicities of the scalar case. For simplicity of presentation and with no loss of generality, let us consider the following prototype 3×3 system of balance laws.

We consider the system of balance laws

$$Q_t + [F(Q)]_x = G(Q), \quad (2.33)$$

where $F(Q) = [f_1(Q), f_2(Q), f_3(Q)]$, $Q = [u, v, w]$, $u = u(x, t)$, $v = v(x, t)$ and $w = w(x, t)$, along with $G(Q) = [g_1(Q), g_2(Q), g_3(Q)]$. System (2.33) can be written in open form as,

$$\begin{aligned} u_t + [f_1(u, v, w)]_x &= g_1(u, v, w), \\ v_t + [f_2(u, v, w)]_x &= g_2(u, v, w), \\ w_t + [f_3(u, v, w)]_x &= g_3(u, v, w). \end{aligned} \quad (2.34)$$

As before, we consider the space-time control finite volumes for each variable u, v, w as follows, (see Figure 5 for an illustration of the integral tubes and its approximations for systems),

$$D_{s,j}^n = \{(t, x) / t^n \leq t \leq t^{n+1}, \quad \sigma_{s,j}^n(t) \leq x \leq \sigma_{s,j+1}^n(t)\}, \quad s = u, v, w, \quad (2.35)$$

where $\sigma_{u,j}^n(t)$, $\sigma_{v,j}^n(t)$ and $\sigma_{w,j}^n(t)$ are parametrized curves such that $\sigma_{u,j}^n(t^n) = x_j^n$, $\sigma_{v,j}^n(t^n) = x_j^n$ and $\sigma_{w,j}^n(t^n) = x_j^n$. These curves $\sigma_{s,j}^n(t)$, $s = u, v, w$ define the “lateral boundaries” of integral tubes for each primitive variable u, v, w , that will be used to design a balancing *unbiased* upwinding Riemann-solver-free discretization between the numerical flux functions and the source terms by forward tracking the boundaries along the so-called integral tubes. Formally, the divergence theorem can be used in the (2.35), the space-time finite volumes $D_{u,j}^n$, $D_{v,j}^n$ and $D_{w,j}^n$. By construction of the algorithm, as before, this implies that curves $\sigma_{s,j}^n(t)$ and $\sigma_{s,j+1}^n(t)$, for $s = u, v, w$ are naturally zero-flux boundaries. Similarly, from this fact the space-time $D_{s,j}^n$, $s = u, v, w$ are then called as “Integral tubes” for $t^n \leq t \leq t^{n+1}$. As a consequence we get, for the normal vectors n_s of each integral curve for each variable $s = u, v, w$, $\left[1, \frac{d\sigma_{s,j}^n(t)}{dt}\right] \perp n_s$ and $\left[1, \frac{d\sigma_{s,j+1}^n(t)}{dt}\right] \perp n_s$ since the slopes $\frac{d\sigma_{s,j}^n(t)}{dt}$ are one-to-one equal to the slope of the vector $[s, f_k(Q)]$, $s = u, v, w$; $k = 1, 2, 3$, respectively, over the parametrized curves $\sigma_{s,j}^n(t)$ and $\sigma_{s,j+1}^n(t)$, $s = u, v, w$, $j \in \mathbb{Z}$. Therefore $\sigma_{s,j}^n(t)$, $s = u, v, w$

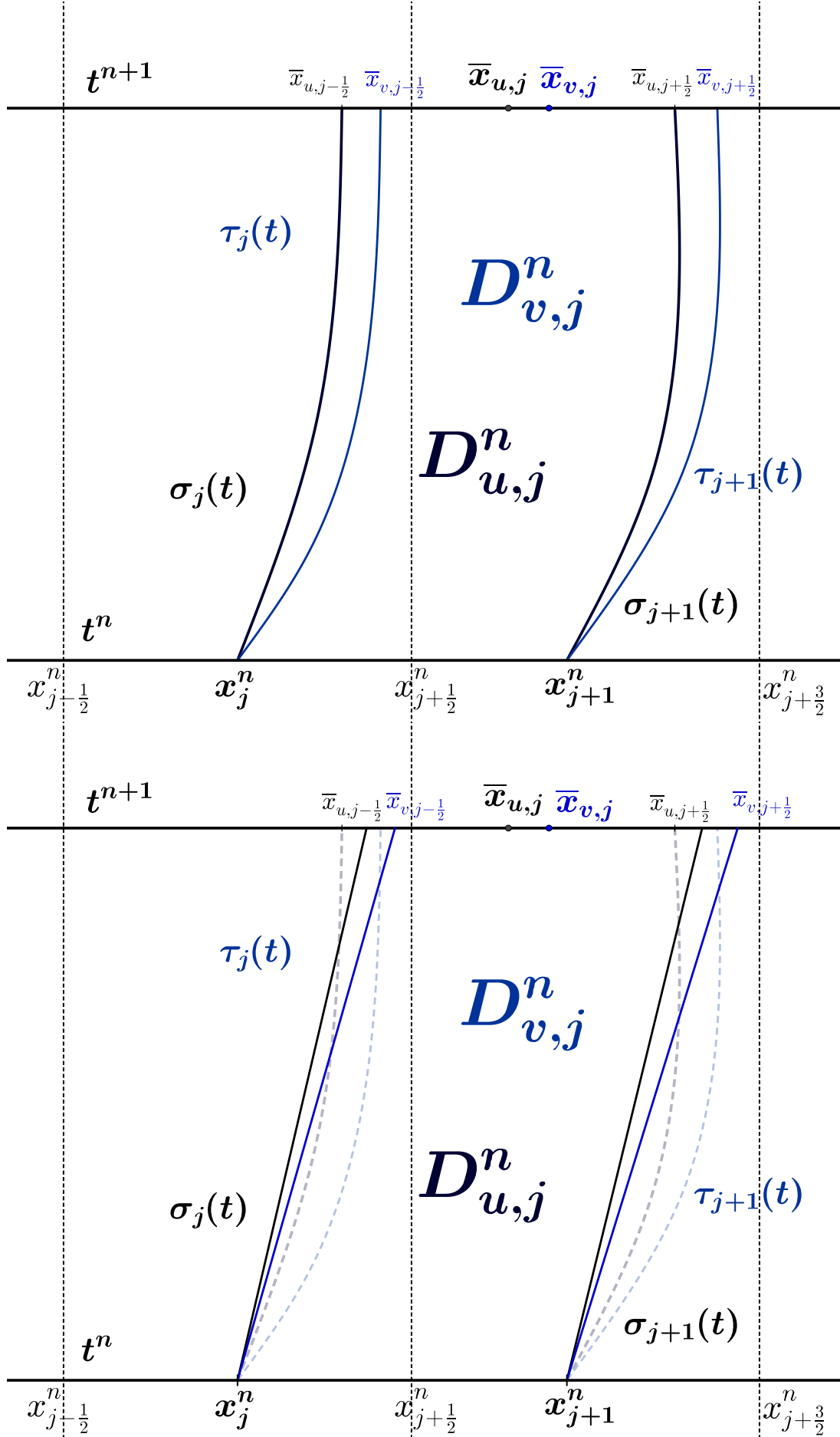


Figure 5 – On the top picture (resp. bottom) we show an illustration of the continuous (resp. discrete) local space-time integral tube domains $D_{s,j}^n$, for each $s = u, v, w$.

are solutions of the set of ODEs,

$$\frac{d\sigma_{s,j}^n(t)}{dt} = \frac{f_k(u, v, w)}{s}, \quad \sigma_{s,j}^n(t^n) = x_j^n, \quad t^n \leq t \leq t^{n+1}, \quad \text{for each } s = u, v, w; k = 1, 2, 3, \quad (2.36)$$

where $u, v, w \neq 0$. As a consequence of the divergence theorem and the above equations (2.35)-(2.36), the integrals over curves $\sigma_{s,j}^n(t)$, $s = u, v, w$ vanish and the line integral over the boundary of the region $\partial D_{s,j}^n$ leads to,

$$\int_{\bar{x}_{j-\frac{1}{2}}^{n+1}}^{\bar{x}_{j+\frac{1}{2}}^{n+1}} s(x, t^{n+1}) dx = \int_{x_j^n}^{x_{j+1}^n} s(x, t^n) dx + \iint_{D_{s,j}^n} g_k(u, v, w) dx dt, \quad (2.37)$$

where $s = u, v, w$; $k = 1, 2, 3$, respectively, and we can define as before $\bar{x}_{s,j-\frac{1}{2}}^{n+1} = \sigma_{s,j}^n(t^{n+1})$ and $\bar{x}_{s,j+\frac{1}{2}}^{n+1} = \sigma_{s,j+1}^n(t^{n+1})$. Equation (2.37) is called “locally conservative relation” to the system of balance laws (2.34). Thus, the approximations of the variables u, v, w for system are a rather component-wise extension of the scalar framework given by (for $S = U, V, W$ and $s = u, v, w$),

$$S_j^n = \frac{1}{h} \int_{x_{j-\frac{1}{2}}^n}^{x_{j+\frac{1}{2}}^n} s(x, t^n) dx, \quad \text{and} \quad \bar{S}_j^{n+1} = \frac{1}{h_{s,j}^{n+1}} \int_{\bar{x}_{j-\frac{1}{2}}^{n+1}}^{\bar{x}_{j+\frac{1}{2}}^{n+1}} s(x, t^{n+1}) dx \quad j \in \mathbb{Z}, \quad (2.38)$$

respectively, and the initial condition is $U(x_j^0, t^0) = U_j^0$, $V(x_j^0, t^0) = V_j^0$ and $W(x_j^0, t^0) = W_j^0$ over the local space-time cells $[x_{j-\frac{1}{2}}^0, x_{j+\frac{1}{2}}^0]$, $j \in \mathbb{Z}$. Next, we use (2.38) into to “locally conservative relation” to get,

$$\begin{aligned} \bar{S}_j^{n+1} &= \frac{1}{h_{s,j}^{n+1}} \int_{\bar{x}_{j-\frac{1}{2}}^{n+1}}^{\bar{x}_{j+\frac{1}{2}}^{n+1}} s(x, t^{n+1}) dx \\ &= \frac{1}{h_{s,j}^{n+1}} \left[\int_{x_j^n}^{x_{j+1}^n} s(x, t^n) dx + \iint_{D_{s,j}^n} g_k(u, v, w) dx dt \right]. \end{aligned} \quad (2.39)$$

In (2.39) $S = (U, V, W)$ and $s = (u, v, w)$ denotes a representation of a component-wise extension of the scalar case to systems of balance laws in compact form (2.33). Next, the local approximations \bar{S}_j^{n+1} , $j \in \mathbb{Z}$ are projected over the original grid and reads,

$$S_j^{n+1} = \frac{1}{h} \left[c_{s,0j} \bar{S}_{j-1}^{n+1} + c_{s,1j} \bar{S}_j^{n+1} \right]. \quad (2.40)$$

Here $c_{s,0j} = (\frac{h}{2} + f_{s,j}^{n+\frac{1}{2}} k)$, $c_{s,1j} = h - c_{s,0j} = (\frac{h}{2} - f_{s,j}^{n+\frac{1}{2}} k)$ and we use the approximation $f_{s,j}^{n+\frac{1}{2}} = \frac{f_k(U_j^{n+\frac{1}{2}}, V_j^{n+\frac{1}{2}}, W_j^{n+\frac{1}{2}})}{S_j^{n+\frac{1}{2}}} \approx \frac{f_k(u, v, w)}{s}$, $S = U, V, W$, $s = u, v, w$

and $k = 1, 2, 3$, respectively. Notice that now the curve $\sigma_{s,j}^n(t)$ is a simple straight line for $f_{s,j}^n$ (see right picture in Figure 5), along with $k^n = \Delta t^n = t^{n+1} - t^n$. Finally, combination

of equations (2.39) and (2.40) form the building-block for the new Lagrangian-Eulerian scheme, which reads as a componentwise extension for equation (2.29) ($S = U, V, W$, $s = u, v, w$ and $k = 1, 2, 3$, respectively):

$$\begin{aligned}
S_j^{n+1} &= \frac{S_{j-1}^n + 2S_j^n + S_{j+1}^n}{4} + \frac{S'_{j-1}{}^n - S'_{j+1}{}^n}{32} \\
&+ \frac{k^n}{4} \left(\frac{f_{k,j-1}^{n+\frac{1}{2}} + f_{k,j}^{n+\frac{1}{2}}}{h_{j-1}^{n+1}} [S_{j-1}^n + S_j^n] - \frac{f_{k,j}^{n+\frac{1}{2}} + f_{k,j+1}^{n+\frac{1}{2}}}{h_j^{n+1}} [S_j^n + S_{j+1}^n] \right) \\
&+ \frac{k^n}{32} \left(\frac{f_{k,j-1}^{n+\frac{1}{2}} + f_{k,j}^{n+\frac{1}{2}}}{h_{j-1}^{n+1}} [S'_{j-1}{}^n - S_j'^n] - \frac{f_{k,j}^{n+\frac{1}{2}} + f_{k,j+1}^{n+\frac{1}{2}}}{h_j^{n+1}} [S_j'^n - S'_{j+1}{}^n] \right) \\
&+ \frac{1}{h_j^{n+1}} \left[\frac{1}{h_j^{n+1}} \left(\frac{h_j^{n+1}}{2} + f_{k,j}^{n+\frac{1}{2}} k^n \right) \iint_{D_{j-1}^n} G_k(s(x, t)) dx dt \right. \\
&\left. + \frac{1}{h_j^{n+1}} \left(\frac{h_j^{n+1}}{2} - f_{k,j}^{n+\frac{1}{2}} k^n \right) \iint_{D_j^n} G_k(s(x, t)) dx dt \right]. \tag{2.41}
\end{aligned}$$

2.4 Two-dimensional hyperbolic conservation laws

We now turn our attention to introducing a new computational approach for the design of a new class of approximate solutions for two-dimensional hyperbolic conservation laws. This novel scheme is based on the same Lagrangian-Eulerian framework discussed for the one-dimensional scalar problem.

A natural first attempt would be a straightforward extension used in the one-dimensional case, but now applied to three-dimensional variables $(x, y \text{ and } t)$ as $D_{i,j}^n \subset \mathbb{R}^3$, see Figure 6 (left), where i and j refer to (x_i, y_j) and n refers to time level t^n . The boundary of control volumes $D_{i,j}^n$ will be denoted by $\partial D_{i,j}^n = R_{i,j}^n \cup S_{i,j}^n \cup \bar{R}_{i,j}^{n+1}$ where the control volume $R_{i,j}^n = [x_{i-\frac{1}{2}}^n, x_{i+\frac{1}{2}}^n] \times [y_{j-\frac{1}{2}}^n, y_{i+\frac{1}{2}}^n]$ in \mathbb{R}^2 is the “inflow” of the integral tube, $\bar{R}_{i,j}^{n+1}$ in \mathbb{R}^2 is the “outflow” of the integral tube, while $S_{i,j}^n$, in \mathbb{R}^3 , is the lateral (impervious) surface of the tube.

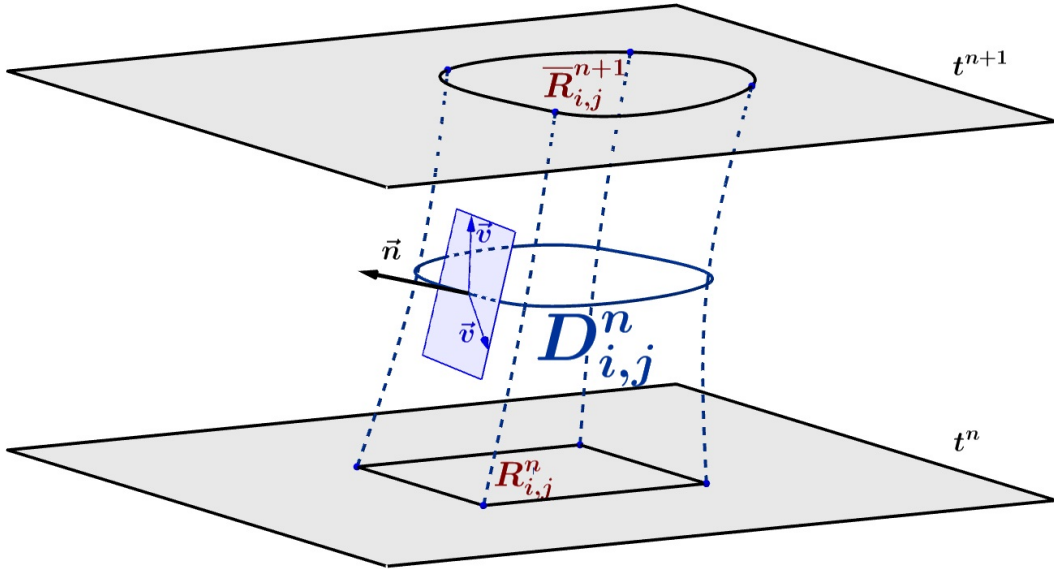


Figure 6 – The integral tube in 3D. We illustrate the challenge of uniquely define the tangent vector. Since here there is a tangent plane, the *integral surfaces* as well as *integral curves* coming from $[u \ f(u) \ g(u)]^T \cdot \vec{n} = 0$ seem to be at first glance not straightforward to construct.

As before, we consider the hyperbolic conservation law in two-dimensional variables in divergence form,

$$\frac{\partial u}{\partial t} + \frac{\partial f(u)}{\partial x} + \frac{\partial g(u)}{\partial y} = 0 \quad \Longleftrightarrow \quad \nabla_{t,x,y} \begin{bmatrix} u \\ f(u) \\ g(u) \end{bmatrix} = 0. \quad (2.42)$$

Again, the integration over the control volume and the application of the

divergence theorem gives,

$$\iiint_{D_{i,j}^n} \nabla_{t,x,y} \begin{bmatrix} u \\ f(u) \\ g(u) \end{bmatrix} dV = 0 \quad \Leftrightarrow \quad \int_{\partial D_{i,j}^n} \begin{bmatrix} u \\ f(u) \\ g(u) \end{bmatrix} \cdot \vec{n} d(\partial D_{i,j}^n) = 0. \quad (2.43)$$

The normal vector with respect to $R_{i,j}^n$ is, in usual convention, $[-1 \ 0 \ 0]^T$ and the vector normal in the outflow $\overline{R}_{i,j}^{n+1}$ is $[1 \ 0 \ 0]$. Then, the right side of (2.43) can be written as,

$$\int_{R_{i,j}^n} \begin{bmatrix} u \\ f(u) \\ g(u) \end{bmatrix} \cdot [-1 \ 0 \ 0]^T dA + \int_{S_{i,j}^n} \begin{bmatrix} u \\ f(u) \\ g(u) \end{bmatrix} \cdot \vec{n} dS + \int_{\overline{R}_{i,j}^{n+1}} \begin{bmatrix} u \\ f(u) \\ g(u) \end{bmatrix} \cdot [1 \ 0 \ 0]^T dA = 0. \quad (2.44)$$

We suppose there is not any flow through the surface $S_{i,j}^n$ ($S_{i,j}^n$ is impervious). So, the surface integral of $S_{i,j}^n$ is zero and therefore,

$$-\int_{R_{i,j}^n} u(x, y, t^n) dA + \int_{\overline{R}_{i,j}^{n+1}} u(x, y, t^{n+1}) dA = 0. \quad (2.45)$$

or

$$\int_{\overline{R}_{i,j}^{n+1}} u(x, y, t^{n+1}) dA = \int_{R_{i,j}^n} u(x, y, t^n) dA, \quad (2.46)$$

which we call conservation identity. The numerical approximations $U_{i,j}^n$ and $\overline{U}_{i,j}^{n+1}$ can be defined from (2.46).

A 2D Approach based on a system of balance laws

We here propose a simple, fast, and also elegant alternative approach. Our procedure is based in writing the two-dimensional scalar conservation law (2.47) in the form of a coupled set of two balance laws along with initial data. The main idea behind our approach is quite simple. First, consider the two-dimensional nonlinear hyperbolic conservation law with initial data,

$$\begin{cases} \frac{\partial U}{\partial t} + \frac{\partial f(U)}{\partial x} + \frac{\partial g(U)}{\partial y} = 0, \\ U(x, y, t^n) = U^n. \end{cases} \quad (2.47)$$

The initial data at a time t^n is given by the set U^n of discrete cell average values $U_{i,j}^n$, where i denotes the x -direction and j denotes the y -direction. Consider now the cell-centered finite-volume cells,

$$\begin{aligned} D_{i,j}^n &= \{(t, x, y) / t^n \leq t \leq t^{n+\frac{1}{2}}, \ y_{j-\frac{1}{2}}^n \leq y \leq y_{j+\frac{1}{2}}^n, \ \sigma_i^n(t) \leq x \leq \sigma_{i+1}^n(t)\}, \\ D_{i,j}^{n+\frac{1}{2}} &= \{(t, x, y) / t^{n+\frac{1}{2}} \leq t \leq t^{n+1}, \ x_{i-\frac{1}{2}}^{n+\frac{1}{2}} \leq x \leq x_{i+\frac{1}{2}}^{n+\frac{1}{2}}, \ \gamma_j^{n+\frac{1}{2}}(t) \leq y \leq \gamma_{j+1}^{n+\frac{1}{2}}(t)\}, \end{aligned}$$

where $\sigma_i^n(t)$ and $\gamma_j^n(t)$ are parameterized curves such that $\sigma_i^n(t^n) = x_i^n$ and $\gamma_j^{n+\frac{1}{2}}(t^{n+\frac{1}{2}}) = y_j^{n+\frac{1}{2}}$. Our approach is based in writing (2.47) in the form of a coupled set of two balance laws along with initial data,

$$\begin{cases} \frac{\partial U}{\partial t} + \frac{\partial f(U)}{\partial x} = - \left(\frac{\partial g(U)}{\partial y} \right)_j, & \text{in } D_{i,j}^n, \\ U(x, y, t^n) = U^n, \end{cases} \quad (2.48a)$$

$$\begin{cases} \frac{\partial U}{\partial t} + \frac{\partial g(U)}{\partial y} = - \left(\frac{\partial f(U)}{\partial x} \right)_i, & \text{in } D_{i,j}^{n+\frac{1}{2}}, \\ U(x, y, t^{n+\frac{1}{2}}) = U^{n+\frac{1}{2}}. \end{cases} \quad (2.48b)$$

where $\left(\frac{\partial g(U)}{\partial y} \right)_j$ and $\left(\frac{\partial f(U)}{\partial x} \right)_i$ are numerical approximations of derivatives respectively. Denote $S_x(t)$ and $S_y(t)$ as approximate solution operators for (2.48a) and (2.48b), respectively. Indeed, such approximate solution operators can be given by scheme (2.29)-(2.32). but in both directions x or y . Thus, $U_{i,j}^{n+\frac{1}{2}} = S_x(\Delta t/2)U_{i,j}^n$ and $U_{i,j}^{n+1} = S_y(\Delta t/2)U_{i,j}^{n+\frac{1}{2}}$, so that, the full scheme is given by,

$$U_{i,j}^{n+1} = S_y(\Delta t/2)S_x(\Delta t/2)U_{i,j}^n, \quad (2.49)$$

along with the CFL condition [84],

$$Mk/h \leq \sqrt{2}/2, \quad (2.50)$$

with $M = \max\{\max_j\{f'(U_{i,j}^n)\}, \max_j\{\frac{f(U_{i,j}^n)}{U_{i,j}^n}\}, \max_j\{g'(U_{i,j}^n)\}, \max_j\{\frac{g(U_{i,j}^n)}{U_{i,j}^n}\}\}$. The equations appearing in (2.48a) and (2.48b) can be viewed as a set of local balance laws in the time step $(t^n, t^{n+1}]$, but coupled via the source terms on the RHS of (2.48) and thus linked to the full problem (2.47). Then the procedure to solve (2.47) is quite simple as follows: in the time step from t^n to $t^{n+\frac{1}{2}}$ the information of the previous time, say, in the y coordinate is accounted through the source term for the balance law in the x coordinate. Similarly, in time step from $t^{n+\frac{1}{2}}$ to t^{n+1} , the information in the x coordinate is also accounted through of the source term for the balance law in the y coordinate. This formulation has allowed us to correctly approximate solutions of two-dimensional hyperbolic conservation law problems from paper [55] as we show in Section 2.5.

Mean and Gaussian Curvature

The core issue of this approach is to define the normal vector \vec{n} along with the unique definition of the tangent vector \vec{v} to the surface $S_{i,j}^n$ in the point (x_i, y_j, t^n) , see Figure 6. Notice that at this point there is a tangent plane, then the *integral surfaces* as well as *integral curves* coming from $[u \ f(u) \ g(u)]^T \cdot \vec{n} = 0$ seem to be at first glance not straightforward to construct. One possibility is to define the concepts of *Mean curvature*

and *Gaussian curvature* associated with the underlying conservation law [62] (see also [75]). In this regard, one possibility is to construct naturally a normal curvature and a geodesic curvature from equation (2.42). They are primarily given by the projection of \vec{v} onto the local normal vector and the local tangent plane, respectively. Thus, it is possible to define a unique curve for each one of the points that appear at the bottom of the integral tube, from time step t^n to t^{n+1} , at least from a theoretical viewpoint. For concreteness, one possible numerical approach is to consider the level set approach introduced in [81] (see also [38]). The construction of efficient robust methods based on such approach needs a novel theory along with feasible numerical algorithms to be pursued later on.

2.5 Numerical experiment studies with applications

We first present a mesh refinement study in order to give some numerical evidence of convergence for the proposed scheme. Next, computations for scalar conservation laws with convex and non-convex flux functions and discussed. A problem modeling three-phase flow in porous media for one-dimensional problems is presented, illustrating an example of system of conservation laws. We then present two examples of two-dimensional conservation laws. Next, we show examples for scalar balance laws, the numerically observed well-balanced property and systems of balance laws modeling shallow water equations. The numerical schemes were written in MATLAB and the numerical experiments were performed in the following computer configuration: Processor: Intel ®Core™i7-4510U and CPU @ 2.60 GHz, Memory(RAM) DDR3/1866MHz 8GB.

2.5.1 Convex and non-convex flux functions for conservation laws

For a first mesh refinement study we test our scheme with a non-convex flux function to the scalar conservation law $u_t + f_x(u) = 0$, for $f(u) = 0.5(e^{-25(u-0.5)^2} + 8(u - 0.5)^2)$, along with Riemann initial data $u(x, 0) \equiv \eta(x) = 0.8$, $x < 0$ and $u(x, 0) \equiv \eta(x) = 0.2$, $x > 0$. In Figure 7 is shown three different mesh grid cells (128, 256 and 512) against a reference numerical solution with 1024 mesh grid cells at dimensionless time $t = 2.0$.

Figure 8 shows numerical solutions for $u_t + \left(\frac{u^2}{2}\right)_x = 0$, along with smooth initial data $u(x, 0) = 0.5 + \sin(x)$. It is well-known that the solution of this problem develops a shock discontinuity at the critical time $T_c = 1$, and then it exhibits pre-shock (resp. post-shock) solution for $T_c < 1$ (resp. $T_c > 1$); on the top figure it is shown the post-shock solution computed with (2.19)-(2.20) at time simulation $t = 2$ for 256 cells. We have also conducted similar numerical experiments to problem $u_t + \left(\frac{u^2}{2}\right)_x = 0$ along with discontinuous initial data $u(x, 0) = 1$, $x < 0$ & $u(x, 0) = 0$, $x > 0$ (middle: shock) and $u(x, 0) = -1$, $x < 0$ & $u(x, 0) = 1$, $x > 0$ (bottom: rarefaction). On these frames are shown snapshot graphs at time $t = 2.4$ of simulation, with waves moving from left to right. We get a very nice looking numerical approximate solution with scheme (2.19)-(2.20), which in turn seems to be propagating at entirely entropy-correct Rankine-Hugoniot speed (middle). Similar good results are shown to the rarefaction case as well. Indeed, in the terminology of gas dynamics to the rarefaction cases for the inviscid Burgers equation we see that the transonic rarefaction (right frame) is well resolved. That is, as the rarefaction wave is crossed, there is a sign change in the characteristic speed u and thus there is one point at which $u = 0$, the sonic point. So, there is no spurious anomalies around $u = 0$.

The classical nonlinear one-dimensional Buckley-Leverett two-phase problem [76], is depicted in top picture in Figure 9. Computed solutions with scheme (2.19)-(2.20) at time simulation $t = 2$ are shown to the Riemann Problem (Initial Value Problem with

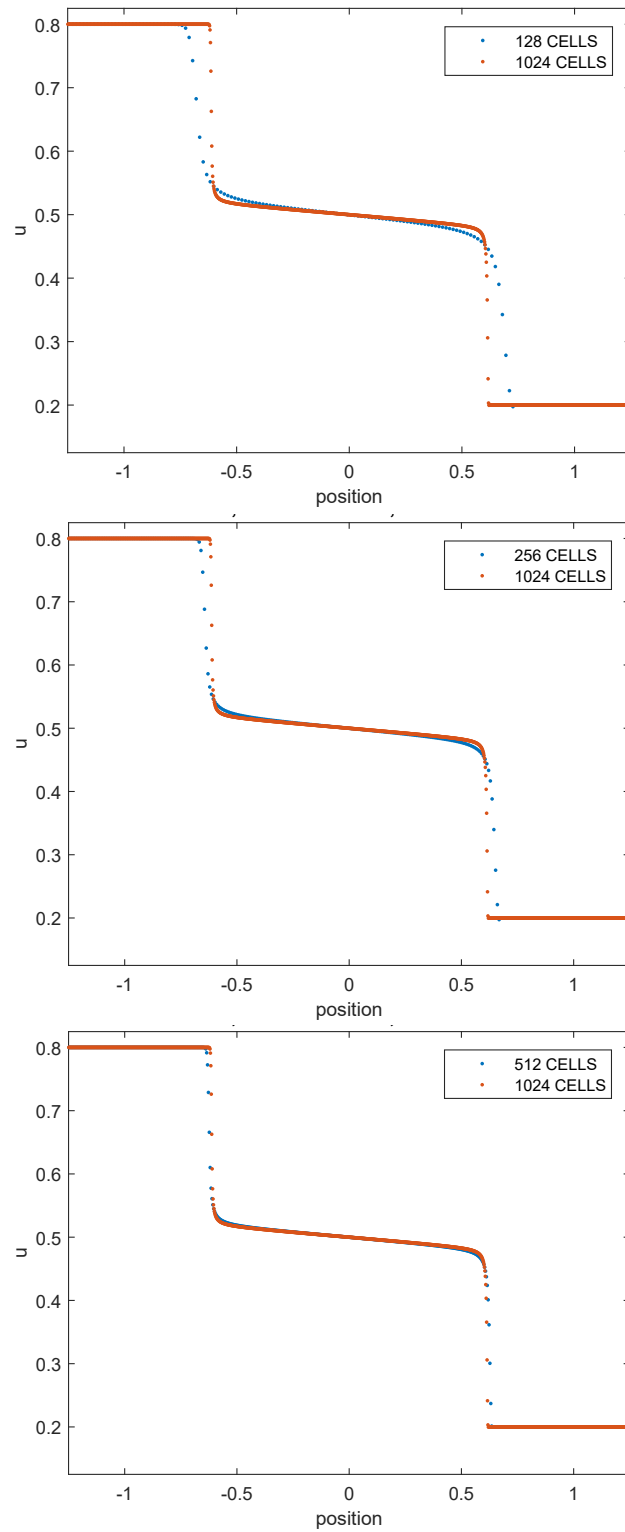


Figure 7 – Mesh refinement study for a non-convex flux function. The finest mesh in this case is a solution with 1024 grid cells.

non-convex flux function): $u_t + f_x(u) = 0$, $f(u) = u^2/(u^2 + a(1 - u)^2)$, $a = 1$, along with Riemann initial data (left) $u(x, 0) \equiv \eta(x) = 1.0$, $x < 0$ and $u(x, 0) \equiv \eta(x) = 0.0$, $x > 0$. On physical ground, such initial data corresponds to water flooding of an oil reservoir. The well known solution for this model comprises a leading shock wave (an oil bank) followed by an attached rarefaction wave. The weak solution satisfying the Oleinik entropy condition is in very good agreement along with the scheme (2.19)-(2.20) propagating at entirely entropy-correct Rankine-Hugoniot speed and with the precisely post-shock value. We have also considered another non-convex flux function (see bottom picture in Figure 9) to the scalar conservation law $u_t + f_x(u) = 0$, with $f(u) = 0.5(e^{-25(u-0.5)^2} + 8(u-0.5)^2)$, along with Riemann initial data (top) $u(x, 0) \equiv \eta(x) = 0.8$, $x < 0$ and $u(x, 0) \equiv \eta(x) = 0.2$, $x > 0$. Again, the numerical solution is in agreement with Oleinik entropy condition, whose approximate left and right shock waves are propagating with correct Rankine-Hugoniot speed and entropy-correct post-shock values.

2.5.2 Porous Media Flow Problems

Transport of fluids in porous media is important both in scientific and technological areas, such as chemical, civil, agricultural, environmental, petroleum and mechanic engineering. Many difficulties and challenges arise on the mathematical formulation of the physical processes that govern multiphase flow in heterogeneous reservoirs, mainly due to their inherent multi-scale nature. Geological properties of the medium like permeability or porosity may present heterogeneities and are modeled in the PDE system as discontinuous coefficients with abrupt gradients [54]. There is a large interest in applying multiphase flow models to oil recovery in heterogeneous reservoirs, while restricting the study to incompressible and immiscible phases. An oil reservoir is a deep underground sedimentary rock body, formed by non-uniform deposits that abruptly vary along spatial dimensions, and contains a mixture of fluids in the interstitial space between grains (around $10 - 100\mu m$). The available space volume, denoted porosity, normally varies in the scale $0.1 - 0.3 [m^3/m^3]$ and contains water and at least a hydrocarbon (gas or oil) in liquid or gaseous phase. Erosion, natural faults and fractures complicate even more the precise knowledge of heterogeneities in the porous medium. Rock permeability can vary in magnitude orders, from 10^{-2} miliDarcy to 10^3 miliDarcy ($1 \text{ Darcy} = 1.0 \times 10^{-12} m^2$ = the permeability that gives the $1 cm s^{-1}$ flow for a fluid with 1 centipoise ($1 gm^{-1} s^{-1}$) viscosity under the pressure gradient of $1 atm cm^{-1}$). These heterogeneities happen in multiple scales, from the microscopic pore scale to the macroscopic field scale, preventing the detailed information of the rock properties variations that strongly influence the fluid transport in the porous medium. We discuss now the modeling via phase formulation of transport of fluids in heterogeneous porous media, specifically with two and three phases. In the phase formulation, the governing differential equations are rewritten in function of a reference pressure (hereafter the oil phase pressure) together with the saturation

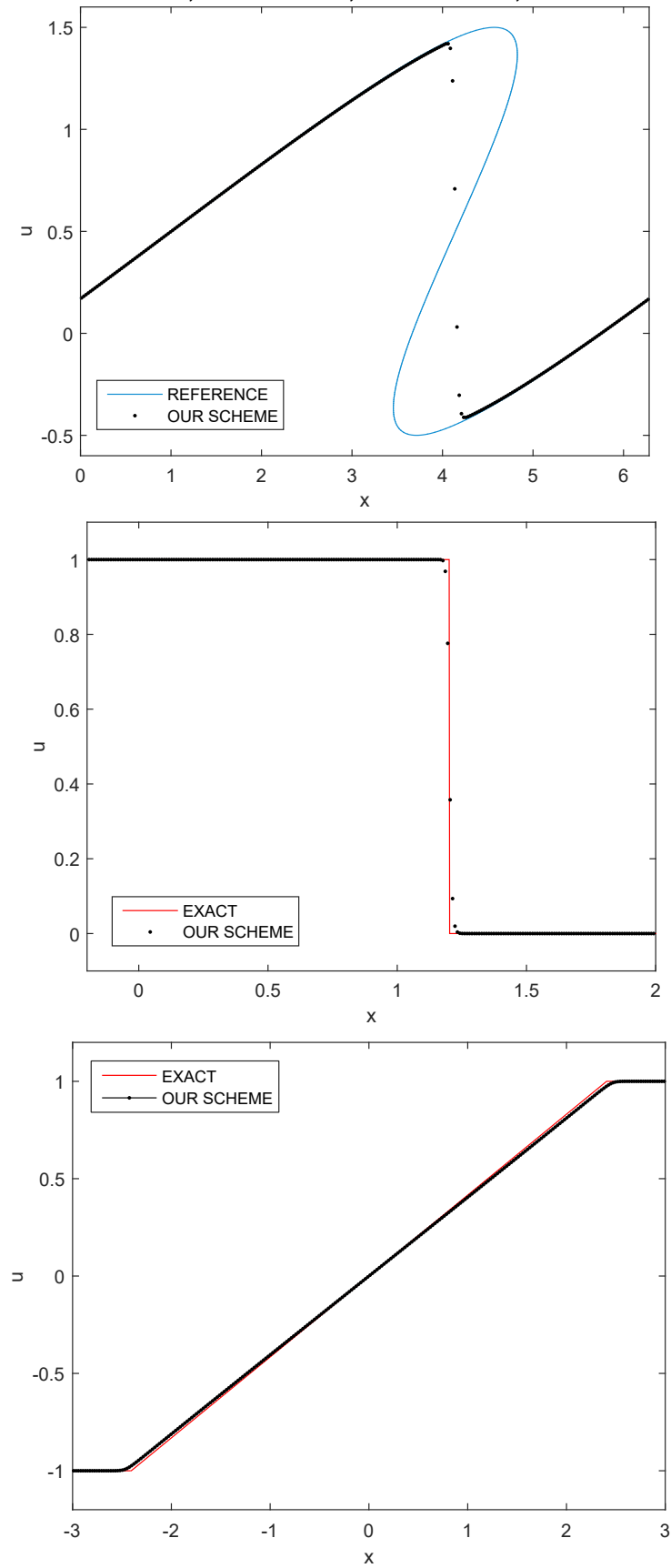


Figure 8 – Inviscid nonlinear Burgers' problem: post-shock solution for smooth initial data (top), Riemann problem with shock wave (middle), Riemann problem with rarefaction fan (bottom).

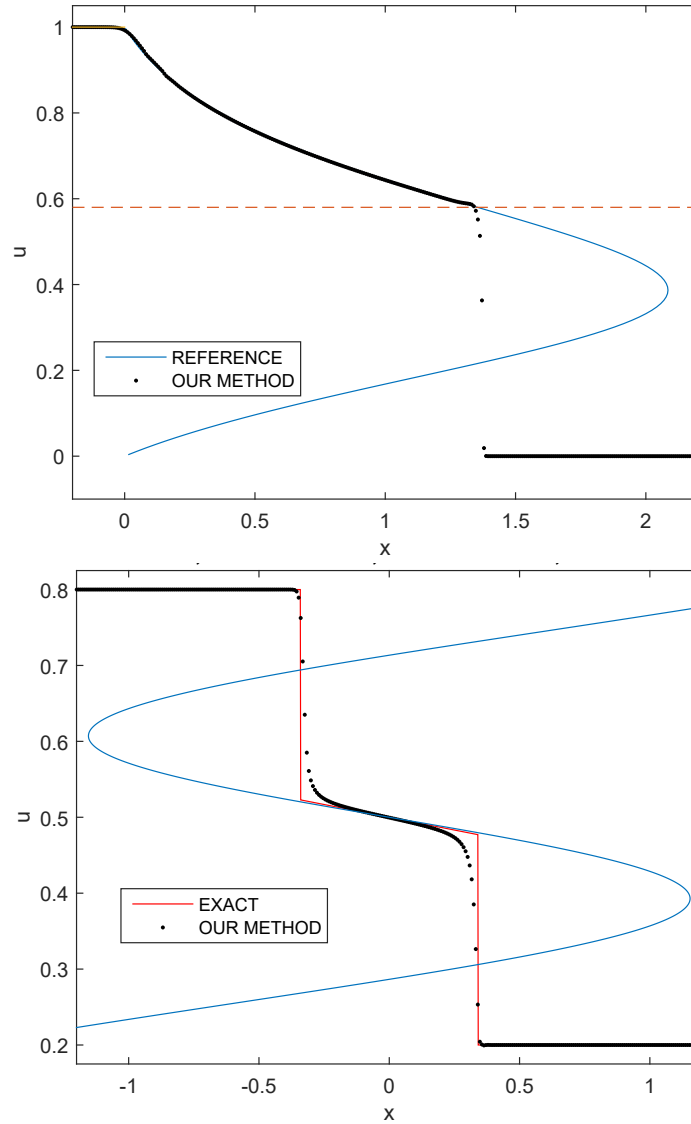


Figure 9 – Top: Classical one-dimensional Buckley-Leverett two-phase problem computed by scheme (2.19)-(2.20). Bottom: A non-convex flux function.

transport equations regarding other phases present in the flow [1]. The motivation for the choice of this formulation to describe transport process is that it is more general [33]. The governing equations coming from this formulation keeps the same form for two- and three-phase flow. Another motivation for the usage is that it keeps a general form for the relative permeability functions and capillary pressure models [33, 36]. Because of these facts, its application is advantageous for the purpose of developing approximation tools and simulations in transport problems of flow in heterogeneous porous media in multiple scales.

Mathematical Model

Three-phase immiscible flow can be typically modeled by conservation equations coupled with a direct extension of Darcy's law for multiphase flow in terms of the relative

permeability functions for each of the three phases. The mathematical model considered here takes into account capillary forces, general expressions for the relative permeability functions, variable porosity and permeability fields and gravitational effects. We assume the three phases are immiscible and incompressible through the entire heterogeneous porous media. We consider that there are no internal sources or sinks and there is no mass transfer between the phases and thermal effects are negligible. Here, the three phases water, oil and gas are indicated by subscripts w , o and g , respectively. We assume the phases completely saturate the medium. This way, denoting the saturation (fraction of local volume) of phase i by S_i [m^3/m^3], with $0 \leq S_i \leq 1$, we must have

$$\sum_i S_i = 1, \quad i = g, o, w. \quad (2.51)$$

Numerical Experiments

In one dimension the pressure equation implies that the total fluid velocity is independent of position, so we take it to be constant. We have the following system of partial differential equations [1, 79]:

$$\frac{\partial s_w}{\partial t} + \frac{\partial}{\partial x} f_w(s_w, s_g) = \frac{\partial w_w}{\partial x}, \quad (2.52)$$

$$\frac{\partial s_g}{\partial t} + \frac{\partial}{\partial x} f_g(s_w, s_g) = \frac{\partial w_g}{\partial x}, \quad (2.53)$$

where

$$w_w = \left(\lambda_w(1 - f_w) \frac{\partial p_{wo}}{\partial s_w} - \lambda_w f_g \frac{\partial p_{go}}{\partial s_w} \right) \frac{\partial s_w}{\partial x} + \left(\lambda_w(1 - f_w) \frac{\partial p_{wo}}{\partial s_g} - \lambda_w f_g \frac{\partial p_{go}}{\partial s_g} \right) \frac{\partial s_g}{\partial x}, \quad (2.54)$$

and

$$w_g = \left(-\lambda_g f_w \frac{\partial p_{wo}}{\partial s_w} + \lambda_g(1 - f_g) \frac{\partial p_{go}}{\partial s_w} \right) \frac{\partial s_w}{\partial x} + \left(-\lambda_g f_w \frac{\partial p_{wo}}{\partial s_g} + \lambda_g(1 - f_g) \frac{\partial p_{go}}{\partial s_g} \right) \frac{\partial s_g}{\partial x}. \quad (2.55)$$

In our model we choose, for convenience, to work with the saturations of water and gas. The diffusive term is represented by the right-hand side of the system (2.52)-(2.53) and it incorporates the capillary pressure effects. We neglect the capillary diffusive effect, by just taking $w_w = 0$ and $w_g = 0$ in (2.52)-(2.55), but we do know from [1, 79] how is the correct structure of the solutions of the non-classical three-phase model under consideration. However, we point out that for a wave to be truly defined as a “shock wave”, a discontinuity must be the zero-diffusion limit of traveling wave solutions. For such solutions, diffusion balances the convergence of waves caused by hyperbolic nonlinearity. Moreover, the set of non-classical wave solutions obtained in the zero-diffusion (zero-capillarity) limit might depends sensitively on the form of the diffusion matrix and not only on the hyperbolic structure of the equations; see [1, 79] and the references cited therein for further technical details.

We present the results of numerical grid refinement for the simulation of two Riemann problems, namely RP_1 and RP_2 , given by:

$$RP_1 : \begin{cases} s_w^L = 0.613 & \text{and} & s_w^R = 0.05, \\ s_g^L = 0.387 & \text{and} & s_g^R = 0.15, \end{cases} \quad RP_2 : \begin{cases} s_w^L = 0.621 & \text{and} & s_w^R = 0.05, \\ s_g^L = 0.279 & \text{and} & s_g^R = 0.15. \end{cases} \quad (2.56)$$

We use the quadratic model by Corey-Pope, extensively used for phase relative permeabilities,

$$k_w = s_w^2, \quad k_o = s_o^2 \quad \text{and} \quad k_g = s_g^2. \quad (2.57)$$

As in [1, 79], we consider the following viscosity values $\mu_o = 1.0$, $\mu_w = 0.5$, and $\mu_g = 0.3$. From the analysis discussed in [79], we remark that for the choice of parameters described above, a transitional shock wave is present in the solution of RP_2 , which in turn is not present in the solution of RP_1 .

Since the oil phase saturation can be directly obtained from the other two phase saturations (i.e., $s_o = 1 - s_w - s_g$), we display the oil saturation profile in Figure 11, showing the effect of a grid refinement in the numerical solution of (2.52)-(2.53) – $w_w = 0$ and $w_g = 0$ – with Riemann data RP_1 on the top and RP_2 on the bottom. The computed saturation profiles are shown at dimensionless time 2.50. In each frame we compare numerical solutions obtained on grids having 256, 512 and 1024 cells against a reference numerical solution of 2048 cells. It is clear from the pictures in Figure 11, that as the grid is refined we have some good evidence of numerical convergence of our scheme. We remark that the numerical solutions presented here are in very good agreement with the semi-analytic results reported in [79], yielding a numerical verification of our computations. We now show numerical experiments concerning the three-phase flow problem (2.52)-(2.53) – $w_w = 0$ and $w_g = 0$ and with Riemann data RP_1 on left and RP_2 on the right – in order to show that our scheme is able to capture analytical properties of the wave structures, as originally introduced in [79]; see also [1] and the references cited therein. For completeness we describe the non-classical solution. Right picture in Figure 10: the slow wave group comprises a strong slow rarefaction fan from left (injection) state to the post-shock value and an adjoining slow front wave from the post-shock value to the first plateau. The fast wave group is a Buckley-Leverett front wave from the second plateau. Between the slow and fast wave groups is a non-classical front wave. For the classical solution, we have only the slow and fast wave groups (Left picture in Figure 10). We point out that in both numerical solutions the plateau are located in the correct heights, with respect to the semi-analytical solutions presented in [79].

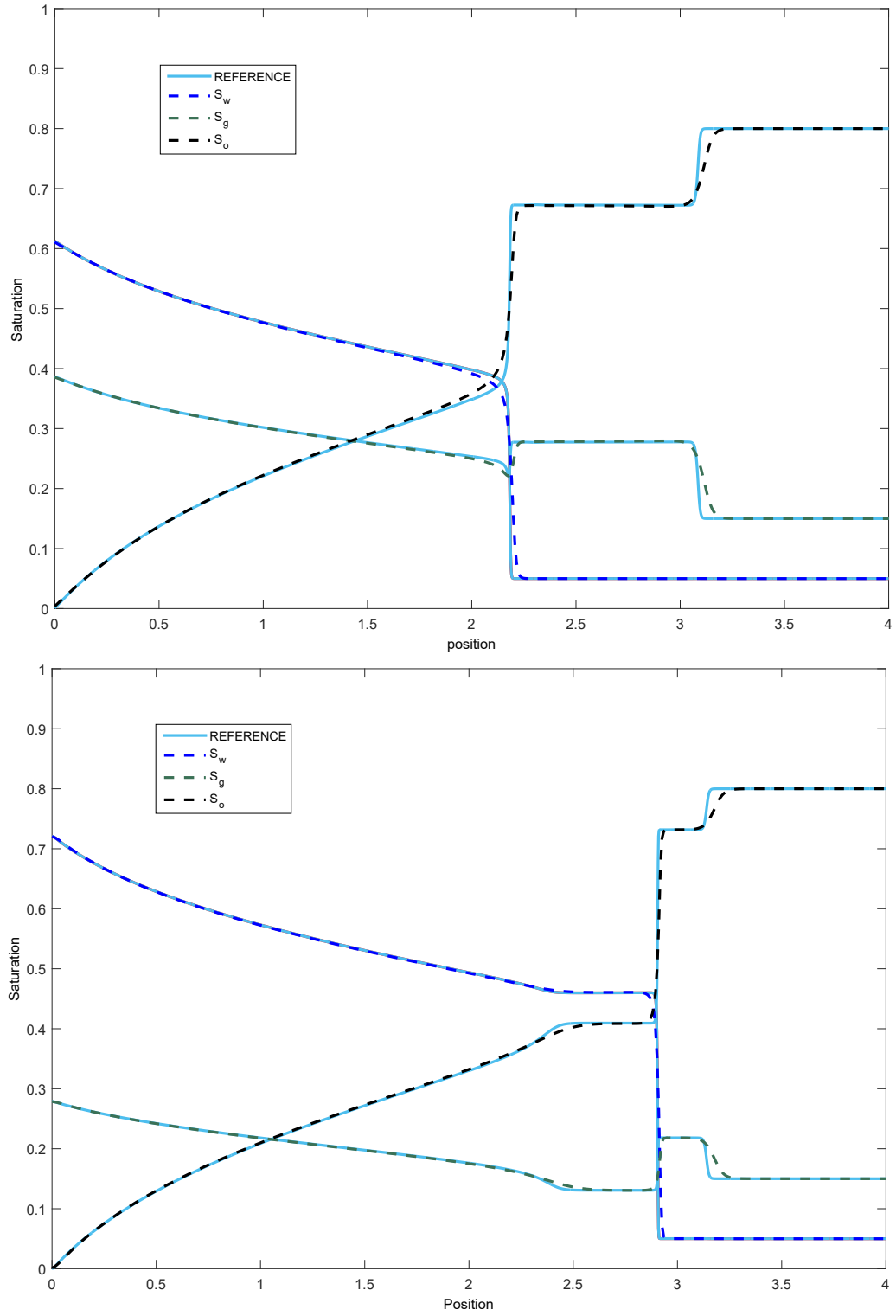


Figure 10 – Oil, water and gas saturation profiles are shown as a function of distance. RP_1 on the top and RP_2 on the bottom.

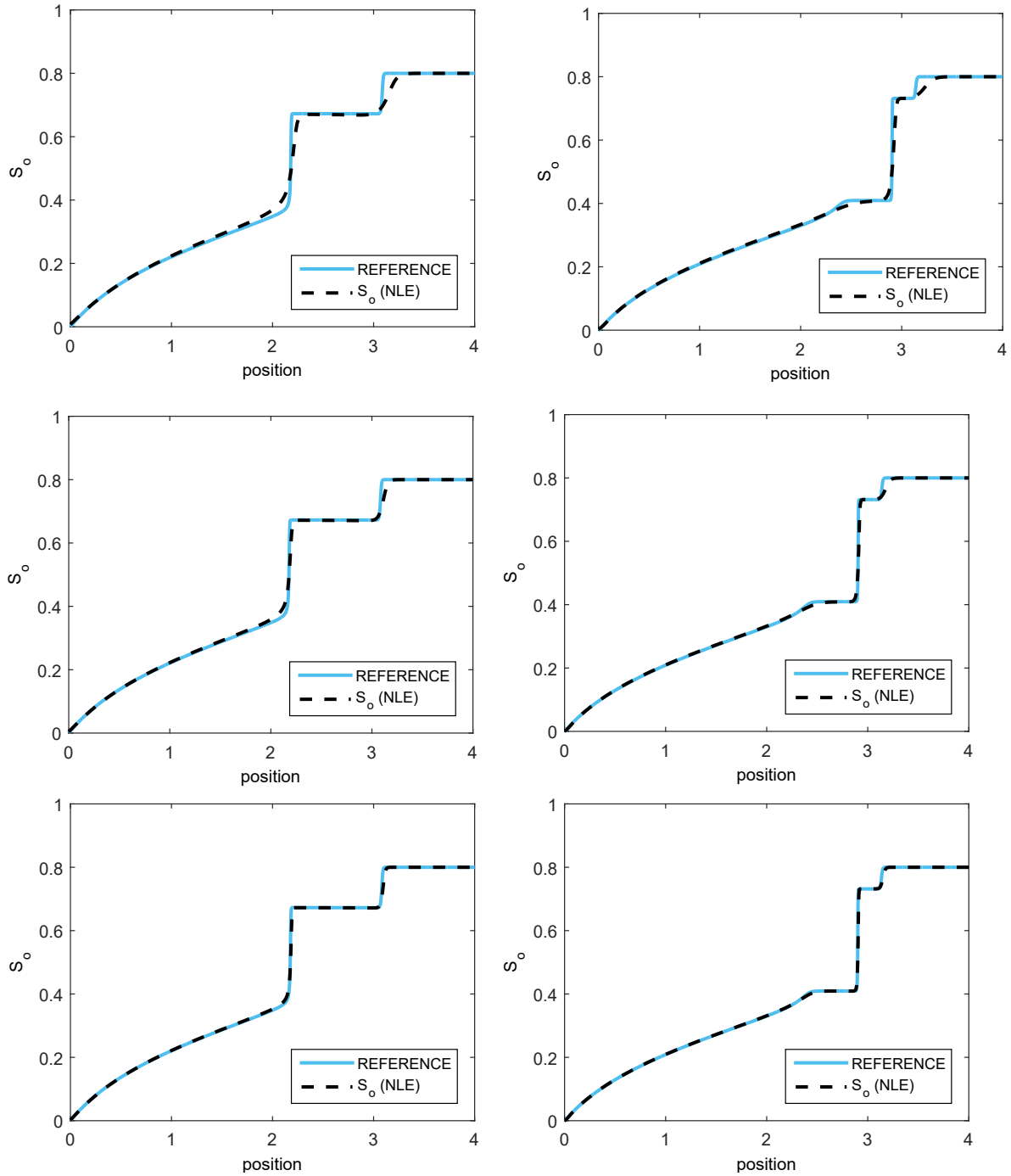


Figure 11 – Mesh refinement study for mesh values 256, 512 and 1024 against a reference solution of 2048 mesh points. Oil saturations are shown as a function of distance. RP_1 on the left and RP_2 on the right.

2.5.3 Shallow Water Equations

Shallow water equations have been proposed by Adhémar Barré de Saint-Venant in 1871 to model flows in a channel [89]. Three-dimensional Navier-Stokes equations can be used to simulate such flows directly, but in the case where the horizontal length scale is much greater than the vertical length scale, one can average over the depth to get rid of the vertical direction and reduce the model into two-dimensional nonlinear shallow water equations. Nowadays, they are widely used to model flows in various contexts, such as overland flow, river and flooding simulations, dam breaks, nearshore and tsunami [25, 42, 58, 78, 93, 95]. These equations consist in a nonlinear system of partial differential equations (PDEs), more precisely conservation laws describing the evolution of the height and mean velocity of the fluid. In real situations (realistic geometry, sharp spatial or temporal variations of the parameters in the model, etc.), there is no hope to solve explicitly this system of PDEs, that is, to produce analytic formulas for the solutions. It is therefore necessary to develop specific numerical methods to compute approximate solutions of such PDEs. The rather general settings of viscous shallow water equations in two space dimensions is described with topography, rain, infiltration and soil friction. The simplified system arising in one space dimension is then given and several classical properties of the equations are recalled.

In the past two decades, many well-balanced numerical methods have been developed for the shallow water equations, such as upwind methods [20, 22]. Bermudez and Vazquez in [22] extended upwind methods to the shallow water equations with source terms. Following this pioneering work, many other schemes for the shallow water equations with such well-balanced property have been developed in the finite volume community, such as, finite difference/volume weighted essentially non-oscillatory (WENO) schemes with well-balanced property and finite element discontinuous Galerkin. Several well-balanced DG methods have been proposed by the idea of special decomposition of the source term, hydrostatic reconstruction, and path-conservative methods. There are also a crescent number of positivity-preserving schemes in the finite volume framework.

Mathematical Model

The unknowns of the equations are the water height $h(t, x, y)$ ($[L]$) and $u(t, x, y)$, $v(t, x, y)$ the horizontal components of the vertically averaged velocity $[L/T]$. The equations take the following form of balance laws, where $g = 9.81m/s^2$ is the gravity constant:

$$\begin{cases} \partial_t h + \partial_x(hu) + \partial_y(hv) = R - I, \\ \partial_t(hu) + \partial_x\left(hu^2 + \frac{gh^2}{2}\right) + \partial_y(huv) = gh(S_{0,x} - S_{f,x}) + \mu S_{d,x}, \\ \partial_t(hv) + \partial_x(huv) + \partial_y\left(hv^2 + \frac{gh^2}{2}\right) = gh(S_{0,y} - S_{f,y}) + \mu S_{d,y}. \end{cases} \quad (2.58)$$

The first equation is a mass balance. The fluid density can be replaced by the height because of incompressibility. The other two equations are momentum balances, and involve forces such as gravity and friction.

- z is the topography $[L]$, when no erosion is considered it is a fixed function of space, $z(x, y)$, and it is classically denoted by $S_{0,x}$ (resp. $S_{0,y}$) the opposite of the slope in the x (resp. y) direction, $S_{0,x} = -\partial_x z(x, y)$ (resp. $S_{0,y} = -\partial_y z(x, y)$);
- $R \geq 0$ is the rain intensity $[L/T]$, it is a given function $R(t, x, y) \geq 0$.
- I is the infiltration rate $[L/T]$.
- $S_f = (S_{f,x}, S_{f,y})$ is the friction force. The friction law may take several forms, depending on both soil and flow properties. Here, U is the velocity vector $U = (u, v)$ with $|U| = \sqrt{u^2 + v^2}$, and Q is the discharge $Q = (hu, hv)$. In hydrological models, two families of friction laws are encountered on the basis of empirical considerations [43].
- Finally, $\mu S_d = (\mu S_{d,x}, \mu S_{d,y})$ is the viscous term with $\mu \geq 0$ the viscosity of the fluid $[L^2/T]$.

Properties

For the sake of simplicity, we present the one-dimensional case. Equations rewrite into

$$\begin{cases} \partial_t h + \partial_x(hu) = R - I, \\ \partial_t(hu) + \partial_x\left(hu^2 + \frac{gh^2}{2}\right) = gh(S_{0,x} - S_{f,x}) + \mu(h\partial_x u). \end{cases} \quad (2.59)$$

The left-hand side of this system is the transport operator, corresponding to the flow of an ideal fluid in a flat channel, without friction, rain or infiltration. This is actually the model introduced by Saint-Venant in [89], and it contains several important properties of the flow. To emphasize these properties, we rewrite the one-dimensional equations using vector form:

$$\partial_t \mathbf{w} + \partial_x \mathbf{w} = 0, \quad \text{where } \mathbf{w} = \begin{pmatrix} h \\ hu \end{pmatrix}, \quad \mathbf{F}(\mathbf{w}) = \begin{pmatrix} hu \\ hu^2 + \frac{gh^2}{2} \end{pmatrix}, \quad (2.60)$$

with $\mathbf{F}(\mathbf{w})$ as the flux of the equation. The transport is more clearly evidenced in the following nonconservative form, where $\mathbf{A}(\mathbf{w}) = \mathbf{F}'(\mathbf{w})$ is the matrix of transport coefficients:

$$\partial_t \mathbf{w} + \mathbf{A}(\mathbf{w}) \partial_x \mathbf{w} = 0, \quad \text{where } \mathbf{A}(\mathbf{w}) = \mathbf{F}'(\mathbf{w}) = \begin{pmatrix} u & 1 \\ u^2 + gh & 2u \end{pmatrix}. \quad (2.61)$$

More precisely, when $h > 0$, the matrix $\mathbf{A}(\mathbf{w})$ turns out to be diagonalizable, with eigenvalues

$$\lambda_1 = u - \sqrt{gh} < u + \sqrt{gh} = \lambda_2 \quad (2.62)$$

This important property is called strict hyperbolicity. The eigenvalues are indeed velocities, namely the ones of surface waves on the fluid, which are basic characteristics of the flow. Notice that the eigenvalues coincide if $h = 0$, that is, for dry zones. In that case, the system is no longer hyperbolic, and this induces difficulties at both theoretical and numerical levels. Designing numerical schemes that preserve positivity for h is very important in this context and is subject of many well-developed numerical techniques [17, 23, 53].

From these formulas, we recover a useful classification of flows, based on the relative values of the velocities of the fluid, u , and of the waves, \sqrt{gh} . Indeed if $|u| < \sqrt{gh}$, the characteristic velocities have opposite signs, and information propagate upward as well as downward of the flow, which is then said subcritical or fluvial. On the other hand, when $|u| > \sqrt{gh}$, the flow is supercritical, or torrential, all the information go downwards. A transcritical regime exists when some parts of a flow are subcritical, others supercritical.

Because we have two unknowns h and u (or equivalently h and $q = hu$), a subcritical flow is therefore determined by one upstream and one downstream value, whereas a supercritical flow is completely determined by the two upstream values. Thus, for numerical simulations, we have to impose one variable for subcritical inflow/outflow. We impose both variables for supercritical inflow; for supercritical outflow, free boundary conditions are considered.

In this context, two quantities are useful. The first one is a dimensionless parameter called the Froude number:

$$Fr = \frac{|u|}{\sqrt{gh}}. \quad (2.63)$$

It is the analog of the Mach number in gas dynamics, and the flow is subcritical (resp. supercritical) if $Fr < 1$ (resp. $Fr > 1$). The other important quantity is the so-called critical height h_c which writes

$$h_c = \left(\frac{|q|}{\sqrt{h}} \right)^{\frac{2}{3}}, \quad (2.64)$$

for a given discharge $q = hu$. It is a very readable criterion for criticality: the flow is subcritical (resp. supercritical) if $h > h_c$ (resp. $h < h_c$). When additional terms are present, other properties have to be considered, for instance, the occurrence of steady state (or equilibrium) solutions.

Numerical Experiments

Here we consider a numerical approximation of the well known system of balance laws modeling the shallow-water problem. The model under consideration is as follows:

$$\begin{cases} \frac{\partial h}{\partial t} + \frac{\partial(hu)}{\partial x} = 0, \\ \frac{\partial(hu)}{\partial t} + \frac{\partial(hu^2 + \frac{g}{2}h^2)}{\partial x} = -ghZ_x, \end{cases} \quad (2.65)$$

which we rewrite as

$$\begin{cases} \frac{\partial h}{\partial t} + \frac{\partial(hu)}{\partial x} = 0, \\ \frac{\partial(hu)}{\partial t} + \frac{\partial(hu^2)}{\partial x} = -\frac{\partial}{\partial x} \left(\frac{g}{2}h^2 \right) - gh\frac{\partial Z}{\partial x}, \end{cases} \quad (2.66)$$

where $h \geq 0$ denotes the water height, $u \in \mathbb{R}$ is the water velocity in the x direction, and $g > 0$ stands for the gravity constant. The function Z denotes the smooth topography.

Nonconservative formulations

In the recent past, several articles have been published trying to explain a proper definition as well as stability of nonconservative products, and its application to the definition of weak solutions of non-conservative hyperbolic systems, see e.g., [31, 83] and balance laws models [40]. Essentially, this means that one might use a proper modelling linked to the underlying problem to construct equivalent modified equations to better acomodate non-homogeneous terms yielding a discretization with good properties. The Lagrangian-Eulerian framework was helpful in this matter with the shallow water equations with good approximations, and here we describe one possible application [6].

Conservative formulations

Applying the Lagrangian-Eulerian method to each equation, we get

$$\begin{cases} \int_{D_{h,j}^n} \left(\frac{\partial h}{\partial t} + \frac{\partial(hu)}{\partial x} \right) dA = 0, \\ \int_{D_{m,j}^n} \left(\frac{\partial(hu)}{\partial t} + \frac{\partial(hu^2)}{\partial x} \right) dA = -g \int_{D_{m,j}^n} h \left(\frac{\partial h}{\partial x} + \frac{\partial Z}{\partial x} \right) dA. \end{cases} \quad (2.67)$$

The integrals on the left side in (2.67) were previously discussed. We will focus on how to approximate the integral on the right side. We have

$$I_{m,j}^n = \int_{D_{m,j}^n} h \left(\frac{\partial h}{\partial x} + \frac{\partial Z}{\partial x} \right) dA = \int_{t^n}^{t^{n+1}} \int_{\sigma_j^n(t)}^{\sigma_{j+1}^n(t)} h \frac{\partial(h+Z)}{\partial x} dx dt. \quad (2.68)$$

Therefore from (2.68) we get,

$$I_{m,j}^n \approx H_j^n \int_{t^n}^{t^{n+1}} (h(\sigma_{j+1}^n(t), t) + Z(\sigma_{j+1}^n(t)) - (h(\sigma_j^n(t), t) + Z(\sigma_j^n(t)))) \, dt. \quad (2.69)$$

The last integral can be approximated using Taylor series expansion of order one, where we use a slope limiter to approximate the derivatives $(H_x)_j$ and $(Z_x)_j$, and the trapezoidal rule for the integral on time. The final approximation gives

$$\begin{aligned} I_{m,j}^n &\approx H_j^n (H_{j+1}^n + Z_{j+1} - (H_j^n + Z_j)) \\ &\quad + 0.5 H_j^n (\Delta t)^2 (f_{h,j+1}^n (H_x)_{j+1}^n + f_{h,j}^n (Z_x)_{j+1} - (f_{h,j}^n (H_x)_j - f_{h,j+1}^n (Z_x)_{j+1})). \end{aligned} \quad (2.70)$$

The three following test cases come from [59] (see [24, 43, 90] and references therein). The topography is flat with a bump for $x \in [8, 12]$, as follows: $Z(x) = 0.2 - 0.05(x - 10)^2$. The transcritical flow without shock, transcritical flow with shock and subcritical flow test cases are performed according to the initial and boundary conditions given by [43, 59, 90]. The first test models the transcritical flow without shock [90]. For this case, the initial water height is 0.33 m. A unit discharge of $1.53 \text{ m}^2/\text{s}$ is imposed at the upstream boundary, and open boundary conditions ($\frac{dh}{dx} = 0$, $\frac{du}{dx} = 0$) are applied at the downstream side. The numerical solutions for water height and discharge can be seen in Figure 12 after the steady state has been reached (which happens at time 41.5 sec.). We show in Figure 12 the numerically evaluated water height and discharge with the corresponding analytical solutions, with three levels of refinement (200, 600 and 1000 mesh points). At the end of the bump a constant level is again reached. Discharge shows an underestimation near the bump, reduced on refinement. The elapsed computation time was 35.842, 238.702 and 613.800 seconds respectively. The second test models the transcritical flow with a shock. The initial water height is also 0.33 m. A unit discharge of $0.18 \text{ m}^2/\text{s}$ is imposed on the upstream boundary and a depth of 0.33 m is imposed on the downstream boundary. The steady state here is reached at 175.5 sec. We show in Figure 13 the analytical and numerical solution for water surface profile and discharge, with three levels of refinement (200, 600 and 1000 mesh points). A local peak in numerical solution for discharge is observed on the jump after the bump (for more details on this behavior see [90] and references therein). The elapsed computation time was 24.363, 122.283 and 330.639 seconds respectively. The third test models the subcritical flow over a bump without a shock. Subcritical flow conditions are maintained in the same channel as taken in the above two cases. A unit discharge of $4.42 \text{ m}^2/\text{s}$ is imposed on the upstream boundary and a depth of 2.0 m is imposed on the downstream boundary. The steady state is reached at time 85.5 sec. Figure 14 shows the solutions for this case after reaching the steady state, with three levels of refinement (200, 600 and 1000 mesh points). The elapsed computation time was 38.186, 227.651 and 482.891 seconds respectively. For all the three cases, the

Lagrangian-Eulerian scheme produced qualitatively correct results compared to analytical solutions with 200 mesh grid cells.

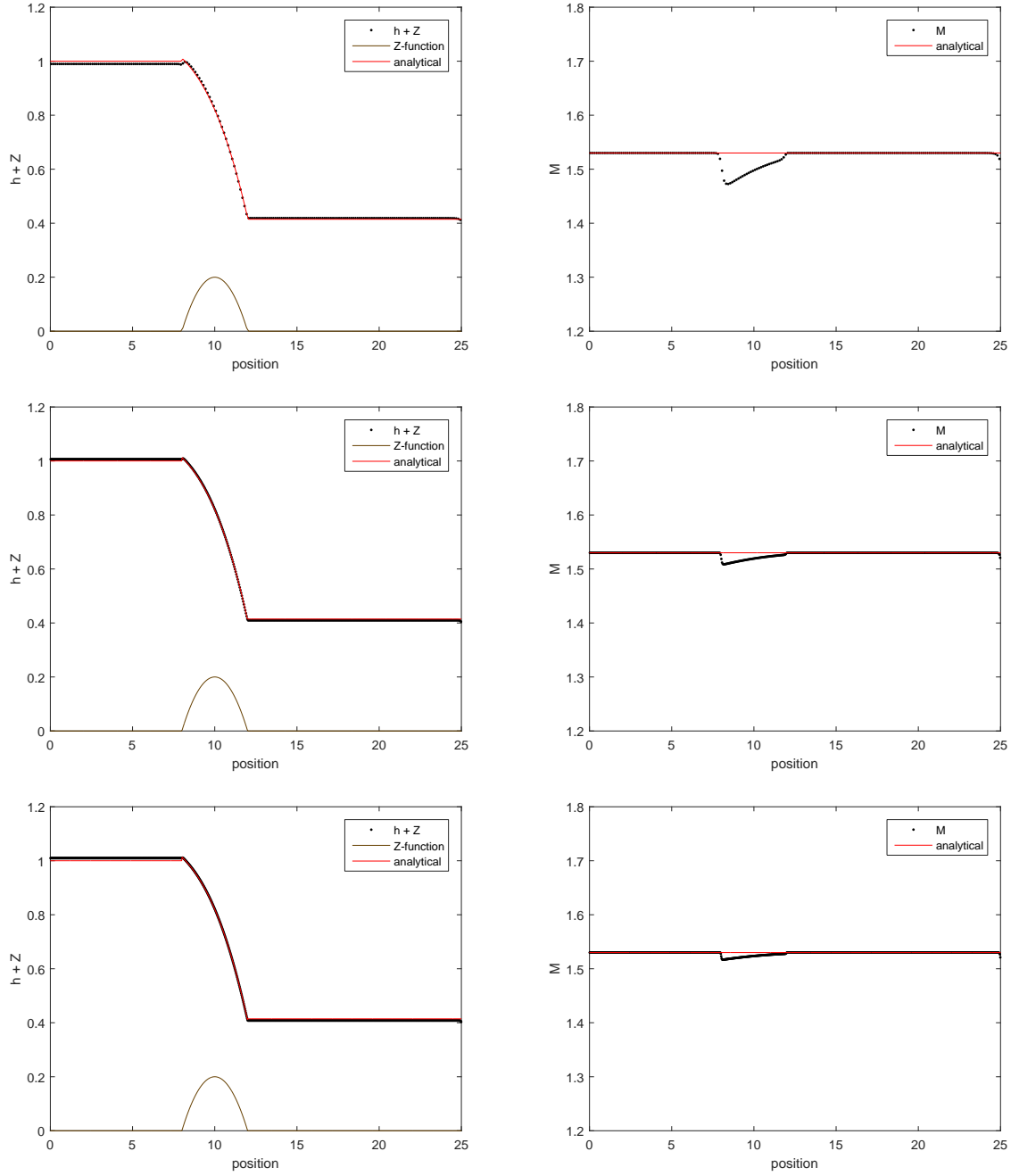


Figure 12 – Transcritical without shock test case. The steady-state has been already reached (exhibited time is $t = 600$ sec.). Left: $h + Z$ solutions with 200, 600 and 1000 mesh grid points. Right: discharge M with 200, 600 and 1000 mesh grid points.

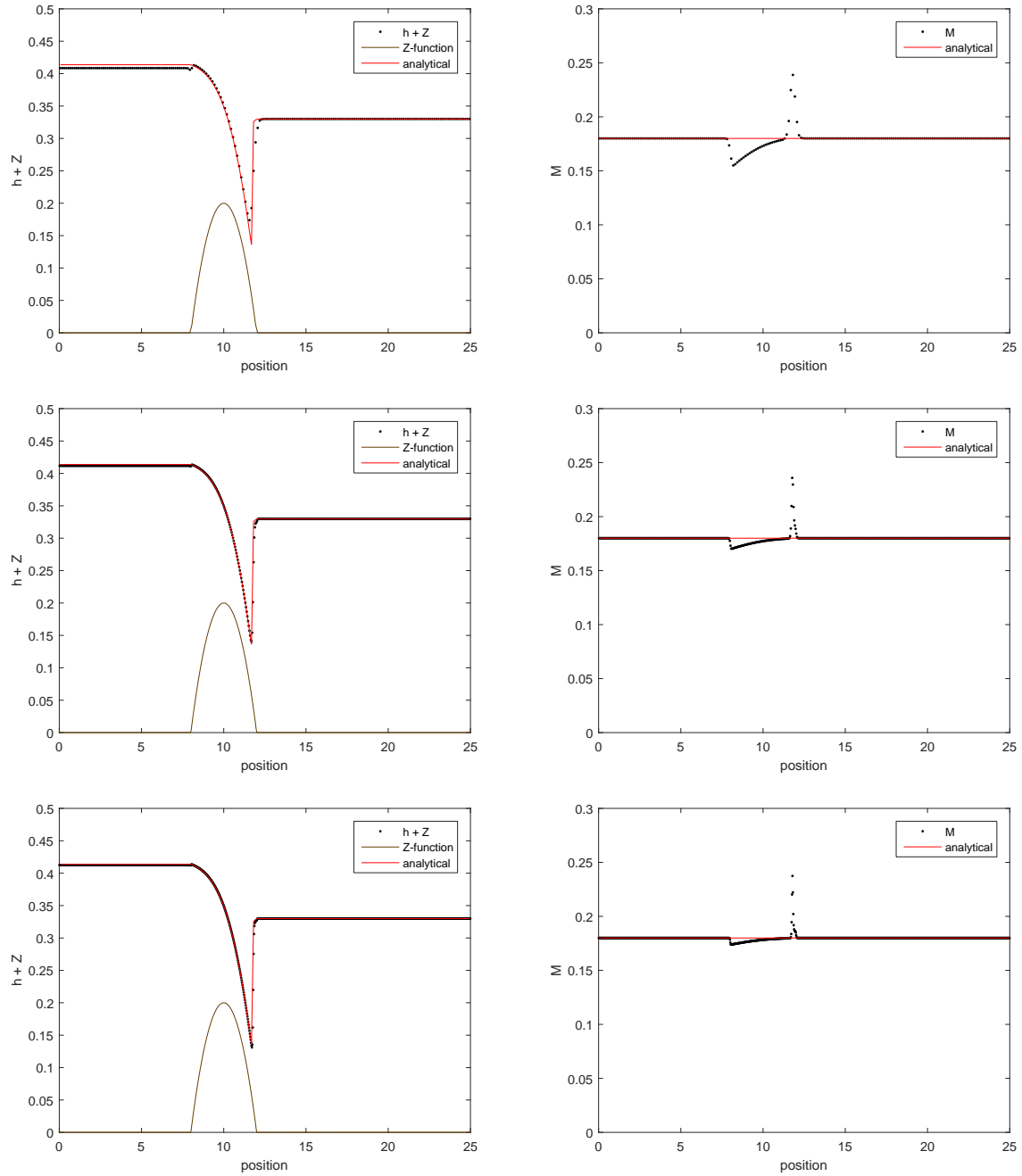


Figure 13 – Transcritical with shock test case. The steady-state has been already reached (exhibited time is $t = 600$ sec.). Left: $h + Z$ solutions with 200, 600 and 1000 mesh grid points. Right: discharge M with 200, 600 and 1000 mesh grid points

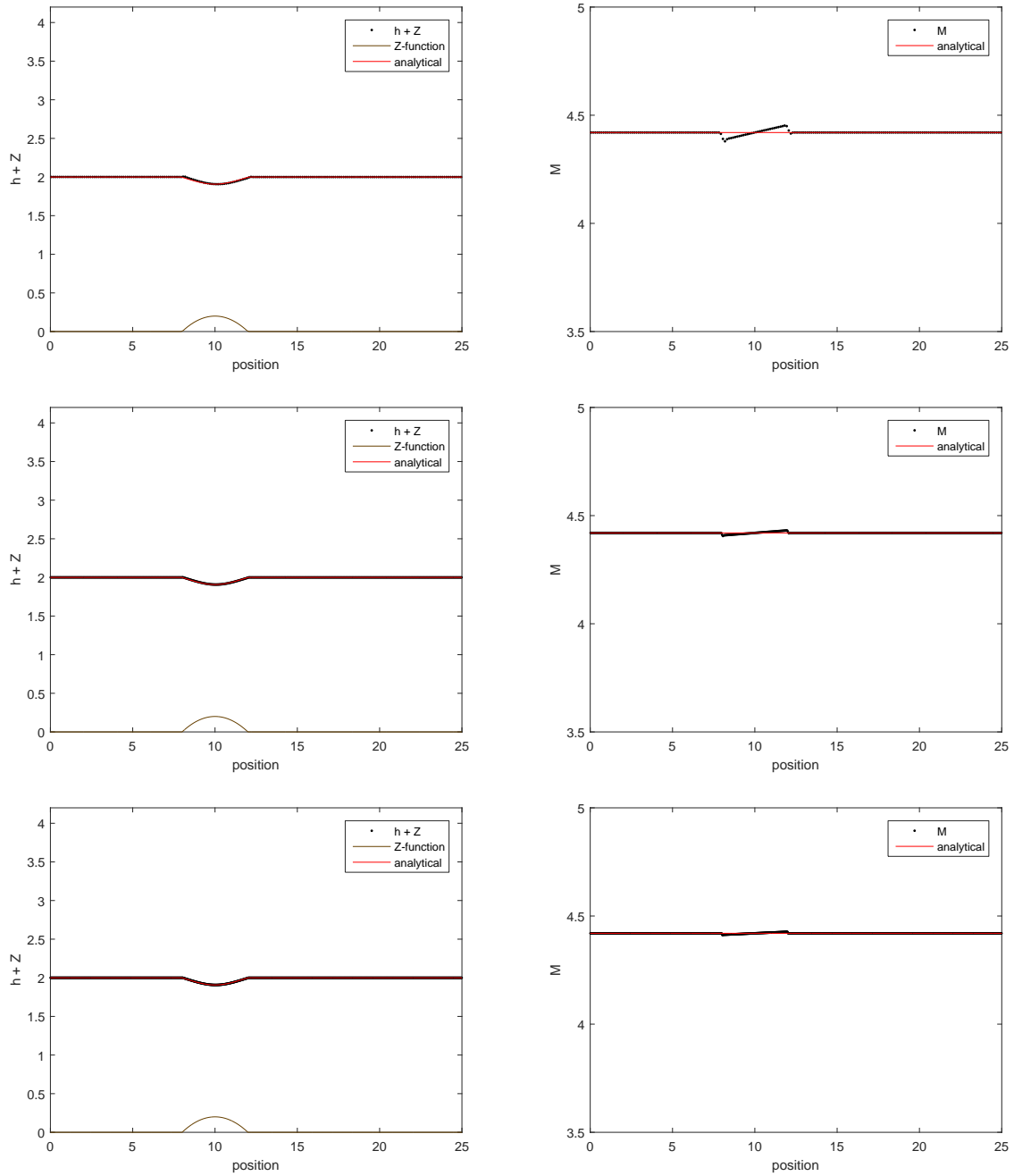


Figure 14 – Subcritical test case. The steady-state has been already reached (exhibited time is $t = 600$ sec.). Left: $h + Z$ solutions with 200, 600 and 1000 mesh grid points. Right: discharge M with 200, 600 and 1000 mesh grid points

Next, the following results are reproductions of the test cases presented in [35] - Small perturbation of steady flow over a slanted surface. We consider the modified system for shallow water equations presented in the cited paper, with water source term $R(x, t)$ (which for the test cases is identically zero) and a bottom friction term with the classical Manning formulation. In one spatial dimension the equation is reduced to:

$$\begin{cases} \frac{\partial h}{\partial t} + \frac{\partial(hu)}{\partial x} = R(x, t), \\ \frac{\partial(hu)}{\partial t} + \frac{\partial(hu^2 + \frac{g}{2}h^2)}{\partial x} = -ghZ_x - g\frac{n^2}{h^{\frac{1}{3}}}u|u|, \end{cases} \quad (2.71)$$

We consider the initial data

$$h(x, 0) = h_0 + \begin{cases} 0.2h_0, & 1 \leq x \leq 1.25, \\ 0, & \text{otherwise} \end{cases} \quad q(x, 0) = q_0 \quad (2.72)$$

The first test is a supercritical case, with $h_0 = 0.09564$, $q_0 = 0.1$, $n = 0.02$ and the (constant) slope of topography $Z_x = -0.01$. We show on Figure 15 the initial state, a snapshot at time $t = 1.0$ sec., where the perturbation propagates to the right and the steady state at time $t = 100$ sec. Next, the subcritical case is presented with $h_0 = 0.02402$, $q_0 = 0.002$, $n = 0.1$ and the slope of topography again as -0.01 . Here, the shape of the propagated solution is different from the previous case. The ellapsed computation time was 0.650 and 105.299 seconds respectively. We show on Figure 16 the initial state, a snapshot at time $t = 0.5$ sec. and the steady state solution at time $t = 100$ sec. The ellapsed computation time was 0.078 and 6.157 seconds respectively. Then, the last case on Figure 17 shows a magnitude of topography slope larger than the other cases, $Z_x = \frac{1}{\sqrt{3}}$. In this case, the perturbation propagates faster than in previous tests, but the numerical steady state is achieved at large times. The ellapsed computation time was 0.515 and 70.977 seconds respectively. These tests are evaluated with 200 grid cells.

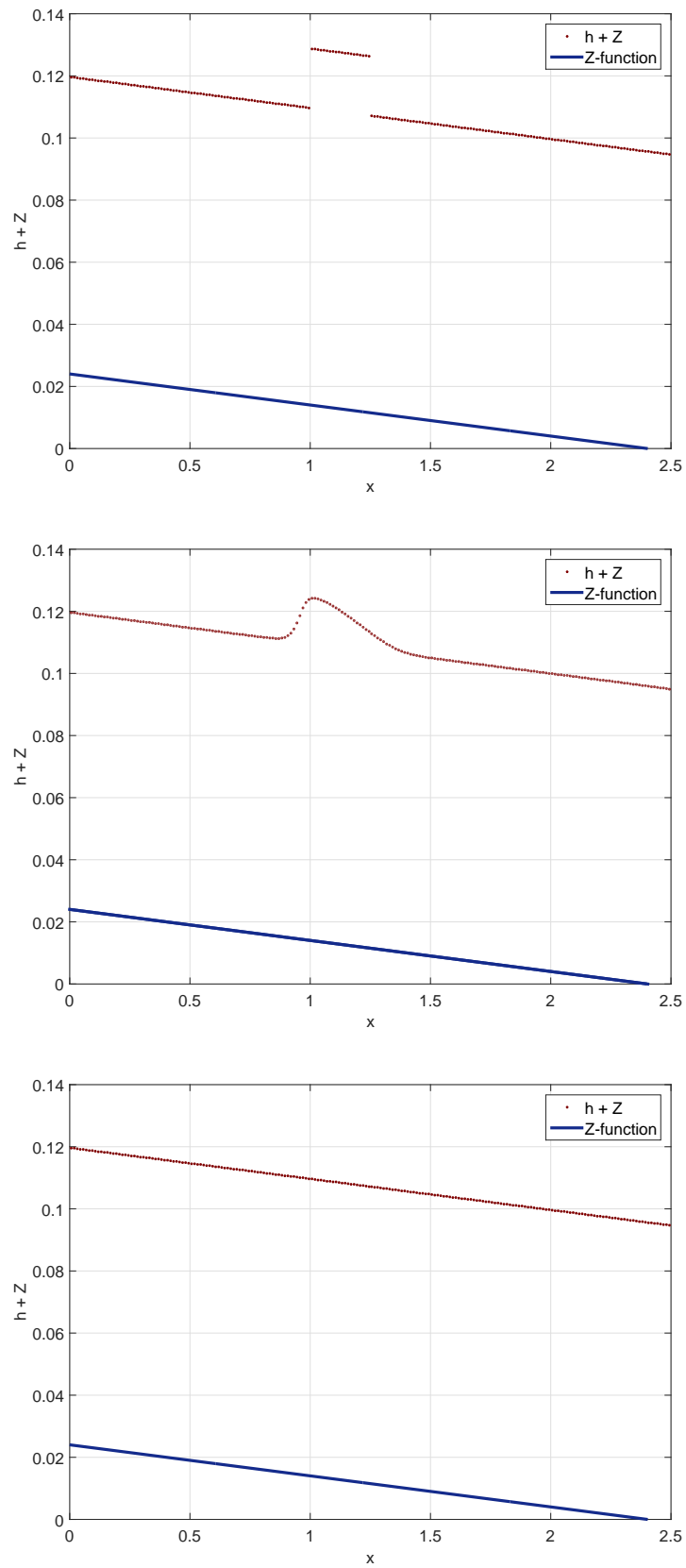


Figure 15 – Supercritical test case at initial time (top), $t = 1.0$ sec. (middle), and steady state at $t = 100$ sec. (bottom).

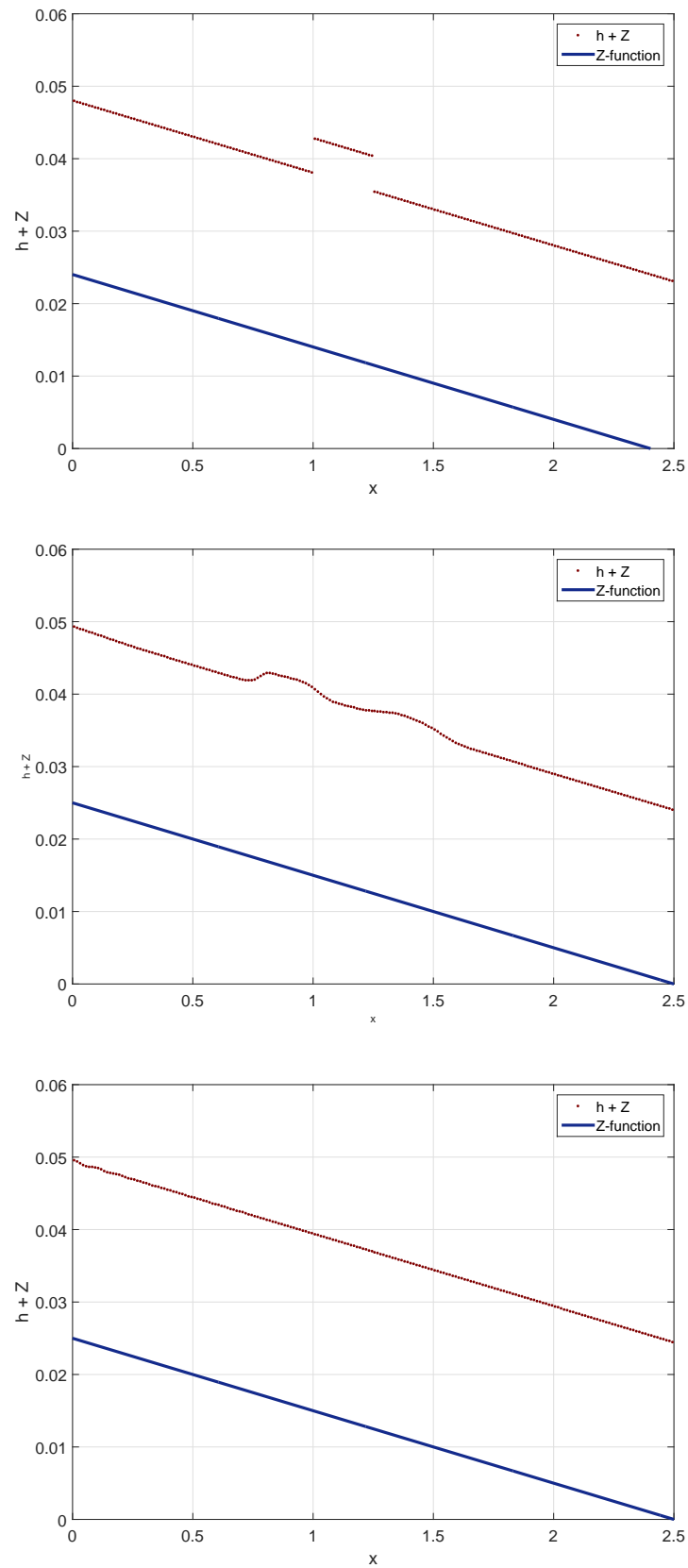


Figure 16 – Subcritical test case at initial time (top), $t = 0.5$ sec. (middle), and steady state at $t = 100$ sec. (bottom).

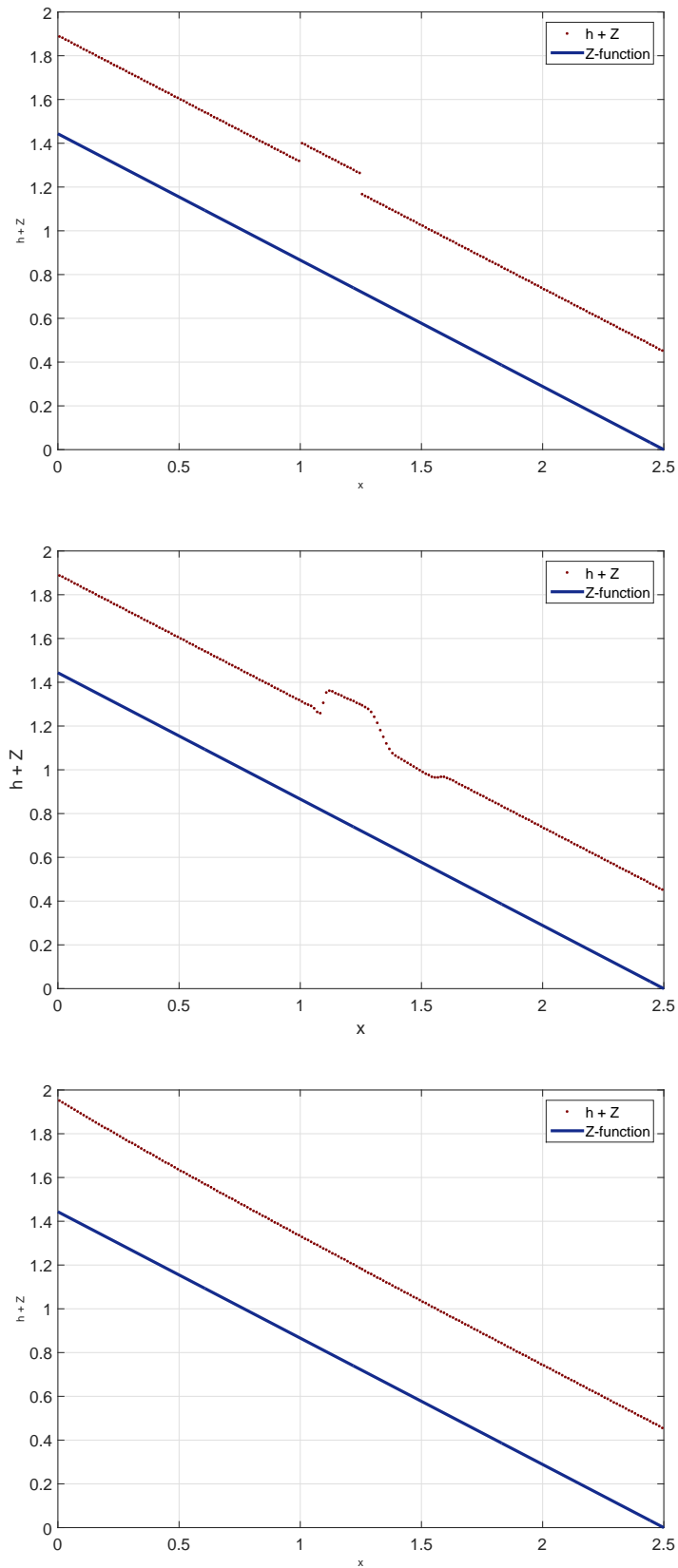


Figure 17 – Larger slope topography test case at initial time (top), $t = 0.05$ sec. (middle), and steady state at $t = 100$ sec. (bottom).

2.5.3.1 Zero velocity and steady-state solutions

One particular case occurs when $f_j^n = 0$. The integral curves now are vertical lines, so the original grid does not change in time and we obtain the steady-state solution of the simulated problem. To illustrate such situation, we present in this section an example from [61]:

$$\begin{cases} \frac{\partial u}{\partial t} + \frac{\partial(f(u))}{\partial x} = -u Z_x(x), & t > 0, \quad (x, t) \in \mathbb{R} \times (0, T], \\ u(x, 0) + Z(x) = 1, \end{cases} \quad (2.73)$$

where $Z(x) = 0.9 \left(\cos(\pi \left(\frac{x-1}{2} \right)) \right)^{30}$ if $0 \leq x \leq 2$ and zero otherwise. With $f(u) = u^2/2$ the steady-state solution of this problem is $u + Z(x) = 1$. Note that the steady-state solution is achieved when the following identity is satisfied:

$$0 = \frac{\partial u}{\partial t} = -\frac{\partial(\frac{u^2}{2})}{\partial x} - u Z_x(x) = -u(u + Z)_x. \quad (2.74)$$

The control volume is

$$D_j^n = \{(t, x) / t^n \leq t \leq t^{n+1}, x_j^n \leq x \leq x_{j+1}^n\},$$

where the integrals curves are the vertical lines $x = x_j^n$ i.e the original grid does not change in time. Hence, the projection step is not necessary anymore. This is the geometrical interpretation of the tracing forward of the cell dual grid being identical to the original grid. Integrating (2.74) over D_j^n gives:

$$\begin{aligned} \int_{t^n}^{t^{n+1}} \int_{x_j^n}^{x_{j+1}^n} \nabla_{t,x} \cdot \begin{bmatrix} u \\ 0 \end{bmatrix} dx dt &= \int_{t^n}^{t^{n+1}} \int_{x_j^n}^{x_{j+1}^n} (u_t + [0]_x) dx dt \\ &= \int_{t^n}^{t^{n+1}} \int_{x_j^n}^{x_{j+1}^n} (-u(u + Z)_x) dx dt. \end{aligned} \quad (2.75)$$

By the application of the divergence theorem on the left side of (2.75), we get

$$\oint_{\partial D_j^n} \vec{n} \cdot \begin{bmatrix} u \\ 0 \end{bmatrix} \partial D_j^n = \int_{t^n}^{t^{n+1}} \int_{x_j^n}^{x_{j+1}^n} (-u(u + Z)_x) dx dt. \quad (2.76)$$

Since the integrals curves $x = x_j^n$ are impervious, the flux is vertical from t^n to t^{n+1} . Dividing by h , we get

$$\frac{1}{h} \int_{x_j^n}^{x_{j+1}^n} u(x, t^{n+1}) dx - \frac{1}{h} \int_{x_j^n}^{x_{j+1}^n} u(x, t^n) dx = \frac{1}{h} \int_{t^n}^{t^{n+1}} \int_{x_j^n}^{x_{j+1}^n} (-u(u + Z)_x) dx dt. \quad (2.77)$$

Thus

$$U_{j+\frac{1}{2}}^{n+1} - U_{j+\frac{1}{2}}^n = \frac{1}{h} \int_{t^n}^{t^{n+1}} \int_{x_j^n}^{x_{j+1}^n} (-u(u + Z)_x) dx dt. \quad (2.78)$$

With this, the numerical scheme can be written as follows

$$\begin{aligned} U_{j+\frac{1}{2}}^{n+1} &= U_{j+\frac{1}{2}}^n + \frac{1}{h} \int_{t^n}^{t^{n+1}} \int_{x_j^n}^{x_{j+1}^n} (-u(u+Z)_x) dx dt \\ &\approx U_{j+\frac{1}{2}}^n - \frac{1}{h} U_{j+\frac{1}{2}}^n ((u+Z)_x)_j^n \int_{t^n}^{t^{n+1}} \int_{x_j^n}^{x_{j+1}^n} dx dt. \end{aligned} \quad (2.79)$$

Notice that we approximate the derivative $(u+Z)_x$ with the previously discussed slope limiters. We show in Figure 18 the steady-state solution approximated by this numerical scheme. This example exhibits a numerical version of a well-balancedness property for our framework, see Figure 18 (left). We also show an example from [24], see Figure 18 (right), with $Z(x) = 0.4e^{(\sin(x)-1)}$ and the steady-state solution of the simulated problem given by $u + Z = 0.5$.

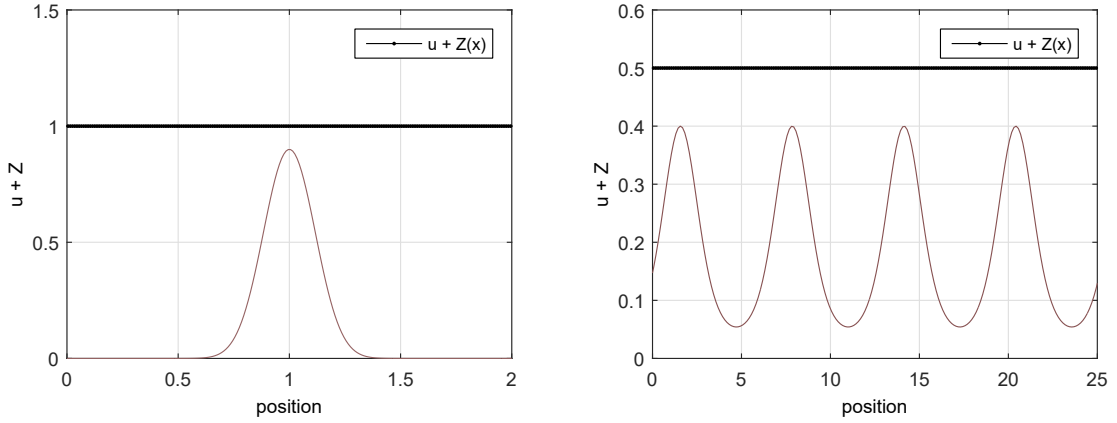


Figure 18 – Steady-state solution for the problem modeled by equation 2.73 with different topographies. The solution for both cases is approximated with 200 mesh grid cells at time $t = 100$.

2.5.4 Two-dimensional simulations of nonlinear scalar conservation laws

The first example is taken from [55]. The test consists in considering the simple flux functions

$$f(u) = g(u) = \frac{u^2}{u^2 + 2(1-u)^2},$$

with the Gaussian initial data $u_0(x, y) = \exp(-10((x+0.25)^2 + (y+0.25)^2))$, $x, y \in (-1, 1)$. Numerical solutions with 512 cells and end time $t = 1.5$ of simulation are shown in Figure 19, left picture is the approximation with our proposed scheme given by (2.29)-(2.32) and (2.48)-(2.50) (performed in 59.846 sec), middle picture with a Strang splitting approximation along with the well-known high-resolution, non-oscillatory, second order Nessyahu-Tadmor central scheme (see e.g., [76]), used here as reference solution, and finally in right picture it is shown the absolute error between both solutions. The next test is called “fingering test”

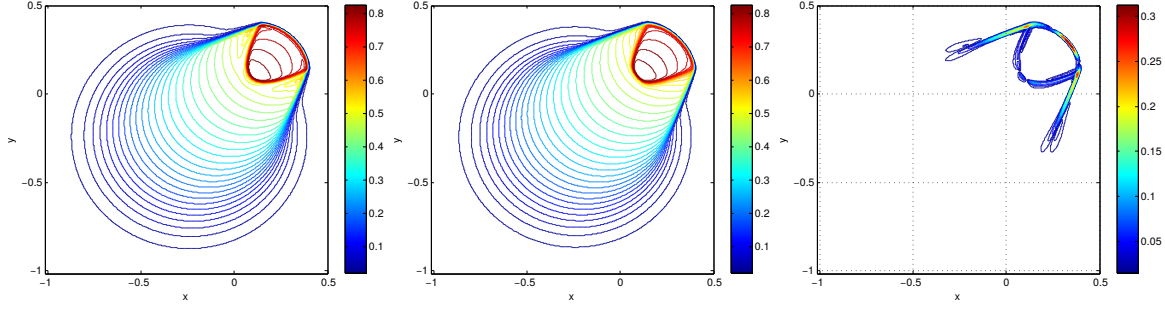


Figure 19 – Numerical solutions for the Buckley-Leveret equation. Left the solution with 512 grid points approximated with the Lagrangian-Eulerian framework. Center: The Strang splitting approach with Nessyahu-Tadmor numerical scheme with 512 points. Right: The difference error between the two approximations.

in [55]. In this test, it is used two different flux functions $f(u) = \frac{u^2}{2}$ and $g(u) = \frac{2u^2}{5}$, along with the initial condition $u(x, y, 0) = 1$ in the circle $\{(x, y)/(x + 0.5)^2 + (y + 0.5)^2 \leq 0.16\}$, $u(x, y, 0) = -1$ in the circle $\{(x, y)/(x - 0.5)^2 + (y - 0.5)^2 \leq 0.16\}$ and zero in otherwise, when $(x, y) \in [-1, 1]^2$. The accurate numerical solutions displayed in Figure 20 is arranged as above for Figure 19, but for an end time $t = 2$ of simulation.

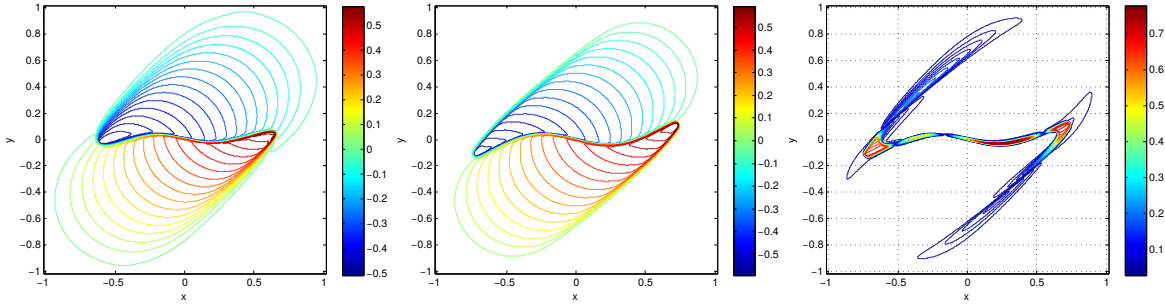


Figure 20 – Numerical solutions for the “fingering test”. Left the solution with 512 grid points approximated with the Lagrangian-Eulerian framework. Center: The Strang splitting approach with Nessyahu-Tadmor numerical scheme with 512 points. Right: The difference error between the two approximations.

2.5.5 Sources with space-discontinuous functions and nontrivial topography

We discuss the hard case of a balance law $u_t + f_x(u) = g(x, u)$ with g discontinuous in x , along with our method as developed in Section 2.2. In other words, we have not made any special treatment for approximation of the discontinuous source term. In particular, our results (see Figure 21) are in very good agreement with the numerical experiment reported in [66]. This means that our novel approach is able to capture the delicate nonlinear local interaction between the flux and the source within the control volume of the Lagrangian-Eulerian framework. In addition, we mention that the discontinuity of the source term might lead to significant influences on the shock or

rarefaction waves generated by the initial Riemann data, and produces some new and interesting phenomena such as the appearance of weak discontinuities and the appearance and absorption of new shocks (see [52] for details). In [66], Shi Jin considered the model,

$$u_t + (f(u))_x = g(x, u) \quad (2.80)$$

with flux function $f(u) = \frac{u^2}{2}$ and source term $g(x, u) = z'(x)u$ with $z(x) = \cos(\pi x)$, $4.5 \leq x \leq 5.5$ and 0 otherwise with $0 < x < 10$. Note that $z'(x)$ is then a discontinuous function, so that $g(x, u)$ is a discontinuous source term in x . Figure 21 shows approximations with initial data $u(x, 0) = 0$, $x > 0$ and $u(0, t) = 2$, $t > 0$. In the right pictures of Figure 21 it is shown solutions of $u + z = 2$ compared with the exact solution (solid line) at steady state for a continuous topography in a mesh refinement study; from top to bottom we have numerical solutions (dashed lines): 128, 256 and 512 cells. In the left pictures of Figure 21 it is shown solutions at finite time the steady state counterpart solutions for the same situation. The numerical scheme gives clearly qualitatively correct approximations at $t = 10$ even in numerical coarse grids.

We now discuss the shallow water equations over non-trivial topography $g(x, u)$ of the seminal work of Greenberg and LeRoux [61] (see also [60]) given by

$$u_t + \left(\frac{u^2}{2} \right)_x = g(x, u),$$

with flux function $f(u) = \frac{u^2}{2}$ and source term $G(u) = a'(x)u$. In this test, the function $a(x)$ is defined as $a(x) = 0.9 \cos(\pi(\frac{x-1}{2}))^{30}$, $x \leq 2$ and 0 otherwise. Figure 22 shows a non-stationary shock wave connecting two states that correspond to steady solutions for which $u + a = 1.3$ on the left and $u + a = 1$ on the right. In this numerical test, the initial data is $u(x, 0) = 1 - a(x)$, $x > 0.2$ and $u(x, 0) = 1.3 - a(x)$, $x < 0.2$. The scheme produces a qualitatively correct monotone curve as the mesh grid is refined keeping the total height $u + a$ at $t = 1.5$.

2.5.6 A hard test case with exponential growth of the source term

The main goal of this example is, as in [56], to emphasize the qualitative difference between time-splitting, (or fractional step methods) and well-balanced numerical schemes when it comes to computing the entropy solution of a simple scalar, yet non-resonant, balance law $\partial_t u + \partial_x(f(u)) = k(x)g(u)$, $0 < k \in L^1 \cap C^0(\mathbb{R})$, f is genuinely non-linear and $g \in C^1(\mathbb{R})$, see [56] for more details. In this particular problem it is considered $f(u) = u^2/2$, $k(x) = 0.2$ and $g(u) = u$ with initial data $u_0(x) = Y(x)$, Y the Heaviside function. This results in the classical “one-half” order of convergence in L^1 , which is known to be optimal for Godunov type [88, 92], denoting the entropy solution u and its numerical approximation by $u^{\Delta t}$; see [92] that states: $\forall t \in [0, T]$, $\|u^{\Delta t}(t, \cdot) - u(t, \cdot)\|_{L^1(\mathbb{R})} \leq C\sqrt{\Delta t}$.

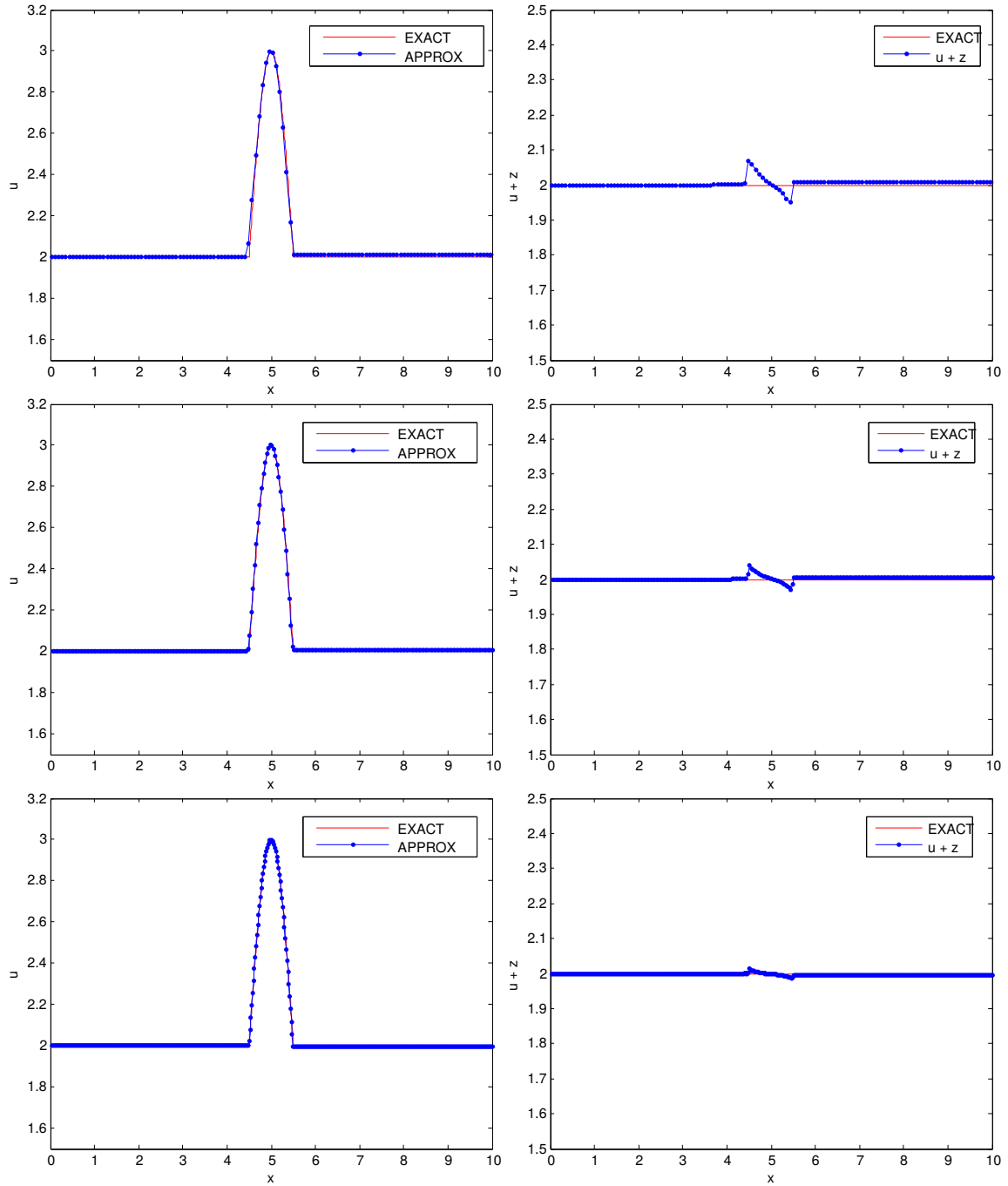


Figure 21 – Numerical solutions with nontrivial spatial-discontinuous source term $g(x, u) = z'(x)u$. We present a grid refinement study for u and $u + z$ with 128, 256 and 512 mesh grid points.

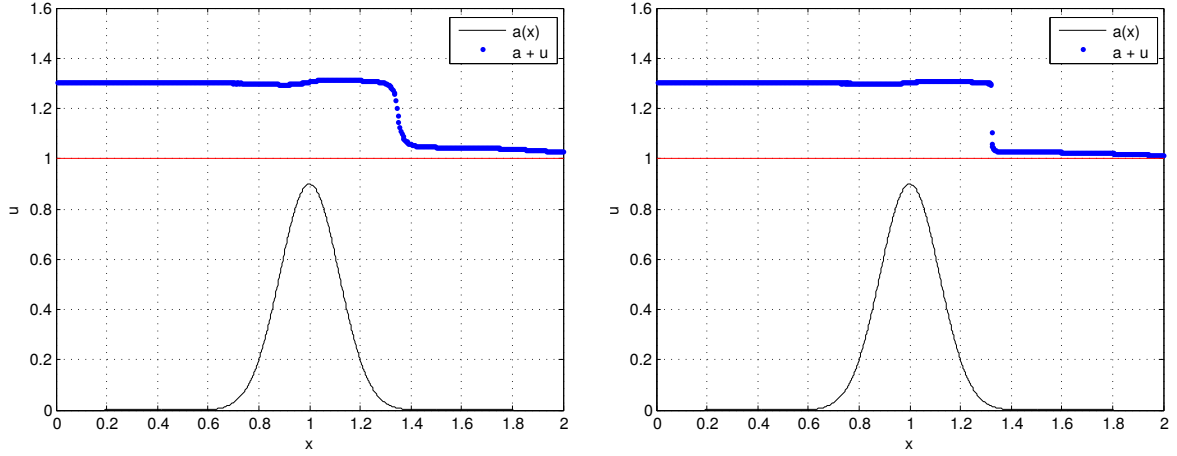


Figure 22 – Numerical solutions with source term $g(x, u)$. 512 cells (left), 1024 cells (right).

The analysis discussed in [92] reveals that the “constant C” is actually an exponential in time, which results in the more rigorous statement: $\forall t \in [0, T], \|u^{\Delta t}(t, \cdot) - u(t, \cdot)\|_{L^1(\mathbb{R})} \leq C \exp(\max[g'(u)]t) \sqrt{\Delta t}$. This estimate is disastrous from a computational standpoint, because in order to keep the absolute error below a given tolerance, the computational grid’s parameters are meant to decrease exponentially with time (except if $g' \leq 0$, for which $TV(u)(t, \cdot)$ decays exponentially too). Figure 23 shows numerical approximations with 256 and 512 cells.

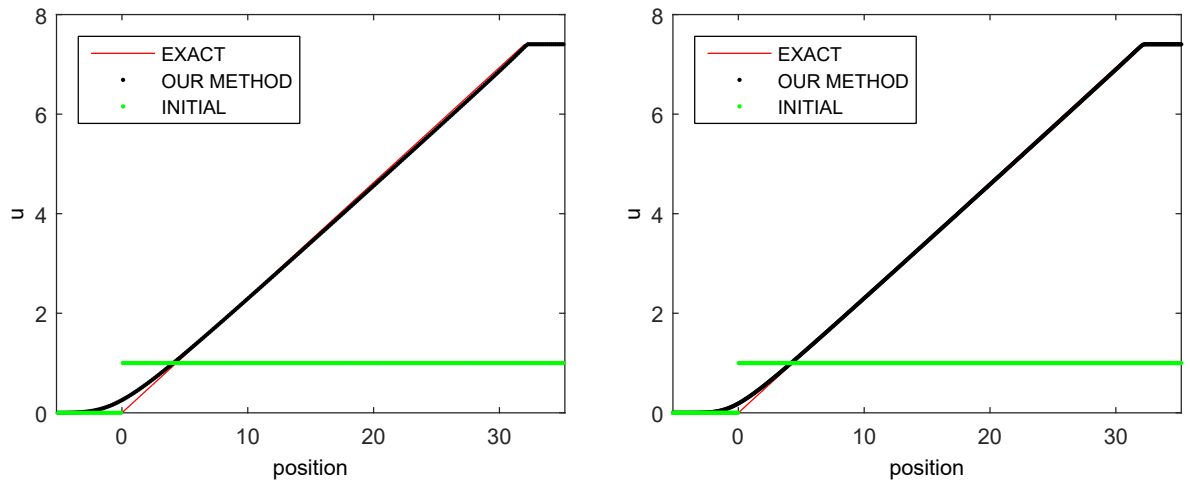


Figure 23 – Numerical approximations of the scalar balance law. The solution is shown with 256 cells (left) and 512 cells (right).

2.5.7 Error analysis

We first present an error analysis study performed for the linear conservation law $u_t + au_x = 0$, with $a = 1.0$ and a smooth initial condition. We observe from information below that our method presents first-order accuracy behavior. Figure 24 shows the log-log plot of the error against the analytical solution $u(x, t) = u_0(x - t)$ for 32, 64, 128, 256 and 512 mesh grid cells, in various norms. Table 1 presents the exact values of the errors and a convergence rate in various norms.

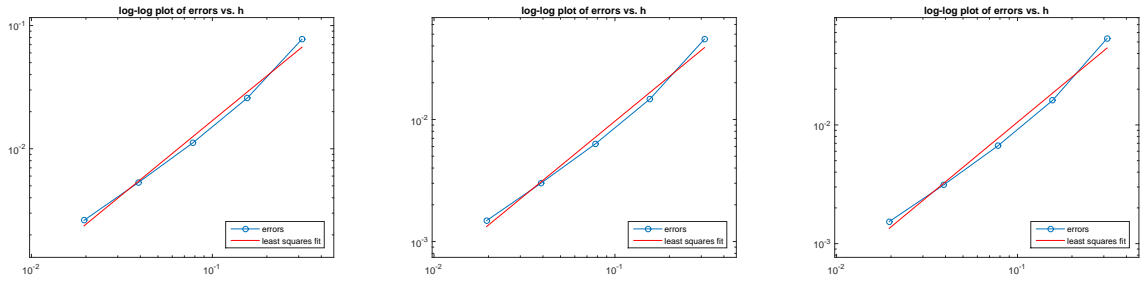


Figure 24 – Log-log plots for norms L^1 (left), L^2 (middle) and L^∞ (right) of the error versus the cell sizes, for the the linear problem $u_t + u_x = 0$ at time $T = 1.0$ with smooth initial condition $u(x, 0) = e^{-x^2}$; we can see first-order behavior of accuracy in the numerical solutions.

Cells	h	$\ u - U\ _{l_h^1}$	$\ u - U\ _{l_h^2}$	$\ u - U\ _{l_h^\infty}$
32	0.31250	4.13831×10^{-2}	2.39536×10^{-2}	5.34744×10^{-2}
64	0.15625	1.35621×10^{-2}	7.75141×10^{-3}	1.61009×10^{-2}
128	0.07813	5.61517×10^{-3}	3.17689×10^{-3}	6.68850×10^{-3}
256	0.03906	2.69301×10^{-3}	1.52179×10^{-3}	3.12262×10^{-3}
512	0.01953	1.32042×10^{-3}	7.46087×10^{-4}	1.53242×10^{-3}
LSF $E(h)$		$0.147 \times h^{1.227}$	$0.085 \times h^{1.235}$	$0.192 \times h^{1.261}$

Table 1 – Corresponding errors between the numerical approximations (U) and exact solutions (u) for the scalar advection problem.

A study of the numerical error for the balance law problem 2.80 with discontinuous source term is shown in Figure 25 for 32, 64, 128, 256 and 512 mesh grid cells, in various norms, along with the observed first-order behavior of accuracy in the computed solutions in several discrete norms (presented in Table 2).

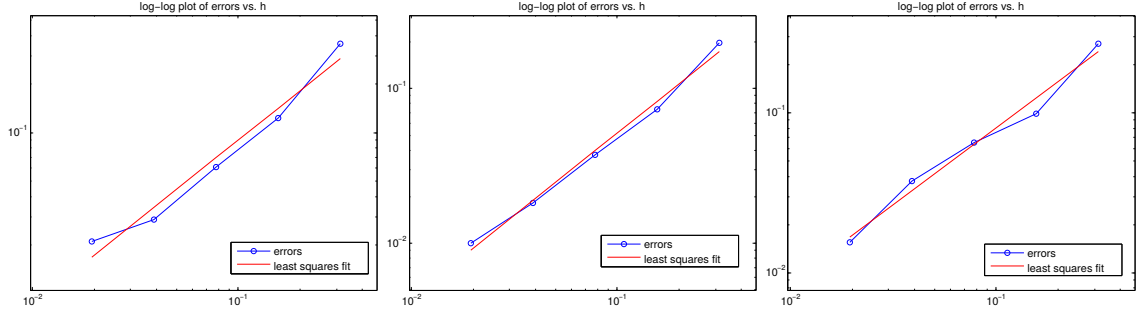


Figure 25 – Log-log plots for norms L^1 (left), L^2 (middle) and L^∞ (right) of the error versus the cell sizes, for the situation with a source term $g(x, u)$ discontinuous in x ; we can see first-order behavior of accuracy in the numerical solutions.

Cells	h	$\ u - U\ _{l_h^1}$	$\ u - U\ _{l_h^2}$	$\ u - U\ _{l_h^\infty}$
32	0.31250	3.57138×10^{-1}	1.98505×10^{-1}	2.27229×10^{-1}
64	0.15625	1.23307×10^{-1}	7.32096×10^{-2}	9.87682×10^{-2}
128	0.07813	6.13928×10^{-2}	3.73888×10^{-2}	6.50388×10^{-2}
256	0.03906	2.88161×10^{-2}	1.81468×10^{-2}	3.74213×10^{-2}
512	0.01953	2.10403×10^{-2}	9.98296×10^{-3}	1.55670×10^{-2}
LSF $E(h)$		$0.95 \times h^{1.027}$	$0.6 \times h^{1.064}$	$0.74 \times h^{0.966}$

Table 2 – Corresponding errors between the numerical approximations (U) and exact solutions (u) for the balance law with discontinuous source term.

3 Further developments in the Lagrangian-Eulerian Framework

The Lagrangian-Eulerian approach is a promising tool for numerically solving differential models of several types [5, 6, 9, 84]. In the previous chapter, we presented the framework and some numerical experiments for the numerical scheme. In the present chapter, we present further advances within the framework, some of the current progress pushing the boundaries of this technique. Much of this work is currently under development. First, we present a variation in which the control volume is defined in a way so that the final mesh grid of the finite volume scheme is not staggered. Such nonstaggered version has also presented good numerical results, in a similar fashion to the staggered more classical form. We include an elaborate discussion on how to extend this formulation to two-dimensional problems in an alternative fashion of the previous proposed. We also sketch a convergence proof following the weak asymptotic methods theory from [8], since this alternate staggered approach can be formulated in a way to mimic procedures of the proof of convergence.

3.1 The nonstaggered Lagrangian-Eulerian conservative finite volume method

We present a nonstaggered form of the Lagrangian-Eulerian framework for the first-order scalar hyperbolic conservation law, with $x \in \mathbb{R}, t > 0, u : (\mathbb{R}, \mathbb{R}^+) \rightarrow \mathbb{R}$:

$$\frac{\partial u}{\partial t} + \frac{\partial H(u)}{\partial x} = 0, \quad x \in \mathbb{R}, \quad t > 0, \quad u(x, 0) = u_0(x). \quad (3.1)$$

Following the usual Lagrangian-Eulerian ideas, local conservation is obtained by integrating the conservation law over the region in the space-time domain where the conservation of the mass flux takes place. We now, however, define the control volume in a slightly different manner. Consider the Lagrangian-Eulerian finite-volume cell centers

$$D_j^n = \{(t, x) / t^n \leq t \leq t^{n+1}, \sigma_{j-\frac{1}{2}}^n(t) \leq x \leq \sigma_{j+\frac{1}{2}}^n(t)\}, \quad (3.2)$$

where $\sigma_{j-\frac{1}{2}}^n(t)$ is the parameterized integral curve such that $\sigma_{j-\frac{1}{2}}^n(t^n) = x_{j-\frac{1}{2}}^n$. These curves are the lateral boundaries of the domain D_j^n in (3.2) and we define $\bar{x}_{j-\frac{1}{2}}^n := \sigma_{j-\frac{1}{2}}^n(t^{n+1})$ and $\bar{x}_{j+\frac{1}{2}}^n := \sigma_{j+\frac{1}{2}}^n(t^{n+1})$ as their endpoints in time t^{n+1} . The numerical scheme is expected to satisfy some type of mass conservation (due to the inherent nature of the conservation law) from time t^n in the space domain $[x_{j-\frac{1}{2}}^n, x_{j+\frac{1}{2}}^n]$ to time t^{n+1} in the space domain

$[\bar{x}_{j-\frac{1}{2}}^{n+1}, \bar{x}_{j+\frac{1}{2}}^{n+1}]$. With this, we must have the flux through curves $\sigma_{j-\frac{1}{2}}^n(t)$ to be zero. From the integration of (3.1) and the divergence theorem, using the fact that the line integrals over curves $\sigma_j^n(t)$ vanish, we get

$$\int_{\bar{x}_{j-\frac{1}{2}}^{n+1}}^{\bar{x}_{j+\frac{1}{2}}^{n+1}} u(x, t^{n+1}) dx = \int_{x_{j-\frac{1}{2}}^n}^{x_{j+\frac{1}{2}}^n} u(x, t^n) dx. \quad (3.3)$$

The linear case from [15] is essentially imitated, but here the curves $\sigma_{j-1/2}^n(t)$ are not straight lines in general, but rather solutions of the set of local nonlinear differential equations [15, 84]:

$$\frac{d\sigma_{j-1/2}^n(t)}{dt} = \frac{H(u)}{u}, \quad \text{for } t^n < t \leq t^{n+1}, \quad (3.4)$$

with the initial condition $\sigma_{j-1/2}^n(t^n) = x_{j-1/2}^n$, assuming $u \neq 0$ (for the sake of presentation). This construction follows naturally from the finite volume formulation of the linear Lagrangian-Eulerian scheme as building block to construct local approximations such as (with the initial condition $\sigma_{j-1/2}^n(t^n) = x_{j-1/2}^n$)

$$f_{j-1/2}^n = \frac{H(U_{j-1/2}^n)}{U_{j-1/2}^n} \approx \frac{H(u)}{u}. \quad (3.5)$$

Indeed, distinct and high-order approximations are also acceptable for $\frac{d\sigma_{j-1/2}^n(t)}{dt}$ and can be viewed as ingredients to improve accuracy of the new family of Lagrangian-Eulerian methods. Equation (3.3) defines mass conservation but in a different mesh cell-centered in points $\bar{x}_{j+\frac{1}{2}}^n$ of width h_j^{n+1} . Along the linear approximation for $f_{j-1/2}^n$, we find out that $\bar{x}_{j-\frac{1}{2}} = x_{j-\frac{1}{2}} + f_{j-1/2} \Delta t$ and $\bar{x}_{j+\frac{1}{2}} = x_{j+\frac{1}{2}} + f_{j+1/2} \Delta t$.

The piecewise constant numerical data is reconstructed into a piecewise linear approximation (but high-order reconstructions are acceptable), through the use of MUSCL-type interpolants:

$$L_j(x, t) = u_j(t) + (x - x_j) \frac{1}{\Delta x} u_j'. \quad (3.6)$$

For the numerical derivative $\frac{1}{\Delta x} u_j'$, there are several choices of slope limiters; in book [76] there is a good compilation of many options. A priori choice of such slope limiters is quite hard, but they are chosen upon the underlying model problem under investigation. One possible for the slope limiter is

$$U_j' = MM \left\{ \alpha \Delta u_{j+\frac{1}{2}}, \frac{1}{2} (u_{j+1} - u_{j-1}), \alpha \Delta u_{j-\frac{1}{2}} \right\}, \quad (3.7)$$

and this choice for slope limiter allows steeper slopes near discontinuities and retain accuracy in smooth regions. The range of the parameter α is typically guided by the CFL condition [80]. Equation (3.3) defines a local mass balance between space intervals at time

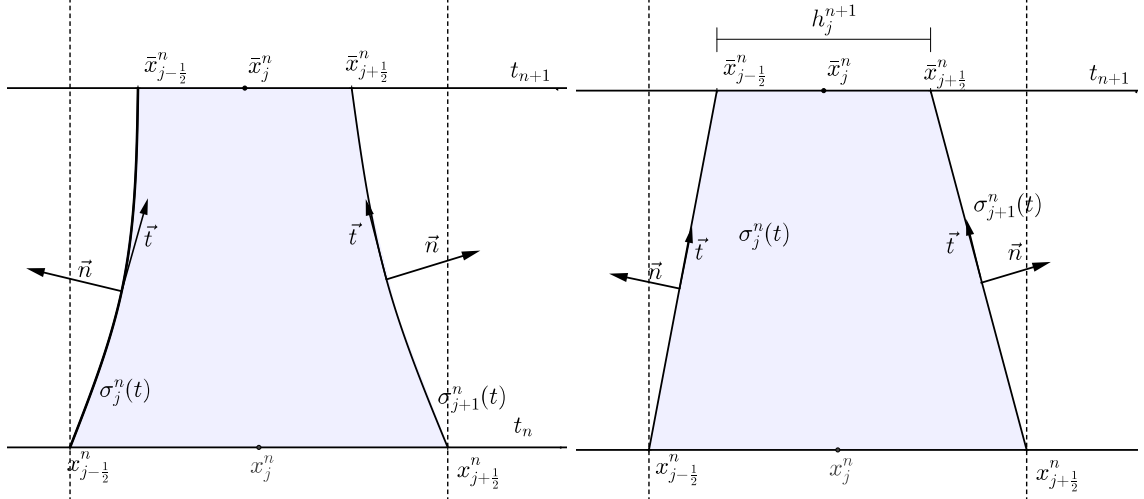


Figure 26 – An illustration of the local space-time nonstaggered integral tube for the continuous (left) and discrete (right).

t^n and intervals at time t^{n+1} . We will later address how to project these volumes back to the original mesh.

Using the approximations

$$\bar{U}_j^{n+1} := \frac{1}{h_j^{n+1}} \int_{\bar{x}_{j-1/2}^{n+1}}^{\bar{x}_{j+1/2}^{n+1}} u(x, t^{n+1}) dx, \quad \text{and} \quad U_j^n := \frac{1}{h} \int_{x_{j-1/2}^n}^{x_{j+1/2}^n} u(x, t^n) dx,$$

the discrete version of equation (3.3) is

$$\bar{U}_j^{n+1} = \frac{1}{h_j^{n+1}} \int_{\bar{x}_{j-1/2}^{n+1}}^{\bar{x}_{j+1/2}^{n+1}} u(x, t^{n+1}) dx = \frac{1}{h_j^{n+1}} \int_{x_{j-1/2}^n}^{x_{j+1/2}^n} u(x, t^n) dx = \frac{h}{h_j^{n+1}} U_j^n, \quad (3.8)$$

Solutions $\sigma_{j-1/2}^n(t)$ of the differential system are obtained using the approximations

$$\begin{aligned} U_{j-1/2} &= \frac{1}{h} \int_{x_{j-1}^n}^{x_j^n} L(x, t) dx = \frac{1}{h} \left(\int_{x_{j-1}^n}^{x_{j-1/2}^n} L_{j-1}(x, t) dx + \int_{x_{j-1/2}^n}^{x_j^n} L_j(x, t) dx \right) \\ &= \frac{1}{2} (U_{j-1} + U_j) + \frac{1}{8} (U'_j - U'_{j-1}). \end{aligned} \quad (3.9)$$

We must notice that the approximation of $f_{j-1/2}^n$ may cause spurious oscillation in Riemann problems, specially in shocks and discontinuity regions. For that, we use a polynomial reconstruction of second degree to smooth out the approximation and also slope limiters approximation of the form (3.7). The numerical solutions have shown qualitatively correct behavior for nonlinear hyperbolic conservation laws. The convergence order remains unchanged even with the reconstruction, being a first-order approximation.

In the reconstruction we use the nonlinear Lagrange polynomial in U_{j-1} , U_j and U_{j+1} . So, equation (3.8) reads

$$\bar{U}_j^{n+1} = \frac{1}{h_j^{n+1}} \int_{x_{j-\frac{1}{2}}^n}^{x_{j+\frac{1}{2}}^n} P_2(x) dx, \quad (3.10)$$

where $P_2(x) = U_{j-1}^n L_{-1}(x - x_j) + U_j^n L_0(x - x_j) + U_{j+1}^n L_1(x - x_j)$ and

$$L_{\pm 1}(x) = \frac{1}{2} \left[\left(\frac{x}{h} \pm \frac{1}{2} \right)^2 - \frac{1}{4} \right], \quad L_0(x) = 1 - \left(\frac{x}{h} \right)^2. \quad (3.11)$$

Next, we obtain the resulting projection formula as follows

$$U_j^{n+1} = \frac{1}{\Delta x} (c_{-1,j} \bar{U}_{j-1}^n + c_{0,j} \bar{U}_j^n + c_{1,j} \bar{U}_{j+1}^n), \quad (3.12)$$

where the projection coefficients are

$$c_{-1,j} = \frac{1}{2} \left(1 + \text{sgn}(f_{j-\frac{1}{2}}) \right) f_{j-\frac{1}{2}} \Delta t =: f^+(U_{j+\frac{1}{2}}) \Delta t, \quad (3.13)$$

$$c_{1,j} = \frac{1}{2} \left(1 - \text{sgn}(f_{j+\frac{1}{2}}) \right) f_{j+\frac{1}{2}} \Delta t =: f^-(U_{j+\frac{1}{2}}) \Delta t, \quad (3.14)$$

$$c_{0,j} = (h - c_{-1,j} - c_{1,j}). \quad (3.15)$$

Here Δt is obtained under CFL-condition

$$\max_j \left\{ |f_{j-\frac{1}{2}}| \Delta t \right\} \leq \frac{h}{2},$$

which is taken by construction of method. We note that in the linear case, when $a(x, t) = a > 0$ (or $a < 0$), the numerical scheme (3.8)-(3.12) is a generalization of the Upwind scheme, but our scheme can approximate solution in both cases $a > 0$ and $a < 0$. The CFL-condition in this case is $|a \Delta t| \leq h$ as in the Upwind scheme.

3.1.1 Extension to balance law problems

For simplicity, we consider the particular scalar equation with $u = u(x, t)$

$$\frac{\partial u}{\partial t} + \frac{\partial(u f(u))}{\partial x} = g(x, u), \quad x \in \mathbb{R}, t > 0; \quad u(x, 0) = u_0(x) \in L^\infty(\mathbb{T}), \quad x \in \mathbb{R}, \quad (3.16)$$

with f Lipschitz, with Lipschitz coefficient bounded on bounded sets and source term $g(x, u)$ integrable over the previously developed finite volume D_j^n . Again, from the integration of (3.16), from the divergence theorem applied on the hyperbolic operator (left side of equation (3.16)), and using the fact that the line integrals over curves $\sigma_j^n(t)$ vanish, we get the local balance mass equation

$$\int_{\bar{x}_{j-\frac{1}{2}}^{n+1}}^{\bar{x}_{j+\frac{1}{2}}^{n+1}} u(x, t^{n+1}) dx = \int_{x_{j-\frac{1}{2}}^n}^{x_{j+\frac{1}{2}}^n} u(x, t^n) dx + \iint_{D_j^n} g(x, u) dx dt. \quad (3.17)$$

Using the same approximations from the previous section,

$$\bar{U}_j^{n+1} := \frac{1}{h_j^{n+1}} \int_{\bar{x}_j^{n+1}-\frac{1}{2}}^{\bar{x}_j^{n+1}+\frac{1}{2}} u(x, t^{n+1}) dx, \quad \text{and} \quad U_j^n := \frac{1}{h} \int_{x_j^n-\frac{1}{2}}^{x_j^n+\frac{1}{2}} u(x, t^n) dx,$$

equation (3.17) can be recast into

$$\bar{U}_j^{n+1} = \frac{1}{h_j^{n+1}} \left(h U_j^n + \iint_{D_j^n} g(x, u) dx dt \right). \quad (3.18)$$

Finally, the projection equation is obtained with same coefficients, resulting in

$$U_j^{n+1} = \frac{1}{\Delta x} (c_{-1,j} \bar{U}_{j-1}^n + c_{0,j} \bar{U}_j^n + c_{1,j} \bar{U}_{j+1}^n), \quad (3.19)$$

3.1.2 Two-dimensional Hyperbolic Conservation Laws

In Section 2.4 we discussed some of the challenges of directly extending the Lagrangian-Eulerian framework for the case of multidimensional problems. In fact, we then presented several approaches to tackle this very difficult problem. Here, we formulate another alternative approach based on a novel nonstaggered formulation. Consider the two-dimensional nonlinear hyperbolic conservation law with initial data,

$$\begin{cases} \frac{\partial U}{\partial t} + \frac{\partial f(U)}{\partial x} + \frac{\partial g(U)}{\partial y} = 0, \\ U(x, y, t^n) = U^n. \end{cases} \quad (3.20)$$

Suppose we follow the path of each vertex in a regular square grid by means of the integral curves and the usual ODE formulation for the Lagrangian-Eulerian framework, given by equation (3.4). An example of this is shown in Figure 27:

It is a nontrivial problem to define the projection of the coefficients based on this approach, since even under CFL-like restrictions of such moving vertices not evolving into adjacent cells we would obtain unfortunate scenarios. Figure 28 present some examples of such cases.

One way to work around such difficulty is to define the new grid as intersection of the planes produced by each midpoint of the original cell. Such planes are nothing more than linear local approximations of the integral surfaces defined by each edge of the original cell. This way, we may find at most nine rectangles, each of which will locally preserve mass conservation from the previous data. We present in Figure 29 these ideas, in an example with all midpoints moving inwards. Original cell is the square $ABCD$, whereas the new cell is the square $A_1B_1C_1D_1$.

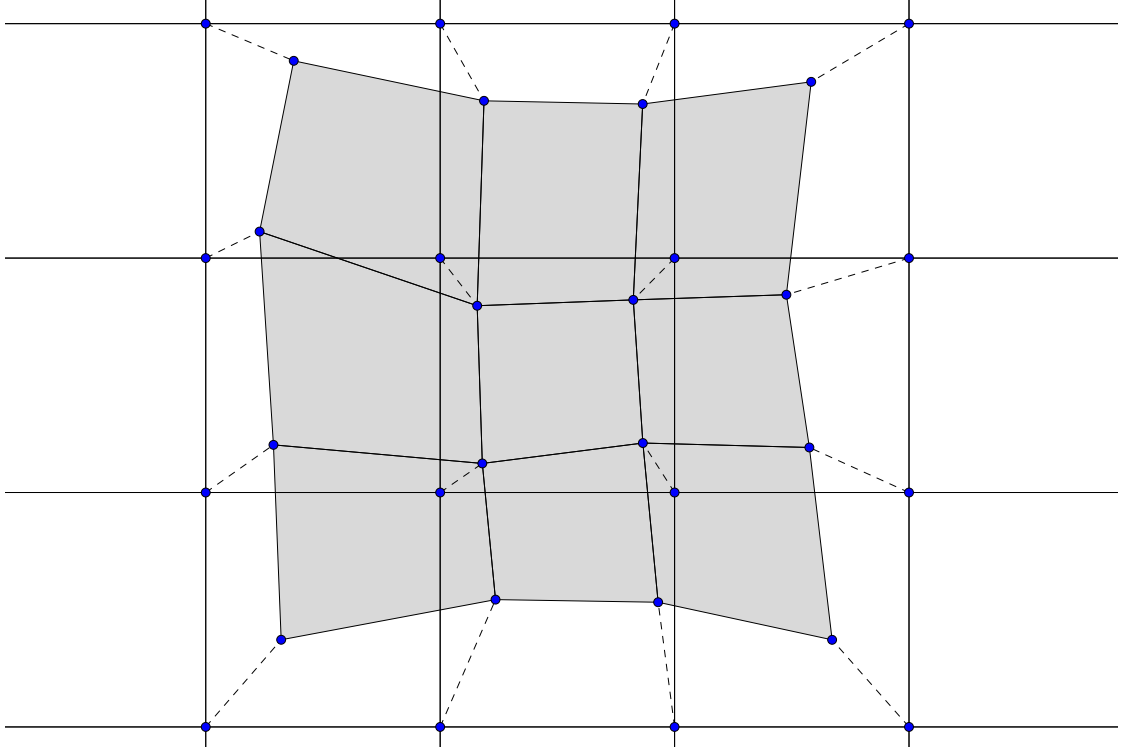


Figure 27 – A 2D mesh grid and its evolution in time by the integral curves. Darker cells represent the evolution in time of the previous mesh, guided by the dotted lines representing integral curves on the vertices. In this example, for the central cell, all vertices are moving inwards.

This approach easily extend our Nonstaggered Lagrangian-Eulerian method, since it is based on coefficients of the same nature. Thus, the numerical scheme can be written in the following manner (as an extension of equation (3.19)):

$$U_{i,j}^{n+1} = \frac{1}{\Delta x \Delta y} \begin{pmatrix} c_{-1}d_{-1}\bar{U}_{i-1,j-1}^n & +c_0d_{-1}\bar{U}_{i,j-1}^n & +c_1d_{-1}\bar{U}_{i+1,j-1}^n \\ +c_{-1}d_0\bar{U}_{i-1,j}^n & +c_0d_0\bar{U}_{i,j}^n & +c_1d_0\bar{U}_{i+1,j}^n \\ +c_{-1}d_1\bar{U}_{i-1,j+1}^n & +c_0d_1\bar{U}_{i,j+1}^n & +c_1d_1\bar{U}_{i+1,j+1}^n \end{pmatrix}. \quad (3.21)$$

It is important to point out that the areas of each of the nine rectangles are given by the projection coefficients products $c_i d_j$. Whenever the information goes outwards the cell, the respective coefficient will be zero and will not contribute to the final projection within the cell. The expression of such coefficients is straightforwardly given by:

$$\begin{aligned} c_0 &= \Delta x - c_{-1} - c_{+1} & d_0 &= \Delta y - d_{-1} - d_{+1}, \\ c_{-1} &= \frac{1}{2}(1 + \operatorname{sgn} f_{i-\frac{1}{2}})|f_{i-\frac{1}{2}}|\Delta t, & d_{-1} &= \frac{1}{2}(1 + \operatorname{sgn} g_{j-\frac{1}{2}})|g_{j-\frac{1}{2}}|\Delta t, \\ c_{+1} &= \frac{1}{2}(1 - \operatorname{sgn} f_{i-\frac{1}{2}})|f_{i-\frac{1}{2}}|\Delta t, & d_{+1} &= \frac{1}{2}(1 - \operatorname{sgn} g_{j-\frac{1}{2}})|g_{j-\frac{1}{2}}|\Delta t. \end{aligned} \quad (3.22)$$

Or even,

$$\begin{aligned} c_{-1} &= f_{i-\frac{1}{2}}^+ \Delta t, & d_{-1} &= g_{j-\frac{1}{2}}^+ \Delta t, \\ c_{+1} &= g_{j-\frac{1}{2}}^+ \Delta t, & d_{+1} &= g_{j-\frac{1}{2}}^- \Delta t. \end{aligned} \quad (3.23)$$

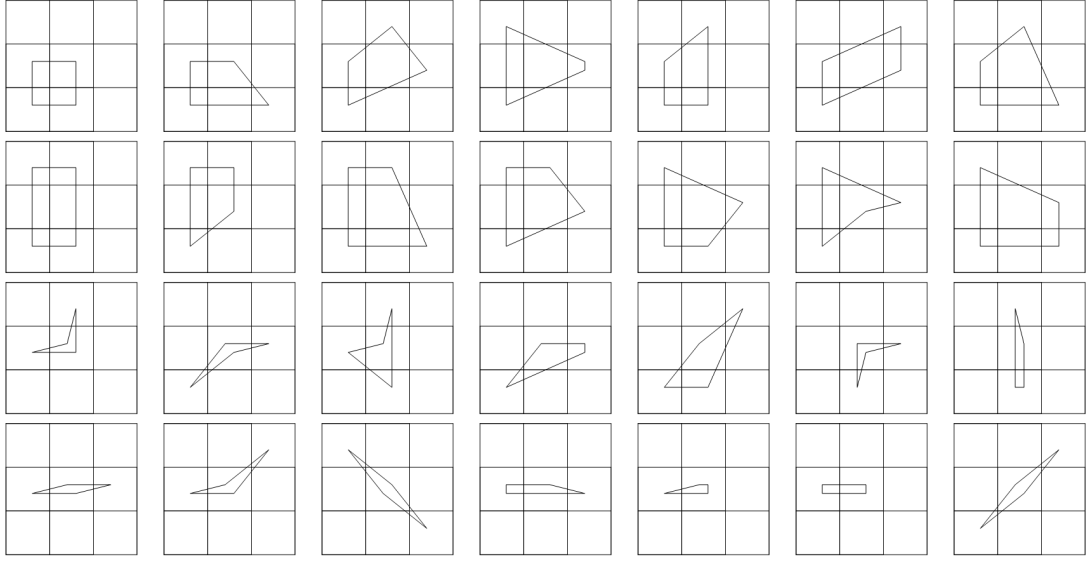


Figure 28 – Even within CFL-like stability conditions, finding projection coefficients in this approach would be a challenging problem, since the control volume may unpredictably change. In this example, each vertex travels no further than 0.4 of the grid width/height.

The evaluation of the fluxes $f_{i\pm\frac{1}{2}}$ and $g_{j\pm\frac{1}{2}}$ is done in the same fashion as before (see equation (3.5)), but with a componentwise reconstruction for each flux function.

3.1.3 Numerical Experiments

We present and discuss computations for scalar linear and nonlinear conservation laws with convex and non-convex flux functions. In Figure 30, it is shown numerical solutions for $u_t + (a(x, t) u)_x = 0$ along with various $a(x, t)$ functions. For instance, on the left picture we take a standard test case, called Shu's linear test [63, 65] with $a(x, t) = 0.5$ and 256 cells. On the center picture we show a test of our scheme on the case with $a(x, t) = \sin(x)$ over $[0, 2\pi]$, 128 cells and with the exact solution (see [63])

$$u(x, t) = \frac{\sin(2 \arctan(e^{-t} \tan(x/2)))}{\sin(x)}.$$

Figure 30 shows on the right (as in [63]), a case with $a(x, t) = \sin(t)$ on $[0, 2]$ and 256 cells, for which the exact solution is $u(x, t) = u_0(x + 1 + \cos(t))$ where $u_0(x) = 0.75 + 0.25 \sin(\pi x)$ over $[0, 2]$ simulated at time $t = 4$. Second and third cases present different velocity signals in space (center case) and over time (right case), and our method shows robustness by not needing any special treatment for that. In Figure 31, we present the solutions of the problem with Burgers' flux function $u_t + (u^2/2)_x = 0$ along with discontinuous initial data $u(x, 0) = 1, x < 0$ and $u(x, 0) = 0, x > 0$ (left picture), and $u(x, 0) = -1, x < 0$ and $u(x, 0) = 1, x > 0$ (right picture), without the reconstruction. The shock discontinuity on the left exhibits spurious oscillations. The

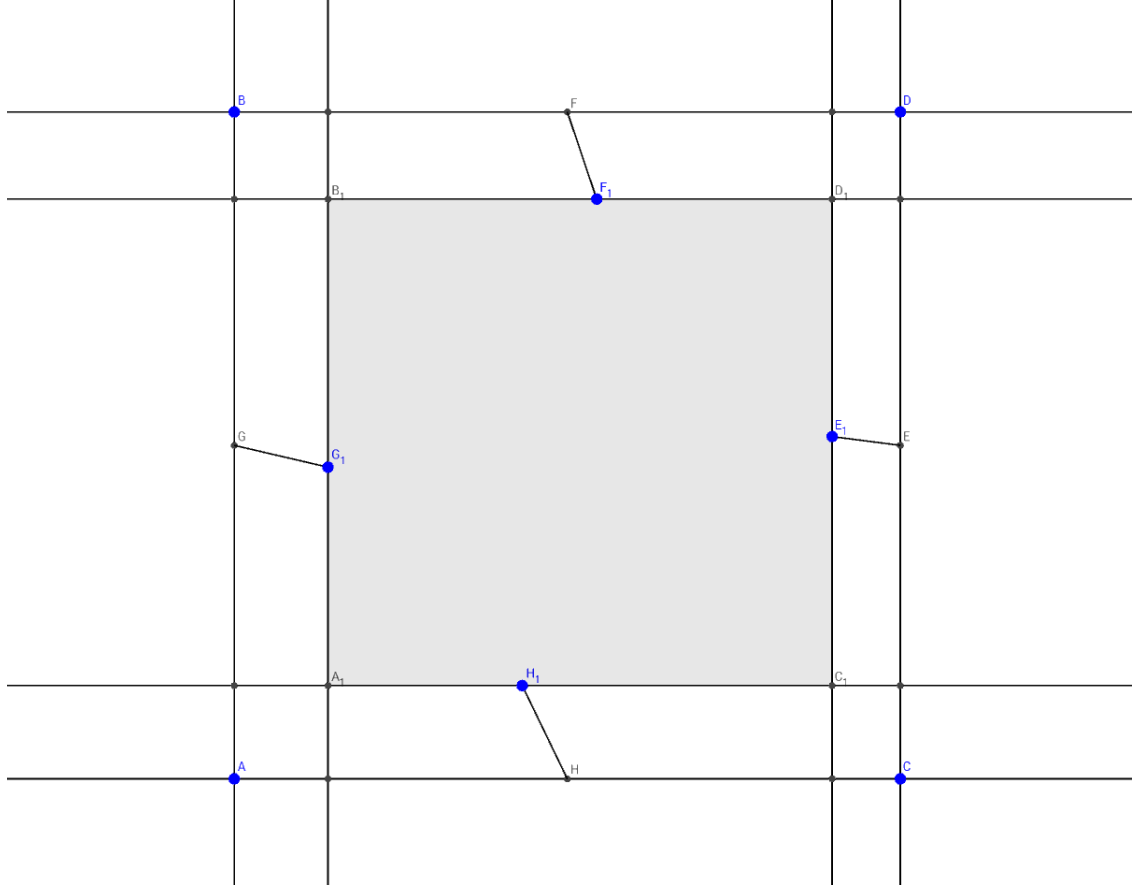


Figure 29 – Evolution of midpoints generates at most nine rectangles in which local mass conservation is preserved. In this example, for the central cell, all midpoints are moving inwards, but whenever a midpoint travel outwards, the respective adjacent cell will treat it as inward information.

right picture is a transonic rarefaction wave. In Figure 32, it is shown again the numerical solutions for $u_t + (u^2/2)_x = 0$ along with same discontinuous initial data $u(x, 0) = 1$, $x < 0$ and $u(x, 0) = 0$, $x > 0$ (left picture), and $u(x, 0) = -1$, $x < 0$ and $u(x, 0) = 1$, $x > 0$ (middle picture), now with polynomial reconstruction. On these frames are shown snapshot graphs with waves moving from left to right. We get a very nice looking numerical approximate solution with scheme (3.10)-(3.12), which in turn seems to be propagating at entirely entropy-correct Rankine-Hugoniot speed and similar good results are shown to the rarefaction case as well. Here, as the rarefaction wave is crossed, there is a sign change in the characteristic speed u and thus there is one point at which $u = 0$, the sonic point. However, our numerical scheme now shows no spurious anomalies around $u = 0$. The classical nonlinear one-dimensional Buckley-Leverett case is depicted on the right picture in Figure 32 at time $t = 1$. These test cases here were simulated with 256 cells. Another example with the Buckley-Leverett flux function is seen on Figure 33, where we set a square wave as initial condition, $u(x, 0) = 1$, $-1 < x < 1$ and $u(x, 0) = 0$, otherwise (left picture). The solution profile starts as a rarefaction wave followed by a shock on

the left side and a rarefaction wave followed by a shock on the right side for small times (middle picture). When the left shock meets the right rarefaction (see middle and right pictures in Figure 33), we observe the expected decaying pattern.

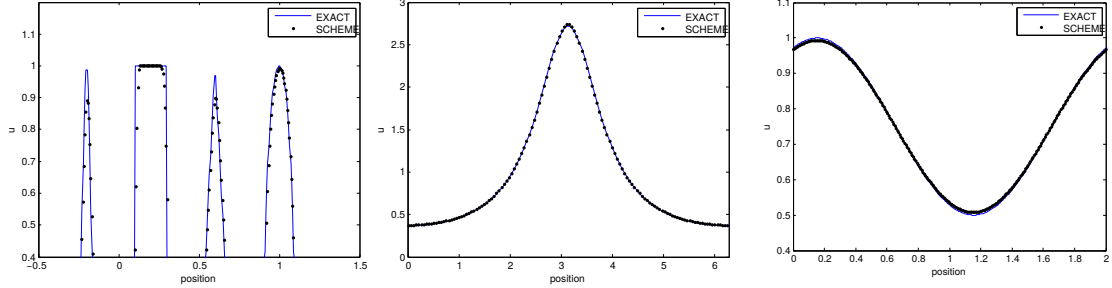


Figure 30 – Left: Shu's linear test, with spatial-dependent advection coefficient $a(x, t)$. Middle: Test case with $a(x, t) = \sin(x)$, the velocity is variable in space. Right: Test case with $a(x, t) = \sin(t)$, the velocity is variable in time.

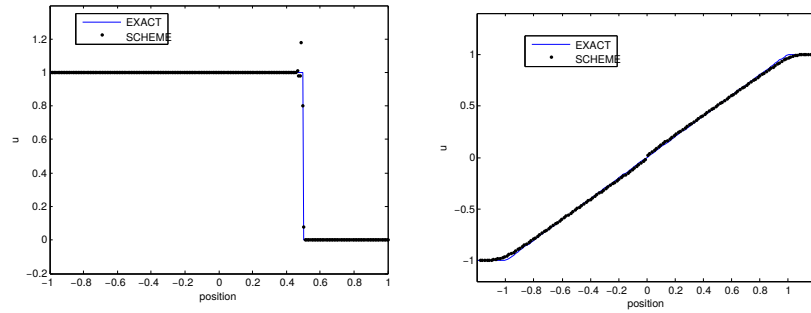


Figure 31 – Nonlinear tests for Burgers' flux function without reconstruction. Left: shock wave, initial condition $u(x, 0) = 1, x < 0$ and $u(x, 0) = 0, x > 0$, end time $t = 0.5$. Right: rarefaction wave, $u(x, 0) = -1, x < 0$ and $u(x, 0) = 1, x > 0$, end time $t = 1.0$.

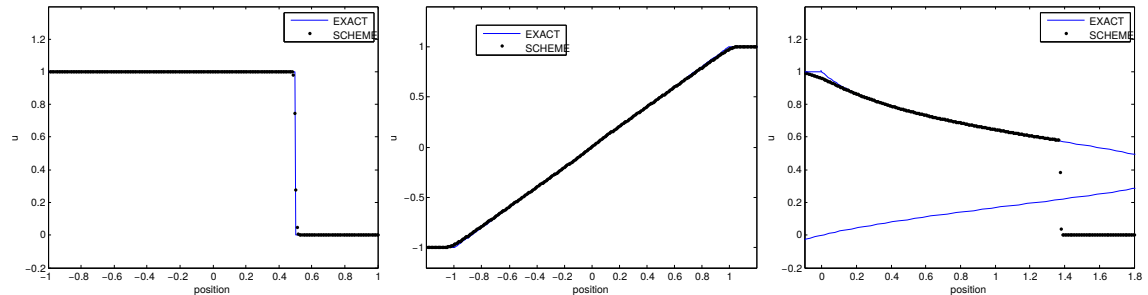


Figure 32 – Nonlinear tests with reconstruction. Left: Burgers' flux function, shock wave solution with initial condition $u(x, 0) = 1, x < 0$ and $u(x, 0) = 0, x > 0$, end time $t = 0.5$. Middle: Burgers' flux function, rarefaction wave with initial condition $u(x, 0) = -1, x < 0$ and $u(x, 0) = 1, x > 0$, end time $t = 1.0$. Right: Buckley-Leverett flux function ($H(u) = u^2/(u^2 + 0.5(1 - u)^2)$) with initial condition $u(x, 0) = 1, x < 0$ and $u(x, 0) = 0, x > 0$.

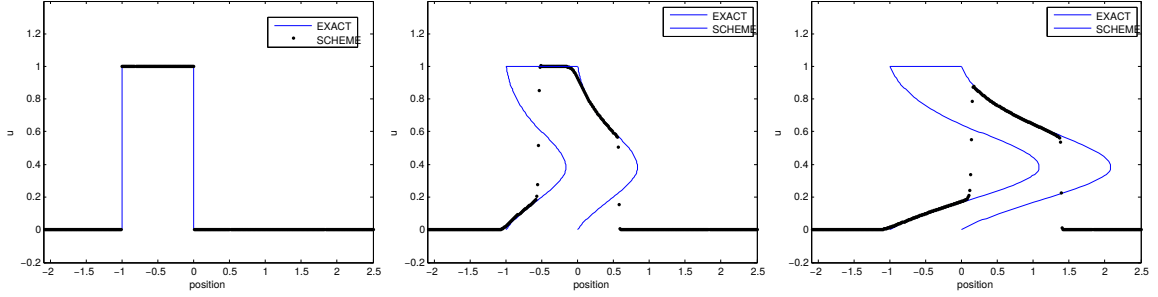


Figure 33 – Buckley-Leverett flux function with initial condition $u(x, 0) = 1$, $-1 < x < 1$ and $u(x, 0) = 0$, otherwise. Snapshots at $t = 0$, $t = 0.4$ and $t = 1$, respectively.

Now, we present and discuss approximate computations for scalar balance laws and systems of balance laws. The first test is an example of linear advection with a smooth (polynomial) source:

$$u_t + 2u_x = x^3 + 6tx^2, \quad u(x, 0) = 0. \quad (3.24)$$

The initial data here is zero, but the exact solution of this differential equation is $u(x, t) = tx^3$. In $x = 0$ we have a sonic point accurately captured by our simulations. Figure 34 presents numerical solutions at times $t = 0$, $t = 1.5$ and $t = 3.0$ for a 256 cells mesh. For this case we have a natural and robust generalization for the upwind method for balance laws. The observed convergence rate was studied at time $t = 3.0$ with 32, 64, 128, 256, 512 and 1024 mesh grid cells and second-order convergence was observed (see Figure 35). Here we used the midpoint rule for the source term quadrature, but the linear advection hyperbolic operator is being exactly calculated due to exact CFL condition.

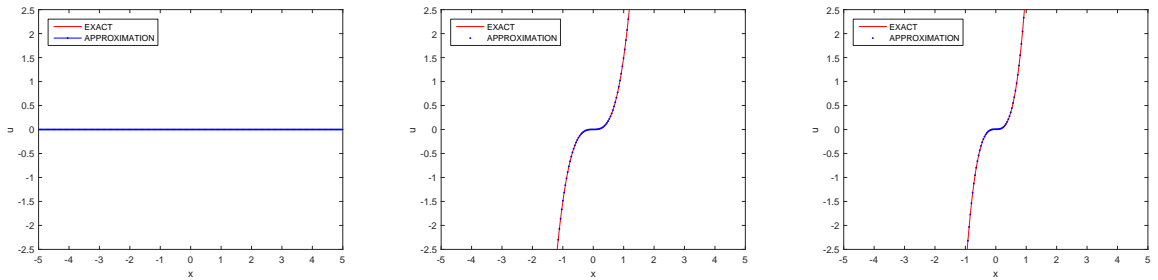


Figure 34 – Numerical solutions of model problem 3.24 with smooth source term $g(x, t) = x^3 + 6tx^2$ at times $t = 0$, $t = 1.5$ and $t = 3.0$.

For the second test, proposed in [66], the source term is of the discontinuous form $g(x, u) = z'(x)u$.

$$u_t + (uf(u))_x = g(x, u) \quad (3.25)$$

with flux function $uf(u) = \frac{u^2}{2}$ and $z(x) = \cos(\pi x)$, $4.5 \leq x \leq 5.5$ and 0 otherwise with $0 < x < 10$. Note that $z'(x)$ is a discontinuous function, so that $g(x, u)$ is a discontinuous

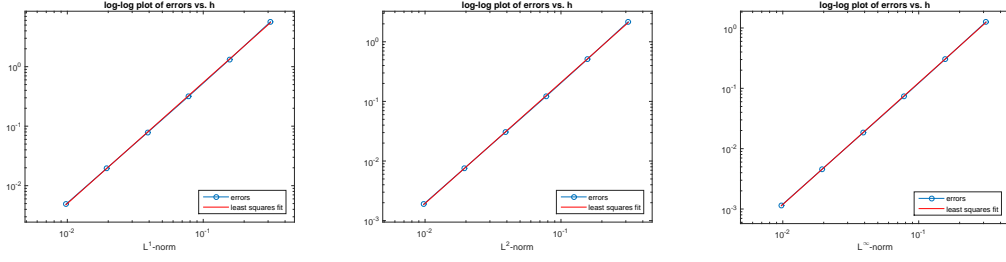


Figure 35 – Convergence of error in L^1 , L^2 and L^∞ norms with uniform mesh refinement for the smooth source term test. Second-order convergence is observed in this example.

source term in x . Figure 36 involves approximations with initial data $u(x, 0) = 0$, $x > 0$ and $u(0, t) = 2$, $t > 0$. The steady state solution of this problem is $u + z = 2$. The pictures in Figure 36 show approximations with 128 cells (top), 256 (middle) and 512 cells (bottom) for u (left pictures) and for steady state $u + z$ (right pictures). The numerical results present clearly qualitatively correct approximations at $t = 1$.

We also consider, as in [74], a 2×2 nonlinear system of balance laws modeling the flow of water downing in a channel having a rectangular cross section and inclined at a constant angle θ to the horizontal. This is a prototype model for shallow-water flow (see [84]) in an inclined channel with friction the system may be written as (in dimensionless variables)

$$\begin{cases} \frac{\partial h}{\partial t} + \frac{\partial(hu)}{\partial x} = 0, \\ \frac{\partial(hu)}{\partial t} + \frac{\partial(hu^2 + \frac{1}{2}h^2)}{\partial x} = h - C \frac{1+h}{\tan(\theta)} v^2, \end{cases} \quad (3.26)$$

where h is the height of the free surface and v is the averaged horizontal velocity. Precisely, as in [74], the friction coefficient C is taken to be 0.1, while the inclination angle $\theta = \frac{\pi}{6}$. On physical grounds, in this model problem it was assumed the hydrostatic balance in the vertical direction and ignored any surface tension. Here, the initial velocity is taken to be $v_0 = 1.699$, while the initial height of the free surface consists of a triangular perturbation of the uniform flow level, $h_0(x) = x + 1.5$, $-0.5 \leq x \leq 0$, $h_0(x) = -x + 1.5$, $0 \leq x \leq 0.5$, and 1 elsewhere. Numerical approximations are shown in Figure 37 with a clearly qualitatively correct approximations at $t = 1$.

Finally, for the two-dimensional simulations we present the model problem from [73] with nonconvex fluxes

$$\frac{\partial u}{\partial t} + \frac{\partial(\sin u)}{\partial x} + \frac{\partial(\cos u)}{\partial y} = 0. \quad (3.27)$$

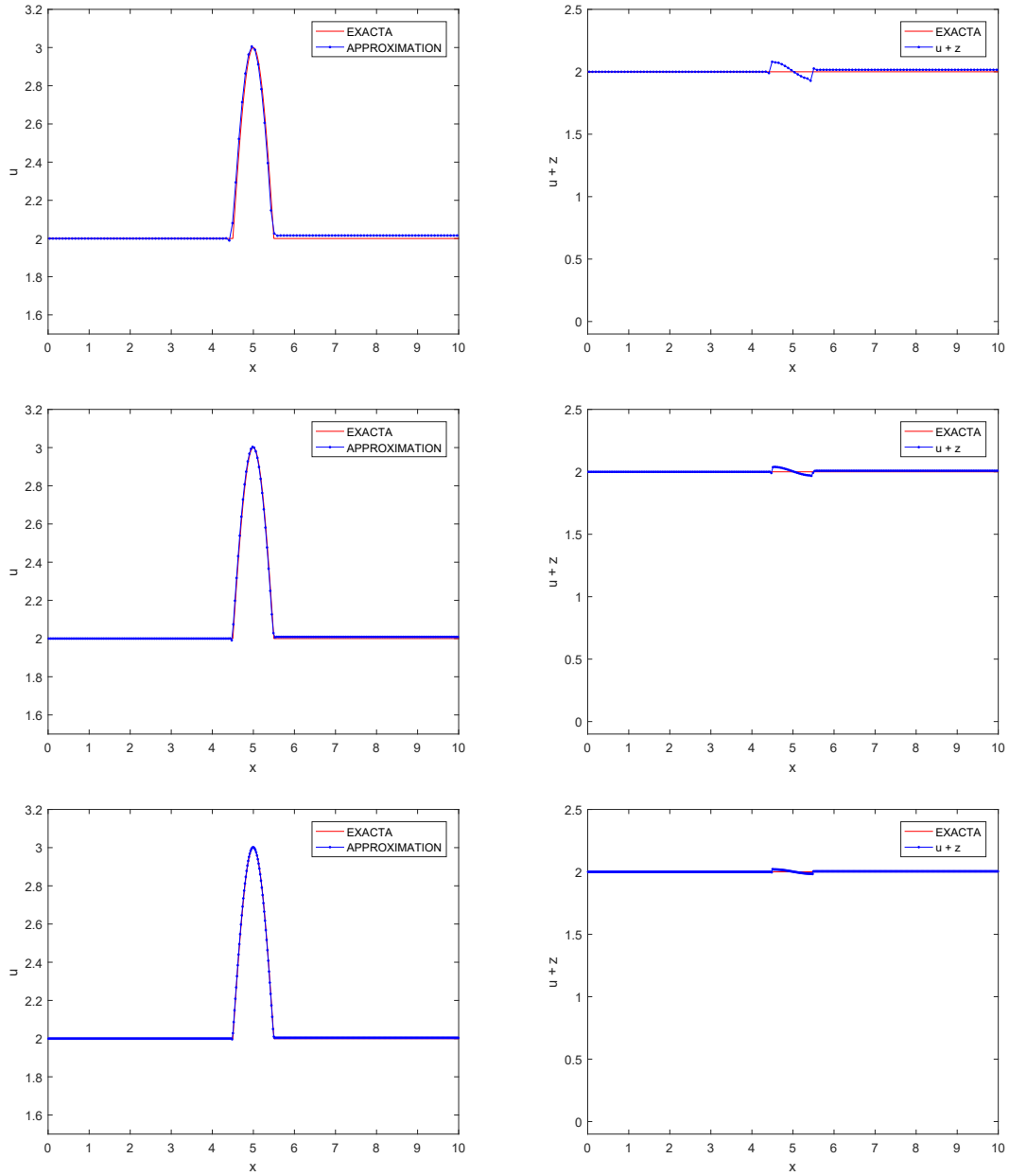


Figure 36 – Numerical solutions of model problem 3.25 with discontinuous source term $g(x, u)$. Grid refinement study with meshgrids 128, 256 and 512.

with $(x, y, t) \in [-2.5, 2.5] \times [-2.5, 2.5] \times [0, 1]$ and initial condition

$$u(x, y, 0) = \begin{cases} 3.5\pi, & x^2 + y^2 \leq 1 \\ 0.25\pi, & \text{otherwise} \end{cases} \quad (3.28)$$

For this initial condition, the x-direction flux has three inflection points, and the y-direction flux has four. The solution to the Riemann problem is advanced from $T = 0$ to $T = 0.5$ and is shown in the Figure 38. From left to right, we show the numerical solutions computed with the two-dimensional Nonstaggered Lagrangian-Eulerian scheme with respect to the nonlinear model with nonconvex flow function described above for

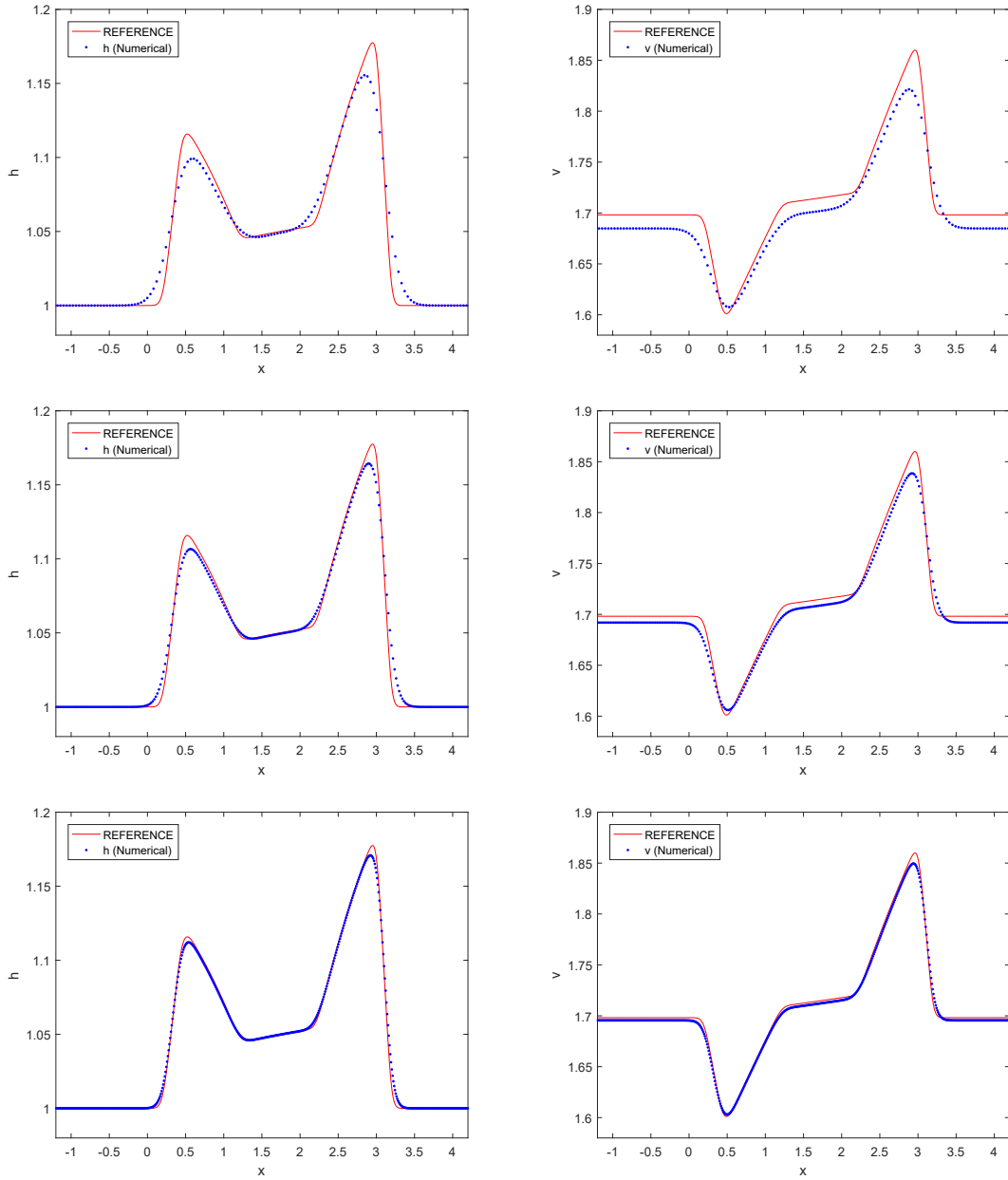


Figure 37 – Numerical solutions to shallow water system (3.26) with 128, 256 and 512 cells (top to bottom), h (height) on the left and v (velocity) on the right.

four mesh grid values, $n \times m = 128 \times 128$ (2.051 sec), $n \times m = 256 \times 256$ (8.290 sec), $n \times m = 512 \times 512$ (119.266 sec) and $n \times m = 1024 \times 1024$ (1108.079 sec). The numerical solutions are comparable with the solutions obtained with the central-upwind schemes proposed in [73]. We highlight no dependence of mesh orientation, particularly in this example where the flux functions are trigonometric functions with high frequencies and several roots.

3.2 An Algorithm for Convection Dominated Flow Problems with a Diffusive Correction Step

For convection-dominated transport problems linked to hyperbolic conservation laws with discontinuous-flux function (discontinuity in space), there may exist several consistent notions of entropy solutions in the setting of vanishing limit solutions for the Buckley-Leverett equation with gravity in porous media with heterogeneous contrast (see e.g., [13, 68]. The difference among such notions of entropy solutions – or connections – lies in the choice of the coupling across the flux discontinuity interface. We notice that in [13], it was found that connections may appear at the vanishing capillarity limit for a associated parabolic problem linked to the purely underlying hyperbolic conservation law. In this section we propose a numerical procedure based on a diffusive correction step that permits to capture the correct solution for a Buckley-Leverett equation with gravity and discontinuous capillarity pressure. We support our findings along with a comparison with existing numerical examples available in the literature.

Indeed, we claim that our correction approach allows to be plugged into any other scheme developed for hyperbolic conservation laws, resulting in a new numerical method for the Buckley-Leverett equation as well as for related parabolic equations for porous media flow problems. We were able to make use of the diffusive correction step linked to the scheme [39] and also to our Lagrangian-Eulerian Finite Volume Scheme.

3.2.1 The Two-phase Buckley-Leverett Problem with Gravity and Discontinuous Capillary Pressure

By following [13], we will consider the two-phase flow model with discontinuous coefficients, for $x \in \Omega_\alpha = \Omega^L \cup \Omega^R$:

$$\phi^\alpha \frac{\partial S_w}{\partial t} + \nabla \cdot \left(\mathbf{v} f_w(S_w) + \sigma_G \mathbf{G}_w^\alpha(S_w) - \sigma_P K^\alpha \lambda_w(S_w) (1 - f_w(S_w)) \frac{\partial p_{wo}^\alpha}{\partial x} \right) = 0, \quad (3.29)$$

with the following parameters: flow rate $\mathbf{v} = 0$, gravity $g = -9.81$, diffusive group $\sigma_G = 1.0$, absolute permeabilities $K^L = 10^{-2}$, $K^R = 5 \times 10^{-3}$, porosities $\phi^L = \phi^R = 1.0$, viscosities $\mu_w = 10^{-3}$, $\mu_o = 3 \times 10^{-3}$, densities $\rho_w = 0.87$, $\rho_o = 1.0$, relative permeability functions $k_w(S_w) = S_w$, $k_o(S_w) = 1 - S_w$, fractional flow function $f_w(S_w) = \frac{\lambda_w(S_w)}{\lambda(S_w)}$, phase mobility $\lambda_w(S_w) = \frac{k_w(S_w)}{\mu_w}$, total mobility $\lambda(S_w) = \lambda_w + \frac{k_o(S_w)}{\mu_o}$, gravity convection $\mathbf{G}_w^\alpha = K^\alpha \lambda_w(S_w) (1 - f_w) (\rho_w - \rho_o)$, diffusive coefficient $\sigma_P = 1.0 \times 10^{-3}$, and capillary pressure function:

$$p_{wo}^\alpha = P^\alpha - \log(1 - s). \quad (3.30)$$

The initial condition for this problem is the constant function $\eta(x) = 0.5$.

In [13], the authors discussed two sets of entry pressures P^α , in which each of them produces a different entropy solution. For the first set of entry pressures ($P^L = 0$ and $P^R = 0.5$), the capillary diffusive effect may be neglected, since the solution for only the hyperbolic operator is the same as the complete parabolic model. However, for the second set of entry pressures ($P^L = 0$ and $P^R = 2$), diffusive effects must be taken into account, since it changes considerably the structure of the entropic solution (there is a wave group traveling right).

3.2.2 The correction diffusive step procedure

We propose a numerical approach for the model problem (3.29), through which the convective operator is approximated by specific numerical methods for hyperbolic conservation laws and the diffusive correction step procedure. Within our formulation, the convective transport step may be substituted for any method for hyperbolic conservation laws, so that we must couple it with the correction step for diffusion. For the sake of presentation, we have chosen here the numerical scheme for singular shocks from [39]. For both sets of entry pressures, our proposal captures the correct entropy solutions presented in [13].

We can rewrite model problem (3.29) into the following parabolic equation

$$\frac{\partial u}{\partial t} + \frac{\partial}{\partial x}(uF(u, x)) = \frac{\partial}{\partial x} \left(\nu D(u, x) \frac{\partial}{\partial x} B(u, x) \right), \quad x \in \mathbb{R}. \quad (3.31)$$

by means of setting $F(u, x) = K(x)g(u)$, with $g = \lambda_w(u)(1 - f_w(u))(\rho_w - \rho_o)$ being the continuous part of gravity convection \mathbf{G}_w^α and $K(x)$ is the discontinuous absolute permeability function $K(x) = K^L$, for $x \leq 0$ and $K(x) = K^R$, for $x > 0$ (in [39], it was initially presented as a Heaviside function). $D(u, x)$ is the diffusive coefficient function $K^\alpha \lambda_w(u)(1 - f_w(u))$ and $B(u, x)$ is the capillary pressure.

This equation is numerically approximated in three steps:

(1) Transport step (any explicit numerical method Φ for hyperbolic problems)

$$\bar{u}_i = \Phi(u_{i-k}^n, \dots, u_{i-1}^n, u_i^n, u_{i+1}^n, \dots, u_{i+k}^n). \quad (3.32)$$

(2) Averaging step

$$\tilde{u}_i = \beta \bar{u}_{i-1} + (1 - 2\beta) \bar{u}_i + \beta \bar{u}_{i+1}, \quad 0 < \beta < \frac{1}{2}. \quad (3.33)$$

(3) Difusive Correction step

$$A_i = \nu D(\tilde{u}_i, x_i) \frac{B(\tilde{u}_{i+1}, x_{i+1}) - B(\tilde{u}_{i-1}, x_{i-1})}{2\Delta x}, \quad (3.34)$$

$$u_i^{n+1} = \tilde{u}_i + r \frac{A_{i+1} - A_{i-1}}{2\Delta x}. \quad (3.35)$$

The above numerical procedure from [39] with the correction step for the diffusive part and our Lagrangian-Eulerian method for the convective part has reproduced the model problem from [13] for two-phase flow problems with gravity and a discontinuity in the capillary pressure function.

We show in Figure 39 solutions of model problem (3.31) at times $t = 0.06, 0.12, 0.18, 0.24$, and 0.3 with a mollified shock width parameter $\gamma = 0.78$ and the set of entry pressures $P^L = 0$ and $P^R = 0.5$. Then, we show in Figure 40 solutions of model problem (3.31) at times $t = 0.06, 0.12, 0.18, 0.24$, and 0.3 with a mollified shock width parameter $\gamma = 0.78$ and a second set of entry pressures $P^L = 0$ and $P^R = 2$. From this second example it is clear (pointed out in [13]) that in the presence of gravity the structure of the solution changes considerably, the effect from the heterogeneity of the capillary pressure cannot be always neglected. In each of these figures, on the left we have $n = 240$ mesh grid cells and on the right $n = 480$ mesh grid cells. The numerical schemes for this section were written in C programming language and the numerical experiments were performed in the same previously cited computer configuration.

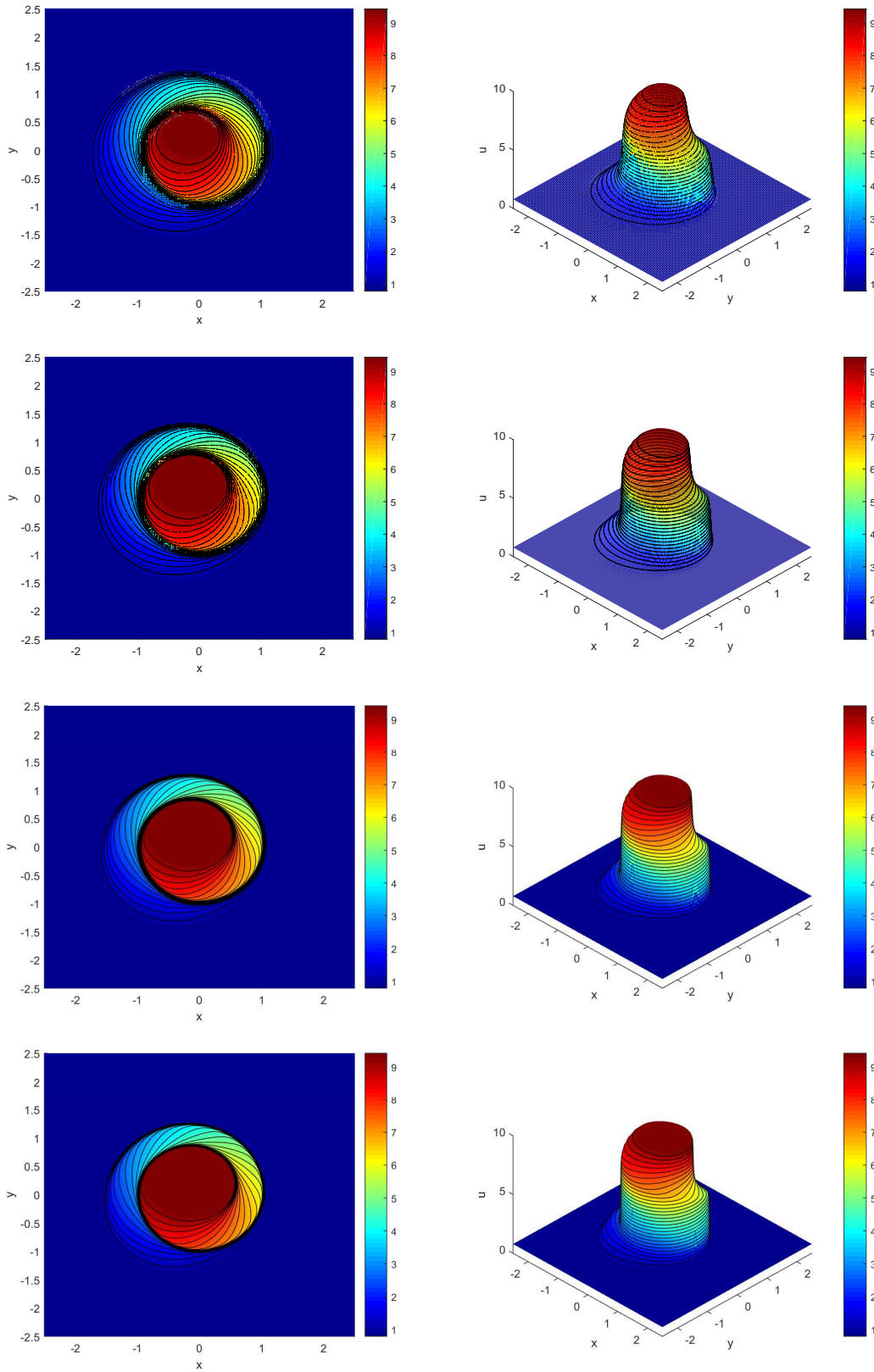


Figure 38 – Numerical solutions of a two-dimensional problem with nonconvex (trigonometric) flux functions in a grid refinement study ($n \times n = 128 \times 128, 256 \times 256, 512 \times 512, 1024 \times 1024$).

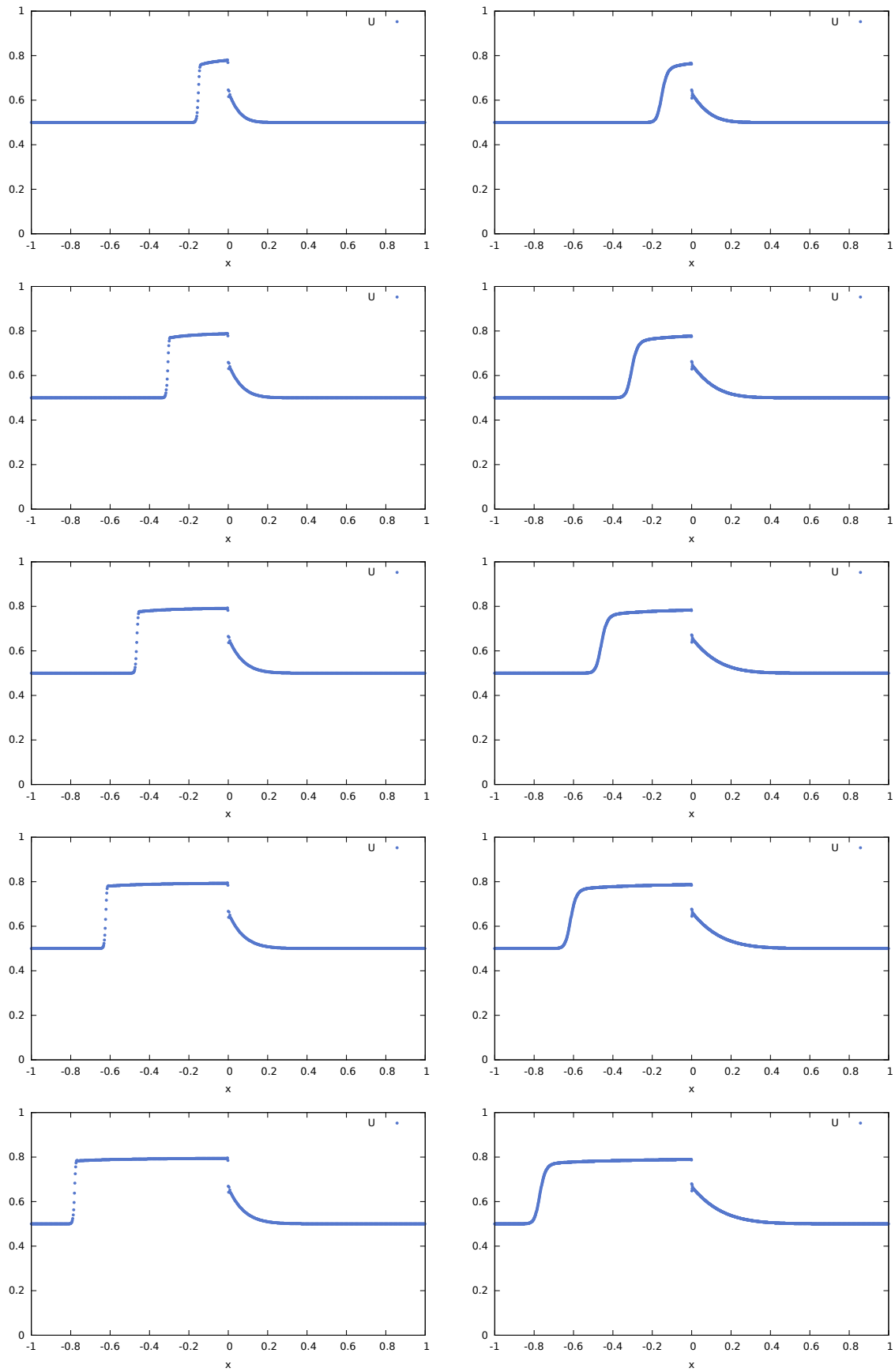


Figure 39 – Solutions of model problem (3.29) at times $t = 0.06, 0.12, 0.18, 0.24$, and 0.3 for the set of entry pressures $P^L = 0$ and $P^R = 0.5$. Here $r = 0.01$ and the mollification width is $\gamma = 0.85$. We have only one wave profile traveling left. Left: $n = 240$, right: $n = 480$.

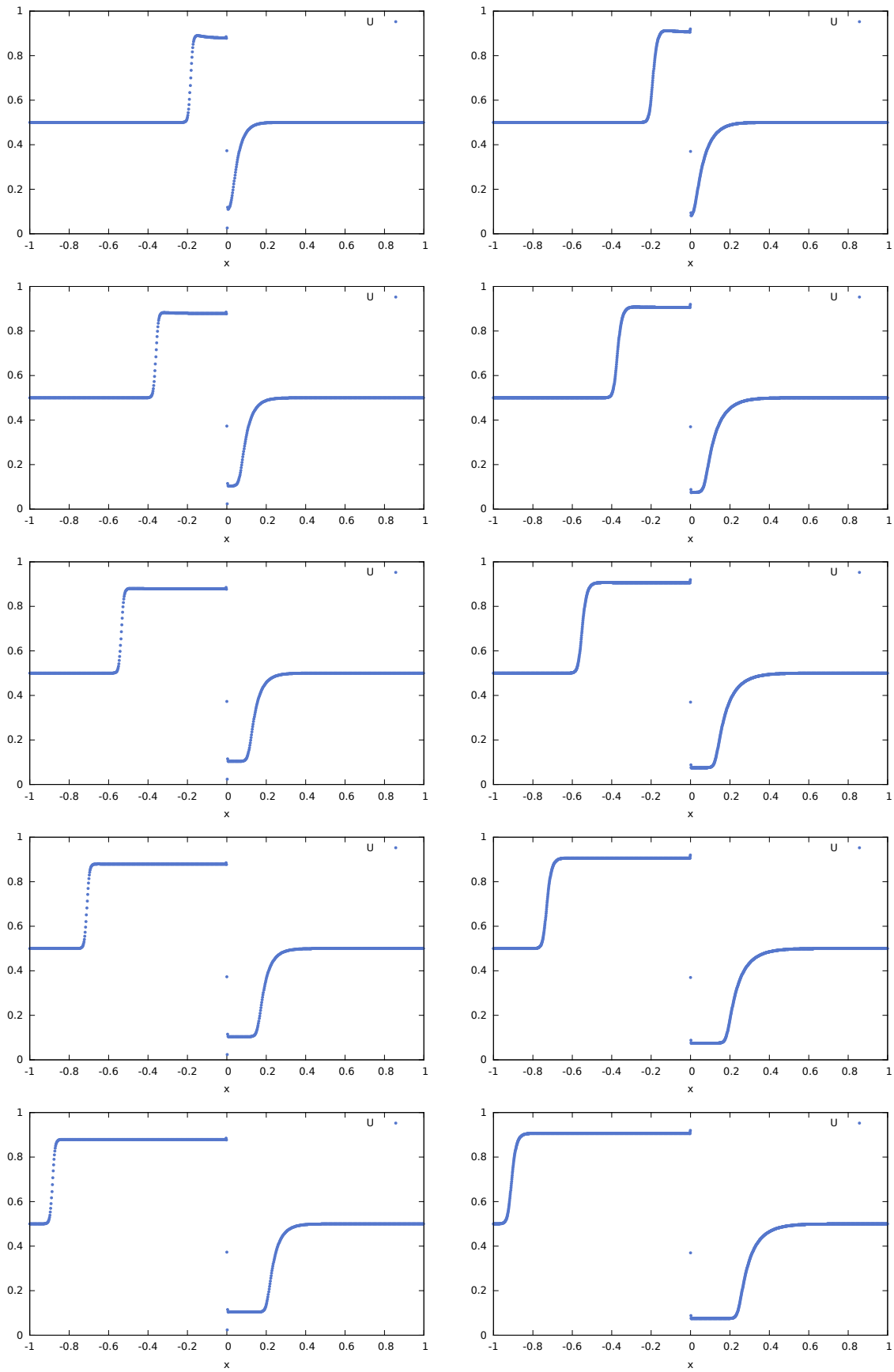


Figure 40 – Solutions of model problem (3.29) at times $t = 0.06, 0.12, 0.18, 0.24$, and 0.3 for the set of entry pressures $P^L = 0$ and $P^R = 2.0$. Here $r = 0.006$ and the mollification width is $\gamma = 0.85$. We have only a wave profile traveling left and a slower wave traveling right. Left: $n = 240$, right: $n = 480$.

Part II

Mixed Hybrid Finite Element Methods for Multiphase Flow Problems

4 Conservative Mixed Hybrid Finite Element and Finite Volume Methods with a New Coupling Condition for Solving Multiphase Flow Problems

In this chapter, we will use a unified hybrid mixed finite element and finite volume formalism along a novel reinterpretation of Robin coupling conditions for numerically solving convection-diffusion problems with gravity and discontinuous capillary pressure. We would like to point out that recently a finite volume/hybrid mixed finite element fully-coupled formulation has shown good results for the numerical approximation of several nontrivial transport models [44, 45, 96], such as pseudo-parabolic equations modeling two-phase flow with dynamic capillary pressure problems, nonlinear transport equations with nonlocal flux and measure data and nonlinear evolution problems governed by Kardar-Parisi-Zhang (KPZ) equations.

To this end, we will first review the classical hybrid and mixed finite elements for convection-diffusion problems applied to multiphase flow in porous media in order to motivate our novel approach. Indeed, this will be convenient to highlight a link between Robin-type inter-element transmission conditions and Rankine-Hugoniot jump conditions.

Hybridized mixed finite elements formulations for parabolic and elliptic problems have been widely and successfully applied in three-phase flow problems [1, 2, 3] and previously for water-oil two-phase flow simulation and numerical approximation, established by Jim Douglas Jr., Richard Ewing, Thomas F. Russell e Mary F. Wheeler in the joint works [49, 51, 87, 98] and more recently in the works [3, 11, 47, 48]. In such works, hybrid mixed finite element methods were identified as very well suited for the accurate calculation of gradient flow associated with velocity fields (Darcy's law) and diffusive fluxes, in the presence of high contrast geological properties in permeability and porosity fields. Besides, it is worth mentioning that the finite element method in the mixed hybrid form possesses rigorous mathematical foundation, delicately connected to distinct approaches in numerical analysis for elliptical problems [28, 29, 85, 97].

In this chapter, we first introduce in Section 4.1 the hybrid mixed finite element method for the parabolic equation with diffusive terms that does not have any kind of spatial dependency. It has been shown in [4, 71] that this technique can be very effective in capturing the correct nonclassical fronts in one spatial dimension as well as in multidimensional heterogeneous three-phase flow with [1] and without [3] gravitational

influence.

As discussed before, the diffusive capillary function depends on the rock type, so the capillary pressure field might be discontinuous across the interior interface between the rocks. In Section 4.2 we then present two approaches for two-phase flow problems [13] and three-phase flow problems [1] with spatial discontinuities. The recent work [1] has presented a combination of a conservative central scheme to handle a system of nonlinear conservation laws modeling the convective transport of the fluid phases and locally conservative mixed finite elements for the associated parabolic and elliptic problems. Such algorithm for approximating the solution of three-phase, two-dimensional immiscible flow in porous media takes into account gravity, variable permeability and porosity, and explicit spatially varying capillary pressure models and discontinuous flux functions. However, the capillary pressure models studied in [1] are multiplicative ($P_c = P_c(S(x, t), K(x)) = P_c(S(x, t)) K(x)$), based on a Leverett-like J-function:

$$P_c(S, K(x)) = p_c(S) \sqrt{\frac{K(x)}{\phi(x)}}, \quad (4.1)$$

where p_c incorporates the dependency on S and the remaining term incorporates spatial-dependency; Such method would fail to capture the correct entropy solution with nonclassical shocks arising in more general models of capillary pressure. On the other hand, the model studied in [13] is additive and as follows:

$$P_c(S, K(x)) = P_{L,R} - \log(1 - S), \quad (4.2)$$

where the term $P_{L,R}$ incorporates the spatial dependency of the model (for $x < 0$ we must have P_L and for $x > 0$ we must have P_R). Paper [13] handles the identification of the correct entropy solution by giving a procedure that determines the appropriate connection in terms of the flux profiles and capillary pressure profiles. Such procedure constructs a finite volume numerical method for the Buckley–Leverett equation with an interface coupling that retains information from the vanishing capillarity model. This formulation, though, is challenged by the difficulty in extending the two-phase scalar problem to the three-phase system problem.

Then, in Section 4.3, following the lines of the previously cited works, we make use of the finite element method in a hybridized mixed formulation with the Raviart-Thomas approximating spaces [29, 85] for the diffusive transport. However, in such formulation, we propose a reinterpretation of the interface conditions between elements to accommodate the effects of heterogeneities in the diffusive capillary pressure. The hybrid mixed finite element method with this novel interface condition is then coupled with finite volume methods in a conservative form for approximating the convective transport. We finish the chapter with our numerical experiments for such method.

4.1 Multiphase Flow Transport Problems without Spatially-Dependent Diffusion Terms

We outline the ideas of the methods presented in [3, 47]. These methods mainly use operator splitting techniques for solving the transport equations in a two-stage manner, using the mixed hybrid finite element for the diffusive and for the elliptic subproblems and various approaches for the convective transport. The finite element method in a hybridized mixed form for the diffusive subproblem is a building block for our formulation.

4.1.1 Two-phase flow problems

Here, the model problem is the nonlinear parabolic transport equation from the convection-diffusion two-phase flow problem in two space dimensions as defined in equation (3.29):

$$\frac{\partial}{\partial t}(\phi(\mathbf{x})S_w) + \nabla \cdot (\mathbf{v}f_w + \sigma_G \mathbf{G}_w) = \sigma_P \nabla \cdot \mathbf{w}_w. \quad (4.3)$$

We define the fractional flow function $f_w(S_w) = \frac{\lambda_w(S_w)}{\lambda(S_w)}$, the phase mobility $\lambda_w(S_w) = \frac{k_w(S_w)}{\mu_w}$, total mobility $\lambda(S_w) = \lambda_w + \frac{k_o(S_w)}{\mu_o}$, and gravity convection $\mathbf{G}_w^\alpha = K^\alpha \lambda_w(S_w)(1 - f_w)(\rho_w - \rho_o)$. In this section we focus only on presenting the operator splitting technique for this parabolic transport equation, but we remark that this is only part of the complete system of two-phase flow equations in phase formulation: there is also the elliptic pressure-velocity subproblem, which we will address later. The cited works also formulate a mixed hybrid finite element method to numerically solve the pressure-velocity problem. For the sake of notation simplification we drop the w subscript from variables S_w and \mathbf{w}_w .

Equation (4.3) needs an initial condition, which we here define as,

$$S(\mathbf{x}, 0) = S_0(\mathbf{x}) \quad \text{for } \mathbf{x} \in \Omega = (\Omega_L, \Omega_R), \quad (4.4)$$

and boundary conditions

$$S(\Omega_L, t) = S_L, \quad S_w(\Omega_R, t) = S_R \quad \text{for } t > 0. \quad (4.5)$$

Operator splitting

Operator splitting techniques aim the computational efficiency and have been frequently used in the numerical simulation of reservoir flow problems. Instead of solving directly the governing system of equations in the form given by the basic conservation and constitutive relations (as described above for three-phase flow), the equation is rewritten such that its mathematical nature is better understood. Then, the appropriate numerical techniques are used for systems of partial differential equations of distinct mathematical types.

The operator splitting for the equation (4.3) allows the use of time steps for the diffusive calculation to be longer than the steps used for the advection part of the saturation calculation; computational efficiency can be achieved by solving less diffusion (implicit) than hyperbolic (explicit) problems. Two time steps are introduced: Δt_t for the solution of the hyperbolic problem associated with advection and Δt_d for the diffusive calculation.

Let $\Delta t_d = i_1 \Delta t_t$, where i_1 is a positive integer. Of course the relation $\Delta t_d \geq \Delta t_t$ holds. The time discretization is given by

$$t_n = n\Delta t_d, \quad t_{n,\kappa} = t_n + \kappa\Delta t_t, \quad 0 \leq \kappa < i_1. \quad (4.6)$$

Consider the spatial variable $\mathbf{x} \in \Omega$. Then, the operator splitting algorithm is defined for $n = 1, \dots, n_1$:

a) For $\kappa = 0, \dots, (i_1 - 1)$, in $[t_{n,\kappa}, t_{n,\kappa+1}]$ solve the advection system

$$\frac{\partial}{\partial t}(\phi(\mathbf{x})\zeta_{n,\kappa+1}) + \nabla \cdot (\mathbf{v}f_w + \sigma_G \mathbf{G}_w) = 0, \quad (4.7)$$

with initial conditions

$$\zeta_{n,\kappa} = \begin{cases} S_n, & \kappa = 0, \\ \zeta_{n,\kappa-1}, & \kappa = 1, \dots, (i_1 - 1), \end{cases} \quad (4.8)$$

b) Set

$$\bar{S}_n = \zeta_{n,i_1-1}. \quad (4.9)$$

c) Compute the diffusive effects in $[t_n, t_{n+1}]$ solving the system

$$\frac{\partial}{\partial t}(\phi(\mathbf{x})S_{n+1}) - \sigma_P \nabla \cdot \mathbf{w}_{n+1} = 0 \quad (4.10)$$

with the boundary condition

$$\mathbf{w}(\mathbf{x}) \cdot \nu = 0, \quad x \in \partial\Omega, \quad (4.11)$$

and initial conditions given by

$$S_n = \bar{S}_n. \quad (4.12)$$

4.1.1.1 Mixed formulation

The following diffusive subproblem is then approximated by a hybrid mixed finite element formulation.

$$\frac{\partial}{\partial t}(\phi(\mathbf{x})S_w) - \sigma_P \nabla \cdot \mathbf{w}_w = 0 \quad (4.13)$$

For now, the diffusive coefficient from the nondimensionalization σ_P is dropped for simplicity on describing the method. It is possible to identify a gradient flux for the saturation, by applying the chain rule for the capillary pressure in (4.3)

$$\mathbf{w}(S, \mathbf{x}) = -K(\mathbf{x}) \lambda_w(S) (1 - f_w) \frac{\partial p_{wo}}{\partial S} \nabla S. \quad (4.14)$$

Defining $B(S) = \lambda_w(S) (1 - f_w) \frac{\partial p_{wo}}{\partial S}$, the equation is rewritten into a mixed formulation for the pair (S, \mathbf{w}) :

$$\begin{cases} \mathbf{w} + K(\mathbf{x}) B(S) \nabla S = 0 \\ \frac{\partial}{\partial t} (\phi(\mathbf{x}) S) - \nabla \cdot \mathbf{w} = 0. \end{cases} \quad (4.15)$$

Weak form of diffusive equation

Equation (4.15) can be put in a weak global formulation by means of the spaces V and W ,

$$\begin{aligned} L^2(\Omega) &= \left\{ v \mid \int_{\Omega} |v(\mathbf{x})|^2 d\mathbf{x} < \infty \right\}, & H(\mathbf{div}; \Omega) &= \{ \mathbf{w} \in L^2(\Omega) \mid \nabla \cdot \mathbf{w} \in L^2(\Omega) \}. \\ V &= \{ v \in L^2(\Omega) \}, & W &= \{ \mathbf{w} \in H(\mathbf{div}; \Omega) \mid \mathbf{w}|_{\partial\Omega} \cdot \nu = 0 \}. \end{aligned} \quad (4.16)$$

The global weak formulation of the diffusive system is given by finding $(S, \mathbf{w}) \in V \times W$ so that for every test functions $\varphi \in V$ and $\psi \in W$ the following weak equations are satisfied,

$$\begin{cases} ((K(\mathbf{x}) B(S))^{-1} \mathbf{w}, \psi)_{\Omega} + (\nabla S, \psi)_{\Omega} = 0, & \forall \psi \in W \\ \left(\frac{\partial}{\partial t} (\phi(\mathbf{x}) S), \varphi \right)_{\Omega} - (\nabla \cdot \mathbf{w}, \varphi)_{\Omega} = 0, & \forall \varphi \in V. \end{cases} \quad (4.17)$$

where $(f, g)_{\Omega}$ is the usual inner product by integration in Ω .

The next step is to localize such equations using domain decomposition ideas. Let $\{\Omega_j, j = 1, \dots, M\}$ be a partition of the spatial domain Ω into rectangles of size h_x, h_y ,

$$\Omega = \bigcup_{j=1}^M \Omega_j; \quad \Omega_j \cap \Omega_k = \emptyset, j \neq k, \quad \Omega_j = (x_j, x_{j+1}) \times (y_j, y_{j+1}), \quad (4.18)$$

with the domain interfaces

$$\Gamma = \partial\Omega; \quad \Gamma_j = \Gamma \cap \Omega_j \quad \Gamma_{j,k} = \Gamma_{k,j} = \partial\Omega_j \cap \partial\Omega_k. \quad (4.19)$$

Consider, for $j = 1, \dots, M$ the local spaces

$$V_j = V(\Omega_j), \quad W_j = \{ \mathbf{w} \in H^1(\Omega_j) \mid \mathbf{w} \cdot \nu = 0 \text{ on } \Gamma_j \}.$$

The localized weak formulation of the diffusive system corresponding to the domain decomposition above is given by seeking $S \in V$ and $\mathbf{w} \in W$ such that $(S_j, \mathbf{w}_j) \in V_j \times W_j$ for $j = 1, \dots, M$ satisfying

$$\begin{cases} ((K(\mathbf{x}) B(S_j))^{-1} \mathbf{w}_j, \psi_j)_{\Omega_j} - (S_j, \nabla \psi_j)_{\Omega_j} + \sum_{k \neq j} \langle S_j, \psi_j \cdot \nu_j \rangle_{\Gamma_{kj}} = 0, & \forall \psi_j \in W_j \\ \left(\frac{\partial}{\partial t} (\phi(\mathbf{x}) S_j), \varphi_j \right)_{\Omega_j} - (\nabla \cdot \mathbf{w}_j, \varphi_j)_{\Omega_j} = 0, & \forall \varphi_j \in V_j. \end{cases} \quad (4.20)$$

Notice that, in this step, an integration by parts was performed on the first equation. The local solutions (S, \mathbf{w}) can be extended to be global solutions of (4.17). For this, it is necessary to require that the localized weak formulation also satisfies the following consistency conditions on the interfaces Γ_{jk} ,

$$S_j = S_k, \quad \text{for } x \in \Gamma_{jk}, \quad (4.21)$$

$$\mathbf{w}_j \cdot \nu_j + \mathbf{w}_k \cdot \nu_k = 0, \quad \text{for } x \in \Gamma_{jk}. \quad (4.22)$$

where ν is the outward normal unit vector in Ω_j .

Hybridized mixed finite element approximation

For several families of mixed finite elements, the functions $\varphi \in V_j$ are allowed to be discontinuous in each element interface Γ_{jk} . Trying to impose the consistency conditions could cause errors in the flux conservation, i.e., the consistency conditions would only be satisfied if the approximate solution $S \in V_j$ for the discrete problem is globally a polynomial, which is an uninteresting case. To overcome this, the Lagrange multipliers on the edges Γ_{ij} are introduced, allowing such discontinuities. Such variables are defined on the space Λ of constant trace functions on the edges of the elements. Then, the hybrid mixed finite element method is given by:

Find $\mathbf{w}_j \in W_j$, $S \in V_j$ and $\ell_{ij} \in \Lambda$ such that

$$\begin{cases} ((K(\mathbf{x}) B(S_j))^{-1} \mathbf{w}_j, \psi_j)_{\Omega_j} - (S_j, \nabla \psi_j)_{\Omega_j} + \sum_{k \neq j} \langle \ell_j, \psi_j \cdot \nu_j \rangle_{\Gamma_{kj}} = 0, & \forall \psi_j \in W_j \\ \left(\frac{\partial}{\partial t} (\phi(x) S_j), \varphi_j \right)_{\Omega_j} - (\nabla \cdot \mathbf{w}_j, \varphi_j)_{\Omega_j} = 0, & \forall \varphi_j \in V_j, \end{cases} \quad (4.23)$$

subject to the consistency conditions, written equivalently as Robin transmission boundary conditions in order to define an iterative method for solving the parabolic problem.

Robin consistency conditions

The Robin consistency conditions for the diffusive system are given by

$$\begin{aligned} -\chi_{k,j} \mathbf{w}_j \cdot \nu_j + \ell_{k,j} &= \chi_{k,j} \mathbf{w}_k \cdot \nu_k + \ell_{k,j}, & \mathbf{x} \in \Gamma_{k,j} \subset \partial\Omega_k \\ -\chi_{j,k} \mathbf{w}_k \cdot \nu_k + \ell_{j,k} &= \chi_{j,k} \mathbf{w}_j \cdot \nu_j + \ell_{j,k}, & \mathbf{x} \in \Gamma_{j,k} \subset \partial\Omega_j. \end{aligned} \quad (4.24)$$

The coefficients $\chi_{k,j}$ from the Robin consistency condition are determined by means of a dimensional analysis. It is expected that during the iterative procedure the conditions are satisfied. On the other hand, the balance will be exact only when the iteration index goes to infinity. So is natural to search for a definition for the coefficient χ_{ij} by considering its physical dimensions. There must be a compatibility between the dimensions of S (and ℓ) and \mathbf{w} , that represents the values on the element interface. Equations (4.24) can be rewritten as

$$h \left(\frac{l_{jk} - l_{kj}}{h} \right) = \pm \chi_{kj} (\mathbf{w}_k - \mathbf{w}_j), \quad (4.25)$$

which, in terms of the units of the mentioned quantities,

$$[h] [\nabla S] = [\chi] [K(\mathbf{x})B(S)] [\nabla S], \quad (4.26)$$

from what follows that χ being

$$[\chi] = \frac{[h]}{[K(\mathbf{x})B(S)]}, \quad (4.27)$$

will ensure unit compatibility. Thus, dimensional analysis suggest that χ must be

$$\chi_{jk} = \xi \frac{h}{H_{\text{eff}}} \quad (4.28)$$

where ξ is an acceleration of convergence parameter and $H(S, \mathbf{x}) = K(\mathbf{x})B(s)$ and H_{eff} is defined by the harmonic mean on the interface Γ_{jk} :

$$H_{\text{eff}} = \frac{2H(S_j, \mathbf{x}_j)H(S_k, \mathbf{x}_k)}{H(S_j, \mathbf{x}_j) + H(S_k, \mathbf{x}_k)} \quad (4.29)$$

This choice is motivated by the hybrid mixed finite element approach [47]. Its well understood in the literature that the dimensional analysis can be useful in the elaboration of strategies for the choice of the discretization time interval for the numerical integration [1, 2, 69, 70].

Reduction to lowest index Raviart-Thomas space

The hybrid mixed finite element spaces are chosen to be the lowest index Raviart-Thomas spaces over the intervals. The natural degrees of freedom on the element Ω_j for saturation variable is the constant value S_j , which can be interpreted as the value

on the center of the element. For the diffusive flux variable, it is used an outward normal component across the edges of the element. For consistency, the Lagrange multipliers are also constant and defined on the edges of the element. It is assumed that the porosity and the absolute permeability are constant on each element, and that the relative permeability functions are independent of the position with respect to the space variable on each Ω_j . The discrete form of equations (4.24) are then,

$$\ell_j^\alpha = \chi_j^\alpha (\mathbf{w}_k^{\tilde{\alpha}} - \mathbf{w}_j^\alpha) + \ell_k^{\tilde{\alpha}}, \quad \alpha = R, L, D, U, \text{ and } \tilde{\alpha} = L, R, U, D, \text{ respectively.} \quad (4.30)$$

where each variable are defined on the L, R, U, D interfaces, representing the right (R), left (L), up (U) and down (D) edges of Ω_j ; $\tilde{\alpha}$ represents the variable associated with the adjacent element of Ω_j connected by the interface α .

Approximating the integrals by the trapezoidal rule, substituting the discrete Robin consistency equations and using an specific basis for the discrete Raviart-Thomas spaces, the discrete forms of (4.23) are

$$\begin{cases} \left(\frac{h}{2} (K_j B_j)^{-1} + \chi_j^\alpha \right) \mathbf{w}_j^\alpha + S_j = \chi_j^\alpha \mathbf{w}_k^{\tilde{\alpha}} + l_k^{\tilde{\alpha}}, \\ \frac{\partial}{\partial t} (\phi(\mathbf{x}) S_j) - \frac{\mathbf{w}_j^R - \mathbf{w}_j^L}{h_x} - \frac{\mathbf{w}_j^U - \mathbf{w}_j^D}{h_y} = 0. \end{cases} \quad (4.31)$$

where $\alpha = R, L, D, U$, and $\tilde{\alpha} = L, R, U, D$, respectively.

It is necessary, however, to discretize equation (4.31) on time. For that, let $N \in \mathbb{N}$ and take $\Delta t = T/N$ and $t_n = n\Delta t$. The saturation variable S must accommodate the diffusion effect in each time step. This way, it is used a backward Euler method (implicit) for the time discretization, where \bar{S} represents the saturation in previous time step and S , the saturation in the present time step. Note that it is defined a completely implicit form to calculate S , so the variables are evaluated on time $n + 1$. Together with the discrete Lagrange multiplier equations, the final form of the discrete system is (here, $\alpha \in \{L, R, U, D\}$ and $\tilde{\alpha} \in \{R, L, D, U\}$):

$$\begin{cases} \phi_j \frac{S_j - \bar{S}_j}{\Delta t} - \frac{\mathbf{w}_j^R - \mathbf{w}_j^L}{h_x} - \frac{\mathbf{w}_j^U - \mathbf{w}_j^D}{h_y} = 0, \\ \left(\frac{h}{2} (K_j B_j)^{-1} + \chi_j^\alpha \right) \mathbf{w}_j^\alpha + S_j = \chi_j^\alpha \mathbf{w}_k^{\tilde{\alpha}} + l_k^{\tilde{\alpha}}, \\ \ell_j^\alpha = \chi_j^\alpha (\mathbf{w}_k^{\tilde{\alpha}} - \mathbf{w}_j^\alpha) + \ell_k^{\tilde{\alpha}}. \end{cases} \quad (4.32)$$

Development of the iterative procedure

The final step of numerically solving the diffusion equation is to identify an iterative procedure for solving the linear system on variables S_j , \mathbf{w}_j^α and ℓ_j^α . Here, the system is implicitly solved with a Red-Black-type strategy, so that each variable on element

is solved with the previous iteration on adjacent elements. Thus, for each time step, we solve the problem by means of an iterative procedure. Let k be an iteration index. Denote by $S_j^{n,k}$ an approximation for $S(\mathbf{x}_j, t^n)$ in the iteration level k and S_j^n the approximation after convergence. The convergence criterion for the iterative procedure is given by,

$$\frac{\sqrt{\sum_{j=0}^M |S_j^{n,k} - S_j^{n,k-1}|^2}}{N} < \text{tol} \quad (4.33)$$

where tol is a tolerance for the difference between iterations k and $k - 1$.

For a fixed time t_{n+1} , the iterative procedure is defined as

1. Set $S_j^{n+1,0} = S_j^n$ and $\mathbf{w}_j^{\alpha,n+1,0} = \mathbf{w}_j^{\alpha,n}$,
2. Calculate coefficients B_j and χ_j^L, χ_j^R with S_j^n ,
3. Solve the linear system given by (4.32) for the variables in each element j , using the variables from outer elements as being the ones from iteration n ,
4. Update the Lagrange multipliers for the domains according to equations (4.30),
5. Verify convergence for S . If not achieved, repeat steps 2-4. If achieved, set $S_j^{n+1} = S_j^{n+1,k}$ and go to the next time step.

4.1.2 Three-phase flow problems

The nonlinear transport equations from the convection-diffusion three-phase flow problem are,

$$\begin{aligned} \frac{\partial}{\partial t}(\phi(\mathbf{x})S_w) + \nabla \cdot (\mathbf{v}f_w + \epsilon_G \mathbf{G}_w) &= \nabla \cdot (\epsilon_P \mathbf{w}_w), \\ \frac{\partial}{\partial t}(\phi(\mathbf{x})S_g) + \nabla \cdot (\mathbf{v}f_g + \epsilon_G \mathbf{G}_g) &= \nabla \cdot (\epsilon_P \mathbf{w}_g), \end{aligned} \quad (4.34)$$

where

$$\begin{pmatrix} \mathbf{w}_w \\ \mathbf{w}_g \end{pmatrix} = \mathbf{K}(x)B(S_w, S_g) \begin{pmatrix} \nabla S_w \\ \nabla S_g \end{pmatrix}, \quad (4.35)$$

and

$$B(S_w, S_g) = Q(S_w, S_g)P'(S_w, S_g), \quad (4.36)$$

$$Q(S_w, S_g) = \begin{pmatrix} \lambda_w(1 - f_w) & -\lambda_w f_g \\ -\lambda_g f_w & \lambda_g(1 - f_g) \end{pmatrix}, \quad P'(S_w, S_g) = \begin{pmatrix} \frac{\partial p_{wo}}{\partial S_w} & \frac{\partial p_{wo}}{\partial S_g} \\ \frac{\partial p_{go}}{\partial S_w} & \frac{\partial p_{go}}{\partial S_g} \end{pmatrix}. \quad (4.37)$$

$\lambda = \sum_i \lambda_i$ is the total mobility and $f_i(S_w, S_g) = \lambda_i/\lambda$ are the fractional flow functions. Given the constraint

$$\sum_{i=w,o,g} S_i = 1,$$

any pair of saturations inside the triangle of saturations $\Delta := \{(S_w, S_g) : S_w, S_g \geq 0, S_w + S_g \leq 1\}$ can be chosen to describe the state of the fluid. A mixed hybrid finite element method is also formulated to numerically solve the associated pressure-velocity problem.

Equation (4.34) needs an initial condition, which we here define as,

$$S(\mathbf{x}, 0) = S_0(\mathbf{x}) \quad \text{for } x \in \Omega, \quad (4.38)$$

and boundary conditions

$$S(\Omega_L, t) = S_L, \quad S_w(\Omega_R, t) = S_R \quad \text{for } t > 0. \quad (4.39)$$

Operator splitting

The operator splitting technique is applied in the same fashion it was used in two-phase flow. The appropriate numerical techniques are used for systems of partial differential equations of distinct mathematical types. Two time steps are again introduced: Δt_t and Δt_d , defined as in (4.6). Then, in the three-phase case, the operator splitting algorithm is defined analogous as the two-phase case. For $n = 1, \dots, n_1$:

a) For $\kappa = 0, \dots, (i_1 - 1)$, in $[t_{n,\kappa}, t_{n,\kappa+1}]$ solve the convection system

$$\frac{\partial}{\partial t}(\phi(\mathbf{x})\zeta_{w,n,\kappa+1}) + \nabla \cdot (\mathbf{v}f_w + \sigma_G \mathbf{G}_w) = 0, \quad (4.40)$$

$$\frac{\partial}{\partial t}(\phi(\mathbf{x})\zeta_{g,n,\kappa+1}) + \nabla \cdot (\mathbf{v}f_g + \sigma_G \mathbf{G}_g) = 0, \quad (4.41)$$

with initial conditions

$$\zeta_{w,n,\kappa} = \begin{cases} S_{w,n}, & \kappa = 0, \\ \zeta_{w,n,\kappa-1}, & \kappa = 1, \dots, (i_1 - 1), \end{cases} \quad (4.42)$$

$$\zeta_{g,n,\kappa} = \begin{cases} S_{g,n}, & \kappa = 0, \\ \zeta_{g,n,\kappa-1}, & \kappa = 1, \dots, (i_1 - 1), \end{cases} \quad (4.43)$$

b) Set

$$\bar{S}_{w,n} = \zeta_{w,n,i_1-1} \quad \text{and} \quad \bar{S}_{g,n} = \zeta_{g,n,i_1-1}. \quad (4.44)$$

c) Compute the diffusive effects in $[t_n, t_{n+1}]$ solving the system

$$\frac{\partial}{\partial t} (\phi(\mathbf{x}) S_{w,n+1}) - \sigma_P \nabla \cdot \mathbf{w}_{w,n+1} = 0, \quad (4.45)$$

$$\frac{\partial}{\partial t} (\phi(\mathbf{x}) S_{g,n+1}) - \sigma_P \nabla \cdot \mathbf{w}_{g,n+1} = 0, \quad (4.46)$$

with the boundary condition

$$\mathbf{w}_i(\mathbf{x}) \cdot \nu = 0, \quad x \in \partial\Omega, \quad i = w, g \quad (4.47)$$

and initial conditions given by

$$S_{w,n} = \bar{S}_{w,n} \quad S_{g,n} = \bar{S}_{g,n}. \quad (4.48)$$

Mixed formulation

The diffusive system is then approximated by the hybrid mixed finite element formulation

$$\frac{\partial}{\partial t} (\phi(\mathbf{x}) \underline{S}) - \sigma_P \nabla \cdot \underline{\mathbf{w}} = 0. \quad (4.49)$$

where $\underline{S} = (S_w, S_g)$ and $\underline{\mathbf{w}} = (\mathbf{w}_w, \mathbf{w}_g)$.

Again, the diffusive coefficient from the nondimensionalization σ_P is dropped for simplicity. It is possible to identify a gradient flux for the saturation, given by equation (4.35). The system is rewritten into a mixed formulation for the pair $(\underline{S}, \underline{\mathbf{w}})$:

$$\begin{cases} \underline{\mathbf{w}} + K(\mathbf{x}) B(\underline{S}) \begin{pmatrix} \nabla S_w \\ \nabla S_g \end{pmatrix} = 0 \\ \frac{\partial}{\partial t} (\phi(\mathbf{x}) \underline{S}) - \begin{pmatrix} \nabla \cdot \mathbf{w}_w \\ \nabla \cdot \mathbf{w}_g \end{pmatrix} = 0. \end{cases} \quad (4.50)$$

Weak form of diffusive equation

Equation (4.50) can be put in a weak global formulation by means of the spaces V and W ,

$$\begin{aligned} L^2(\Omega) &= \left\{ v \left| \int_{\Omega} |v(\mathbf{x})|^2 d\mathbf{x} < \infty \right. \right\}, & H(\mathbf{div}; \Omega) &= \{ \mathbf{w} \in L^2(\Omega) \mid \nabla \cdot \mathbf{w} \in L^2(\Omega) \}. \\ V &= \{ v \in (L^2(\Omega))^2 \}, & W &= \{ \mathbf{w} \in H(\mathbf{div}; \Omega)^2 \mid \mathbf{w}|_{\partial\Omega} \cdot \nu = 0 \}. \end{aligned} \quad (4.51)$$

The global weak formulation of the diffusive system is given by finding $(S, \mathbf{w}) \in V \times W$ so that for every test functions $\varphi \in V$ and $\psi \in W$ the following weak equations are satisfied,

$$\begin{cases} (\mathcal{G}\underline{\mathbf{w}}, \psi)_{\Omega} + ((\nabla S_w, \nabla S_g)^T, \psi)_{\Omega} = 0, & \forall \psi \in W \\ \left(\frac{\partial}{\partial t} (\phi(\mathbf{x}) \underline{S}), \varphi \right)_{\Omega} - (\nabla \cdot \underline{\mathbf{w}}, \varphi)_{\Omega} = 0, & \forall \varphi \in V. \end{cases} \quad (4.52)$$

where $\mathcal{G} = (K(\mathbf{x}) B(\underline{S}))^{-1}$.

The localized weak formulation of the diffusive system corresponding to the domain decomposition above is given by seeking $\underline{S} \in V$ and $\underline{\mathbf{w}} \in W$ such that $(\underline{S}_j, \underline{\mathbf{w}}_j) \in V_j \times W_j$ for $j = 1, \dots, M$ satisfying

$$\begin{cases} \left(\mathcal{G}\underline{\mathbf{w}}_j, \psi_j \right)_{\Omega_j} - (\underline{S}_j, \nabla \cdot \psi_j)_{\Omega_j} + \sum_{k \neq j} \langle \underline{S}_j, \psi_j \cdot \nu_j \rangle_{\Gamma_{kj}} = 0, & \forall \psi_j \in W_j, \\ \left(\frac{\partial}{\partial t} (\phi(\mathbf{x}) \underline{S}_j), \varphi_j \right)_{\Omega_j} - (\nabla \cdot \underline{\mathbf{w}}_j, \varphi_j)_{\Omega_j} = 0, & \forall \varphi_j \in V_j. \end{cases} \quad (4.53)$$

As with the two-phase problem, the solutions $(\underline{S}, \underline{\mathbf{w}})$ are required to satisfy the following consistency conditions on the interfaces Γ_{jk} ,

$$S_{w,j} = S_{w,k}, \quad \text{for } \mathbf{x} \in \Gamma_{jk}, \quad (4.54)$$

$$\mathbf{w}_{w,j} \cdot \nu_j + \mathbf{w}_{w,k} \cdot \nu_k = 0, \quad \text{for } \mathbf{x} \in \Gamma_{jk}. \quad (4.55)$$

$$S_{g,j} = S_{g,k}, \quad \text{for } \mathbf{x} \in \Gamma_{jk}, \quad (4.56)$$

$$\mathbf{w}_{g,j} \cdot \nu_j + \mathbf{w}_{g,k} \cdot \nu_k = 0, \quad \text{for } \mathbf{x} \in \Gamma_{jk}. \quad (4.57)$$

where ν is the outward normal unit vector in Ω_j .

The discrete equations for the hybridized mixed finite element for the three-phase problem are analogous to the two-phase problem. But now we have two set of discrete equations, one for the transport of water saturation and one for the transport of gas saturation.

Hybridized mixed finite element approximation

Just like in the two-phase flow, trying to impose the consistency conditions could cause errors in the flux conservation. The Lagrange multipliers on the edges Γ_{ij} are again introduced, allowing such discontinuities. Then, the hybrid mixed finite element method is given by:

Find $\underline{\mathbf{w}}_j \in W_j$, $\underline{S}_j \in V_j$ and $\ell_{kj} \in \Lambda$ such that

$$\begin{cases} (\mathcal{G}\mathbf{w}_j, \psi_j)_{\Omega_j} - (S_j, \nabla \cdot \psi_j)_{\Omega_j} + \sum_{k \neq j} \langle \ell_{kj}, \psi_j \cdot \nu_j \rangle_{\Gamma_{kj}} = 0, & \forall \psi_j \in W_j \\ \left(\frac{\partial}{\partial t} (\phi(x) S_j), \varphi_j \right)_{\Omega_j} - (\nabla \cdot \mathbf{w}_j, \varphi_j)_{\Omega_j} = 0, & \forall \varphi_j \in V_j, \end{cases} \quad (4.58)$$

subject to the consistency conditions, written equivalently as Robin transmission boundary conditions in order to define an iterative method for solving the parabolic problem.

$$\begin{aligned} -\chi_{w,kj} \mathbf{w}_{w,j} \cdot \nu_j + \ell_{w,kj} &= \chi_{w,k,j} \mathbf{w}_{w,k} \cdot \nu_k + \ell_{w,kj}, & \mathbf{x} \in \Gamma_{k,j} \subset \partial\Omega_k, \\ -\chi_{w,jk} \mathbf{w}_{w,k} \cdot \nu_k + \ell_{w,jk} &= \chi_{w,j,k} \mathbf{w}_{w,j} \cdot \nu_j + \ell_{w,kj}, & \mathbf{x} \in \Gamma_{jk} \subset \partial\Omega_j, \\ -\chi_{g,kj} \mathbf{w}_{g,j} \cdot \nu_j + \ell_{g,kj} &= \chi_{g,k,j} \mathbf{w}_{g,k} \cdot \nu_k + \ell_{g,kj}, & \mathbf{x} \in \Gamma_{kj} \subset \partial\Omega_k, \\ -\chi_{g,jk} \mathbf{w}_{g,k} \cdot \nu_k + \ell_{g,jk} &= \chi_{g,j,k} \mathbf{w}_{g,j} \cdot \nu_j + \ell_{g,kj}, & \mathbf{x} \in \Gamma_{jk} \subset \partial\Omega_j. \end{aligned} \quad (4.59)$$

Reduction to lowest index Raviart-Thomas space

The hybrid mixed finite element spaces are again chosen to be the lowest index Raviart-Thomas spaces over the intervals. The natural degrees of freedom on the element Ω_j for each saturation variable is the constant value $S_{w,j}$ and $S_{g,j}$, which can be interpreted as the value on the center of the element. For the diffusive flux variables, it is used the outward normal components across the edges of the element. The Lagrange multipliers are also constant and defined on the edges of the element. The discrete form of equations (4.59) are then,

$$\begin{aligned} \ell_{w,j}^\alpha &= \chi_{w,j}^\alpha (\mathbf{w}_{w,k}^{\tilde{\alpha}} - \mathbf{w}_{w,j}^\alpha) + \ell_{w,k}^{\tilde{\alpha}}, \\ \ell_{g,j}^\alpha &= \chi_{g,j}^\alpha (\mathbf{w}_{g,k}^{\tilde{\alpha}} - \mathbf{w}_{g,j}^\alpha) + \ell_{g,k}^{\tilde{\alpha}}, \end{aligned} \quad (4.60)$$

$\alpha = R, L, D, U,$ and $\tilde{\alpha} = L, R, U, D,$ respectively.

where each variable are defined on the L, R, U, D interfaces, representing the right (R), left (L), up (U) and down (D) edges of Ω_j ; $\tilde{\alpha}$ represents the variable associated with the adjacent element of Ω_j connected by the interface α .

Approximating the integrals by the trapezoidal rule, substituting the discrete Robin consistency equations and using an specific basis for the discrete Raviart-Thomas

spaces, the discrete forms of (4.58) are

$$\left\{ \begin{array}{l} \frac{\partial}{\partial t} (\phi(\mathbf{x}) S_j) - \frac{\mathbf{w}_{w,j}^R - \mathbf{w}_{w,j}^L}{h_x} - \frac{\mathbf{w}_{w,j}^U - \mathbf{w}_{w,j}^D}{h_y} = 0, \\ \mathcal{G}_{11}^\alpha \mathbf{w}_{w,j}^\alpha + \mathcal{G}_{12}^\alpha \mathbf{w}_{g,j}^\alpha = \frac{2}{h_x} (S_{w,j} - l_{w,j}^\alpha), \quad \alpha = R, L, \\ \mathcal{G}_{11}^\alpha \mathbf{w}_{w,j}^\alpha + \mathcal{G}_{12}^\alpha \mathbf{w}_{g,j}^\alpha = \frac{2}{h_y} (S_{w,j} - l_{w,j}^\alpha), \quad \alpha = U, D, \\ \frac{\partial}{\partial t} (\phi(\mathbf{x}) S_j) - \frac{\mathbf{w}_{w,j}^R - \mathbf{w}_{w,j}^L}{h_x} - \frac{\mathbf{w}_{w,j}^U - \mathbf{w}_{w,j}^D}{h_y} = 0, \\ \mathcal{G}_{21}^\alpha \mathbf{w}_{w,j}^\alpha + \mathcal{G}_{22}^\alpha \mathbf{w}_{g,j}^\alpha = \frac{2}{h_x} (S_{g,j} - l_{g,j}^\alpha), \quad \alpha = R, L, \\ \mathcal{G}_{21}^\alpha \mathbf{w}_{w,j}^\alpha + \mathcal{G}_{22}^\alpha \mathbf{w}_{g,j}^\alpha = \frac{2}{h_y} (S_{g,j} - l_{g,j}^\alpha), \quad \alpha = U, D. \end{array} \right. \quad (4.61)$$

By defining D_x^α and D_y^α the matrices,

$$D_x^\alpha = \begin{pmatrix} \mathcal{G}_{11} + \frac{2}{h_x} \chi_w^\alpha & \mathcal{G}_{12} \\ \mathcal{G}_{21} & \mathcal{G}_{22} + \frac{2}{h_x} \chi_g^\alpha \end{pmatrix}, \quad D_y^\alpha = \begin{pmatrix} \mathcal{G}_{11} + \frac{2}{h_y} \chi_w^\alpha & \mathcal{G}_{12} \\ \mathcal{G}_{21} & \mathcal{G}_{22} + \frac{2}{h_y} \chi_g^\alpha \end{pmatrix}, \quad (4.62)$$

the following discrete equations for the fluxes are obtained:

$$\begin{aligned} \mathbf{w}_{w,x}^\alpha &= \frac{2}{h_x} \left((D_x^\alpha)^{-1}_{11} (S_{w,j} + \chi_w^\beta \mathbf{w}_{w,x}^{\tilde{\alpha}} + \ell_{w,j}^{\tilde{\alpha}}) - (D_x^\alpha)^{-1}_{12} (S_{g,j} + \chi_g^\beta \mathbf{w}_{g,x}^{\tilde{\alpha}} + \ell_{g,j}^{\tilde{\alpha}}) \right), \\ \mathbf{w}_{g,x}^\alpha &= \frac{2}{h_x} \left((D_x^\alpha)^{-1}_{21} (S_{w,j} + \chi_w^\beta \mathbf{w}_{w,x}^{\tilde{\alpha}} + \ell_{w,j}^{\tilde{\alpha}}) - (D_x^\alpha)^{-1}_{22} (S_{g,j} + \chi_g^\beta \mathbf{w}_{g,x}^{\tilde{\alpha}} + \ell_{g,j}^{\tilde{\alpha}}) \right), \end{aligned} \quad (4.63)$$

where $\alpha = R, L$ and $\tilde{\alpha} = L, R$, respectively, and

$$\begin{aligned} \mathbf{w}_{w,y}^\alpha &= \frac{2}{h_y} \left((D_y^\alpha)^{-1}_{11} (S_{w,j} + \chi_w^\beta \mathbf{w}_{w,y}^{\tilde{\alpha}} + \ell_{w,j}^{\tilde{\alpha}}) - (D_y^\alpha)^{-1}_{12} (S_{g,j} + \chi_g^\beta \mathbf{w}_{g,y}^{\tilde{\alpha}} + \ell_{g,j}^{\tilde{\alpha}}) \right), \\ \mathbf{w}_{g,y}^\alpha &= \frac{2}{h_y} \left((D_y^\alpha)^{-1}_{21} (S_{w,j} + \chi_w^\beta \mathbf{w}_{w,y}^{\tilde{\alpha}} + \ell_{w,j}^{\tilde{\alpha}}) - (D_y^\alpha)^{-1}_{22} (S_{g,j} + \chi_g^\beta \mathbf{w}_{g,y}^{\tilde{\alpha}} + \ell_{g,j}^{\tilde{\alpha}}) \right), \end{aligned} \quad (4.64)$$

where $\alpha = U, D$, and $\tilde{\alpha} = D, U$, respectively.

The backward Euler method (implicit) for the time discretization is used, where \bar{S} represents the saturation in previous time step and S , the saturation in the current time step. Together with the discrete Lagrange multiplier equations, the final form of the

discrete system is (here, $\alpha \in \{L, R, U, D\}$ and $\tilde{\alpha} \in \{R, L, D, U\}$):

$$\left\{ \begin{array}{l} \phi_j \frac{S_{w,j} - \bar{S}_{w,j}}{\Delta t} - \frac{\mathbf{w}_{w,j}^R - \mathbf{w}_{w,j}^L}{h_x} - \frac{\mathbf{w}_{w,j}^U - \mathbf{w}_{w,j}^D}{h_y} = 0, \\ \phi_j \frac{S_{g,j} - \bar{S}_{g,j}}{\Delta t} - \frac{\mathbf{w}_{g,j}^R - \mathbf{w}_{g,j}^L}{h_x} - \frac{\mathbf{w}_{g,j}^U - \mathbf{w}_{g,j}^D}{h_y} = 0, \\ \mathbf{w}_{w,x}^\alpha = \frac{2}{h_x} \left((D_x^\alpha)^{-1} (S_{w,j} + \chi_w^\beta \mathbf{w}_{w,x}^{\tilde{\alpha}} + \ell_{w,j}^{\tilde{\alpha}}) - (D_x^\alpha)^{-1} (S_{g,j} + \chi_g^\beta \mathbf{w}_{g,x}^{\tilde{\alpha}} + \ell_{g,j}^{\tilde{\alpha}}) \right), \\ \mathbf{w}_{g,x}^\alpha = \frac{2}{h_x} \left((D_x^\alpha)^{-1} (S_{w,j} + \chi_w^\beta \mathbf{w}_{w,x}^{\tilde{\alpha}} + \ell_{w,j}^{\tilde{\alpha}}) - (D_x^\alpha)^{-1} (S_{g,j} + \chi_g^\beta \mathbf{w}_{g,x}^{\tilde{\alpha}} + \ell_{g,j}^{\tilde{\alpha}}) \right), \\ \mathbf{w}_{w,y}^\alpha = \frac{2}{h_y} \left((D_y^\alpha)^{-1} (S_{w,j} + \chi_w^\beta \mathbf{w}_{w,y}^{\tilde{\alpha}} + \ell_{w,j}^{\tilde{\alpha}}) - (D_y^\alpha)^{-1} (S_{g,j} + \chi_g^\beta \mathbf{w}_{g,y}^{\tilde{\alpha}} + \ell_{g,j}^{\tilde{\alpha}}) \right), \\ \mathbf{w}_{g,y}^\alpha = \frac{2}{h_y} \left((D_y^\alpha)^{-1} (S_{w,j} + \chi_w^\beta \mathbf{w}_{w,y}^{\tilde{\alpha}} + \ell_{w,j}^{\tilde{\alpha}}) - (D_y^\alpha)^{-1} (S_{g,j} + \chi_g^\beta \mathbf{w}_{g,y}^{\tilde{\alpha}} + \ell_{g,j}^{\tilde{\alpha}}) \right), \\ \ell_{w,j}^\alpha = \chi_{w,j}^\alpha (\mathbf{w}_{w,k}^{\tilde{\alpha}} - \mathbf{w}_{w,j}^\alpha) + \ell_{w,k}^{\tilde{\alpha}}, \\ \ell_{g,j}^\alpha = \chi_{g,j}^\alpha (\mathbf{w}_{g,k}^{\tilde{\alpha}} - \mathbf{w}_{g,j}^\alpha) + \ell_{g,k}^{\tilde{\alpha}}. \end{array} \right. \quad (4.65)$$

Here, there are two transport equations, eight discrete flux equations and eight discrete lagrange multipliers equations. Similar dimensional analysis for the coefficients χ_w and χ_g is done, and their values are found through a mean across the interfaces between elements.

4.2 Multiphase Flow Transport Problems with Spatially-Dependent Diffusion Terms

In many applications, the capillary diffusion plays a small role in the dynamical process, so that it is interesting to replace the two-phase convection-diffusion equation by the apparently more simple first order equation

$$\phi \frac{\partial}{\partial t} (\phi(x) S_w) + \nabla \cdot \mathbf{F}(x, s_w, \mathbf{v}) = 0. \quad (4.66)$$

Even in the case where the whole problem (4.3) is considered, one might be interested in the resolution of (4.7) for using a splitting approach, as presented before. In the more simple case of two-phase flow (corresponding to the case $S_g \equiv 0$ in three-phase flow problems), it has been recently pointed out in [13] that in presence of gravitational effects and of heterogeneities (i.e. $\phi, \mathbf{K}, k_\alpha$ and p_{wo} also depend on $x \in \mathbb{R}^d$), steady undercompressive waves can be generated by the rock discontinuities. Moreover, for given \mathbf{v} , the solutions of the first order problem depend on the capillary pressure functions p_{wo}, p_{go} despite capillary diffusion has been neglected in the model. Since the two-phase flow case is a subcase of the three-phase flow case, then such a phenomenon also appears in the three-phase feature.

For immiscible three-phase flow, there are physical assumptions under which singularities such as umbilic points and elliptic regions are a necessary consequence of Buckley–Leverett behavior on each two-phase edge of the saturation phase space [67]. In [18] the authors present a recent survey of aspects of the general theory of conservation laws that bear on the construction of immiscible three-phase solutions in the petroleum engineering literature. For several injection problems [18], solutions for Corey’s model are very similar to those for Stone’s model, despite the presence of an elliptic region in the latter; and they are very different from those for the Juanes–Patzek model [67], which preserves strict hyperbolicity. In [18, 79], it is also addressed the question of the physical existence of nonclassical waves in actual three-phase flows.

Dealing with hyperbolicity over the whole saturation domain, works [36, 37] describe the construction of Total Differential (TD) three-phase data for the implementation of the exact global pressure formulation for the modeling of three-phase compressible flow in porous media. The difficulty in obtaining physically realistic TD three-phase relative permeabilities and capillary pressures data [36, 37] has limited the use of the global pressure in numerical simulation codes. Nevertheless, when such data is available, this global formulation is preferred since it reduces the coupling between the pressure and saturation equations, compared to phase or weighted formulations [18, 33]. In addition, such total differential three phase permeabilities formulation also simplifies the numerical analysis of the problem along with computational efficiency [36, 37].

For a wave to be truly defined as a “shock wave”, a discontinuity must be the zero-diffusion limit of traveling wave solutions. In such solutions, the diffusive effect balances the convergence of waves caused by hyperbolic nonlinearity [79, 94]. With gravity, the three-phase model yields elliptic regions for any combination of viscosities [21, 94], and these regions occupy a significant fraction of the saturation space. Jackson and Blunt in [64] demonstrate that, even when capillary forces are small relative to viscous forces, they have a significant effect on solutions [94] for a realizable model of a porous medium. As a consequence, the capillary pressure should be included explicitly in three-phase numerical simulators to obtain stable solutions which reproduce the correct sequence of saturation changes in the interior of the phase space.

4.2.1 Two-phase flow problems

Assume for simplicity that the one-dimensional domain Ω is made of only two sets Ω^L and Ω^R separated by a Lipschitz continuous interface Γ . For $x \in \Gamma$, we denote by ν_α the outward unit normal vector to Γ with respect to Ω_α . Because of the rock discontinuity, the physical quantities p_α, S_α and \mathbf{v}_α can *a priori* be discontinuous at the interface Γ . Two-phase flow with discontinuities on convective flux functions and diffusive capillary functions can be modeled by the following equation with discontinuous coefficients:

$$\phi^\alpha \frac{\partial S_w}{\partial t} + \nabla \cdot \left(\mathbf{v} f_w^\alpha(S_w) + \sigma_G \mathbf{G}_w^\alpha(S_w) - K^\alpha \lambda_w^\alpha(S_w) (1 - f_w^\alpha(S_w)) \frac{\partial p_{wo}^\alpha}{\partial x} \right) = 0, \quad x \in \Omega_\alpha. \quad (4.67)$$

The work [13] investigated the so-called vanishing capillary limit, by making $\epsilon \rightarrow 0$ on the system (for $x \in \Omega_\alpha$ and $t \in (0, T)$),

$$\begin{cases} \phi^\alpha \frac{\partial S_\epsilon}{\partial t} + \nabla \cdot (\mathbf{v} f_w^\alpha(S_\epsilon) + \sigma_G \mathbf{G}_w^\alpha(S_\epsilon) - \epsilon \nabla \cdot \varphi^\alpha(S_\epsilon)) = 0, \\ \lim_{x \rightarrow 0^-} (\mathbf{v} f_w^L(S_\epsilon) + \sigma_G \mathbf{G}_w^L(S_\epsilon) - \epsilon \nabla \cdot \varphi^L(S_\epsilon)) = \lim_{x \rightarrow 0^+} (\mathbf{v} f_w^R(S_\epsilon) + \sigma_G \mathbf{G}_w^R(S_\epsilon) - \epsilon \nabla \cdot \varphi^R(S_\epsilon)). \end{cases} \quad (4.68)$$

where $\alpha = L, R$ and $\varphi^\alpha(S) = \int_0^S K^\alpha \lambda_w^\alpha(z) (1 - f_w^\alpha(z)) \frac{\partial p_{wo}^\alpha}{\partial S} dz$ is the Kirchoff transform function.

This study is close to the one performed by E. Kaasschieter [68], but in such work, the recent developments in the theory of the scalar conservation laws with discontinuous-flux function are taken into account (see [14, 30] and references therein). It was identified the correct interface coupling in the discontinuous-flux Buckley–Leverett model in terms of the profiles of the flux functions and capillary pressure functions on two sides from the interface. In particular, the conclusions of the work [68] were clarified by proving that “optimal entropy solution” is not always the right notion of solution in the Buckley–Leverett context.

4.2.1.1 Extension to three-phase flow problems

There is an inherent difficulty on extending the ideas from [13]. There must be an admissible continuous capillary pressure state (p_{wo}, p_{go}) at the interface, even if this is hidden in a boundary layer, but the capillary pressure models proposed in [19] may be non-physical to some extent [82].

The work [1] combines distinct methods for the resolution of different types of equations that appears in the three-phase flow model. This is done despite the presence or not of constitutive relationships of relative permeability, saturation and capillary pressure which ensure hyperbolicity over the whole saturation domain [18, 36, 37, 79]. A fractional-step time-marching method combines a conservative central scheme to handle a system of nonlinear conservation laws with locally conservative mixed finite elements for the associated parabolic and elliptic problems. It has been shown in [4, 71] that the operator splitting technique can be effective in capturing the correct nonclassical fronts in one spatial dimension as well as in multidimensional heterogeneous three-phase gravity-free flows [3].

Similar ideas involving alternative fractional-step procedures as discussed in this work have been presented in [69, 70, 72, 73]. The works [69, 70] are based in a front tracking approach, relies heavily on a Riemann solver and the method of polygonal approximations. In [72, 73] the authors have shown that using semidiscrete central-upwind schemes may fail to converge to the unique entropy solution of nonconvex conservation laws, and thus may fail to recover the Kruzhkov solution [13, 46]. Besides, the Strang splitting [91] is not an alternative since the hyperbolic nature of the three-phase differential flow system is not completely understood [18, 79]. The splitting approach proposed in [34] is based on the solution of a parabolic problem via a discretization of the formula for the exact kernel solution of a heat equation with constant coefficients as opposed to the present work.

The numerical procedure developed in [1] is based on the before mentioned two-stage operator-splitting method for decoupling the nonlinear three-phase flow equations with mixed discretization methods, leading to purely hyperbolic, parabolic and elliptic subproblems. For the convective flux, the numerical approach is based on the central scheme [3, 71, 80] rather than a semidiscrete central upwind scheme formulation [72]. Such scheme accommodates the discontinuous hyperbolic flux functions as well as the effects of spatially variable porosity. No upwinding techniques were used in order to stabilize the numerical solution of the hyperbolic subproblem. In addition, neither dimensional splitting and Riemann solvers (exact or approximate) are necessary. The hybrid mixed finite elements method is used for accurate velocity field computation for the elliptic subproblem even in the presence of highly variable permeability fields [3, 47, 51].

4.3 A Fully-Coupled Finite Volume/Hybrid Mixed Finite Elements Approach for Multiphase Flow Problems

We now present our proposal of a coupled formulation between finite volume methods approximating the convective operator and hybrid mixed finite element methods approximating the diffusive operator. Such formulation has a reinterpretation of the Robin coupling conditions presented before. This new coupling condition can also be seen as a weak form of the Robin condition, and has a natural relation with the Rankine-Hugoniot jump condition, traditionally associated with hyperbolic conservation laws. Besides, this formulation, first presented for one-dimensional two-phase problems, can readily be extended to three-phase flow problems and to multidimensional formulations.

4.3.1 Two-phase flow problem

We present the one-dimensional two-phase flow problem, where the capillary diffusive term may have discontinuities

$$\frac{\partial}{\partial t} (\phi(x)S_w) + \frac{\partial \mathbf{F}_w}{\partial x} = \varepsilon \frac{\partial \mathbf{w}_w}{\partial x}, \quad (4.69)$$

with \mathbf{F}_w and \mathbf{w}_w being the convective and diffusive fluxes defined by:

$$\mathbf{F}_w(S_w, x) = \mathbf{v}f_w + \mathbf{G}_w \quad \text{and} \quad \mathbf{w}_w(S_w, x) = -K(x)[\lambda_w(S_w)(1 - f_w)] \frac{\partial p_{wo}}{\partial x}. \quad (4.70)$$

The convective flux here has two components: f_w (the fractional flow) multiplied by \mathbf{v} (Darcy velocity from the pressure-velocity subproblem) and \mathbf{G}_w , which incorporates gravitational effects and can be defined by

$$\mathbf{G}_w(S_w, x) = K(x)[\lambda_w(1 - f_w)\rho_{wo}]g \frac{\partial Z}{\partial x}. \quad (4.71)$$

On the definition of the diffusive flux, there is a nonlinear gradient of the capillary pressure function $p_{wo} = p_{wo}(S_w, \mathbf{x})$.

Equation (4.69) needs an initial condition, which we here define as

$$S_w(x, 0) = S_0(x) \quad \text{for } x \in \Omega, \quad (4.72)$$

and boundary conditions

$$S_w(\Omega_L, t) = S_L, \quad S_w(\Omega_R, t) = S_R \quad \text{for } t > 0. \quad (4.73)$$

where $\Omega = [\Omega_L, \Omega_R] \subset \mathbb{R}$ is the spatial one-dimensional domain. One of the key differences of our formulation from the previous hybrid mixed finite element is that we carry the calculations of the finite elements along with the convective flux function. This operator will be approximated by the conservative flux function of a finite volume method.

4.3.1.1 Mixed formulation for the transport equation

We identify the gradient flux for the saturation, by applying the chain rule for the capillary pressure in 4.3. Such derivation is possible since we are following the lines from previous developments [1, 47] of hybrid mixed finite element methods for multiphase flow problems, in which calculations are performed on an element level, where we suppose permeability, porosity and capillary functions to be constant.

$$\mathbf{w}(S, x) = -K(x) \lambda_w(S) (1 - f_w) \frac{\partial p_{wo}}{\partial S} \frac{\partial S}{\partial x}. \quad (4.74)$$

Defining $B(S) = \lambda_w(S) (1 - f_w) \frac{\partial p_{wo}}{\partial S}$, it is possible to rewrite the equation into a mixed formulation for the pair (S, \mathbf{w}) :

$$\begin{cases} \mathbf{w} + K(x) B(S) \frac{\partial S}{\partial x} = 0 \\ \frac{\partial}{\partial t} (\phi(x) S) + \frac{\partial \mathbf{F}}{\partial x} - \varepsilon \frac{\partial \mathbf{w}}{\partial x} = 0. \end{cases} \quad (4.75)$$

4.3.1.2 Weak form of the transport system

We put (4.75) in a weak global formulation by means of the spaces V and W ,

$$\begin{aligned} L^2(\Omega) &= \left\{ v \mid \int_{\Omega} |v(x)|^2 dx < \infty \right\}, & H^1(\Omega) &= \left\{ \mathbf{w} \in L^2(\Omega) \mid \frac{\partial}{\partial x} \mathbf{w} \in L^2(\Omega) \right\}. \\ V &= \{v \in L^2(\Omega)\}, & W &= \{\mathbf{w} \in H^1(\Omega) \mid \mathbf{w}|_{\Gamma_j} \nu = 0\}. \end{aligned}$$

The global weak formulation of the diffusive system is given by finding $(S, \mathbf{w}) \in V \times W$ so that for every test functions $\varphi \in V$ and $\psi \in W$ the following weak equations are satisfied,

$$\begin{cases} ((K(x) B(S))^{-1} \mathbf{w}, \psi)_{\Omega} + \left(\frac{\partial S}{\partial x}, \psi \right)_{\Omega} = 0, & \forall \psi \in W \\ \left(\frac{\partial}{\partial t} (\phi(x) S), \varphi \right)_{\Omega} + \left(\frac{\partial \mathbf{F}}{\partial x}, \varphi \right)_{\Omega} - \left(\varepsilon \frac{\partial \mathbf{w}}{\partial x}, \varphi \right)_{\Omega} = 0, & \forall \varphi \in V. \end{cases} \quad (4.76)$$

where $(f, g)_{\Omega}$ is the usual inner product by integration in Ω .

We localize the equations using the domain decomposition ideas. Let $\{\Omega_j, j = 1, \dots, M\}$ be a partition of the spatial domain Ω into intervals of size h

$$\Omega = \bigcup_{j=1}^M \Omega_j; \quad \Omega_j \cap \Omega_k = \emptyset, j \neq k, \quad \Omega_j = (x_j, x_{j+1}), \quad (4.77)$$

with the domain interfaces

$$\Gamma = \partial\Omega = \{x_0, x_M\}; \quad \Gamma_j = \Gamma \cap \Omega_j = \{x_j, x_{j+1}\}, \quad \Gamma_{j,j+1} = \Gamma_{j+1,j} = \partial\Omega_j \cap \partial\Omega_{j+1} = x_{j+1}. \quad (4.78)$$

Consider, for $j = 1, \dots, M$ the local spaces

$$V_j = V(\Omega_j), \quad W_j = \{ \mathbf{w} \in H^1(\Omega_j) \mid \mathbf{w} \cdot \nu = 0 \text{ on } \Gamma_j \}.$$

The localized weak formulation of the diffusive system corresponding to the domain decomposition is given by seeking $S \in V$ and $\mathbf{w} \in W$ such that $(S_j, \mathbf{w}_j) \in V_j \times W_j$ for $j = 1, \dots, M$ satisfying

$$\begin{cases} ((K(x) B(S_j))^{-1} \mathbf{w}_j, \psi_j)_{\Omega_j} - \left(S_j, \frac{\partial \psi_j}{\partial x} \right)_{\Omega_j} + S_j^R \psi_j^R - S_j^L \psi_j^L = 0, & \forall \psi_j \in W_j \\ \left(\frac{\partial}{\partial t} (\phi(x) S_j), \varphi_j \right)_{\Omega_j} + \left(\frac{\partial \mathbf{F}_j}{\partial x}, \varphi_j \right)_{\Omega_j} - \left(\varepsilon \frac{\partial \mathbf{w}_j}{\partial x}, \varphi_j \right)_{\Omega_j} = 0, & \forall \varphi_j \in V_j. \end{cases} \quad (4.79)$$

where $S_j^L = S_j(x_j)$ and $S_j^R = S_j(x_{j+1})$ are the saturation variables S_j defined on the interfaces Γ_j . Note that, in this step, an integration by parts was performed on the first equation. In order that the functions (S, \mathbf{w}) extend to be solutions of (4.76), it is necessary to require the following consistency conditions on the interfaces Γ_{jk}

$$S_j = S_k, \quad \text{for } x \in \Gamma_{jk}, \quad (4.80)$$

$$\mathbf{w}_j \cdot \nu_j + \mathbf{w}_k \cdot \nu_k = 0, \quad \text{for } x \in \Gamma_{jk}. \quad (4.81)$$

where ν is the outward normal unit vector in Ω_j .

4.3.1.3 Hybridized mixed finite element approximation

We allow discontinuities in each element interface Γ_{jk} . If we try to impose the consistency conditions, it could cause errors in the flux conservation. We introduce the Lagrange multipliers on the edges Γ_{ij} , allowing such discontinuities. Since we are here considering the unidimensional case, the Lagrange multipliers λ_{ij} become real scalars, defined only on x_{ij} . The hybrid mixed finite element method is given by:

Find $\mathbf{w}_j \in W_j$, $S \in V_j$ and $\ell_{ij} \in \mathbb{R}$ such that

$$\begin{cases} ((K(x) B(S_j))^{-1} \mathbf{w}_j, \psi_j)_{\Omega_j} - \left(S_j, \frac{\partial \psi_j}{\partial x} \right)_{\Omega_j} + \ell_{j+1,j} \psi_j^R - \ell_{j,j-1} \psi_j^L = 0, & \forall \psi_j \in W_j \\ \left(\frac{\partial}{\partial t} (\phi(x) S_j), \varphi_j \right)_{\Omega_j} + \left(\frac{\partial \mathbf{F}_j}{\partial x}, \varphi_j \right)_{\Omega_j} - \left(\varepsilon \frac{\partial \mathbf{w}_j}{\partial x}, \varphi_j \right)_{\Omega_j} = 0, & \forall \varphi_j \in V_j, \end{cases} \quad (4.82)$$

subject to the consistency conditions which we discuss in the following section.

4.3.1.4 Weakening of Robin coupling conditions

Another key aspect of our method is the reinterpretation of the Robin consistency condition for coupling elements, in a manner that we weaken it to incorporate the

effects of capillary diffusion without the derivative eliminating any additive term of its definition, something the method presented in the previous section fails to capture [1].

Around an interface Γ_{jk} between elements j and k , we set a strip of length e , which we denote by Γ_e . On this strip, we multiply the Robin coupling condition by the constant test function $\varphi_j = 1$ (we discuss the use of other test functions later) and perform an integration step, so that we have a weakened version of the coupling condition. This way, we must have,

$$\int_{\Gamma_e} \ell_j^L dx + \int_{\Gamma_e} \chi^L \mathbf{w}_j^L dx = \int_{\Gamma_e} \ell_{j-1}^R dx + \int_{\Gamma_e} \chi^L \mathbf{w}_{j-1}^R dx. \quad (4.83)$$

By defining $|\Gamma_e|$ the integral of the characteristic function over the strip, and since we assume the lagrange multipliers and the function S to be constant over the elements, we have,

$$\ell_j^L |\Gamma_e| + \chi^L \int_{\Gamma_e} \mathbf{w}_j^L dx = \ell_{j-1}^R |\Gamma_e| + \chi^L \int_{\Gamma_e} \mathbf{w}_{j-1}^R dx. \quad (4.84)$$

From the definition of the flux

$$\mathbf{w} = v(S, x) \frac{\partial p_{wo}}{\partial x}.$$

where $v(S, x) = -K(x)\lambda(1 - f)$, the integral of a flux must be,

$$\begin{aligned} \int_{\Gamma_e} \mathbf{w}_j^L dx &= \int_{\Gamma_e} v^L \frac{\partial p_{wo}^L}{\partial x} dx \\ &= \int_{\Gamma_e} \frac{\partial}{\partial x} (v^L p_{wo}^L) dx - \int_{\Gamma_e} \frac{\partial v^L}{\partial x} p_{wo}^L dx \\ &= v^L p_{wo}^L|_{\partial \Gamma_e} - \int_{\Gamma_e} \frac{\partial v^L}{\partial S} \frac{\partial S}{\partial x} p_{wo}^L dx \\ &= -|\Gamma_e| \frac{\partial v^L}{\partial S} p_{wo}^L \frac{\partial S^L}{\partial x}. \end{aligned} \quad (4.85)$$

We observe that the function v has a known derivative in S , since it is a product of known mobility and fractional flow functions. With this weak version of a flux, we transfer the derivative operator from the capillary pressure to its coefficient. The spatial derivative of the function S must be approximated, and we discuss this later on. Substituting equation (4.85) into the weakened Robin condition, we have,

$$\ell_j^L |\Gamma_e| + \chi^L \int_{\Gamma_e} \mathbf{w}_j^L dx = \ell_{j-1}^R |\Gamma_e| + \chi^L \int_{\Gamma_e} \mathbf{w}_{j-1}^R dx. \quad (4.86)$$

For the purpose of developing an iterative procedure to solve the linear system, we cannot weaken both fluxes in a same equation, since it would eliminate the flux variable from the equation by substituting it with nonlinear functions of S . This way, we have

some options in choosing which variables to weaken. By selecting the flux variables on the adjacent elements to be weakened (i.e. the right hand side of the previous equation), the new coupling conditions are obtained,

$$\begin{aligned}\ell_j^L &= \ell_{j-1}^R + \chi_j^L \tilde{\mathbf{w}}_{j-1}^R - \chi_j^L \mathbf{w}_j^L, \\ \ell_j^R &= \ell_{j+1}^L - \chi_j^R \tilde{\mathbf{w}}_{j+1}^L + \chi_j^R \mathbf{w}_j^R.\end{aligned}\tag{4.87}$$

where $\tilde{\mathbf{w}}_{j-1}^R = \frac{1}{|\Gamma_e|} \int_{\Gamma_e} \mathbf{w}_{j-1}^R dx$ and $\tilde{\mathbf{w}}_{j+1}^L = \frac{1}{|\Gamma_e|} \int_{\Gamma_e} \mathbf{w}_{j+1}^L dx$ are the weakened fluxes given by equation (4.85).

4.3.1.5 Discrete equations and iterative procedure

Following the same ideas presented on the previous sections for the discretization of equations (4.79), we obtain the system,

$$\begin{cases} \frac{h}{2} \mathcal{G} \mathbf{w}_j^L + S_j = \ell_j^L, \\ \frac{h}{2} \mathcal{G} \mathbf{w}_j^R - S_j = -\ell_j^R, \\ \phi_j \frac{S_j - \bar{S}_j}{\Delta t} + \frac{F^R - F_j^L}{h} + \frac{\varepsilon}{h} (\mathbf{w}_j^R - \mathbf{w}_j^L) = 0. \end{cases}\tag{4.88}$$

Now, substitute (4.87) into (4.88) and along the new coupling conditions, we obtain

$$\begin{cases} \phi_j \frac{S_j - \bar{S}_j}{\Delta t} + \frac{F^R - F_j^L}{h} + \frac{\varepsilon}{h} (\mathbf{w}_j^R - \mathbf{w}_j^L) = 0, \\ \left(\frac{h}{2} \mathcal{G} + \chi_j^L \right) \mathbf{w}_j^L = R_j^L - S_j, & R_j^L := \chi_j^L \tilde{\mathbf{w}}_{j-1}^R + \ell_{j-1}^R, \\ \left(\frac{h}{2} \mathcal{G} + \chi_j^R \right) \mathbf{w}_j^R = R_j^R + S_j, & R_j^R := \chi_j^R \tilde{\mathbf{w}}_{j+1}^L - \ell_{j+1}^L, \\ \ell_j^L = R_j^L - \chi_j^L \mathbf{w}_j^L, \\ \ell_j^R = R_j^R + \chi_j^R \mathbf{w}_j^R. \end{cases}\tag{4.89}$$

The substitution of the flux equations into the transport equation result in

$$S_j = \left[\phi_j \frac{h}{\Delta t} + \varepsilon(C^R + C^L) \right]^{-1} \left[\phi_j \bar{S}_j \frac{h}{\Delta t} - (F_j^R - F_j^L) - \varepsilon(C^R R_j^R - C^L R_j^L) \right],\tag{4.90}$$

where $C^L = \left(\frac{h}{2} \mathcal{G} + \chi_j^L \right)^{-1}$ and $C^R = \left(\frac{h}{2} \mathcal{G} + \chi_j^R \right)^{-1}$.

We note that the convective fluxes F^L and F^R are defined on the interfaces, so that we can use any finite volume numerical scheme in a conservative form, with a conservative flux function to approximate such values in each element.

4.3.2 Numerical Experiments

In this section we present numerical experiments for the proposed coupled mixed hybrid finite element and finite volume method with a new coupling condition for a variety of problems. The numerical scheme for this section was written in C programming language and the numerical experiments were performed in the same previously cited computer configuration. We first start with the classical advection problem with a exponential pulse traveling right and a small diffusive effect guided by the ε parameter. The advection equation is given by

$$\begin{aligned} u_t + au_x &= \varepsilon u_{xx}, \quad x \in \mathbb{R}, t > 0 \\ u(x, 0) &= \exp(-x^2), \quad x \in \mathbb{R}. \end{aligned} \quad (4.91)$$

We must observe that the weakened flux deviate from the classical numerical flux only by a stretching factor. By employing an ad-hoc correction factor, we are able to recover the correct flux and obtain the correct solution of the problem. Figure 41 shows the correct numerical solution of this problem and the fluxes \mathbf{w} (classical), $\tilde{\mathbf{w}}$ (weakened), and corrected $\tilde{\mathbf{w}}$.

For the viscid Burger's equation with a exponential pulse traveling right and a small diffusive effect guided by the ε parameter, the equation is given by

$$\begin{aligned} u_t + uu_x &= \varepsilon u_{xx}, \quad x \in \mathbb{R}, t > 0 \\ u(x, 0) &= \exp(-x^2), \quad x \in \mathbb{R}. \end{aligned} \quad (4.92)$$

Then again the weakened flux deviate from the classical numerical flux by a stretching factor. We employ the ad-hoc correction factor, and we are able to recover the correct flux and obtain the correct solution of the problem. Figure 42 shows the correct numerical solution of this problem and the fluxes \mathbf{w} (classical), $\tilde{\mathbf{w}}$ (weakened).

The same problem but with a sinusoid initial condition $u(x, 0) = \sin x$ presents similar behavior. Figure 43 shows the correct numerical solution of this problem and the fluxes \mathbf{w} (classical), $\tilde{\mathbf{w}}$ (weakened). We must point out that the structure of the flux is preserved by our method, differing by this stretching factor.

Finally, we present solutions to model problem (3.29) for the set of entry pressures $P^L = 0$ and $P^R = 2.0$, for $x \in \Omega_\alpha = \Omega^L \cup \Omega^R$:

$$\phi^\alpha \frac{\partial S_w}{\partial t} + \nabla \cdot \left(\mathbf{v} f_w(S_w) + \sigma_G \mathbf{G}_w^\alpha(S_w) - \sigma_P K^\alpha \lambda_w(S_w) (1 - f_w(S_w)) \frac{\partial p_{wo}^\alpha}{\partial x} \right) = 0, \quad (4.93)$$

with the following parameters: flow rate $\mathbf{v} = 0$, gravity $g = -9.81$, $\sigma_G = 1.0$, absolute permeabilities $K^L = 10^{-2}$, $K^R = 5 \times 10^{-3}$, porosities $\phi^L = \phi^R = 1.0$, viscosities $\mu_w = 10^{-3}$, $\mu_o = 3 \times 10^{-3}$, densities $\rho_w = 0.87$, $\rho_o = 1.0$, diffusive coefficient $\sigma_P = 1.0 \times 10^{-3}$, and capillary pressure function:

$$p_{wo}^\alpha = P^\alpha - \log(1 - s). \quad (4.94)$$

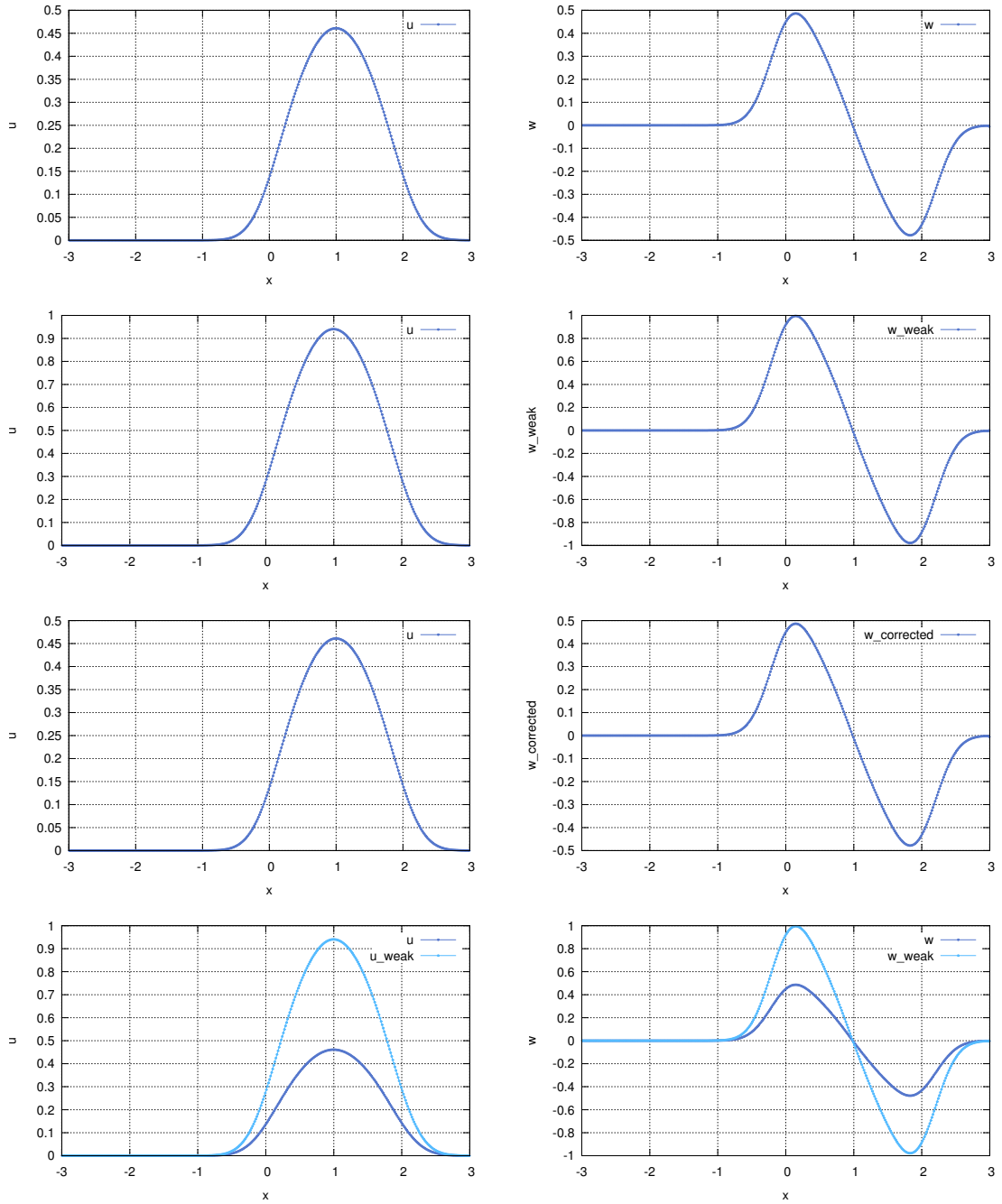


Figure 41 – From top to bottom: first, second and third rows depicts the solutions of linear advection problems (on the left column) with the usual (\mathbf{w}), weakened ($\tilde{\mathbf{w}}$) and corrected weakened ($\tilde{\mathbf{w}}_c$) fluxes (on the right column). We show on the bottom row the solutions combined in order to explicit the difference of the scales (we omit the corrected weakened for the sake of presentation).

The initial condition for this problem is the constant function $\eta(x) = 0.5$. We have only a wave profile traveling left. Here, the stretching factor is different for each entry-pressure region inducing discontinuity in the diffusive effect, but the structure of the flux profile is also captured.

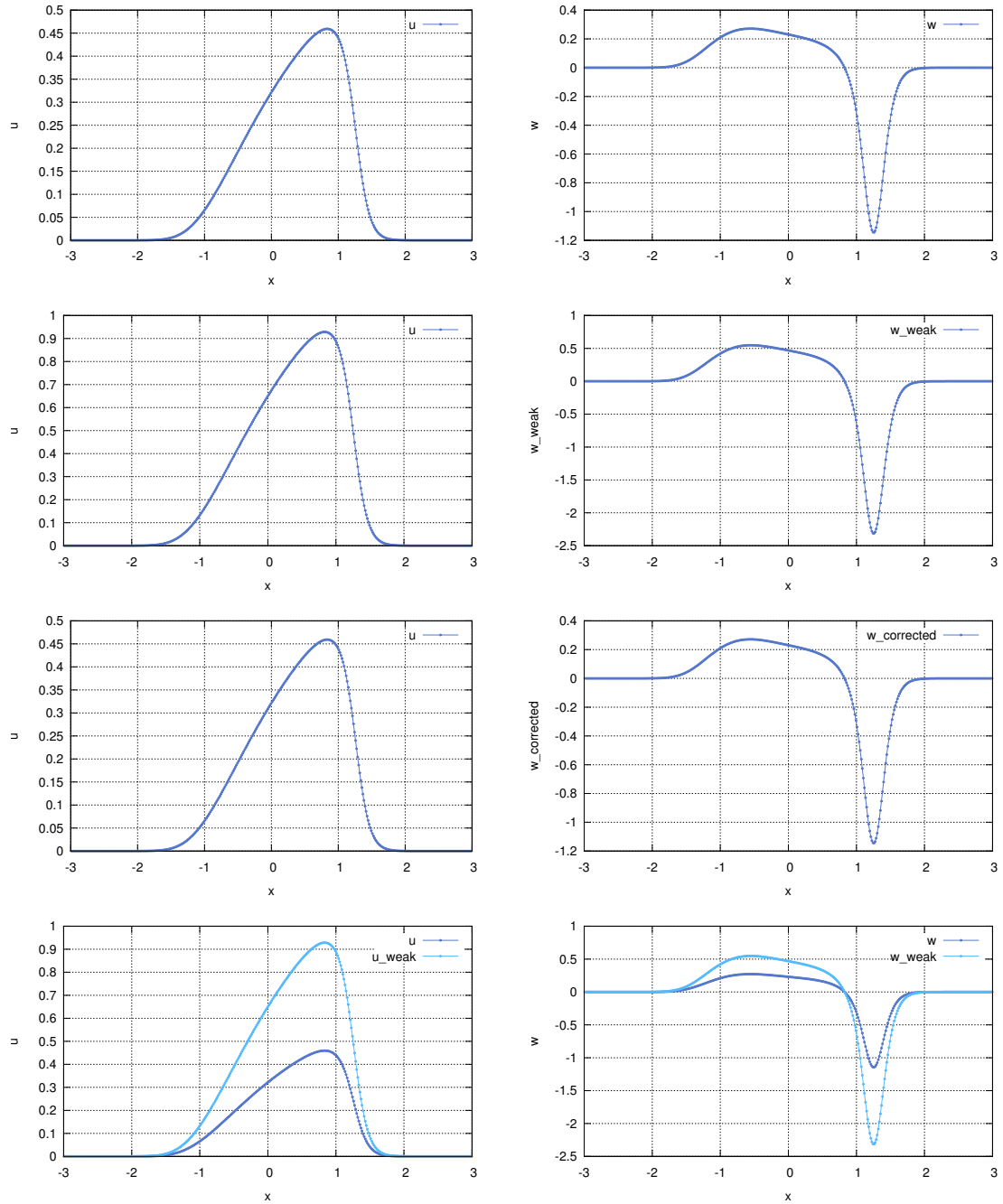


Figure 42 – From top to bottom: first, second and third rows depicts the solutions of Burgers' viscous equation solution with exponential pulse as initial condition (on the left column) with the usual (\mathbf{w}), weakened ($\tilde{\mathbf{w}}$) and corrected weakened ($\tilde{\mathbf{w}}_c$) fluxes (on the right column). We show on the bottom row the solutions combined in order to explicit the difference of the scales (we omit the corrected weakened for the sake of presentation).

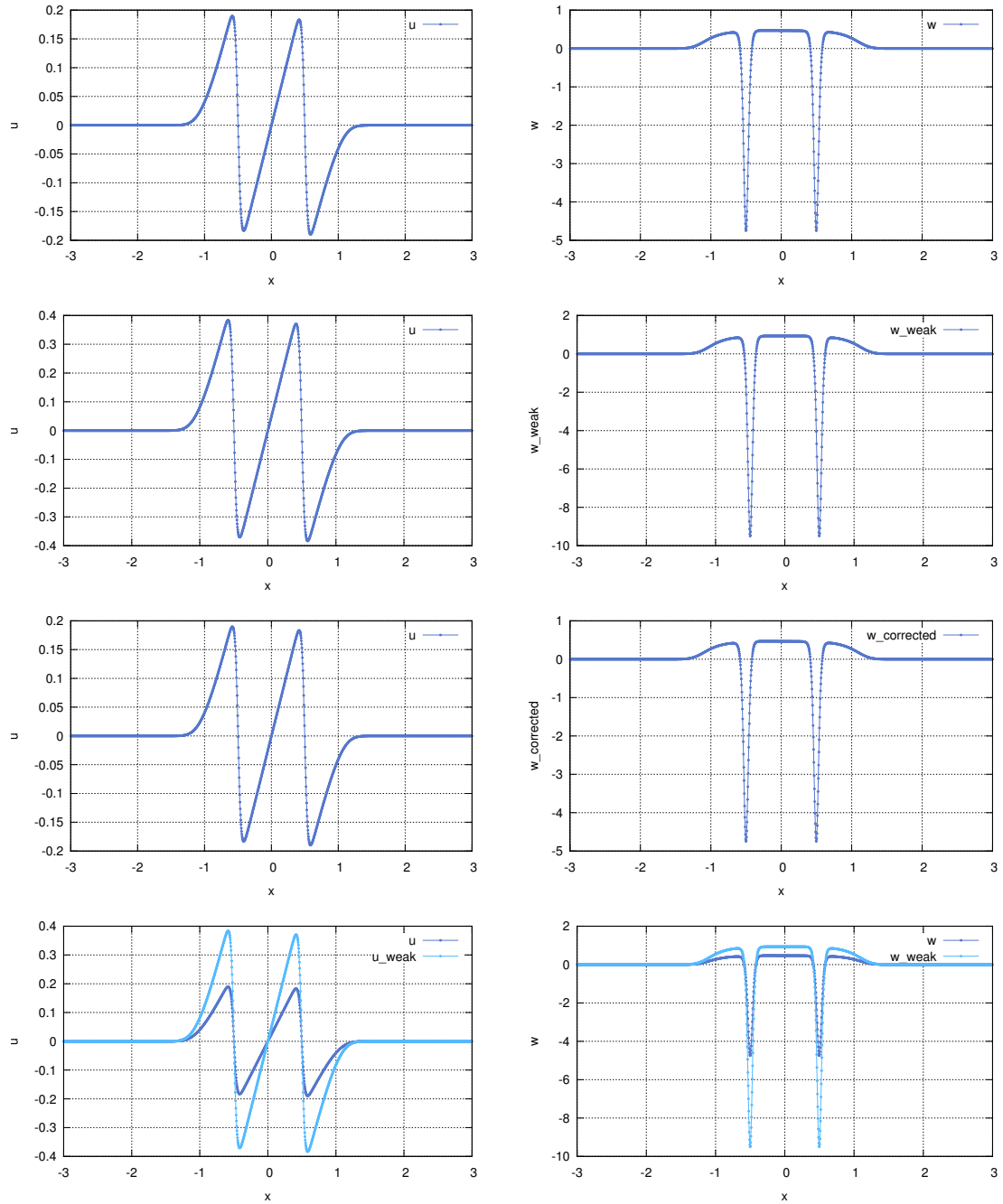


Figure 43 – From top to bottom: first, second and third rows depicts the solutions of Burgers' viscous equation solution with sine wave as initial condition (on the left column) with the usual (\mathbf{w}), weakened ($\tilde{\mathbf{w}}$) and corrected weakened ($\tilde{\mathbf{w}}_c$) fluxes (on the right column). We show on the bottom row the solutions combined in order to explicit the difference of the scales (we omit the corrected weakened for the sake of presentation).

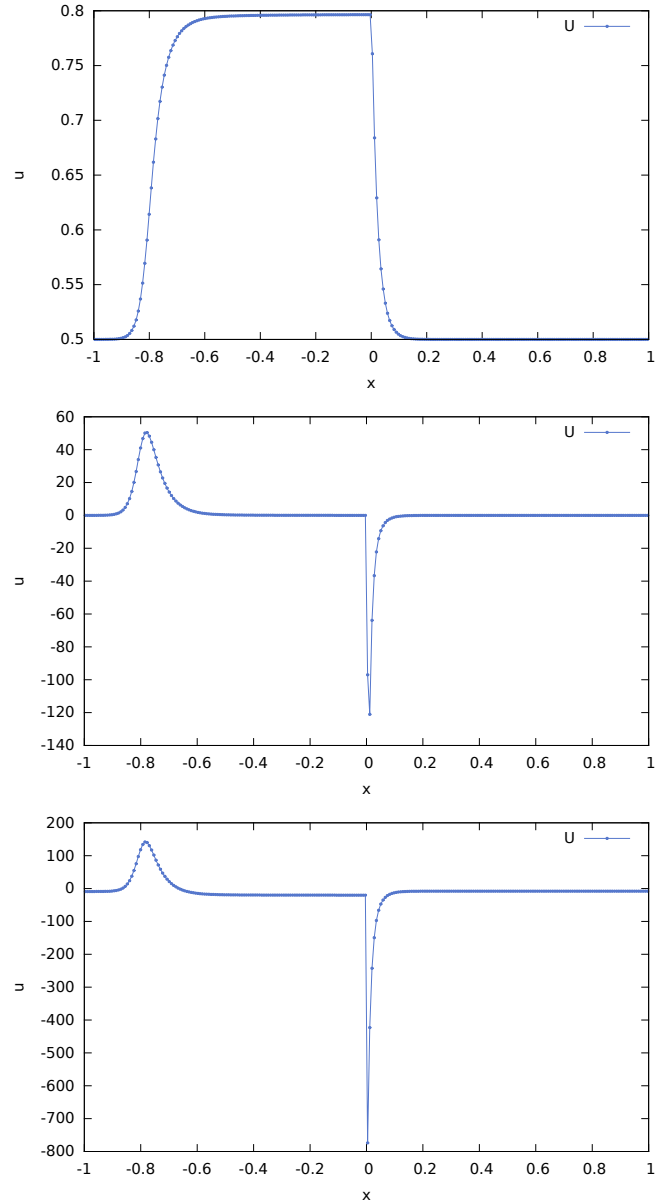


Figure 44 – The first picture represents the numerical solution of Model problem (3.29) with the constant initial condition $u \equiv 0.5$ and capillary pressure functions $P^{R,L} - \log(1 - u)$ and the following pictures are the classical (\mathbf{w}) and weakened ($\tilde{\mathbf{w}}$) fluxes.

5 Concluding Remarks and Outlook for Future Work

5.1 Preliminary advances and achievements

In this thesis we have achieved some progress in the formulation and development of numerical methods for various classes of differential problems. We constructed numerical schemes in local conservative form for solving nonlinear hyperbolic conservation and balance law problems – both for the scalar case and for systems of equations – using the novel Lagrangian-Eulerian approach. The framework is based on a reformulation of the equation regarding an equivalent locally conservative space-time divergence form problem. In this work we made use of piecewise linear reconstruction along with predictor-corrector techniques for improvements of the computed numerical solutions, yielding a robust numerical scheme.

We discussed qualitatively correct numerical solutions for classical and non-classical problems such as the inviscid Burgers equation, two-phase and three-phase flow problems in porous media and a variety of nonlinear shallow water equations examples, including test cases with bottom friction. In particular, we were also able to reproduce qualitatively correct approximations for the situation of balance laws with discontinuous source terms. One of the key aspects of this framework is to be independent of a particular structure of the flux function and the (possibly stiff) source term. We do not have a rigorous mathematical analysis, but we presented new numerical evidence of the well-balanced property within the framework, recovering the correct structure of equilibrium solutions.

We must point out that the Lagrangian-Eulerian framework allows a natural a priori analysis of the underlying model to enforce mass conservation. In the current thesis, we have deepened this discussion, for instance, for models with the null-velocity terms. The resulting numerical scheme presented for such cases is naturally different, but the Eulerian-Lagrangian framework remains the same. The balance of the steady state of the equation seems to be respected, even if this balance is somewhat “hidden” into the original system. After extensive numerical experiments, we observed that our numerical scheme seems to simulate inside the integral tube both the information related to mass conservation (possibly from a source term) and the computation of the correct velocity (linked to the purely hyperbolic operator).

We discussed ideas on how to extend our Lagrangian-Eulerian numerical scheme for higher dimensions. By using the concepts of Mean curvature and Gaussian curvature associated with the underlying conservation law, we were able to propose a natural

construction of a normal curvature and a geodesic curvature, by the projection onto the local normal vector and the local tangent plane, at least from a theoretical viewpoint. The uniqueness of the definition of this curve for each one of the points that appear at the bottom of the integral tube circumvents a customary challenge on how to extend mass conservation of the framework to higher dimensions. We also presented a usual approach, based in writing the two-dimensional scalar conservation law in the form of a coupled set of two balance laws along with initial data, so that our numerical scheme for systems of balance laws could be readily used. Nontrivial test cases that can be found in recent specialized literature we simulated with very good numerical results.

There was some further comprehension within this framework developed in the current thesis, including a nonstaggered form of the numerical scheme that can be plugged into the proofs of convergence by means of weak asymptotic solutions, by which there is no need of convexity assumptions on the flux functions. This nonstaggered formulation also provides another alternative way of extending the framework to two-dimensional problems with good numerical results. There was an inherent difficulty on directly extending the nonstaggered approach to higher dimensions since the projection coefficients of this approach were nontrivially defined. Thus, we worked around this difficulty by evolving the midpoints of the control volume and defining the evolved control volume. We were again able to approximate problems with a variety of challenges without making intrusive changes to our framework.

We also mention as an advance of the Lagrangian-Eulerian framework the application to a specific convection-diffusion problem of multiphase flow in porous media with discontinuous coefficients. We were able to correctly approximate its solution by means of a numerical technique that encompasses a corrective step for the diffusive operator, coupled with our Lagrangian-Eulerian numerical scheme. We also presented an alternative formulation for this very hard problem, whose structure might sensitively depend on the diffusive operator, by means of a hybrid mixed finite element method coupled with a finite volume method. However, in such formulation, we proposed a reinterpretation of the interface conditions between elements to accommodate the effects of heterogeneities in the diffusive operator. The hybrid mixed finite element method with this novel interface condition was coupled with finite volume methods in a conservative form for approximating the convective transport. We performed numerical experiments for this new technique in order to best analyze the effect of weakening Robin conditions.

List of Scientific Communications:

- Journal article entitled “A new finite volume approach for transport models and related applications with balancing source terms” published in *Mathematics and Computers in Simulation*, January, 2017 [6];
- Conference paper published in the *Proceedings of the 6th International Conference on Approximation Methods and Numerical Modelling in Environment and Natural Resources*, 2016 [5];
- Conference paper published in the *Proceeding Series of the Brazilian Society of Computational and Applied Mathematicss* titled “A Lagrangian-Eulerian algorithm for solving hyperbolic conservation laws with applications”, 2017 [9];
- Talk given at the *International Conference on Approximation Methods and Numerical Modelling in Environment and Natural Resources MAMERN VI (2015)*, in Pau, France;
- Talk given at the *XXXVI Congresso Nacional de Matemática Aplicada e Computacional* in September 2016, Gramado, Brazil;
- Poster presentation at the *2nd IMPA-InterPore Conference on Porous Media: Conservation Laws, Numerics and Applications* titled “A numerical scheme based in a conservative formulation for solving hyperbolic conservation laws” and “An approximation to hyperbolic conservation laws using a Lagrangian-Eulerian approach” in October 2016, Rio de Janeiro, Brazil.

5.2 Perspectives for future work and some final considerations

We finally explicit the main directions that may guide the development of conservative numerical schemes both within the Lagrangian-Eulerian framework, also for mixed hybrid finite element methods for convection-diffusion problems. Here are some that deserve our special attention and that can be considered a continuation of this thesis.

- In the current work, one of the key aspects of the Lagrangian-Eulerian framework is to define the following (local) nonlinear differential equations (from Section 2.2),

$$\frac{d\sigma_j^n(t)}{dt} = \frac{H(u(\sigma_j^n(t), t))}{u(\sigma_j^n(t), t)}, \quad \text{for } t^n < t \leq t^{n+1},$$

with the initial condition $\sigma_j^n(t^n) = x_j^n$. This equation cannot be directly solved for σ due to its dependence of the unknown function u and for that we used the simplest

approximations $f_j^n = \frac{H(U_j^n)}{U_j^n} \approx \frac{H(u)}{u}$, obtaining good numerical results in terms of qualitatively recovering the correct structure of several problems. In this direction, a possible evolution of the numerical scheme could be to approximate solutions of this system by means of specialized numerical methods for ordinary differential equations, such as Runge-Kutta numerical schemes.

- In our numerical scheme [6] it is possible to propose a semidiscrete numerical formulation. Such methods could benefit from the more precise information of the local propagation speeds that central semidiscrete schemes provide.
- Classical techniques to prove convergence to the entropic solution were successfully applied in the work [84] for Lagrangian-Eulerian schemes. Modern techniques such as the weak asymptotic solutions theory can also be used for this intent and such direction is a front to be explored.
- We also cite as a possible future work to consider a Level Set numerical approach for higher dimensional conservation law problems to approximate the proposed formulation involving Mean and Gaussian curvature from Section 2.2 (see [62, 75]). The Level Set Approach was first proposed in [81] to model evolving fronts with curvature. In the level set approach, the front is modeled using a higher dimensional smooth function ϕ , where $\phi = 0$ represents the front. This approach allows the numerical evaluation of geometric quantities such as the normal direction and the curvature by benefiting on the smoothness of the level set function. There is also a natural connection between this approach and adaptive mesh refinement. Explicit high order schemes for advancing this implicit representation of evolving interfaces have been described in the specialized literature, but the computational cost of such approaches are expensive. Thus, under this perspective, the development of fast, effective and robust numerical schemes in this approach is of utter importance.
- The meticulous study of the alternative weak Robin condition presented in Section 4.3 also needs to be pursued on. Even though we obtained the qualitatively correct structure of the flux variable for some of the presented problems after the correction factor, for problems with discontinuous coefficients the exact influence of this weakening is not completely understood yet. This must be carefully done before the extension to systems of convection-diffusion problems with spatial discontinuities in the diffusive operator. It is a main goal of this approach to be extended in a straightforward manner to case of systems, and the lack of theory for such problems has always been a considerable source of difficulties.

When it comes to future developments on this thesis, there is a lot of continuation that could be carried out. This work was mainly concerned with advances and

enhancements within the Lagrangian-Eulerian framework for nontrivial problems and our results helped to push the boundaries of this prosperous technique.

Bibliography

- 1 ABREU, E. Numerical modelling of three-phase immiscible flow in heterogeneous porous media with gravitational effects. **Mathematics and Computers in Simulation**, Elsevier, v. 97, p. 234–259, 2014. Cit. on pp. [50–52](#), [95](#), [96](#), [101](#), [112](#), [114](#), [116](#).
- 2 ABREU, E. Numerical simulation of three-phase flow in heterogeneous media with spatially varying nonlinear hyperbolic-parabolic flux functions. In: FOURTEENTH INTERNATIONAL CONFERENCE ON HYPERBOLIC PROBLEMS HELD IN PADOVA. **Hyperbolic Problems: Theory, Numerics, Applications**. Ed. by F. Ancona, A. Bressan, P. Marcati and A. Marson, 2012. v. 8. (AIMS on Applied Mathematics), p. 233–240. Cit. on pp. [95](#), [101](#).
- 3 ABREU, E.; DOUGLAS JR, J.; FURTADO, F.; MARCHESIN, D.; PEREIRA, F. Three-phase immiscible displacement in heterogeneous petroleum reservoirs. **Mathematics and Computers in Simulation**, Elsevier, v. 73, n. 1, p. 2–20, 2006. Cit. on pp. [95](#), [97](#), [112](#).
- 4 ABREU, E.; FURTADO, F.; PEREIRA, F. On the Numerical Simulation of Three-Phase Reservoir Transport Problems. **Transport Theory and Statistical Physics**, Taylor & Francis, v. 33, n. 5-7, p. 503–526, 2004. Cit. on pp. [95](#), [112](#).
- 5 ABREU, E.; LAMBERT, W.; PEREZ, J.; SANTO, A. A Lagrangian-Eulerian algorithm for solving hyperbolic conservation laws with applications. In: PROCEEDINGS of the 6th International Conference on Approximation Methods and Numerical Modelling in Environment and Natural Resources. Pau, France: Editorial Universidad de Granada, June 2015. p. 600–617. Cit. on pp. [22](#), [75](#), [125](#).
- 6 ABREU, E.; LAMBERT, W.; PEREZ, J.; SANTO, A. A new finite volume approach for transport models and related applications with balancing source terms. **Mathematics and Computers in Simulation**, Elsevier, v. 137, p. 2–28, 2017. Cit. on pp. [20](#), [58](#), [75](#), [125](#), [126](#).
- 7 ABREU, E.; BUSTOS, A.; LAMBERT, W. Non-monotonic traveling wave and computational solutions for gas dynamics Euler equations with stiff relaxation source terms. **Computers & Mathematics with Applications**, Elsevier, v. 70, n. 9, p. 2155–2176, 2015. Cit. on p. [25](#).
- 8 ABREU, E.; COLOMBEAU, M.; PANOV, E. Weak asymptotic methods for scalar equations and systems. **Journal of Mathematical Analysis and Applications**, Elsevier, v. 444, n. 2, p. 1203–1232, 2016. Cit. on p. [75](#).

- 9 ABREU, E.; PÉREZ, J.; SANTO., A. Solving hyperbolic conservation laws by using Lagrangian-Eulerian approach. **Proceeding Series of the Brazilian Society of Computational and Applied Mathematics**, v. 5, n. 1, 2017. ISSN 2359-0793. DOI: <http://dx.doi.org/10.5540/03.2017.005.01.0329>. Cit. on pp. 21, 22, 75, 125.
- 10 ALBERTI, G.; BIANCHINI, S.; CARAVENNA, L. Eulerian, Lagrangian and Broad continuous solutions to a balance law with non-convex flux I. **Journal of Differential Equations**, Elsevier, v. 261, n. 8, p. 4298–4337, 2016. Cit. on p. 24.
- 11 ALMEIDA, C.; DOUGLAS JR, J.; PEREIRA, F.; ROMAN, L. C.; YEH, L.-M. Algorithmic aspects of a locally conservative Eulerian-Lagrangian method for transport-dominated diffusive systems. **Contemporary Mathematics**, Providence, RI; American Mathematical Society; 1999, v. 295, p. 37–48, 2002. Cit. on p. 95.
- 12 AMADORI, D.; GOSSE, L. **Error Estimates for Well-Balanced Schemes on Simple Balance Laws: One-Dimensional Position-Dependent Models**. Springer, 2015. Cit. on p. 25.
- 13 ANDREIANOV, B.; CANCÈS, C. Vanishing capillarity solutions of Buckley–Leverett equation with gravity in two-rocks' medium. **Computers & Geosciences**, Springer, v. 17, n. 3, p. 551–572, 2013. Cit. on pp. 88–90, 96, 110–112.
- 14 ANDREIANOV, B.; KARLSEN, K. H.; RISEBRO, N. H. A theory of L1-dissipative solvers for scalar conservation laws with discontinuous flux. **Archive for Rational Mechanics and Analysis**, Springer, v. 201, n. 1, p. 27–86, 2011. Cit. on p. 111.
- 15 AQUINO, J.; FRANCISCO, A. S.; PEREIRA, F.; PEREIRA, T. J.; SOUTO, H. P. A. A Lagrangian strategy for the numerical simulation of radionuclide transport problems. **Progress in Nuclear Energy**, Elsevier, v. 52, n. 3, p. 282–291, 2010. Cit. on pp. 24–28, 76.
- 16 ARBOGAST, T.; WHEELER, M. F. A characteristics-mixed finite element method for advection-dominated transport problems. **SIAM Journal on Numerical Analysis**, SIAM, v. 32, n. 2, p. 404–424, 1995. Cit. on p. 24.
- 17 AUDUSSE, E.; BOUCHUT, F.; BRISTEAU, M.-O.; KLEIN, R.; PERTHAME, B. A fast and stable well-balanced scheme with hydrostatic reconstruction for shallow water flows. **SIAM Journal on Scientific Computing**, SIAM, v. 25, n. 6, p. 2050–2065, 2004. Cit. on p. 57.
- 18 AZEVEDO, A. V.; SOUZA, A. J. de; FURTADO, F.; MARCHESIN, D.; PLOHR, B. The solution by the wave curve method of three-phase flow in virgin reservoirs. **Transport in Porous Media**, Springer, v. 83, n. 1, p. 99–125, 2010. Cit. on pp. 110, 112.

- 19 AZIZ, K.; SETTARI, A. **Petroleum reservoir simulation**. Applied Science Publishers London, 1979. v. 476. Cit. on p. [112](#).
- 20 BALE, D. S.; LEVEQUE, R. J.; MITRAN, S.; ROSSMANITH, J. A. A wave propagation method for conservation laws and balance laws with spatially varying flux functions. **SIAM Journal on Scientific Computing**, SIAM, v. 24, n. 3, p. 955–978, 2003. Cit. on p. [55](#).
- 21 BELL, J. B.; TRANGENSTEIN, J. A.; SHUBIN, G. R. Conservation laws of mixed type describing three-phase flow in porous media. **SIAM Journal on Applied Mathematics**, SIAM, v. 46, n. 6, p. 1000–1017, 1986. Cit. on p. [111](#).
- 22 BERMUDEZ, A.; VAZQUEZ, M. E. Upwind methods for hyperbolic conservation laws with source terms. **Computers & Fluids**, Elsevier, v. 23, n. 8, p. 1049–1071, 1994. Cit. on p. [55](#).
- 23 BERTHON, C.; MARCHE, F. A positive preserving high order VFRoe scheme for shallow water equations: a class of relaxation schemes. **SIAM Journal on Scientific Computing**, SIAM, v. 30, n. 5, p. 2587–2612, 2008. Cit. on p. [57](#).
- 24 BERTHON, C.; DE LEFFE, M.; MICHEL-DANSAC, V. A conservative well-balanced hybrid SPH scheme for the shallow-water model. In: *FINITE Volumes for Complex Applications VII-Elliptic, Parabolic and Hyperbolic Problems*. Springer, 2014. p. 817–825. Cit. on pp. [25](#), [59](#), [68](#).
- 25 BORTHWICK, A. G. L.; CRUZ LEON, S.; JÓZSA, J. The shallow flow equations solved on adaptive quadtree grids. **International Journal for Numerical Methods in Fluids**, Wiley Online Library, v. 37, n. 6, p. 691–719, 2001. Cit. on pp. [19](#), [55](#).
- 26 BOTCHORISHVILI, R.; PERTHAME, B.; VASSEUR, A. Equilibrium schemes for scalar conservation laws with stiff sources. **Mathematics of Computation**, v. 72, n. 241, p. 131–157, 2003. Cit. on pp. [25](#), [26](#).
- 27 BOUCHUT, F.; OUNAÏSSA, H.; PERTHAME, B. Upwinding of the source term at interfaces for Euler equations with high friction. **Computers & mathematics with applications**, Elsevier, v. 53, n. 3, p. 361–375, 2007. Cit. on pp. [25](#), [26](#).
- 28 BRENNER, S. C.; SCOTT, R. **The mathematical theory of finite element methods**. Springer, 2008. v. 15. Cit. on p. [95](#).
- 29 BREZZI, F.; FORTIN, M. **Mixed and hybrid finite element methods**. Springer-Verlag New York, Inc., 1991. Cit. on pp. [95](#), [96](#).
- 30 BÜRGER, R.; KARLSEN, K. H.; TOWERS, J. D. An Engquist-Osher-type scheme for conservation laws with discontinuous flux adapted to flux connections. **SIAM Journal on Numerical Analysis**, SIAM, v. 47, n. 3, p. 1684–1712, 2009. Cit. on p. [111](#).

- 31 CASTRO, M. J.; LEFLOCH, P. G.; MUÑOZ-RUIZ, M. L.; PARÉS, C. Why many theories of shock waves are necessary: Convergence error in formally path-consistent schemes. **Journal of Computational Physics**, Elsevier, v. 227, n. 17, p. 8107–8129, 2008. Cit. on pp. [25](#), [58](#).
- 32 CELIA, M. A. Eulerian-Lagrangian localized adjoint methods for contaminant transport simulations. **Computational methods in water resources X**, Kluwer Academic Publishers Dordrecht, Netherlands, v. 1, p. 207–216, 1994. Cit. on p. [24](#).
- 33 CHEN, Z.; EWING, R. E. Comparison of various formulations of three-phase flow in porous media. **Journal of Computational Physics**, Elsevier, v. 132, n. 2, p. 362–373, 1997. Cit. on pp. [50](#), [110](#).
- 34 CHERTOCK, A.; DOERING, C. R.; KASHDAN, E.; KURGANOV, A. A fast explicit operator splitting method for passive scalar advection. **Journal of Scientific Computing**, Springer, v. 45, n. 1-3, p. 200–214, 2010. Cit. on p. [112](#).
- 35 CHERTOCK, A.; CUI, S.; KURGANOV, A.; WU, T. Well-balanced positivity preserving central-upwind scheme for the shallow water system with friction terms. **International Journal for numerical methods in fluids**, Wiley Online Library, v. 78, n. 6, p. 355–383, 2015. Cit. on p. [63](#).
- 36 CHIARA ROUPERT, R. di; CHAVENT, G.; SCHÄFER, G. Three-phase compressible flow in porous media: total differential compatible interpolation of relative permeabilities. **Journal of Computational Physics**, Elsevier, v. 229, n. 12, p. 4762–4780, 2010. Cit. on pp. [50](#), [110](#), [112](#).
- 37 CHIARA ROUPERT, R. di; SCHÄFER, G.; ACKERER, P.; QUINTARD, M.; CHAVENT, G. Construction of three-phase data to model multiphase flow in porous media: Comparing an optimization approach to the finite element approach. **Comptes Rendus Geoscience**, Elsevier, v. 342, n. 11, p. 855–863, 2010. Cit. on pp. [110](#), [112](#).
- 38 CHOPP, D. L.; SETHIAN, J. A. Flow under curvature: singularity formation, minimal surfaces, and geodesics. **Experimental Mathematics**, Taylor & Francis, v. 2, n. 4, p. 235–255, 1993. Cit. on p. [45](#).
- 39 COLOMBEAU, M. A numerical scheme for singular shock solutions and a study of its consistence in the sense of distributions. **Journal of Computational and Applied Mathematics**, Elsevier, v. 294, p. 78–92, 2016. Cit. on pp. [88–90](#).
- 40 COQUEL, F.; HÉRARD, J.-M.; SALEH, K.; SEGUIN, N. A robust entropy-satisfying finite volume scheme for the isentropic Baer- Nunziato model. **ESAIM: Mathematical Modelling and Numerical Analysis**, EDP Sciences, v. 48, n. 1, p. 165–206, 2014. Cit. on p. [58](#).

- 41 DANILOV, V.; SHELKOVICH, V. Dynamics of propagation and interaction of δ -shock waves in conservation law systems. **Journal of Differential Equations**, Elsevier, v. 211, n. 2, p. 333–381, 2005.
- 42 DELESTRE, O.; CORDIER, S.; JAMES, F.; DARBOUX, F. Simulation of rain-water overland-flow. In: AMERICAN MATHEMATICAL SOCIETY. 12TH International Conference on Hyperbolic Problems. 2008. v. 67, p. 537–546. Cit. on pp. [19](#), [55](#).
- 43 DELESTRE, O.; LUCAS, C.; KSINANT, P.-A.; DARBOUX, F.; LAGUERRE, C.; VO, T.-N.; JAMES, F.; CORDIER, S., et al. SWASHES: a compilation of shallow water analytic solutions for hydraulic and environmental studies. **International Journal for Numerical Methods in Fluids**, Wiley Online Library, v. 72, n. 3, p. 269–300, 2013. Cit. on pp. [25](#), [56](#), [59](#).
- 44 DELGADO, J. G. G. **Well-posedness and blow-up of global solutions for a nonlinear transport equation with nonlocal flux and measure data: theory and numerics**. 2016. PhD thesis – University of Campinas. Cit. on p. [95](#).
- 45 DÍAZ, C. **Uso combinado do método de elementos finitos mistos híbridos com decomposição de domínio e de métodos espectrais para um estudo de renormalização do modelo KPZ**. 2015. Cit. on p. [95](#).
- 46 DIEHL, S. A uniqueness condition for nonlinear convection-diffusion equations with discontinuous coefficients. **Journal of Hyperbolic Differential Equations**, World Scientific, v. 6, n. 01, p. 127–159, 2009. Cit. on p. [112](#).
- 47 DOUGLAS JR, J.; FURTADO, F.; PEREIRA, F. On the numerical simulation of waterflooding of heterogeneous petroleum reservoirs. **Computers & Geosciences**, Springer, v. 1, n. 2, p. 155–190, 1997. Cit. on pp. [95](#), [97](#), [101](#), [112](#), [114](#).
- 48 DOUGLAS JR, J.; PEREIRA, F.; YEH, L.-M. A locally conservative Eulerian–Lagrangian numerical method and its application to nonlinear transport in porous media. **Computers & Geosciences**, Springer, v. 4, n. 1, p. 1–40, 2000. Cit. on pp. [24](#), [26](#), [27](#), [95](#).
- 49 DOUGLAS JR, J.; WHEELER, M. F.; EWING, R. E. The approximation of the pressure by a mixed method in the simulation of miscible displacement. **ESAIM: Mathematical Modelling and Numerical Analysis-Modélisation Mathématique et Analyse Numérique**, EDP Sciences, v. 17, n. 1, p. 17–33, 1983. Cit. on p. [95](#).
- 50 DUMBSER, M.; ENAUX, C.; TORO, E. F. Finite volume schemes of very high order of accuracy for stiff hyperbolic balance laws. **Journal of Computational Physics**, Elsevier, v. 227, n. 8, p. 3971–4001, 2008. Cit. on pp. [25](#), [26](#).

- 51 EWING, R. E.; RUSSELL, T. F.; WHEELER, M. F. Convergence analysis of an approximation of miscible displacement in porous media by mixed finite elements and a modified method of characteristics. **Computer Methods in Applied Mechanics and Engineering**, Elsevier, v. 47, n. 1, p. 73–92, 1984. Cit. on pp. [95](#), [112](#).
- 52 FANG, B.; TANG, P.; WANG, Y.-G. The Riemann problem of the Burgers equation with a discontinuous source term. **Journal of Mathematical Analysis and Applications**, Elsevier, v. 395, n. 1, p. 307–335, 2012. Cit. on pp. [25](#), [26](#), [70](#).
- 53 GALLARDO, J. M.; PARÉS, C.; CASTRO, M. On a well-balanced high-order finite volume scheme for shallow water equations with topography and dry areas. **Journal of Computational Physics**, Elsevier, v. 227, n. 1, p. 574–601, 2007. Cit. on p. [57](#).
- 54 GERRITSEN, M. G.; DURLOFSKY, L. J. Modeling fluid flow in oil reservoirs. **Annual Review of Fluid Mechanics**, Annual Reviews, v. 37, p. 211–238, 2005. Cit. on pp. [19](#), [48](#).
- 55 GOSSE, L. A two-dimensional version of the Godunov scheme for scalar balance laws. **SIAM Journal on Numerical Analysis**, SIAM, v. 52, n. 2, p. 626–652, 2014. Cit. on pp. [25](#), [44](#), [68](#), [69](#).
- 56 GOSSE, L. Computing qualitatively correct approximations of balance laws. **SIMAI Springer Series**, Springer, v. 2, 2013. Cit. on pp. [25](#), [26](#), [70](#).
- 57 GOSSE, L.; TOSCANI, G. An asymptotic-preserving well-balanced scheme for the hyperbolic heat equations. **Comptes Rendus Mathématique**, Elsevier, v. 334, n. 4, p. 337–342, 2002. Cit. on p. [25](#).
- 58 GOUTA, N.; MAUREL, F. A finite volume solver for 1D shallow-water equations applied to an actual river. **International Journal for Numerical Methods in Fluids**, Wiley Online Library, v. 38, n. 1, p. 1–19, 2002. Cit. on pp. [19](#), [55](#).
- 59 GOUTAL, N.; MAUREL, F. **Proceedings of the 2nd workshop on dam-break wave simulation**. Electricité de France. Direction des études et recherches, 1997. Cit. on p. [59](#).
- 60 GREENBERG, J.; LEROUX, A.; BARAILLE, R.; NOUSSAIR, A. Analysis and approximation of conservation laws with source terms. **SIAM Journal on Numerical Analysis**, SIAM, v. 34, n. 5, p. 1980–2007, 1997. Cit. on pp. [25](#), [70](#).
- 61 GREENBERG, J. M.; LEROUX, A.-Y. A well-balanced scheme for the numerical processing of source terms in hyperbolic equations. **SIAM Journal on Numerical Analysis**, SIAM, v. 33, n. 1, p. 1–16, 1996. Cit. on pp. [25](#), [67](#), [70](#).
- 62 HÉLEIN, F. **Harmonic maps, conservation laws and moving frames**. Cambridge University Press, 2002. v. 150. Cit. on pp. [45](#), [126](#).

- 63 HUANG, C.-S.; ARBOGAST, T.; QIU, J. An Eulerian–Lagrangian WENO finite volume scheme for advection problems. **Journal of Computational Physics**, Elsevier, v. 231, n. 11, p. 4028–4052, 2012. Cit. on pp. [25](#), [26](#), [37](#), [81](#).
- 64 JACKSON, M. D.; BLUNT, M. J. Elliptic regions and stable solutions for three-phase flow in porous media. **Transport in Porous Media**, Springer, v. 48, n. 3, p. 249–269, 2002. Cit. on p. [111](#).
- 65 JIANG, G.-S.; SHU, C.-W. Efficient implementation of weighted ENO schemes. **Journal of computational physics**, Elsevier, v. 126, n. 1, p. 202–228, 1996. Cit. on p. [81](#).
- 66 JIN, S. A steady-state capturing method for hyperbolic systems with geometrical source terms. **ESAIM: Mathematical Modelling and Numerical Analysis**, EDP Sciences, v. 35, n. 4, p. 631–645, 2001. Cit. on pp. [25](#), [26](#), [69](#), [70](#), [84](#).
- 67 JUANES, R.; PATZEK, T. W. Relative permeabilities for strictly hyperbolic models of three-phase flow in porous media. **Transport in Porous Media**, Springer, v. 57, n. 2, p. 125–152, 2004. Cit. on p. [110](#).
- 68 KAASSCHIETER, E. F. Solving the Buckley–Leverett equation with gravity in a heterogeneous porous medium. **Computers & Geosciences**, Springer, v. 3, n. 1, p. 23–48, 1999. Cit. on pp. [88](#), [111](#).
- 69 KARLSEN, K. H.; LIE, K.-A.; NATVIG, J. R.; NORDHAUG, H. F.; DAHLE, H. K. Operator splitting methods for systems of convection–diffusion equations: nonlinear error mechanisms and correction strategies. **Journal of Computational Physics**, Elsevier, v. 173, n. 2, p. 636–663, 2001. Cit. on pp. [101](#), [112](#).
- 70 KARLSEN, K. H.; RISEBRO, N. H. Corrected operator splitting for nonlinear parabolic equations. **SIAM Journal on Numerical Analysis**, SIAM, v. 37, n. 3, p. 980–1003, 2000. Cit. on pp. [101](#), [112](#).
- 71 KARLSEN, K. H.; TOWERS, J. D. Convergence of the Lax–Friedrichs scheme and stability for conservation laws with a discontinuous space-time dependent flux. **Chinese Annals of Mathematics**, World Scientific, v. 25, n. 03, p. 287–318, 2004. Cit. on pp. [95](#), [112](#).
- 72 KURGANOV, A.; NOELLE, S.; PETROVA, G. Semidiscrete central-upwind schemes for hyperbolic conservation laws and Hamilton–Jacobi equations. **SIAM Journal on Scientific Computing**, SIAM, v. 23, n. 3, p. 707–740, 2001. Cit. on p. [112](#).
- 73 KURGANOV, A.; PETROVA, G.; POPOV, B. Adaptive semidiscrete central-upwind schemes for nonconvex hyperbolic conservation laws. **SIAM Journal on Scientific Computing**, SIAM, v. 29, n. 6, p. 2381–2401, 2007. Cit. on pp. [85](#), [87](#), [112](#).

- 74 LANGSETH, J. O.; TVEITO, A.; WINTHER, R. On the convergence of operator splitting applied to conservation laws with source terms. **SIAM Journal on Numerical Analysis**, SIAM, v. 33, n. 3, p. 843–863, 1996. Cit. on pp. [25](#), [26](#), [85](#).
- 75 LEE, D.; KIM, J. Mean curvature flow by the Allen–Cahn equation. **European Journal of Applied Mathematics**, Cambridge Univ Press, v. 26, n. 04, p. 535–559, 2015. Cit. on pp. [45](#), [126](#).
- 76 LEVEQUE, R. J. **Finite volume methods for hyperbolic problems**. Cambridge university press, 2002. v. 31. Cit. on pp. [28](#), [30](#), [46](#), [68](#), [76](#).
- 77 LIOTTA, S. F.; ROMANO, V.; RUSSO, G. Central schemes for balance laws of relaxation type. **SIAM Journal on Numerical Analysis**, SIAM, v. 38, n. 4, p. 1337–1356, 2000. Cit. on p. [25](#).
- 78 MARCHE, F. **Theoretical and numerical study of shallow water models: applications to nearshore hydrodynamics**. 2005. PhD thesis – Bordeaux 1. Cit. on pp. [19](#), [55](#).
- 79 MARCHESIN, D.; PLOHR, B. J., et al. Wave structure in WAG recovery. **SPE Journal**, Society of Petroleum Engineers, v. 6, n. 02, p. 209–219, 2001. Cit. on pp. [51](#), [52](#), [110–112](#).
- 80 NESSYAHU, H.; TADMOR, E. Non-oscillatory central differencing for hyperbolic conservation laws. **Journal of computational physics**, Elsevier, v. 87, n. 2, p. 408–463, 1990. Cit. on pp. [76](#), [112](#).
- 81 OSHER, S.; SETHIAN, J. A. Fronts propagating with curvature-dependent speed: algorithms based on Hamilton-Jacobi formulations. **Journal of Computational Physics**, Elsevier, v. 79, n. 1, p. 12–49, 1988. Cit. on pp. [45](#), [126](#).
- 82 OTTO, F. The geometry of dissipative evolution equations: the porous medium equation. Taylor & Francis, 2001. Cit. on p. [112](#).
- 83 PARÉS, C. Numerical methods for nonconservative hyperbolic systems: a theoretical framework. **SIAM Journal on Numerical Analysis**, SIAM, v. 44, n. 1, p. 300–321, 2006. Cit. on p. [58](#).
- 84 PEREZ, J. **Lagrangian-Eulerian approximate methods for balance laws and hyperbolic conservation laws**. 2015. PhD thesis – University of Campinas. Cit. on pp. [24–28](#), [32](#), [33](#), [35](#), [37](#), [44](#), [75](#), [76](#), [85](#), [126](#).
- 85 RAVIART, P. A.; THOMAS, J. M. A mixed finite element method for 2-nd order elliptic problems. In: MATHEMATICAL aspects of finite element methods. Springer, 1977. p. 292–315. Cit. on pp. [95](#), [96](#).
- 86 RUSSELL, T. F. **An incompletely iterated characteristic finite element method for a miscible displacement problem**. 1980. PhD thesis – University of Chicago, Department of Mathematics. Cit. on p. [24](#).

- 87 RUSSELL, T. F. Time stepping along characteristics with incomplete iteration for a Galerkin approximation of miscible displacement in porous media. **SIAM Journal on Numerical Analysis**, SIAM, v. 22, n. 5, p. 970–1013, 1985. Cit. on p. 95.
- 88 SABAC, F. The optimal convergence rate of monotone finite difference methods for hyperbolic conservation laws. **SIAM Journal on Numerical Analysis**, SIAM, v. 34, n. 6, p. 2306–2318, 1997. Cit. on p. 70.
- 89 SAINT-VENANT, A. J. C. B. de. Théorie du mouvement non permanent des eaux, avec application aux crues des rivières et à l'introduction des marées dans leurs lits. **Comptes Rendus des séances de l'Académie des Sciences**, v. 73, p. 237–240, 1871. Cit. on pp. 55, 56.
- 90 SINGH, J.; ALTINAKAR, M. S.; DING, Y. Two-dimensional numerical modeling of dam-break flows over natural terrain using a central explicit scheme. **Advances in Water Resources**, Elsevier, v. 34, n. 10, p. 1366–1375, 2011. Cit. on p. 59.
- 91 STRANG, G. On the construction and comparison of difference schemes. **SIAM Journal on Numerical Analysis**, SIAM, v. 5, n. 3, p. 506–517, 1968. Cit. on p. 112.
- 92 TANG, T.; TENG, Z.-H. Error bounds for fractional step methods for conservation laws with source terms. **SIAM Journal on Numerical Analysis**, SIAM, v. 32, n. 1, p. 110–127, 1995. Cit. on pp. 70, 72.
- 93 TATARD, L.; PLANCHON, O.; WAINWRIGHT, J.; NORD, G.; FAVIS-MORTLOCK, D.; SILVERA, N.; RIBOLZI, O.; ESTEVES, M.; HUANG, C. H. Measurement and modelling of high-resolution flow-velocity data under simulated rainfall on a low-slope sandy soil. **Journal of Hydrology**, Elsevier, v. 348, n. 1, p. 1–12, 2008. Cit. on pp. 19, 55.
- 94 TRANGENSTEIN, J. A. Three-phase flow with gravity. **Contemporary Mathematics**, v. 100, p. 147–159, 1989. Cit. on p. 111.
- 95 VALIANI, A.; CALEFFI, V. Closure to “Case Study: Malpasset Dam-Break Simulation Using a Two-Dimensional Finite Volume Method” by Alessandro Valiani, Valerio Caleffi, and Andrea Zanni. **Journal of Hydraulic Engineering**, American Society of Civil Engineers, v. 130, n. 9, p. 945–948, 2004. Cit. on pp. 19, 55.
- 96 VIEIRA, J. **Um estudo computacional de equações pseudo-parabólicas para mecânica dos fluidos e fenômenos de transporte em meios porosos**. 2015. Cit. on p. 95.
- 97 VOHRALÍK, M. Equivalence between lowest-order mixed finite element and multi-point finite volume methods on simplicial meshes. **ESAIM: Mathematical Modelling and Numerical Analysis**, Cambridge Univ Press, v. 40, n. 02, p. 367–391, 2006. Cit. on p. 95.

-
- 98 WHEELER, M. F.; DAWSON, C. N. An operator-splitting method for advection-diffusion-reaction problems. **The Mathematics of Finite Elements and Applications VI**, Academic Press London, UK, p. 463–382, 1987. Cit. on p. [95](#).
- 99 XING, Y.; SHU, C.-W. A survey of high order schemes for the shallow water equations. **Journal of Mathematical Study**, v. 47, n. 221-249, p. 56, 2014. Cit. on p. [18](#).

Appendix

A Lagrangian-Eulerian algorithm for solving hyperbolic conservation laws with applications

**Eduardo Abreu¹, Wanderson Lambert²,
John Perez^{1,3} and Arthur Santo¹**

¹Department of Applied Mathematics,
University of Campinas, IMECC, SP 13083-859, Brazil,
{eabreu,arthurm}@ime.unicamp.br

² Federal University Rural of Rio de Janeiro,
Rod. BR 465, Km 7, 23.890-000, Seropédica, RJ, Brazil
wanderson.lambert@gmail.com

³ Facultad de Ciencias ITM Institución Universitaria
Calle, 73 No 76A, 354 Medellín, Colombia.
johnperez@itm.edu.co

Keywords: Hyperbolic conservation laws, Lagrangian-Eulerian finite Volume, Classical and non-classical solutions with applications.

Abstract. *We construct a simple numerical scheme for solving nonlinear hyperbolic conservation laws problems by means of a Lagrangian-Eulerian approach. The new scheme is based on a reformulation of the hyperbolic conservation law in terms of an equivalent locally conservative space-time in divergence form. The reformulation is exact in the sense that it respects the same fundamental weak form principle for conservation laws as well as with a natural interpretation linked to the classical finite volume framework. Our novel approach is applied to classical and nonclassical nonlinear hyperbolic – scalar and systems – of conservation laws as such for two-phase and three-phase Buckley-Leverett problems as well as to the classical inviscid Burgers equation and to the classical 2 by 2 system of nonlinear shallow water equations.*

1 Introduction

In this work we are interested in the construction and implementation of a simple numerical scheme for solving nonlinear hyperbolic conservation laws problems by means of a Lagrangian-Eulerian approach.

In the work [11] was identified the region in the space-time domain where the mass conservation takes place, but linked to a scalar convection-dominated nonlinear parabolic problem, which models the immiscible incompressible two-phase flow in a porous medium. The key ingredient to finding this conservative region was the use of a Lagrangian-Eulerian framework. Later on, in a sequel paper [5] – see also [6] and the references cited therein – the same authors discussed a formal presentation without rigorous mathematical convergence proofs – of a new type of Lagrangian formulation, named Forward Integral Tube Tracking, to the case of purely linear hyperbolic radionuclide transport problems, in which turn the space-time integral curves coincide with characteristic equations. A similar, but distinct approach, can be found in [7, 15].

On the other hand, more recently in [2, 1], such ideas were extend to nonlinear purely hyperbolic conservation laws and balance laws – scalar and systems. In particular, a convergence proof for the uniqueness of the entropy solution was constructed with the aid of integral tubes by a Lagrangian-Eulerian procedure for hyperbolic conservation laws in one-space dimension to the case of convex flux. Furthermore, convergence proofs for linear hyperbolic and balance law problems were also performed in the context of the Lax equivalence theorem for linear, inhomogeneous equations in ℓ^2 spaces. This means that such Lagrangian approach provides a alternative way to find very accurate approximation for pure advection (hyperbolic) nonlinear problems and balance law problems, both relevant class for applications [17, 13]; see also [21, 22, 16, 14, 11, 19, 8, 5, 6].

We will explore the above mentioned innovative ideas in order to give a formal construction of high order Lagrangian-Eulerian schemes – in conservative form – to account the balance between the numerical approximations of the hyperbolic flux function linked to nonlinear character of classical and non-classical solutions with applications. Our new Lagrangian-Eulerian scheme is aimed to be not dependent of a particular structure of the flux function nor dependent of local Riemann problem solutions. Numerical experiments for nonlinear hyperbolic problems – scalar and system – are presented and discussed in order to contribute to the presentation of the Lagrangian-Eulerian approach as well as to the behavior and applicability to the underlying scheme in a comparison with accurate approximate solutions or exact solutions when-

ever possible.

The rest of the work is organized as follows. The Lagrangian-Eulerian framework for solving purely nonlinear hyperbolic conservation laws is presented and discussed in Section 2. A set of representative numerical experiment studies with applications are discussed in Section 3, along with our concluding remarks in the final Section 4.

2 A Lagrangian-Eulerian constructive approximation scheme for nonlinear hyperbolic conservation laws

We provide a formal development of the analogue Lagrangian-Eulerian scheme [2, 1] – see also the works [11, 5, 6] – for solving numerically first-order hyperbolic equations in divergence form for $x \in \mathbb{R}, t > 0$:

$$\frac{\partial w}{\partial t} + \frac{\partial H(w)}{\partial x} = 0, \quad u(x, 0) = \eta(x). \quad (1)$$

In this work, our primary interest is to give a formal construction of the new method, but without establishing a locally cell entropy inequality and thus a rigorous convergence proof to the corresponding weak form of the entropy inequality to the corresponding conservation law. We expect to address this very relevant issue further later on. As in the Lagrangian-Eulerian schemes [11, 5, 6, 2, 1], local conservation is obtained by integrating the conservation law over “integral tubes”, the region in the space-time domain where the conservation of the mass flux takes place. Thus, we consider the Lagrangian-Eulerian finite-volume cell centers $D_j = \{(t, x) / t^n \leq t \leq t^{n+1}, \sigma_j(t) \leq x \leq \sigma_{j+1}(t)\}$ where $\sigma_j(t)$ is a parameterized curve such that $\sigma_j(t)$ is solution of following system of ODEs, with given initial conditions $\sigma_j(t^n) = x_j^n$,

$$\frac{d\sigma_j(t)}{dt} = \frac{H(u)}{u}, \quad \text{under a CFL condition to be defined.} \quad (2)$$

Next, from (1) and the divergence theorem, and using the fact that the line integrals over curves $\sigma_j^n(t)$ vanish, we get:

$$\int_{\bar{x}_{j-\frac{1}{2}}^{n+1}}^{\bar{x}_{j+\frac{1}{2}}^{n+1}} u(x, t^{n+1}) dx = \int_{x_j^n}^{x_{j+1}^n} u(x, t^n) dx. \quad (3)$$

We essentially mimic the procedures of the linear case [5, 6, 2, 1], but now notice that the curves $\sigma_j^n(t)$ are not straight lines, in general, but rather solutions of the set of nonlinear (local) differential system of equations: $\frac{d\sigma_j^n(t)}{dt} = \frac{H(u)}{u}$,

for $t^n < t \leq t^{n+1}$, with the initial condition $\sigma_j^n(t^n) = x_j^n$, assuming $u \neq 0$ (for the sake of presentation). The extension of construction follows naturally from the finite volume formulation of the linear Lagrangian-Eulerian scheme as building block to construct *local* approximations such as $f_j^n = \frac{H(U_j^n)}{U_j^n} \approx \frac{H(u)}{u}$ with the initial condition $\sigma_j^n(t^n) = x_j^n$. As in [20], we discuss a reconstruction from a piecewise constant numerical data, a piecewise linear approximation, through the use of MUSCL-type interpolants:

$$L_j(x, t) = u_j(t) + (x - x_j) \frac{1}{\Delta x} u'_j. \quad (4)$$

For the numerical derivative $\frac{1}{\Delta x} u'_j$ we shall discuss a few examples of slope limiters, which will retain the desired properties of consistency of the numerical flux function. There are several choices of slope limiters; in book [17] there is a good compilation of many options; a priori choice of such slope limiters is quite hard, but they are chosen upon the underlying model problem under investigation. Here we make use of the following three options. The first is,

$$U'_j = MM \left\{ \Delta u_{j+\frac{1}{2}}, \Delta u_{j-\frac{1}{2}} \right\}, \quad (5)$$

where MM stands for the usual limiter [17, 20], with $\Delta u_{j+\frac{1}{2}} = u_{j+1} - u_j$,

$$MM\{\sigma, \tau\} = \text{MinMod}\{\sigma, \tau\} = \frac{1}{2} [\text{sgn}(\sigma) + \text{sgn}(\tau)] \min\{|\sigma|, |\tau|\}. \quad (6)$$

We can also use the following choice, which allows steeper slopes near discontinuities and retain accuracy in smooth regions, given by,

$$U'_j = MM \left\{ \alpha \Delta u_{j+\frac{1}{2}}, \frac{1}{2}(u_{j+1} - u_{j-1}), \alpha \Delta u_{j-\frac{1}{2}} \right\}, \quad (7)$$

The range of the parameter α is typically guided by the CFL condition [20]. In this work we also makes use of the following choice high order slope limiter, namely, the UNO choice (where $\Delta^2 u_j = u_{j+1} - 2u_j + u_{j-1}$),

$$U'_j = MM \left\{ \Delta u_{j-\frac{1}{2}} + \delta^2(u_{j-1}, u_j), \Delta u_{j-\frac{1}{2}} + \delta^2(u_j, u_{j+1}) \right\}, \quad (8)$$

where $\delta^2(u_j, u_{j+1}) = \frac{1}{2} MM(\Delta^2 u_j, \Delta^2 u_{j+1})$. Preliminary experiments discussed in Section 3 have shown that the UNO option has resulted in more satisfactory approximations for our test cases. The discrete version of equation (3), using the piecewise linear approximation above, is

$$\bar{U}_j^{n+1} = \frac{1}{h_j^{n+1}} \frac{1}{2} h (U_j^n + U_{j+1}^n) + \frac{1}{h_j^{n+1}} \frac{1}{16} h (U_j'^n - U_{j+1}'^n). \quad (9)$$

We also introduce a predictor-corrector approximation, by evaluating $f_j^{n+\frac{1}{2}}$, instead of f_j^n using Taylor expansion and the conservation law, and it reads,

$$U_j^{n+\frac{1}{2}} = u(x_j, t + \frac{\Delta t}{2}) = u_j(t) - \frac{1}{2} \frac{\Delta t}{\Delta x} H'_j, \quad (10)$$

so that $f_j^{n+\frac{1}{2}} = \frac{H(U_j^{n+\frac{1}{2}})}{U_j^{n+\frac{1}{2}}}$. Now, the solutions $\sigma_j^n(t)$ of the differential system equations are (local) straight lines, but they are not parallel as in the linear case, but subject to a CFL stability condition of the form [2, 1],

$$\max_j \left| \frac{f_j \Delta t^n}{h} \right| \leq \frac{\sqrt{2}}{2} \text{ and } k^n = \min_n \Delta t^n. \quad (11)$$

The projection coefficients [2, 1] are as follows $c_{0j} = \frac{h}{2} + f_j^{n+\frac{1}{2}} k^n$ and $c_{1j} = \frac{h}{2} - f_j^{n+\frac{1}{2}} k^n$, along with the resulting projection formula,

$$U_j^{n+1} = \frac{1}{h} c_{0j} \bar{U}_{j-1} + \frac{1}{h} c_{1j} \bar{U}_j. \quad (12)$$

Combining (12) with the discrete version of local conservation (9) reads,

$$\begin{aligned} U_j^{n+1} = & \left[\frac{c_0}{2h_j^{n+1}} (U_{j-1}^n + U_j^n) + \frac{c_0}{16h_j^{n+1}} (U_{j-1}'^n - U_j'^n) \right] \\ & + \left[\frac{c_1}{2h_j^{n+1}} (U_j^n + U_{j+1}^n) + \frac{c_1}{16h_j^{n+1}} (U_j'^n - U_{j+1}'^n) \right]. \end{aligned} \quad (13)$$

Notice, for each $j \in Z$, $h_j^{n+1} = \bar{x}_{j+\frac{1}{2}}^{n+1} - \bar{x}_{j-\frac{1}{2}}^{n+1} = x_{j+1}^n + f_{j+1}^{n+\frac{1}{2}} k^n - (x_j^n + f_j^{n+\frac{1}{2}} k^n) = h + (f_{j+1}^{n+\frac{1}{2}} - f_j^{n+\frac{1}{2}}) k^n$, and, also that: $h_j^{n+1} = c_{0j+1} + c_{1j}$. Thus,

$$c_{0j} = h_{j-1}^{n+1} - c_{1j-1} \quad \text{and} \quad c_{1j} = h_j^{n+1} - c_{0j+1}, \quad \text{with} \quad (14)$$

$$c_{1j-1} = \frac{1}{2} (h_{j-1}^{n+1} - f_{j-1}^{n+\frac{1}{2}} k^n - f_j^{n+\frac{1}{2}} k^n), \quad c_{0j+1} = \frac{1}{2} (h_j^{n+1} + f_j^{n+\frac{1}{2}} k^n + f_{j+1}^{n+\frac{1}{2}} k^n).$$

Finally, plugging (14) into (13) reads, $U_j^{n+1} =$

$$\begin{aligned} &= \frac{U_{j-1}^n + 2U_j^n + U_{j+1}^n}{4} + \frac{U_{j-1}'^n - U_{j+1}'^n}{32} \\ &+ \frac{k^n}{4} \left(\frac{f_{j-1}^{n+\frac{1}{2}} + f_j^{n+\frac{1}{2}}}{h_{j-1}^{n+1}} [U_{j-1}^n + U_j^n] - \frac{f_j^{n+\frac{1}{2}} + f_{j+1}^{n+\frac{1}{2}}}{h_j^{n+1}} [U_j^n + U_{j+1}^n] \right) \\ &+ \frac{k^n}{32} \left(\frac{f_{j-1}^{n+\frac{1}{2}} + f_j^{n+\frac{1}{2}}}{h_{j-1}^{n+1}} [U_{j-1}'^n - U_j'^n] - \frac{f_j^{n+\frac{1}{2}} + f_{j+1}^{n+\frac{1}{2}}}{h_j^{n+1}} [U_j'^n - U_{j+1}'^n] \right). \end{aligned} \quad (15)$$

The analogue finite difference scheme (15) is a *modified Lagrangian-Eulerian scheme* for the nonlinear problem (1). The scheme (15) can also be written in a conservative form (this is a novelty for Lagrangian-Eulerian schemes),

$$U_j^{n+1} = U_j^n - \frac{k^n}{h} [F(U_j, U_{j+1}^n) - F(U_{j-1}^n, U_j^n)], \quad (16)$$

with the *Lagrangian-Eulerian numerical flux functions* defined by

$$\begin{aligned} F(U_j^n, U_{j+1}^n) &= G(U_j^n, U_{j+1}^n) - \\ &\frac{1}{k^n} \left[\left(\frac{h}{2} - \Delta t f_j^{n+\frac{1}{2}} \right) \frac{h}{2h_j^{n+1}} \left(\frac{h}{2} (U_j' + U_{j+1}') \right) \right]. \end{aligned} \quad (17)$$

$$\begin{aligned} F(U_{j-1}^n, U_j^n) &= G(U_{j-1}^n, U_j^n) + \\ &\frac{1}{k^n} \left[\left(\frac{h}{2} + \Delta t f_j^{n+\frac{1}{2}} \right) \frac{h}{2h_{j-1}^{n+1}} \left(\frac{h}{2} (U_{j-1}' + U_j') \right) \right]. \end{aligned} \quad (18)$$

where $U = (U_j^n, U_{j+1}^n)$, along with,

$$G(U) = \frac{1}{4} \left[\frac{h}{k^n} (U_j^n - U_{j+1}^n) + \frac{h}{h_j^{n+1}} \left(f_{j+1}^{n+\frac{1}{2}} + f_j^{n+\frac{1}{2}} \right) (U_{j+1}^n + U_j^n) \right]. \quad (19)$$

We will show in what follows that the Lagrangian-Eulerian numerical flux functions (17)-(18) satisfy a form of *Lipschitz continuous consistency*, which in turn is a nice property for *conservative numerical methods* for nonlinear conservation law problems. Indeed, to show that the Lagrangian-Eulerian numerical flux satisfies a Lipschitz condition, we need (see [2]):

Theorem 2.1 *The pair of numerical flux functions defined by (17)-(18) are consistent with the differential equation (1).*

Proof. Immediate, i.e., $F(\bar{u}, \bar{u}) = H(u)$. Notice that for any choice of slope limiters, we have from (6) that (17) and (18) both satisfy the consistency condition, since $MM(u, u) = 0$. The Lipschitz condition can also be proved by using the results in [2].

3 Numerical experiment studies with applications

We first present a mesh refinement study in order to give some numerical evidence of convergence for the proposed scheme. Next, some computations for scalar and nonlinear system with convex and non-convex flux functions are presented and discussed, as those modeling the shallow water equations and two-phase and three-phase flows in porous media for one-dimensional problems.

3.1 Convex and non-convex flux functions for conservation laws

For a first mesh refinement study we test our scheme with a non-convex flux function to the scalar conservation law $u_t + f_x(u) = 0$, for $f(u) = 0.5(e^{-25(u-0.5)^2} + 8(u-0.5)^2)$, along with Riemann initial data (left) $u(x, 0) \equiv \eta(x) = 0.8$, $x < 0$ and $u(x, 0) \equiv \eta(x) = 0.2$, $x > 0$. In Figure 1 is shown four different mesh grid cells (64, 128, 256 and 512) against a reference numerical solution with 1024 mesh grid cells.

In Figure 2 it is shown numerical solutions for $u_t + \left(\frac{u^2}{2}\right)_x = 0$, along with smooth initial data $u(x, 0) = 0.5 + \sin(x)$ on the left. It is well-known the solution of this problem develops a shock discontinuity at the critical time $T_c = 1$, and then it exhibits pre-shock (resp. post-shock) solution for $T_c < 1$ (resp. $T_c > 1$); on the left it is shown the post-shock solution computed with (16)-(18) at time simulation $t = 2$ for 256 cells. We have also conducted similar numerical experiments to problem $u_t + \left(\frac{u^2}{2}\right)_x = 0$ along with discontinuous initial data $u(x, 0) = 1$, $x < 0$ & $u(x, 0) = 0$, $x > 0$ (middle: shock) and $u(x, 0) = 0$, $x > 0$ & $u(x, 0) = 0$, $x > 1$ (right: rarefaction). On these frames are shown snapshot graphs at time $t = 2.4$ of simulation, with waves moving from left to right. We get a very nice looking numerical approximate solution with scheme (16)-(18), which in turn seems to be propagating at entirely entropy-correct Rankine-Hugoniot speed (middle). Similar good results are shown to the rarefaction case as well.

We now turn attention to the classical nonlinear one-dimensional Buckley-Leverett two-phase problem [18, 17], which in turn is depicted in left picture in Figure 3. Computed solutions with scheme (16)-(18) at time simulation $t = 2$ are shown to the Riemann Problem (Initial Value Problem with non-

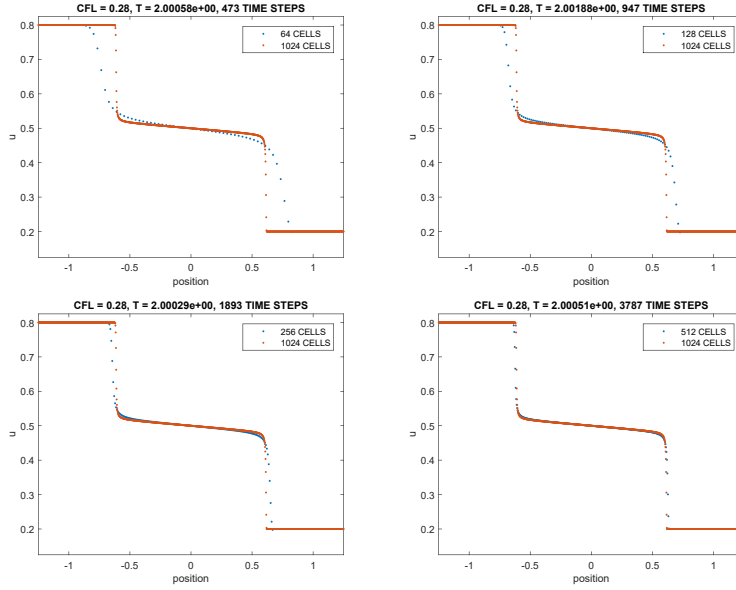


Figure 1: Mesh refinement study for a non-convex flux function. The finest mesh in this case is a solution with 1024 mesh grid cells.

convex flux function): $u_t + f_x(u) = 0$, $f(u) = u^2/(u^2) + a(1-u)^2$, $a = 1$, along with Riemann initial data (left) $u(x,0) \equiv \eta(x) = 1.0$, $x < 0$ and $u(x,0) \equiv \eta(x) = 0.0$, $x > 0$. On physical ground, such initial data corresponds to water flooding of an oil reservoir. The well known solution for this model comprises a leading shock wave (an oil bank) followed by an attached rarefaction wave. The weak solution satisfying the Oleinik entropy condition is in very good agreement along with the scheme (16)-(18) propagating at entirely entropy-correct Rankine-Hugoniot speed and with the precisely post-shock value. We have also considered another non-convex flux function (see right picture in Figure 3) to the scalar conservation law $u_t + f_x(u) = 0$, with $f(u) = 0.5(e^{-25(u-0.5)^2} + 8(u-0.5)^2)$, along with Riemann initial data (left) $u(x,0) \equiv \eta(x) = 0.8$, $x < 0$ and $u(x,0) \equiv \eta(x) = 0.2$, $x > 0$. Again, the numerical solution is in agreement with Oleinik entropy condition, whose approximate left and right shock waves are propagating with correct Rankine-Hugoniot speed and entropy-correct post-shock values.

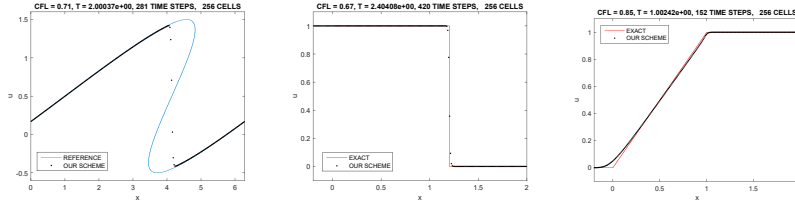


Figure 2: Inviscid nonlinear Burgers' problem: pre-shock and post-shock solutions computed by scheme (16)-(18).

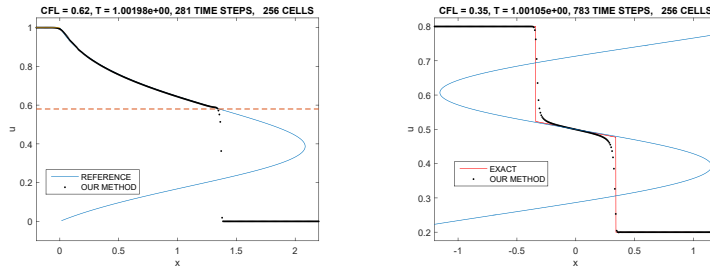


Figure 3: Left: Classical one-dimensional Buckley-Leverett two-phase problem computed by scheme (16)-(18). Right: A non-convex flux function.

3.2 Shallow water equations; Langseth, Tveito, and Winther [16]

It is well-known that solutions of the balance law (20), and likewise, solutions of the counterpart hyperbolic conservation law, i.e. Eq. (20) with the source term on the r.h.s equal to zero, can develop shock discontinuities in a finite time, independent of whether the initial data is smooth or not (as we consider here). Hence, the solutions of balance laws, or hyperbolic conservation laws, must be viewed in the weak sense and in particular are well-defined as long as the sources remains uniformly bounded.

In [16], it was considered a 2×2 nonlinear system of balance laws in the form of (in dimensionless and scaled variables),

$$\begin{bmatrix} h \\ hv \end{bmatrix}_t + \begin{bmatrix} hv \\ v^2h + \frac{1}{2}h^2 \end{bmatrix}_x = \begin{bmatrix} 0 \\ h - C \frac{1+h}{\tan(\theta)} v^2 \end{bmatrix}, \quad (20)$$

where h is the height of the free surface and v is the averaged horizontal velocity, modeling the flow of water downing in a channel having a rectangular cross section and inclined at a constant angle θ to the horizontal. This is a prototype model for shallow-water flow (see also [14, 17] and reference therein

for more details) in an inclined channel with friction. Precisely, as in [16], the friction coefficient C is taken to be 0.1, while the inclination angle $\theta = \pi/6$. On physical grounds, in model problem it was assumed the hydrostatic balance in the vertical direction and ignored surface tension. Further, the viscous effects is approximately through the introduction of a friction force exerted of the fluid by the solid boundaries of the channel (account as a source term that appears on the RHS of (20)). Indeed, model (20) correspond to uniform flow ($v_0=\text{constant}$ and $h_0=\text{constant}$) with the frictional and gravitational forces in perfect balance. In order to study the balance between convective/source in the model (20), it is considered as initial conditions a *perturbation of a uniform flow*, in which the gravitational and frictional forces balance as expected from the model problem. As in [16], the initial velocity is taken to be $v_0 = 1.699$, while the initial height of the free surface consists of a *triangular perturbation* of the uniform flow level, $h_0(x) = x + 1.5$, $-0.5 \leq x \leq 0$, $h_0(x) = -x + 1.5$, $0 \leq x \leq 0.5$, and 1 elsewhere. In Figure 4 it is shown the numerical approximations by means of the scheme (16)-(18) along with to the initial value problem described just above.

As depicted in [16], in Figure 4 and in Figure 5 are shown numerical approximations to the shallow water equations (20) with gravity-friction source terms (on the left columns) and the associated purely counterpart shallow water equations with the source term on the r.h.s equal zero (on the right columns). The balance law shallow water solutions (with 1024 grid cells) were computed with the scheme discussed in [2, 1], while the purely hyperbolic shallow water solutions (with 512 grid cells) were compute with our new scheme introduced in this work in Section 2. In each picture displayed in Figure 4 (to the height topography) and in Figure 5 (to the velocity) are shown, from top to bottom, distinct numerical simulations, namely, at the initial time $t = 0$, $t = 0.5$, $t = 1.0$ and $t = 1.5$, and both problems subject to the same initial data previously described. As expected from the analysis [16] for both cases we have two waves moving in opposite directions. To the purely hyperbolic shallow water solutions (right pictures in Figures 4 and 5) we were able to capture this correct qualitative behavior with a very good accuracy. On the other hand, the introduction of friction not only damp down the velocity of these waves, but also changes the shape. Observe the symmetric shape of the height topography and the velocity waves (right columns in Figures 4 and 5) and the effect of friction-gravity source term to the corresponding balance law shallow water solutions of the left columns.

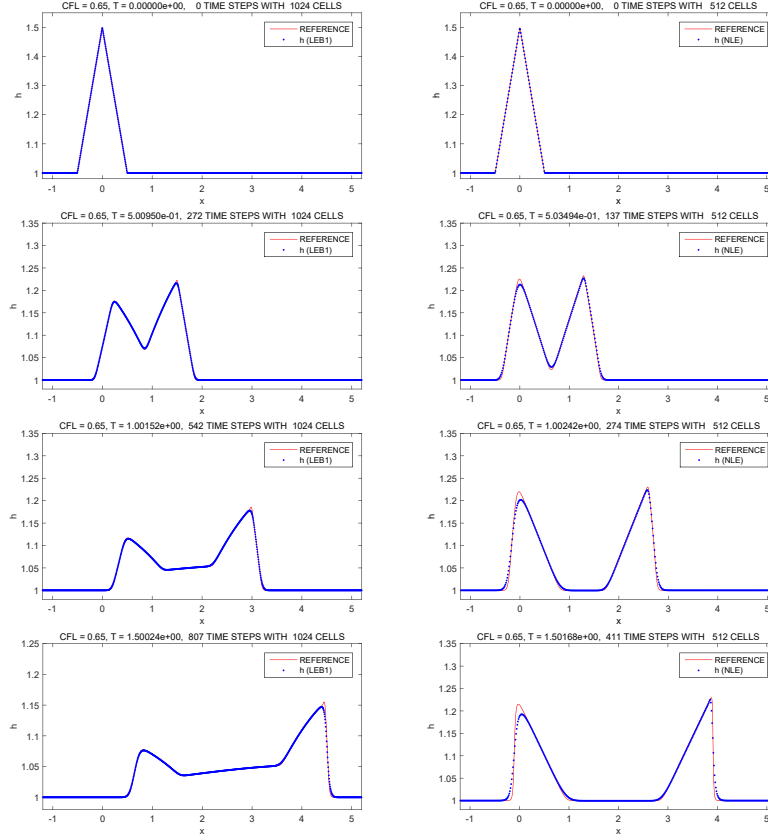


Figure 4: It is shown numerical approximations to the shallow water equations (20) with gravity-friction source terms (on the left columns) and the associated purely counterpart shallow water equations with the source term on the r.h.s equal zero (on the right columns). The numerical solutions to the height topography are shown from top to bottom at simulation times $t = 0$, $t = 0.5$, $t = 1.0$ and $t = 1.5$. As expected from the analysis [16], we were able to compute the correct qualitative behavior with a very good accuracy, along with our new method introduced in Section 2.

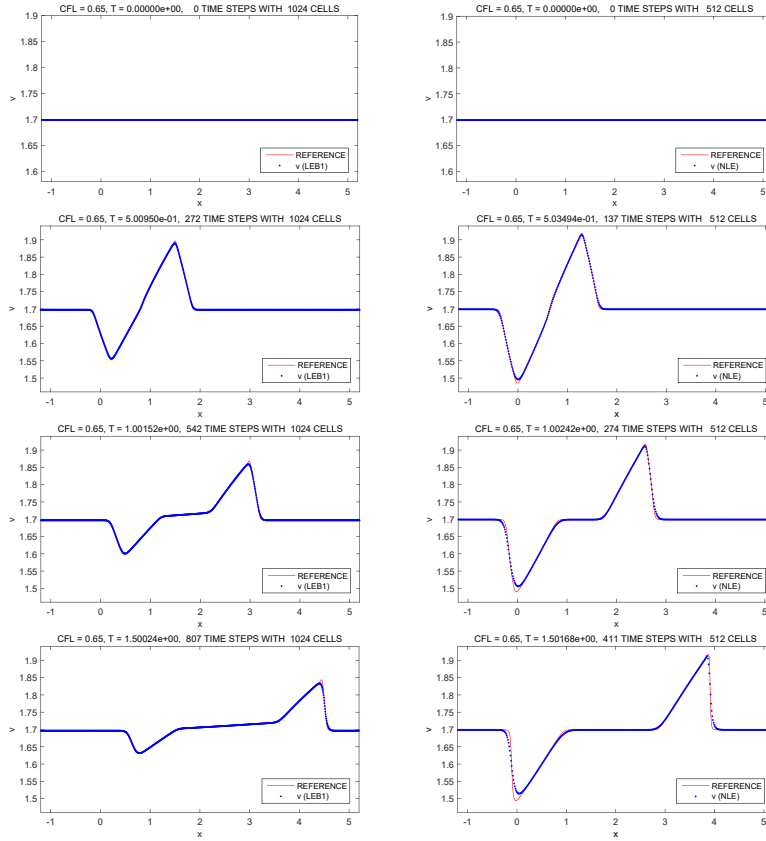


Figure 5: It is shown the corresponding numerical approximations to the shallow water equations with respect to those displayed in Figure (4), but with respect to the velocity variable.

3.3 Non-strictly hyperbolic three-phase system of conservation laws in porous media applications

First, let us briefly review a immiscible incompressible three-phase formulation for porous media [19, 3, 8, 22, 21]. In this formulation the governing equations are written in terms of a pressure, expressing Darcy's law of force, coupled to two saturation equations that express the conservation of mass of water, oil and gas (we refer the reader to [8] for the derivation of this formulation). In one dimension the pressure equation implies that the total fluid velocity is independent of position, so we take it to be constant. After nondimensionalizing the time (we suppose the porosity to be a constant) and space variables, fluid viscosities, and capillary pressures in the standard way, one obtains the following system of partial differential equations [3, 4, 9]:

$$\frac{\partial s_w}{\partial t} + \frac{\partial}{\partial x} f_w(s_w, s_g) = \frac{\partial w_w}{\partial x}, \quad (21)$$

$$\frac{\partial s_g}{\partial t} + \frac{\partial}{\partial x} f_g(s_w, s_g) = \frac{\partial w_g}{\partial x}, \quad (22)$$

where

$$w_w = \left[B_{11} \frac{\partial s_w}{\partial x} + B_{12} \frac{\partial s_g}{\partial x} \right], \quad (23)$$

and

$$w_g = \left[B_{21} \frac{\partial s_w}{\partial x} + B_{22} \frac{\partial s_g}{\partial x} \right]. \quad (24)$$

In the fluxes w_w and w_g introduced above B_{11} , B_{12} , B_{21} and B_{22} are the entries of the matrix

$$B(s_w, s_g) = Q(s_w, s_g) P'(s_w, s_g), \quad (25)$$

where

$$Q = \begin{bmatrix} \lambda_w(1 - f_w) & -\lambda_w f_g \\ -\lambda_g f_w & \lambda_g(1 - f_g) \end{bmatrix}, \quad P' = \begin{bmatrix} \frac{\partial p_{wo}}{\partial s_w} & \frac{\partial p_{wo}}{\partial s_g} \\ \frac{\partial p_{go}}{\partial s_w} & \frac{\partial p_{go}}{\partial s_g} \end{bmatrix}. \quad (26)$$

Here, λ_i is the relative permeability, $\lambda = \sum_i \lambda_i$ is the total mobility and $f_i(s_w, s_g) = \lambda_i/\lambda$ are the fractional flow functions. Given the constraint $s_w + s_g + s_o = 1$, any pair of saturations inside the triangle of saturations $\Delta := \{(s_w, s_g) : s_w, s_g \geq 0, s_w + s_g \leq 1\}$ can be chosen to describe the

state of the fluid. In our model we chose, for convenience, to work with the saturations of water and gas. The diffusive term is represented by the right-hand side of the system (21)-(22) and it incorporates the capillary pressure effects. We neglect the diffusive effect, by just taking $w_w = 0$ and $w_g = 0$ in (21)-26, but we do know from [19, 3, 4] how is the correct structure of the solutions of the non-classical three-phase model under consideration. However, we point out that for a wave to be truly defined as a “shock wave”, a discontinuity must be the zero-diffusion limit of traveling wave solutions. For such solutions, diffusion balances the convergence of waves caused by hyperbolic nonlinearity. Moreover, the set of non-classical wave solutions obtained in the zero-diffusion (zero-capillarity) limit might depend sensitively on the form of the diffusion matrix and not only on the hyperbolic structure of the equations; see [19] and the references cited therein for further technical details.

3.3.1 Numerical Experiments

We present the results of numerical grid refinement studies for the simulation of two Riemann problems, namely RP_1 and RP_2 , given by:

$$RP_1 = \begin{cases} s_w^L = 0.613 & \text{and} & s_w^R = 0.05, \\ s_g^L = 0.387 & \text{and} & s_g^R = 0.15, \end{cases} \quad (27)$$

and

$$RP_2 = \begin{cases} s_w^L = 0.721 & \text{and} & s_w^R = 0.05, \\ s_g^L = 0.279 & \text{and} & s_g^R = 0.15. \end{cases} \quad (28)$$

We use the quadratic model by Corey-Pope [10, 12], which has been used extensively for phase relative permeabilities,

$$k_w = s_w^2, \quad k_o = s_o^2 \quad \text{and} \quad k_g = s_g^2. \quad (29)$$

As is [19, 3, 4], we consider the following viscosity values $\mu_o = 1.0$, $\mu_w = 0.5$, and $\mu_g = 0.3$. From the analysis discussed in [19], we remark that for the choice of parameters described above, a transitional shock wave is present in the solution of (28), which in turn is not present in the solution of (27).

Since the oil phase saturation can be directly obtained from the other two phase saturations (i.e., $s_o = 1 - s_w - s_g$), we display the oil saturation profile in Figure 7, showing the effect of a grid refinement in the numerical solution of (21)-(22) – $w_w = 0$ and $w_g = 0$ – with Riemann data (27) on the left and (28) on the right. The computed saturation profiles are shown at dimensionless time

2.50. In each frame we compare numerical solutions obtained on grids having 128, 256, 512 and 1024 cells against a reference numerical solution of 2048 cells. It is clear from the pictures in Figure 7, that as the grid is refined we have some good evidence of numerical convergence of our scheme. We remark that the numerical solutions presented here are in very good agreement with the semi-analytic results reported in [19], yielding a numerical verification of our computations.

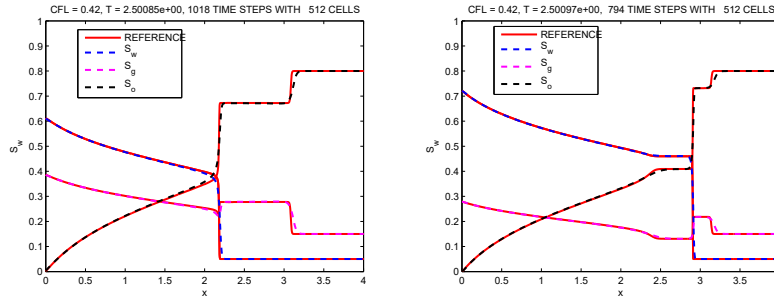


Figure 6: Oil, water and gas saturation profiles are shown as a function of distance. RP_1 on the left and RP_2 on the right.

We now show numerical experiments concerning the three-phase flow problem (21)-(22) – $w_w = 0$ and $w_g = 0$ and with Riemann data (27) on the left and (28) on the right – in order to show that our scheme is able to capture analytical properties of the wave structures, as originally introduced in [19]; see also [4, 3] and the references cited therein. For completeness we describe the non-classical solution. Right picture in Figure 6: the slow wave group comprises a strong slow rarefaction fan from left (injection) state to the post-shock value and an adjoining slow front wave from the post-shock value to the first plateau. The fast wave group is a Buckley-Leverett front wave from the second plateau. Between the slow and fast wave groups is a non-classical front wave. For the classical solution, we have only the slow and fast wave groups (Left picture in Figure 6). We point out that in both numerical solutions the plateau are located in the correct heights, with respect to the semi-analytical solutions presented in [19].

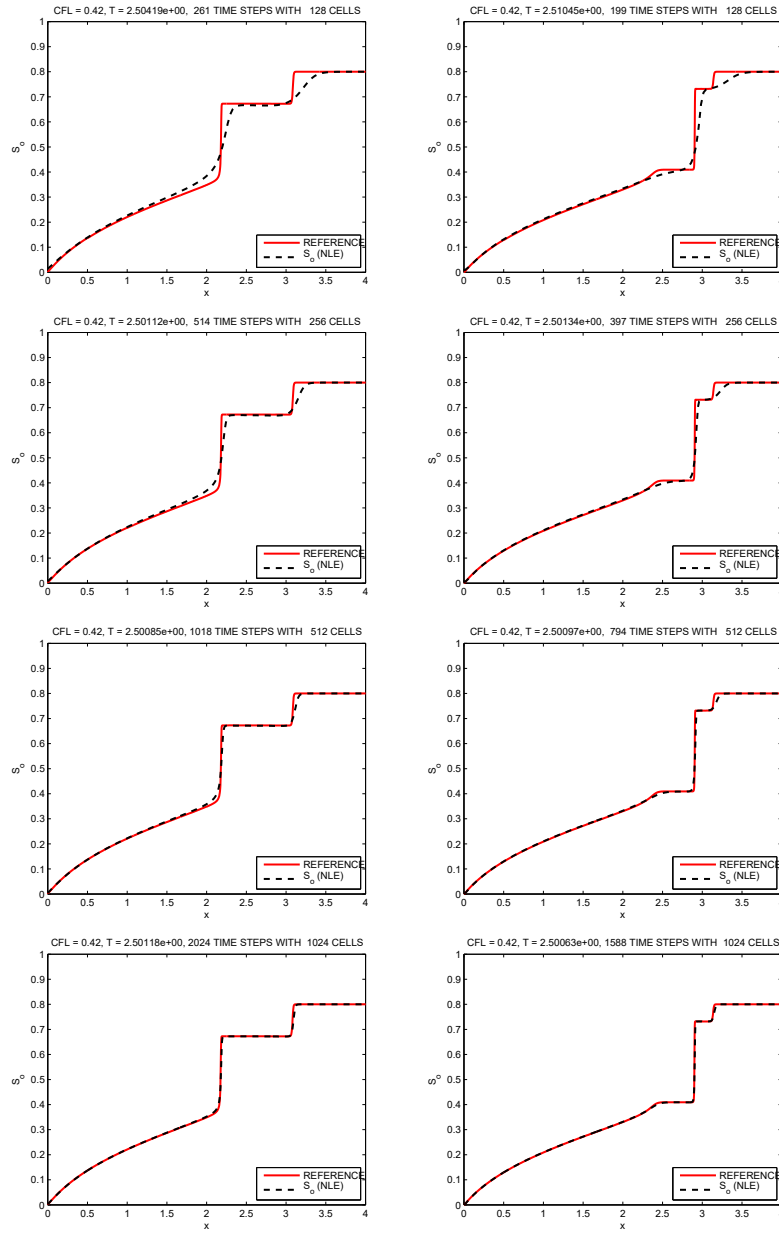


Figure 7: Grid refinement study. Oil saturation profiles are shown as a function of distance. RP_1 on the left and RP_2 on the right.

4 Concluding Remarks

In the present work, we constructed an effective numerical scheme in local conservative form for solving nonlinear hyperbolic conservation laws problems – scalar and systems – by means of a novel Lagrangian-Eulerian approach. This method is based on a reformulation of the conservation laws in terms of an equivalent locally conservative space-time divergence form problem. We make use of piecewise linear reconstructions ideas along with a predictor-corrector type approximations for improvements of the computed numerical solutions. We presented and discussed classical and non-classical qualitatively correct numerical solutions for nonlinear hyperbolic conservation laws: the two-phase and three-phase Buckley-Leverett problems, the classical inviscid Burgers equation and the 2 by 2 system of nonlinear shallow water model problem. Our preliminary numerical experiments show a very good evidence of computational convergence of our new Lagrangian-Eulerian scheme in conservative form. We point out that our focus in this work was to give a formal construction of the new method. However, we are aware of the importance in establish a local cell entropy inequality, and thus a rigorous convergence proof to the corresponding weak form of the entropy inequality with respect to the conservation law under investigation, at least in the scalar case.

Finally, we expect to establish a componentwise extension of the scheme in order to perform numerical experiments for multidimensional problems, which in turn might lead to nonlinear problems along with discontinuous flux functions associated to heterogeneous porous media systems. We expect to address those very relevant issues further later on.

E. Abreu thanks for financial support through grants FAPESP No. 2014/03204-9, FAPESP No. 2011/23628-0, CNPq No. 445758/2014-7 and UNICAMP /FAEPEX No. 519.292-0280/2014. J. Perez and A. Santo thanks, respectively, CAPES-IMECC/UNICAMP and CNPq-IMECC/UNICAMP for a graduate fellowship.

REFERENCES

- [1] E. Abreu, J. Perez. Numerical study of a Eulerian-Lagrangian formulation applied to balance laws and conservation laws (submitted).
- [2] E. Abreu, J. Perez. A Lagrangian-Eulerian algorithm for solving hyperbolic problems and balance laws, Numerical study of a Eulerian-Lagrangian formulation applied to balance laws and conservation laws.

- 15th International Conference: Theory, Numerics and Applications of Hyperbolic Problems 2014, Rio de Janeiro/IMPA (submitted).
- [3] E. Abreu. Numerical modelling of three-phase immiscible flow in heterogeneous porous media with gravitational effects, *Mathematics and Computers in Simulation* 97 (2014) 234–259.
 - [4] E. Abreu, F. Furtado, F. Pereira. On the numerical simulation of three-phase reservoir transport problems, *Transport Theory and Statistical Physics* 33 (2004) 503–526.
 - [5] J. Aquino, F. Pereira, H. P. Amaral Souto, A. S. Francisco. A forward tracking scheme for solving radionuclide advective problems in unsaturated porous media, *Int. J. of Nuclear Energy Science and Technology* 3(2) (2007) 196–205.
 - [6] J. Aquino, A. S. Francisco, F. Pereira, T. Jordem Pereira, H. P. Amaral Souto. A Lagrangian strategy for the numerical simulation of radionuclide transport problems, *Progress in Nuclear Energy* 52 (2010) 282–291.
 - [7] T. Arbogast, C. S. Huang, T. F. Russell. A Locally Conservative Eulerian-Lagrangian Method for a Model Two-Phase Flow Problem in a One-Dimensional Porous Medium, *SIAM J. Sci. Comput.* 34(4) (2012) 1950–1974.
 - [8] G. Chavent, J. Jaffré. Mathematical models and finite elements for reservoir simulation, *Stud. Math. Appl.* Vol. 17, North-Holland, Amsterdam, 1986.
 - [9] Z. Chen, R. Ewing. Comparison of various formulations of three-phase flows in porous media, *Journal of Computational Physics* 132 (1997) 362–373.
 - [10] A. Corey, C. Rathjens, J. Henderson, M. Wyllie. Three-phase relative permeability, *Trans. AIME* 207 (1956) 349–351.
 - [11] J. Douglas, F. Pereira, L. M. Yeh. A locally conservative Eulerian-Lagrangian numerical method and its application to nonlinear transport in porous media, *Computational Geosciences* 4 (2000) 1–40.
 - [12] D. E. Dria, G. A. Pope, K. Sepehrnoori. Three-phase gas/oil/brine relative permeabilities measured under CO_2 flooding conditions, *Society of Petroleum Engineers, SPE* 20184 (1993) 143–150.

- [13] L. Gosse. Computing qualitatively correct approximations of balance laws exponential-fit, well-balanced and asymptotic-preserving, SIMAI Springer Series vol 2, 2013.
- [14] J. M. Greenberg, A. Y. Le Roux. A well-balanced scheme for the numerical processing of source terms in hyperbolic equations, SIAM J. Numer. Anal. 33(1) (1996) 1–16.
- [15] C. S. Huang, T. Arbogast, J. Qiu. An Eulerian-Lagrangian WENO finite volume scheme for advection problems, J. Comp. Phys. 231(11) (2012) 4028–4052.
- [16] J. O. Langseth, A. Tveito, R. Winther. On the Convergence of Operator Splitting Applied to Conservation Laws with Source Terms, SIAM J. Numer. Anal. 33(3) (1996) 843–863.
- [17] R. J. LeVeque. Finite Volume Methods for Hyperbolic Problems, Cambridge Texts in applied Mathematics, UK, 2002.
- [18] M. C. Leverett, W. B. Lewis. Steady flow of gas-oil-water mixtures through unconsolidated sands, Trans. SPE of AIME 142 (1941) 107–16.
- [19] D. Marchesin, B. J. Plohr. Wave structure in WAG recovery, Society of Petroleum Engineers SPE 56480 (1999).
- [20] H. Nessyahu, E. Tadmor. Non-oscillatory central differencing for hyperbolic conservation laws, Journal of Computational Physics 87(2) (1990) 408–463.
- [21] R. Roupert, G. Schafer, P. Ackerer, M. Quintard, G. Chavent. Construction of three-phase data to model multiphase flow in porous media: Comparing an optimization approach to the finite element approach, Comptes Rendus Geoscience 342 (2010) 855–863.
- [22] R. Roupert, G. Chavent, G. Schafer. Three-phase compressible flow in porous media: Total Differential Compatible interpolation of relative permeabilities, Journal of Computational Physics 229 (2010) 4762–4780.

Introduction

In this work we are concerned with the construction and implementation of a Lagrangian-Eulerian method for solving nonlinear hyperbolic conservation laws. We used innovative ideas, first introduced in [5] (see also [1, 6]), to account the balance between numerical approximations of the hyperbolic flux function linked to the underlying nonlinear solutions. Such ideas were used for solving the shallow-water equations [2] and the three-phase flow problem in porous media [3]. We observe that the present numerical solutions are in good agreement with the analytical solutions obtained previously by other researchers [2, 3]. Our Lagrangian-Eulerian scheme is aimed to be not dependent on a particular structure of the flux function. The designed scheme is also independent of Riemann problem solutions.

The Lagrangian-Eulerian Framework

Consider the initial value problem for single conservation laws as follows:

$$\frac{\partial u}{\partial t} + \frac{\partial f(u)}{\partial x} = 0, \quad x \in \mathbb{R}, \quad t > 0 \quad (1)$$

- We consider finite-volume cell centers $D_j = \{(t, x) / t^n \leq t \leq t^{n+1}, \sigma_j(t) \leq x \leq \sigma_{j+1}(t)\}$ where $\sigma_j(t)$ is a parameterized curve such that $\sigma_j(t)$ is solution of system of ordinary differential equations $\frac{d\sigma_j(t)}{dt} = \frac{f(U_j^n)}{U_j^n} = \phi_j^n$, with initial condition $\sigma_j(t^n) = x_j^n$.
- We have from the divergence theorem, based on ideas from [5]:

$$\iint_{D_j} \nabla_{t,x} \begin{bmatrix} u \\ f(u) \end{bmatrix} dV = 0 \Leftrightarrow \oint_{\partial D_j} \begin{bmatrix} u \\ f(u) \end{bmatrix} \cdot n ds = 0 \quad (2)$$

- The parameterized curves $\sigma_j(t)$ and $\sigma_{j+1}(t)$ are the lateral zero-flux boundaries from the control volume D_j^n , which we denote as the “Integral tube”. With that, the integrals over curves $\sigma_j(t)$ vanish.
- We discuss a reconstruction from the piecewise constant numerical data into a piecewise linear approximation, through the use of MUSCL-type interpolants, the numerical derivative being approximated by slope limiters:

$$L_j(x, t) = u_j(t) + (x - x_j) \frac{1}{\Delta x} u'_j. \quad (3)$$

- We now have some type of local conservation identity from t^n to t^{n+1}

$$\bar{U}_j^{n+1} = \frac{1}{h_j^{n+1}} \frac{1}{2} h (U_j^n + U_{j+1}^n) + \frac{1}{h_j^{n+1}} \frac{1}{16} h (U_j^n - U_{j+1}^n). \quad (4)$$

- We also introduce a predictor-corrector approximation, by evaluating $\phi_j^{n+\frac{1}{2}}$, instead of ϕ_j^n using Taylor expansion and the conservation law:

$$U_j^{n+\frac{1}{2}} = u(x_j, t + \frac{\Delta t}{2}) = u_j(t) - \frac{1}{2} \frac{\Delta t}{\Delta x} f'_j, \quad (5)$$

so that $\phi_j^{n+\frac{1}{2}} = \frac{f(U_j^{n+\frac{1}{2}})}{U_j^{n+\frac{1}{2}}}$.

- We must finally project these values onto our original grid:

$$U_j^{n+1} = \frac{1}{h} \left(\frac{h}{2} - \phi_j^{n+\frac{1}{2}} k^n \right) \bar{U}_{j-1} + \frac{1}{h} \left(\frac{h}{2} + \phi_j^{n+\frac{1}{2}} k^n \right) \bar{U}_j. \quad (6)$$

Numerical experiments

We present the following set of numerical experiments, each of them performed in the order of seconds with MATLAB®:

- In Figure 1, we show numerical solutions for $u_t + \left(\frac{u^2}{2}\right)_x = 0$, along with smooth initial data $u(x, 0) = 0.5 + \sin(x)$, with discontinuous initial data $u(x, 0) = 1, x < 0$ & $u(x, 0) = 0, x > 0$ (middle: shock) and $u(x, 0) = -1, x < 0$ & $u(x, 0) = 1, x > 0$ (right: rarefaction). The transonic rarefaction (right frame) is well resolved. That is, as the rarefaction wave is crossed, there is a sign change in the characteristic speed u and thus there is one point at which $u = 0$, the sonic point. So, there is no spurious anomalies around $u = 0$.
- In Figure 2, we present the classical nonlinear one-dimensional Buckley-Leverett two-phase problem, depicted in left picture. $u_t + f_x(u) = 0$, $f(u) = u^2/(u^2 + a(1-u)^2)$, $a = 1$, along with Riemann initial data (left) $u(x, 0) \equiv \eta(x) = 1.0, x < 0$ and $u(x, 0) \equiv \eta(x) = 0.0, x > 0$.
- We have also considered another non-convex flux function (right picture in Figure 2) to the scalar conservation law $u_t + f_x(u) = 0$, with $f(u) = 0.5(e^{-25(u-0.5)^2} + 8(u-0.5)^2)$, along with Riemann initial data (left) $u(x, 0) \equiv \eta(x) = 0.8, x < 0$ and $u(x, 0) \equiv \eta(x) = 0.2, x > 0$.

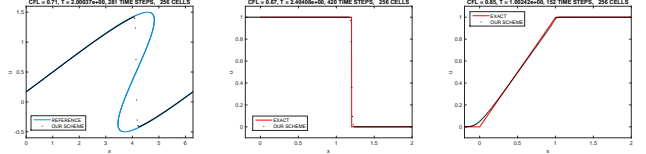


Figure 1: Inviscid nonlinear Burgers' problem: pre-shock and post-shock solutions.

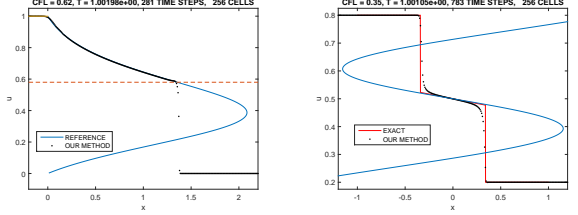


Figure 2: Left: Classical one-dimensional Buckley-Leverett two-phase. Right: A non-convex flux function.

For the systems case, we show a three-phase formulation for porous media [3]

$$\frac{\partial s_w}{\partial t} + \frac{\partial f_w(s_w, s_g)}{\partial x} = \frac{\partial w_w}{\partial x}, \quad (7)$$

$$\frac{\partial s_g}{\partial t} + \frac{\partial f_g(s_w, s_g)}{\partial x} = \frac{\partial w_g}{\partial x}, \quad (8)$$

where w_w and w_g are here the diffusive fluxes that incorporate capillary effects and f_w, f_g are Buckley-Leverett-type fractional flow functions. We neglect the capillary diffusive effect, by just taking $w_w = 0$ and $w_g = 0$ in (7), but we do know from [3] how is the correct structure of the solutions of the non-classical three-phase model under consideration. We simulate two Riemann problems, namely RP_1 and RP_2 , given by:

$$RP_1: \begin{cases} s_w^L = 0.613 \text{ and } s_w^R = 0.05, \\ s_g^L = 0.387 \text{ and } s_g^R = 0.15, \end{cases} \quad RP_2: \begin{cases} s_w^L = 0.721 \text{ and } s_w^R = 0.05, \\ s_g^L = 0.279 \text{ and } s_g^R = 0.15. \end{cases} \quad (9)$$

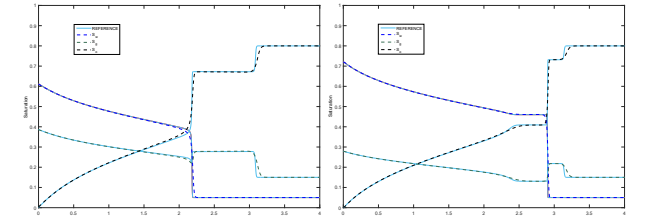


Figure 3: Oil, water and gas saturation profiles are shown as a function of distance. RP_1 on the left and RP_2 on the right.

Conclusions

We constructed an efficient numerical scheme in local conservative form for solving nonlinear hyperbolic conservation laws – both for the scalar case and for systems of equations – using a novel Lagrangian-Eulerian approach. The numerical scheme was able to accurately reproduce numerical results from those reported in [3], including several others. Further studies will follow to the case of multidimensional systems of equations.

Acknowledgements: E. Abreu thanks for financial support through grants FAPESP No. 2014/03204-9 and CNPq No. 445758/2014-7. J. Pérez thanks CAPES for a pos-doc PNP/CAPES fellowship and A. Santo thanks CNPq for a graduate fellowship

References

- [1] E. Abreu, W. Lambert, J. Perez, A. Santo. (2015) A Lagrangian-Eulerian algorithm for solving hyperbolic conservation laws with applications. In Proceedings of the 6th International Conference on Approximation Methods and Numerical Modelling in Environment and Natural Resources. Pau, France 2015. Editorial Universidad de Granada (2015) 600-617
- [2] J. O. Langseth, A. Tveito, R. Winther. (1996). On the Convergence of Operator Splitting Applied to Conservation Laws with Source Terms SIAM J. Numer. Anal. 33(3) 843-863.
- [3] D. Marchesin. and B. J. Plohr. (1999). Wave structure in WAG recovery, Society of Petroleum Engineers, SPE 56480.
- [4] E. Abreu, J. Pérez, A. Santo and W. Lambert, "A new finite volume approach for transport models and related applications with balancing source terms", (Submitted).
- [5] J. Douglas, F. Pereira and L. M. Yeh. "A locally conservative Eulerian-Lagrangian numerical method and its application to nonlinear transport in porous media", Computational Geosciences, 4 (2000), 1-40.
- [6] J. A. Pérez S. Lagrangian-Eulerian approximate methods for balance laws and hyperbolic conservation law. Tese de Doutorado, University of Campinas, 2015.

Solving hyperbolic conservation laws by using Lagrangian-Eulerian approach

Eduardo Abreu¹

Institute of Mathematics, Statistics and Scientific Computing IMECC - UNICAMP, Campinas, SP
John A. Perez S.²

Facultad de Ciencias ITM Institución Universitaria, Medellín, Colombia.

Institute of Mathematics, Statistics and Scientific Computing IMECC - UNICAMP, Campinas, SP
Arthur M. E. Santo³

Institute of Mathematics, Statistics and Scientific Computing IMECC - UNICAMP, Campinas, SP

Abstract. We discuss a procedure for numerically solving nonlinear hyperbolic conservation law problems by means of a Lagrangian-Eulerian framework. The underlying hyperbolic conservation law is written in a space-time divergence form, so that inherent conservation properties of the problem are reflected in the numerical scheme. In order to enhance resolution and accuracy of the approximations, we make use of polynomial reconstruction ideas into the Lagrangian-Eulerian novel approach. Finally, numerical results are given to verify the formal construction as well as to demonstrate its accuracy, efficiency, and versatility. These results for the considered sample problems compare very well to analytical results.

Keywords. Conservation laws, Lagrangian-Eulerian, Finite Volume Methods

1 Introduction

In this work we present a numerical scheme for solving hyperbolic conservation laws by means of a Lagrangian-Eulerian approach. This framework has been used for numerically solving partial differential equations of several types, such as hyperbolic conservation laws [8, 11], balance laws problems [3, 6] and parabolic equations [4]. In the work [4], it was identified the region in the space-time domain where the mass conservation takes place, but linked to a scalar convection-dominated nonlinear parabolic problem, which models the immiscible incompressible two-phase flow in a porous medium [1]. Some similar developments based on Lagrangian-Eulerian framework, with focus on increasing order and accuracy of such schemes can be found in [6]. More recently in [2, 11], such ideas were extended to a wide range of nonlinear purely hyperbolic conservation laws and balance laws – scalar and systems. Our goal on the current work is to present the formal construction of an accurate Lagrangian-Eulerian scheme for hyperbolic conservation laws. Preliminary results showed qualitatively correct solutions with accurate resolution.

¹eabreu@ime.unicamp.br

²jhonperez@itm.edu.co

³arthurm@ime.unicamp.br

2 Numerical Method

Consider the following hyperbolic conservation law for $u = u(x, t)$

$$\frac{\partial u}{\partial t} + \frac{\partial H(u)}{\partial x} = 0, \quad x \in \mathbb{R}, t > 0 \quad u(x, 0) = \eta(x), \quad x \in \mathbb{R}. \quad (1)$$

We provide a formal development of the analogue Lagrangian-Eulerian scheme [2–4, 11] for numerically solving the initial value problem with $x \in \mathbb{R}, t > 0$. As in the Lagrangian-Eulerian schemes [3, 4], local conservation is obtained by integrating the conservation law over the region in the space-time domain where the conservation of the mass flux takes place. Consider the Lagrangian-Eulerian finite-volume cell centers

$$D_j^n = \{(t, x) / t^n \leq t \leq t^{n+1}, \sigma_{j-\frac{1}{2}}^n(t) \leq x \leq \sigma_{j+\frac{1}{2}}^n(t)\}, \quad (2)$$

where $\sigma_{j-\frac{1}{2}}^n(t)$ is the parameterized integral curve such that $\sigma_{j-\frac{1}{2}}^n(t^n) = x_{j-\frac{1}{2}}^n$. These curves are the lateral boundaries of the domain D_j^n in (2) and we define $\bar{x}_{j-\frac{1}{2}}^{n+1} := \sigma_{j-\frac{1}{2}}^n(t^{n+1})$ and $\bar{x}_{j+\frac{1}{2}}^{n+1} := \sigma_{j+\frac{1}{2}}^n(t^{n+1})$ as their endpoints in time t^{n+1} . The numerical scheme is expected to satisfy some type of mass conservation (due to the inherent nature of the conservation law) from time t^n in the space domain $[x_{j-\frac{1}{2}}^n, x_{j+\frac{1}{2}}^n]$ to time t^{n+1} in the space domain $[\bar{x}_{j-\frac{1}{2}}^{n+1}, \bar{x}_{j+\frac{1}{2}}^{n+1}]$. With this, we must have the flux through curves $\sigma_{j-\frac{1}{2}}^n(t)$ to be zero. From the integration of (1) and the divergence theorem, using the fact that the line integrals over curves $\sigma_j^n(t)$ vanish, we get

$$\int_{\bar{x}_{j-\frac{1}{2}}^{n+1}}^{\bar{x}_{j+\frac{1}{2}}^{n+1}} u(x, t^{n+1}) dx = \int_{x_{j-\frac{1}{2}}^n}^{x_{j+\frac{1}{2}}^n} u(x, t^n) dx. \quad (3)$$

The linear case from [3] is essentially imitated, but here the curves $\sigma_{j-1/2}^n(t)$ are not straight lines in general, but rather solutions of the set of local nonlinear differential equations [3, 11]: $\frac{d\sigma_{j-1/2}^n(t)}{dt} = \frac{H(u)}{u}$, for $t^n < t \leq t^{n+1}$, with the initial condition $\sigma_{j-1/2}^n(t^n) = x_{j-1/2}^n$, assuming $u \neq 0$ (for the sake of presentation).

The extension of this construction follows naturally from the finite volume formulation of the linear Lagrangian-Eulerian scheme as building block to construct *local* approximations such as $f_{j-1/2}^n = \frac{H(U_{j-1/2}^n)}{U_{j-1/2}^n} \approx \frac{H(u)}{u}$ with the initial condition $\sigma_{j-1/2}^n(t^n) = x_{j-1/2}^n$.

Indeed, distinct and high-order approximations are also acceptable for $\frac{d\sigma_{j-1/2}^n(t)}{dt}$ and can be viewed as ingredients to improve accuracy of the new family of Lagrangian-Eulerian methods; this will be addressed later. Equation 3 defines conservation of mass but in a different mesh cell-centered in points $\bar{x}_{j+\frac{1}{2}}^n$. We will later address how to project these volumes back to the original mesh. The piecewise constant numerical data is reconstructed into a piecewise linear approximation (but high-order reconstructions are acceptable), through the use of MUSCL-type interpolants:

$$L_j(x, t) = u_j(t) + (x - x_j) \frac{1}{\Delta x} u_j'. \quad (4)$$

For the numerical derivative $\frac{1}{\Delta x}u'_j$, there are several choices of slope limiters; in book [8] there is a good compilation of many options; a priori choice of such slope limiters is quite hard, but they are chosen upon the underlying model problem under investigation. One possible for the slope limiter is

$$U'_j = MM \left\{ \alpha \Delta u_{j+\frac{1}{2}}, \frac{1}{2}(u_{j+1} - u_{j-1}), \alpha \Delta u_{j-\frac{1}{2}} \right\}, \quad (5)$$

and this choice for slope limiter allows steeper slopes near discontinuities and retain accuracy in smooth regions. The range of the parameter α is typically guided by the CFL condition [9]. Here, MM stands for the usual MinMod limiter [8,9], with $\Delta u_{j+\frac{1}{2}} = u_{j+1} - u_j$,

$$MM\{\sigma, \tau\} = \frac{1}{2} [sgn(\sigma) + sgn(\tau)] \min \{|\sigma|, |\tau|\}. \quad (6)$$

The discrete version of equation (3), using the piecewise linear approximation above, is

$$\bar{U}_j^{n+1} = \frac{1}{h_j^{n+1}} \int_{\bar{x}_{j-\frac{1}{2}}^{n+1}}^{\bar{x}_{j+\frac{1}{2}}^{n+1}} u(x, t^{n+1}) dx = \frac{1}{h_j^{n+1}} \int_{x_{j-\frac{1}{2}}^n}^{x_{j+\frac{1}{2}}^n} u(x, t^n) dx = \frac{h}{h_j^{n+1}} U_j^n, \quad (7)$$

in which we use the approximations

$$\bar{U}_j^{n+1} := \frac{1}{h_j^{n+1}} \int_{\bar{x}_{j-\frac{1}{2}}^{n+1}}^{\bar{x}_{j+\frac{1}{2}}^{n+1}} u(x, t^{n+1}) dx, \quad \text{and} \quad U_j^n := \frac{1}{h} \int_{x_{j-\frac{1}{2}}^n}^{x_{j+\frac{1}{2}}^n} u(x, t^n) dx.$$

Solutions $\sigma_{j-1/2}^n(t)$ of the differential system are obtained using the approximations

$$\begin{aligned} U_{j-\frac{1}{2}} &= \frac{1}{h} \int_{x_{j-1}^n}^{x_j^n} L(x, t) dx = \frac{1}{h} \left(\int_{x_{j-1}^n}^{x_{j-\frac{1}{2}}^n} L_{j-1}(x, t) dx + \int_{x_{j-\frac{1}{2}}^n}^{x_j^n} L_j(x, t) dx \right) \\ &= \frac{1}{2}(U_{j-1} + U_j) + \frac{1}{8}(U'_j - U'_{j-1}). \end{aligned} \quad (8)$$

The above approximation is not necessary in the linear case where $H(u) = a(x, t)u$. We must notice that the approximation of $f_{j-1/2}^n$ may cause spurious oscillation in Riemann problems, specially in shocks and discontinuity regions (see Figure 2 in Section 3). For that, we use a polynomial reconstruction of second degree to smooth out the approximation. The numerical solutions have shown qualitatively correct behavior for nonlinear hyperbolic conservation laws. The convergence order remains unchanged even with the reconstruction, being a first-order approximation. In the reconstruction we use the nonlinear Lagrange polynomial in U_{j-1} , U_j and U_{j+1} . So, equation (7) reads

$$\bar{U}_j^{n+1} = \frac{1}{h_j^{n+1}} \int_{x_{j-\frac{1}{2}}^n}^{x_{j+\frac{1}{2}}^n} P_2(x) dx, \quad (9)$$

where $P_2(x) = U_{j-1}^n L_{-1}(x - x_j) + U_j^n L_0(x - x_j) + U_{j+1}^n L_1(x - x_j)$ and

$$L_{\pm 1}(x) = \frac{1}{2} \left[\left(\frac{x}{h} \pm \frac{1}{2} \right)^2 - \frac{1}{4} \right], \quad L_0(x) = 1 - \left(\frac{x}{h} \right)^2. \quad (10)$$

Next, we obtain the resulting projection formula as follows

$$U_j^{n+1} = \frac{1}{h} (C_l \bar{U}_{j-1}^n + (h - C_l - C_r) \bar{U}_j^n + C_r \bar{U}_{j+1}^n), \quad (11)$$

where the projection coefficients are: $C_l = \frac{1}{2} f_{j-1/2}^n \Delta t^n (1 + \text{sign}(f_{j-1/2}^n))$ and $C_r = \frac{1}{2} |f_{j+1/2}^n| \Delta t^n (1 - \text{sign}(f_{j+1/2}^n))$. Here Δt^n is obtained under CFL-condition

$$\max_j \left\{ |f_{j-\frac{1}{2}}| \Delta t^n \right\} \leq \frac{h}{2},$$

which is taken by construction of method. We note that in the linear case, when $a(x, t) = a > 0$ (or $a < 0$), the numerical scheme (7)-(11) is a generalization of the Upwind scheme, but our scheme can approximate solution in both cases $a > 0$ and $a < 0$, the CFL-condition in this case is $|a \Delta t| \leq h$ as in the Upwind scheme.

3 Numerical Experiments

We present and discuss computations for scalar linear and nonlinear conservation laws with convex and non-convex flux functions. In Figure 1, it is shown numerical solutions for $u_t + (a(x, t) u)_x = 0$ along with various $a(x, t)$ functions. For instance on the left picture we take a standard test case, called Shu's linear test [6, 7] with $a(x, t) = 0.5$ and 256 cells. On the center picture we show a test of our scheme on the case with $a(x, t) = \sin(x)$ over $[0, 2\pi]$, 128 cells and with the exact solution (see [6])

$$u(x, t) = \frac{\sin(2 \arctan(e^{-t} \tan(x/2)))}{\sin(x)}.$$

And on the right picture of Figure 1 as in [6], we test a case with $a(x, t) = \sin(t)$ on $[0, 2]$ and 256 cells, for which the exact solution is $u(x, t) = u_0(x + 1 + \cos(t))$ where $u_0(x) = 0.75 + 0.25 \sin(\pi x)$ over $[0, 2]$ simulated at time $t = 4$. Second and third cases present different velocity signals in space (center case) and over time (right case), and our method shows robustness by not needing any special treatment for that. In Figure 2, we present the solutions of the problem with Burgers' flux function $u_t + (u^2/2)_x = 0$ along with discontinuous initial data $u(x, 0) = 1, x < 0$ and $u(x, 0) = 0, x > 0$ (left picture), and $u(x, 0) = -1, x < 0$ and $u(x, 0) = 1, x > 0$ (right picture), without the reconstruction. The shock discontinuity on the left exhibits spurious oscillations. The right picture is a transonic rarefaction wave. In Figure 3, it is shown again the numerical solutions for $u_t + (u^2/2)_x = 0$ along with same discontinuous initial data $u(x, 0) = 1, x < 0$ and $u(x, 0) = 0, x > 0$ (left picture), and $u(x, 0) = -1, x < 0$ and $u(x, 0) = 1,$

$x > 0$ (middle picture), now with polynomial reconstruction. On these frames are shown snapshot graphs with waves moving from left to right. We get a very nice looking numerical approximate solution with scheme (9)-(11), which in turn seems to be propagating at entirely entropy-correct Rankine-Hugoniot speed and similar good results are shown to the rarefaction case as well. Here, as the rarefaction wave is crossed, there is a sign change in the characteristic speed u and thus there is one point at which $u = 0$, the sonic point. However, our numerical scheme now shows no spurious anomalies around $u = 0$. The classical nonlinear one-dimensional Buckley-Leverett case is depicted on the right picture in Figure 3 at time $t = 1$. These test cases here were simulated with 256 cells. Another example with the Buckley-Leverett flux function is seen on Figure 4, where we set a square wave as initial condition, $u(x, 0) = 1, -1 < x < 1$ and $u(x, 0) = 0$, otherwise (left picture). The solution profile starts as a rarefaction wave followed by a shock on the left side and a rarefaction wave followed by a shock on the right side for small times (middle picture). When the left shock meets the right rarefaction (see middle and right pictures in Figure 4), we observe the expected decaying pattern [10]; see also [5], Section 3.

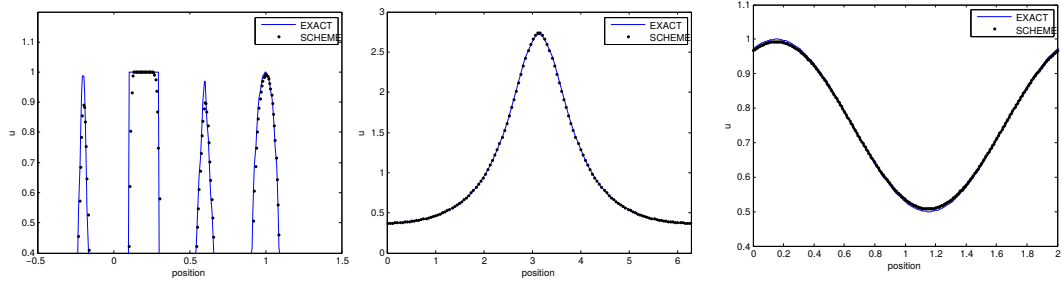


Figure 1: Left: Shu's linear test. Middle: Test case with $a(x, t) = \sin(x)$, the velocity is variable in space. Right: Test case with $a(x, t) = \sin(t)$, the velocity is variable in time.

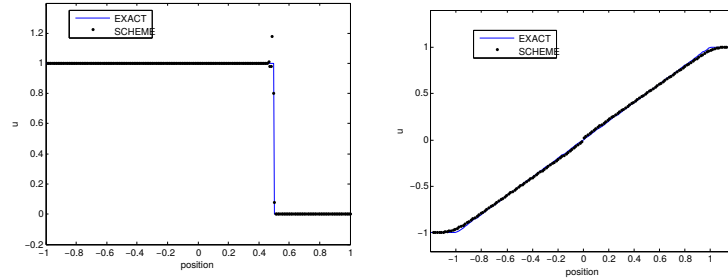


Figure 2: Nonlinear tests for Burgers' flux function without reconstruction. Left: shock wave, initial condition $u(x, 0) = 1, x < 0$ and $u(x, 0) = 0, x > 0$, end time $t = 0.5$. Right: rarefaction wave, $u(x, 0) = -1, x < 0$ and $u(x, 0) = 1, x > 0$, end time $t = 1.0$.

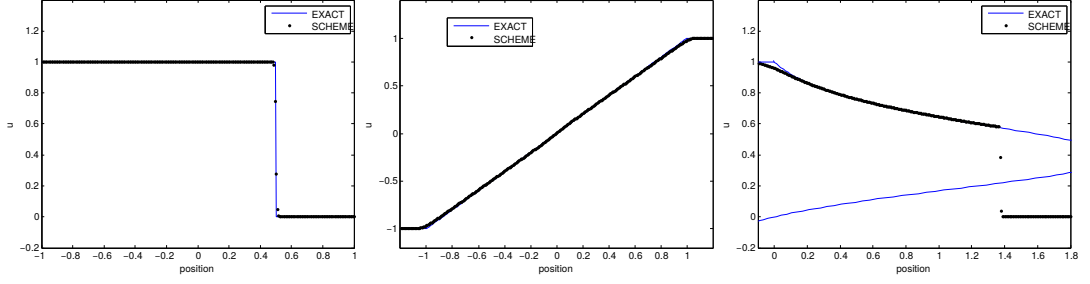


Figure 3: Nonlinear tests with reconstruction. Left: Burgers' flux function, shock wave solution with initial condition $u(x, 0) = 1, x < 0$ and $u(x, 0) = 0, x > 0$, end time $t = 0.5$. Middle: Burgers' flux function, rarefaction wave with initial condition $u(x, 0) = -1, x < 0$ and $u(x, 0) = 1, x > 0$, end time $t = 1.0$. Left: Buckley-Leverett flux function ($H(u) = u^2/(u^2 + 0.5(1 - u)^2)$) with initial condition $u(x, 0) = 1, x < 0$ and $u(x, 0) = 0, x > 0$.

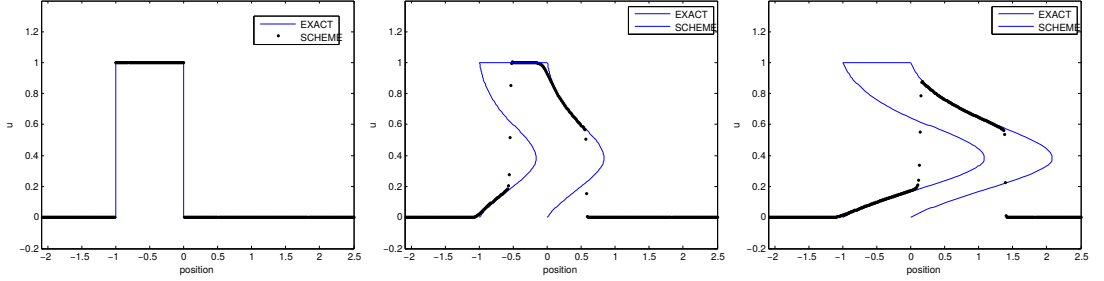


Figure 4: Buckley-Leverett flux function with initial condition $u(x, 0) = 1, -1 < x < 1$ and $u(x, 0) = 0$, otherwise. Snapshots at $t = 0$, $t = 0.4$ and $t = 1$, respectively.

4 Concluding Remarks

We presented the development of an effective numerical scheme for solving nonlinear scalar hyperbolic conservation laws problems with the Lagrangian-Eulerian framework. This method is based on a reformulation of the conservation laws in terms of an equivalent locally conservative space-time problem in divergence form. We make use of piecewise linear and parabolic reconstructions ideas for resolution and accuracy reasons and the resulting method present qualitatively correct numerical approximations. Our method is robust in a way that no special treatment is needed when the sign of velocity changes over time. We expect to establish a componentwise extension of the scheme in order to perform numerical experiments for systems of conservation and balance laws, as well as multidimensional problems. Our numerical experiments show good evidence of computational convergence.

Acknowledgements

E. Abreu thanks for financial support through grants FAPESP No. 2014/03204-9, FAPESP No. 2011/23628-0, CNPq No. 445758/2014-7 and UNICAMP /FAEPEX No. 519.292-0280/2014. J. Perez and A. Santo thanks, respectively, CAPES-IMECC/ UNICAMP and CNPq-IMECC/ UNICAMP for a post-doctoral fellowship and a graduate fellowship.

References

- [1] E. Abreu. Numerical modelling of three-phase immiscible flow in heterogeneous porous media with gravitational effects. *Mathematics and Computers in Simulation*, 97:234–259, 2014.
- [2] E. C. Abreu, W. Lambert, J. A. Perez S., and A. M. E. Santo. A lagrangian-eulerian algorithm for solving hyperbolic conservation laws with applications. In *Proceedings of the 6th International Conference on Approximation Methods and Numerical Modelling in Environment and Natural Resources (MAMERN VI)*, pages 599–617, Pau/Granada, 2015.
- [3] J. Aquino, A. S. Francisco, F; Pereira, T. Jordem Pereira, and H. P. Amaral Souto. A lagrangian strategy for the numerical simulation of radionuclide transport problems. *Progress in Nuclear Energy*, 52(3):282–291, 2010.
- [4] J. Douglas Jr, F. Pereira, and L.-M. Yeh. A locally conservative eulerian–lagrangian numerical method and its application to nonlinear transport in porous media. *Computational Geosciences*, 4(1):1–40, 2000.
- [5] L. C. Evans *Partial differential equations* American Mathematical Society, 2010.
- [6] C-S. Huang, T. Arbogast, and J. Qiu. An eulerian–lagrangian weno finite volume scheme for advection problems. *Journal of Computational Physics*, 231(11):4028–4052, 2012.
- [7] G.-S. Jiang and C.-W. Shu. Efficient implementation of weighted eno schemes. Technical report, DTIC Document, 1995.
- [8] R. J. LeVeque. *Finite volume methods for hyperbolic problems*, volume 31. Cambridge university press, 2002.
- [9] H. Nessyahu and E. Tadmor. Non-oscillatory central differencing for hyperbolic conservation laws. *Journal of computational physics*, 87(2):408–463, 1990.
- [10] O. A. Oleinik Discontinuous solutions of non-linear differential equations *Uspekhi Matematicheskikh Nauk* 12(3):3–73, 1957.
- [11] J. A. Perez S. *Lagrangian-Eulerian approximate methods for balance laws and hyperbolic conservation law*. Tese de Doutorado, University of Campinas, 2015.

A new finite volume approach for transport models and related applications with balancing source terms

E. Abreu^a, W. Lambert^b, J. Perez^{a,c}, A. Santo^{a,*}

^a*University of Campinas (UNICAMP), Department of Applied Mathematics, IMECC, 13083-859, Brazil*

^b*Alfenas Federal University - ICT (BR 267 Km 533), MG, Brazil*

^c*Facultad de Ciencias ITM Institución Universitaria, Calle, 73 No 76A, 354 Medellín, Colombia.*

Abstract

We develop a new finite volume scheme for numerically solving transport models associated with hyperbolic problems and balance laws. The numerical scheme is obtained via a Lagrangian-Eulerian approach that retains the fundamental principle of conservation of the governing equations as it is linked to the classical finite volume framework. As features of the novel algorithm we highlight: the new scheme is locally conservative in balancing the flux and source term gradients and preserves a component-wise structure at a discrete level for systems of equations. The novel approach is applied to several nontrivial examples to evidence that we are calculating the correct qualitatively good solutions with accurate resolution of small perturbations around the stationary solution. We discuss applications of the new method to classical and nonclassical nonlinear hyperbolic conservation and balance laws such as the classical inviscid Burgers equation, two-phase and three-phase flow problems in porous media as well as numerical experiments for nonlinear shallow water equations with friction terms. In addition, we consider the case of the source term which is discontinuous as a function of space x . We also extend the Lagrangian-Eulerian framework to the two-dimensional scalar conservation law, along with pertinent numerical experiments to show the performance of the new method.

Keywords: Conservation laws, Balance laws, Flow in Porous Media, Shallow Water Equations, Lagrangian-Eulerian Finite Volume, Classical and non-classical solutions of PDEs

2010 MSC: 35Q35, 65M08, 68U20, 76E30

1. Introduction

Our aim is to develop a simple and efficient class of finite volume schemes based on a novel Lagrangian-Eulerian framework to account the delicate nonlinear balance between the discretizations of the hyperbolic flux and of the stiff source term at a discrete level. A rigorous mathematical demonstration of such approach is beyond the scope of the present paper, and is to be attempted in future research. In the current stage of this work, we describe the key ideas of our constructive algorithm and we present several nontrivial numerical experiments in order to verify the desired well-balanced properties for one-dimensional and two-dimensional problems involving conservation laws with source terms for transport models and related applications.

It is well known that many well-balanced schemes have been proposed since the milestone work (see [22]) of Greenberg and LeRoux (1996). The focus of many such works was to handle shallow water equations over non-trivial topographies. The key issue is the construction of well-balanced nonlinear schemes that recover the time-asymptotic behavior of the underlying nonlinear balance law. There are many relevant studies for approximation methods and numerical analysis devoted to balance law and hyperbolic law problems. Naturally, all methods exhibit advantages and disadvantages, since the underlying differential equations

*Corresponding author

Email addresses: eabreu@ime.unicamp.br (E. Abreu), wanderson.lambert@gmail.com (W. Lambert), jhonperez@itm.edu.co (J. Perez), arthur@ime.unicamp.br (A. Santo)

are very hard problems with a lack of general theory (see, e.g., [6, 7, 8, 9, 12, 13, 15, 19, 21, 22, 25, 27, 30, 33, 36]) See also [4, 17] for surveys on both analytical and numerical aspects of one-dimensional hyperbolic balance laws and [18] for a good discussion of two-dimensional balance law problems along with an up-to-date and comprehensive list of references. The work [18] also includes relevant theoretical aspects of scalar conservation laws in several spatial dimensions in a more flexible Godunov framework to handle local nonlinear wave patterns to account for the flux computations. These schemes evolved following the natural understanding of fundamental concepts from the theory of nonlinear hyperbolic conservation laws concerning the properties of the characteristic surfaces, such as existence, uniqueness, and solution of the Riemann problems. Also, for a scalar balance law, the solution depends strongly on certain properties of the source term (see, e.g., [5, 17, 19, 22, 24, 25]).

The situation of balance laws $u_t + f_x(u) = g(u, x)$, with $g(u, x)$ discontinuous in x is another challenging problem encountered for such class of differential equations from both a theoretical and a numerical point of view. A kinetic scheme, with convergence proof for the scalar related problem, was introduced in [7]. Essentially, they propose a kinetic interpretation of upwinding techniques, taking into account the source terms to develop an equilibrium scheme as a result. Another approach was introduced in [36] (see also [8]). This method does not use upwinding solvers; it uses the interface value rather than the cell averages for the source terms that balance the nonlinear convection at the cell interface, allowing the numerical capturing of the steady state with a formal high order accuracy. A successful alternative to accounting for the balance between the nonlinear flux and the source terms with $g(u, x)$ discontinuous in x is the use of a central differencing scheme as discussed in [1] for gas dynamics Euler equations with stiff relaxation source terms; see also [8]. A distinct numerical framework, based on Riemann solvers using local characteristic decompositions, can be found in [15]. In paper [16], the authors were concerned with the Riemann problem of the Burgers equation with a discontinuous source term, motivated by the study of propagation of singular waves in radiation hydrodynamics. Moreover, they were able to construct the global entropy solution to the related Riemann problem linked to this model. It turns out that the discontinuity of the source term has clear influences on the shock or rarefaction waves generated by the initial Riemann data. It is worth mentioning that other related problems were also described in the literature supported by numerical experiments. For more details about this subject matter, the interested reader is referred to the papers [1, 4, 7, 8, 15, 16, 17, 36] and papers cited therein.

In this work we are interested in the construction of a numerical scheme for solving nonlinear hyperbolic conservation and balance law problems using a Lagrangian-Eulerian approach [5, 14, 24, 25]. In the work [14], the authors identified the region in the space-time domain where the mass conservation takes place, but linked to a scalar convection-dominated nonlinear parabolic problem, which models the immiscible incompressible two-phase flow in a porous medium. The key ingredient to finding this conservative region was the use of a Lagrangian-Eulerian framework; see [5] for related works with applications to radionuclide transport problems. Recently in [33], such ideas were extended to nonlinear purely hyperbolic conservation and balance laws – scalar case and systems of equations. In particular, a convergence proof for the unique entropy solution was established for the case of a Lagrangian-Eulerian monotone finite difference scheme related to a scalar hyperbolic conservation law. We refer to [3] for other recent developments on this subject.

We will explore the above mentioned innovative ideas to give a formal construction of accurate Lagrangian-Eulerian schemes for transport models and related applications with balancing source terms. As features of the novel algorithm, we highlight: we verified through numerical experiments that the new scheme seems to be locally conservative in balancing the flux and source term gradients and preserves a component-wise structure at the discrete level for systems of equations. Besides, we also discuss a set of numerical experiments to nonlinear scalar two-dimensional problems with non-symmetric and nonconvex flux function for systems of balance laws. This novel approach is applied to several nontrivial examples to show evidence that we are calculating the correct qualitatively good solutions with the accurate resolution of small perturbations around the stationary solution. We discuss applications of the new method to nonlinear hyperbolic conservation and balance laws such as the classical inviscid Burgers equation, two-phase and three-phase flow problems in porous media as well as numerical experiments for nonlinear shallow water equations with friction terms.

Furthermore, our new Lagrangian-Eulerian framework is aimed to be independent of a particular structure of the flux function as well as of the source terms. We were able to reproduce several models indistinctly within the same formalism, and this indicates that our method is general to some extent. It is also important to notice that our scheme does not depend on exact or approximate solutions to Riemann problems.

The rest of the work is organized as follows: The Lagrangian-Eulerian framework for solving scalar nonlinear hyperbolic conservation laws is discussed in Section 2. These ideas are extended to the case of balance laws in Section 3. The case of systems is studied in Section 4, followed by the extension to two-dimensional conservation laws in Section 5. We then discuss a set of representative numerical experiment studies with applications in Section 6, along with our concluding remarks in the final Section 7.

2. A Lagrangian-Eulerian constructive approximation scheme for nonlinear hyperbolic conservation laws

We provide a formal development of the analogue Lagrangian-Eulerian scheme [33] – see also [5, 14] – for solving numerically first-order scalar hyperbolic equations $x \in \mathbb{R}$, $t > 0$, $u : (\mathbb{R}, \mathbb{R}^+) \rightarrow \mathbb{R}$, $H : \mathbb{R} \rightarrow \mathbb{R}$:

$$\frac{\partial u}{\partial t} + \frac{\partial H(u)}{\partial x} = 0, \quad x \in \mathbb{R}, t > 0 \quad u(x, 0) = \eta(x), \quad x \in \mathbb{R}. \quad (1)$$

Although our primary interest is to give a formal construction of the new Lagrangian-Eulerian method, we expect to work on the relevant issue of rigorous convergence proof to the corresponding weak entropy solution further later on. As in the Lagrangian-Eulerian schemes [5, 14], local conservation is obtained by integrating the conservation law over the region in the space-time domain where the conservation of the mass flux takes place. For that, we consider the Lagrangian-Eulerian finite-volume cell centers

$$D_j^n = \{(t, x) / t^n \leq t \leq t^{n+1}, \sigma_j^n(t) \leq x \leq \sigma_{j+1}^n(t)\}, \quad (2)$$

where $\sigma_j^n(t)$ is the parameterized integral curve such that $\sigma_j^n(t^n) = x_j^n$. These curves are the lateral boundaries of the domain D_j^n in (2) and we define $\bar{x}_{j-\frac{1}{2}}^{n+1} := \sigma_j^n(t^{n+1})$ and $\bar{x}_{j+\frac{1}{2}}^{n+1} := \sigma_{j+1}^n(t^{n+1})$ as their endpoints in time t^{n+1} . Due to the inherent nature of conservation laws, the numerical scheme is expected to satisfy some type of mass conservation from time t^n in the space domain $[x_j^n, x_{j+1}^n]$ to time t^{n+1} in the space domain $[\bar{x}_{j-\frac{1}{2}}^{n+1}, \bar{x}_{j+\frac{1}{2}}^{n+1}]$. With this, we have to the flux through curves $\sigma_j^n(t)$ must be zero.

From the integration of (1) and the divergence theorem, using the fact that the line integrals over curves $\sigma_j^n(t)$ vanish, we get

$$\int_{\bar{x}_{j-\frac{1}{2}}^{n+1}}^{\bar{x}_{j+\frac{1}{2}}^{n+1}} u(x, t^{n+1}) dx = \int_{x_j^n}^{x_{j+1}^n} u(x, t^n) dx. \quad (3)$$

We essentially mimic the procedures of the linear case [5], but now notice that the curves $\sigma_j^n(t)$ are not straight lines, in general, but rather solutions of the set of nonlinear (local) differential system of equations [5, 33]:

$$\frac{d\sigma_j^n(t)}{dt} = \frac{H(u)}{u}, \quad \text{for } t^n < t \leq t^{n+1}, \quad (4)$$

with the initial condition $\sigma_j^n(t^n) = x_j^n$, assuming $u \neq 0$ (for the sake of presentation).

Remark 1. For the sake of simplicity of presentation we shall suppose $u \neq 0$ (this assumption can be suppressed by introducing some extra notation in the analysis to define the endpoints $[\bar{x}_{j-\frac{1}{2}}^{n+1}, \bar{x}_{j+\frac{1}{2}}^{n+1}]$ by analytical straight lines), when considering f_j in the case of $U_j = 0$. This means that for the resulting numerical scheme, pertinent to the Lagrangian-Eulerian framework at hand, that the projection step is not necessary anymore since the argument of the flux function (also for the numerical flux function) is now known along the vertical curves associated for the integral tubes, that are defined at the cell centers (see eqs. (2)-(4) and Figure 1).

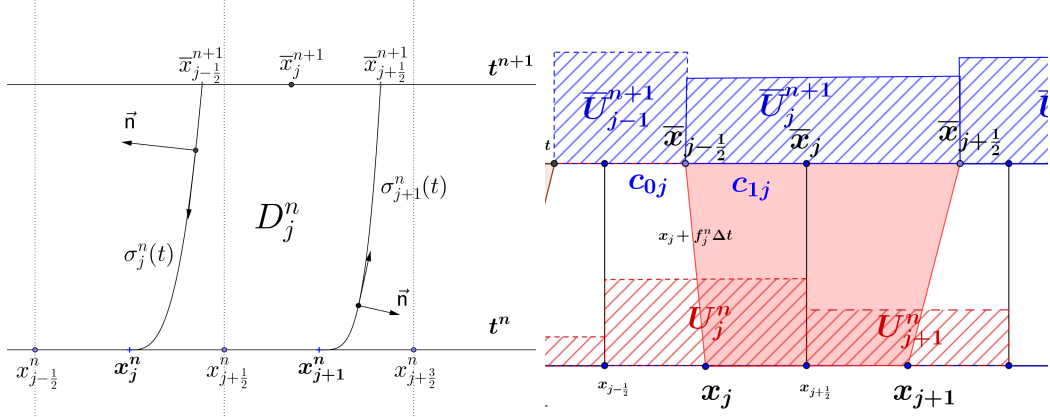


Figure 1: Illustration of the integral tubes. Notice that a first order approximation is performed to the construction of the local Lagrangian-Eulerian space-time control-volume, linked to D_j^n in (4). Indeed, we notice that higher order approximations are naturally permissible as well.

The extension of this construction follows naturally from the finite volume formulation of the linear Lagrangian-Eulerian scheme as building block to construct *local* approximations such as $f_j^n = \frac{H(U_j^n)}{U_j^n} \approx \frac{H(u)}{u}$ with the initial condition $\sigma_j^n(t^n) = x_j^n$. Indeed, distinct and high-order approximations are also acceptable for $\frac{d\sigma_j^n(t)}{dt}$ and can be viewed as free ingredients to improve accuracy of the new family of Lagrangian-Eulerian; this will be addressed later. Equation (3) defines conservation of mass but in a different mesh cell-centered in points $\bar{x}_{j+\frac{1}{2}}$. We will later address how to project these volumes back to the original mesh. For now (e.g., as in [1, 2, 28]) we discuss a reconstruction from a piecewise constant numerical data to a piecewise linear approximation (but high-order reconstructions are acceptable), through the use of MUSCL-type interpolants:

$$L_j(x, t) = u_j(t) + (x - x_j) \frac{1}{\Delta x} u'_j. \quad (5)$$

For the numerical derivative $\frac{1}{\Delta x} u'_j$ we shall discuss a few examples of slope limiters, which will retain the desired properties of consistency of the numerical flux function. There are several choices of slope limiters; in book [28] there is a good compilation of many options; a priori choice of such slope limiters is quite hard, but they are chosen upon the underlying model problem under investigation. Here we make use of the following three options. The first is,

$$U'_j = MM \left\{ \Delta u_{j+\frac{1}{2}}, \Delta u_{j-\frac{1}{2}} \right\}, \quad (6)$$

where MM stands for the usual MinMod limiter [28], with $\Delta u_{j+\frac{1}{2}} = u_{j+1} - u_j$,

$$MM\{\sigma, \tau\} = \frac{1}{2} [\text{sgn}(\sigma) + \text{sgn}(\tau)] \min \{|\sigma|, |\tau|\}. \quad (7)$$

A second choice for the slope limiter can be

$$U'_j = MM \left\{ \alpha \Delta u_{j+\frac{1}{2}}, \frac{1}{2} (u_{j+1} - u_{j-1}), \alpha \Delta u_{j-\frac{1}{2}} \right\}, \quad (8)$$

and this choice for slope limiter allows steeper slopes near discontinuities and retain accuracy in smooth regions. The range of the parameter α is typically guided by the CFL condition (see, e.g., [28]). In this work we also make use of the following high order slope limiter, namely, the UNO choice (where $\Delta^2 u_j = u_{j+1} - 2u_j + u_{j-1}$),

$$U'_j = MM \left\{ \Delta u_{j-\frac{1}{2}} + \delta^2(u_{j-1}, u_j), \Delta u_{j-\frac{1}{2}} + \delta^2(u_j, u_{j+1}) \right\}, \quad (9)$$

where $\delta^2(u_j, u_{j+1}) = \frac{1}{2}MM(\Delta^2 u_j, \Delta^2 u_{j+1})$. Preliminary experiments discussed in Section 6 have shown that the UNO option has resulted in more satisfactory approximations for our test cases.

The discrete version of equation (3), using the piecewise linear approximation above, is

$$\begin{aligned}\overline{U}_j^{n+1} &= \frac{1}{h_j^{n+1}} \int_{\bar{x}_{j-\frac{1}{2}}^{n+1}}^{\bar{x}_{j+\frac{1}{2}}^{n+1}} u(x, t^{n+1}) dx = \frac{1}{h_j^{n+1}} \int_{x_j^n}^{x_{j+1}^n} u(x, t^n) dx \\ &= \frac{h}{h_j^{n+1}} \left(\frac{1}{h} \int_{x_j^n}^{x_{j+\frac{1}{2}}^n} u(x, t^n) dx + \frac{1}{h} \int_{x_{j+\frac{1}{2}}^n}^{x_{j+1}^n} u(x, t^n) dx \right) \\ &= \frac{h}{h_j^{n+1}} \frac{1}{2} (U_j^n + U_{j+1}^n) + \frac{1}{h_j^{n+1}} \frac{1}{16} h (U_j'^n - U_{j+1}'^n),\end{aligned}\tag{10}$$

where, we use the approximations $\overline{U}_j^{n+1} := \frac{1}{h_j^{n+1}} \int_{\bar{x}_{j-\frac{1}{2}}^{n+1}}^{\bar{x}_{j+\frac{1}{2}}^{n+1}} u(x, t^{n+1}) dx$ and $U_j^n := \frac{1}{h} \int_{x_j^n}^{x_{j+1}^n} u(x, t^n) dx$.

Following [1, 2], we also introduce a predictor-corrector approximation by evaluating $f_j^{n+\frac{1}{2}}$, instead of f_j^n using Taylor expansion and the conservation law, and it reads,

$$U_j^{n+\frac{1}{2}} = u(x_j, t + \frac{\Delta t}{2}) = u_j(t) - \frac{1}{2} \frac{\Delta t}{\Delta x} H_j',\tag{11}$$

so that $f_j^{n+\frac{1}{2}} = \frac{H(U_j^{n+\frac{1}{2}})}{U_j^{n+\frac{1}{2}}}$. Now, the solutions $\sigma_j^n(t)$ of the differential system equations are (local) straight lines, but they are not parallel as in the linear case, but subject to a CFL stability condition of the form (see Appendix A),

$$\max_j \left| \frac{f_j^n \Delta t^n}{h} \right| \leq \frac{\sqrt{2}}{2} \quad \text{and} \quad k^n = \min_n \Delta t^n.\tag{12}$$

Next, we obtain the resulting projection formula as follows

$$U_j^{n+1} = \frac{1}{h} c_0 \overline{U}_{j-1} + \frac{1}{h} c_1 \overline{U}_j, \quad \text{where } c_{0j} = \frac{h}{2} + f_j^{n+\frac{1}{2}} k^n \text{ and } c_{1j} = \frac{h}{2} - f_j^{n+\frac{1}{2}} k^n.\tag{13}$$

Here c_{0j} and c_{1j} are the projection coefficients [33]. Combining (13) with the discrete version of local conservation (10) reads,

$$\begin{aligned}U_j^{n+1} &= \left[\frac{c_0}{2h_j^{n+1}} (U_{j-1}^n + U_j^n) + \frac{c_0}{16h_j^{n+1}} (U_{j-1}'^n - U_j'^n) \right] \\ &\quad + \left[\frac{c_1}{2h_j^{n+1}} (U_j^n + U_{j+1}^n) + \frac{c_1}{16h_j^{n+1}} (U_j'^n - U_{j+1}'^n) \right].\end{aligned}\tag{14}$$

Notice that for each $j \in \mathbb{Z}$, $h_j^{n+1} = \bar{x}_{j+\frac{1}{2}}^{n+1} - \bar{x}_{j-\frac{1}{2}}^{n+1} = h + (f_{j+1}^{n+\frac{1}{2}} - f_j^{n+\frac{1}{2}}) k^n$, and, also that: $h_j^{n+1} = c_{0j+1} + c_{1j}$. Thus,

$$c_{0j} = h_{j-1}^{n+1} - c_{1j-1} \quad \text{and} \quad c_{1j} = h_j^{n+1} - c_{0j+1}, \quad \text{with}\tag{15}$$

$c_{1j-1} = \frac{1}{2}(h_{j-1}^{n+1} - f_{j-1}^{n+\frac{1}{2}}k^n - f_j^{n+\frac{1}{2}}k^n)$, $c_{0j+1} = \frac{1}{2}(h_j^{n+1} + f_j^{n+\frac{1}{2}}k^n + f_{j+1}^{n+\frac{1}{2}}k^n)$. Finally, plugging (15) into (14),

$$\begin{aligned} U_j^{n+1} = & \frac{U_{j-1}^n + 2U_j^n + U_{j+1}^n}{4} + \frac{U_{j-1}'^n - U_{j+1}'^n}{32} \\ & + \frac{k^n}{4} \left(\frac{f_{j-1}^{n+\frac{1}{2}} + f_j^{n+\frac{1}{2}}}{h_{j-1}^{n+1}} [U_{j-1}^n + U_j^n] - \frac{f_j^{n+\frac{1}{2}} + f_{j+1}^{n+\frac{1}{2}}}{h_j^{n+1}} [U_j^n + U_{j+1}^n] \right) \\ & + \frac{k^n}{32} \left(\frac{f_{j-1}^{n+\frac{1}{2}} + f_j^{n+\frac{1}{2}}}{h_{j-1}^{n+1}} [U_{j-1}'^n - U_j'^n] - \frac{f_j^{n+\frac{1}{2}} + f_{j+1}^{n+\frac{1}{2}}}{h_j^{n+1}} [U_j'^n - U_{j+1}'^n] \right). \end{aligned} \quad (16)$$

The analogue finite difference scheme (16) is a *Lagrangian-Eulerian scheme* for the nonlinear problem (1). The obtained scheme (16) can also be written in a conservative form (a novelty result for such schemes):

$$U_j^{n+1} = U_j^n - \frac{k^n}{h} [F(U_j, U_{j+1}^n) - F(U_{j-1}^n, U_j^n)], \quad (17)$$

with the *Lagrangian-Eulerian numerical flux function* defined by

$$\begin{aligned} F(U_j^n, U_{j+1}^n) = & \frac{1}{4} \left(\frac{h}{k^n} (U_j^n - U_{j+1}^n) + \frac{h}{h_j^{n+1}} (f_j^{n+\frac{1}{2}} + f_{j+1}^{n+\frac{1}{2}}) (U_j^n + U_{j+1}^n) + \right. \\ & \left. \frac{h}{4k^n} (U_j'^n + U_{j+1}'^n) + \frac{h}{4h_j^{n+1}} (f_j^{n+\frac{1}{2}} + f_{j+1}^{n+\frac{1}{2}}) (U_j'^n - U_{j+1}'^n) \right). \end{aligned} \quad (18)$$

Next, we will show in what follows that the Lagrangian-Eulerian numerical flux function (18) satisfy a form of *Lipschitz continuous consistency*, which in turn is a nice property for *conservative numerical methods* for nonlinear conservation law problems. Indeed, to show that the Lagrangian-Eulerian numerical flux satisfies a Lipschitz condition, we need (see [33]):

Lemma 1. *The numerical flux function defined by (18) is consistent with the differential equation (1).*

Proof. Immediate, i.e., $F(\bar{u}, \bar{u}) = H(\bar{u})$. Notice that for any choice of slope limiters, we have from (7) that (18) satisfy the consistency condition, the MinMod limiter in this case will be zero. The Lipschitz condition can also be proved by a straightforward argument and it is omitted.

3. The Lagrangian-Eulerian scheme for hyperbolic balance laws

One may find, in a variety of physical problems, source terms that are balanced by internal forces and this balance supports multiple steady-state solutions that are stable. We are interested in designing well-balanced conceptually simple schemes, which have a well balanced property for static and moving equilibrium, applicable to a wide class of systems with source terms. The well-balance property can be formally enunciated as follows. Consider the system of balance laws as such,

$$\frac{\partial u}{\partial t} + \frac{\partial(H(u))}{\partial x} = G(u), \quad (19)$$

we denote u^e the stationary solution, which satisfies the equation,

$$\frac{\partial(H(u^e))}{\partial x} = G(u^e), \quad (20)$$

A numerical scheme is said to be *well-balanced*, if it fully satisfies a discrete version of the equilibrium equation (20). If a method is not well-balanced, the truncation error of solutions near of equilibrium state

may be larger than $u(x, t) - u^e(x)$. Numerical experiments for solving balance laws have shown strong numerical evidence that such well-balanced property is satisfied when we applied the Lagrangian-Eulerian scheme for several models of balance laws [33].

Consider the scalar balance law problem,

$$\frac{\partial u}{\partial t} + \frac{\partial H(u)}{\partial x} = G(u), \quad t > 0, \quad x \in \mathbb{R}, \quad u(x, 0) = \eta(x) \quad x \in \mathbb{R}, \quad (21)$$

under the assumption $\iint_{D_j^n} G(u) \, dx \, dt < \infty$.

Now, write (21) as follows,

$$\nabla_{t,x} \cdot \begin{bmatrix} u \\ H(u) \end{bmatrix} = G(u) \quad t > 0, \quad x \in \mathbb{R}, \quad u(x, 0) = \eta(x) \quad x \in \mathbb{R}. \quad (22)$$

Now, let us write (22) over the local space-time “Integral tube” D_j^n ,

$$\iint_{D_j^n} \nabla_{t,x} \cdot \begin{bmatrix} u \\ H(u) \end{bmatrix} \, dx \, dt = \iint_{D_j^n} G(u) \, dx \, dt. \quad (23)$$

Following the same arguments in Section 2, we apply first the divergence theorem in (23) and, by means of the impervious boundaries given by $\sigma_j^n(t)$, reads:

$$\int_{\bar{x}_j^{n+1} - \frac{1}{2}}^{\bar{x}_j^{n+1} + \frac{1}{2}} u(x, t^{n+1}) \, dx = \int_{x_j^n}^{x_j^{n+1}} u(x, t^n) \, dx + \iint_{D_j^n} G(u) \, dx \, dt. \quad (24)$$

This equation can be viewed as *the local space-time Lagrangian-Eulerian conservation relation* for the balance law (24). Finally, we use (24) then to define,

$$\bar{U}_j^{n+1} = \frac{1}{h_j^{n+1}} \int_{\bar{x}_j^{n+1} - \frac{1}{2}}^{\bar{x}_j^{n+1} + \frac{1}{2}} u(x, t^{n+1}) \, dx = \frac{1}{h_j^{n+1}} \left[\int_{x_j^n}^{x_j^{n+1}} u(x, t^n) \, dx + \iint_{D_j^n} G(u) \, dx \, dt \right], \quad (25)$$

and its associated projection step over the original mesh grid,

$$U_j^{n+1} = \frac{1}{h} \left[\left(\frac{h}{2} + f_j^{n+\frac{1}{2}} k \right) \bar{U}_{j-1}^{n+1} + \left(\frac{h}{2} - f_j^{n+\frac{1}{2}} k \right) \bar{U}_j^{n+1} \right]. \quad (26)$$

The Lagrangian-Eulerian scheme for balance law is fully defined by combining equations (25) and (26). The key point here is how to design a discretization in a manner that an accurate balance between the gradients of the flux function and the source term is retained. Thus, let us now first extend the proposed scheme for linear hyperbolic conservation laws designed in the previous section to the case of balance laws in order to describe the features of the Lagrangian-Eulerian procedure.

Thus, combining equations (25)-(26) gives the Lagrangian-Eulerian scheme for nonlinear balance laws:

$$\begin{aligned} U_j^{n+1} &= \frac{U_{j-1}^n + 2U_j^n + U_{j+1}^n}{4} + \frac{U_{j-1}'^n - U_{j+1}'^n}{32} \\ &+ \frac{k^n}{4} \left(\frac{f_{j-1}^{n+\frac{1}{2}} + f_j^{n+\frac{1}{2}}}{h_{j-1}^{n+1}} [U_{j-1}^n + U_j^n] - \frac{f_j^{n+\frac{1}{2}} + f_{j+1}^{n+\frac{1}{2}}}{h_{j+1}^{n+1}} [U_j^n + U_{j+1}^n] \right) \\ &+ \frac{k^n}{32} \left(\frac{f_{j-1}^{n+\frac{1}{2}} + f_j^{n+\frac{1}{2}}}{h_{j-1}^{n+1}} [U_{j-1}'^n - U_j'^n] - \frac{f_j^{n+\frac{1}{2}} + f_{j+1}^{n+\frac{1}{2}}}{h_{j+1}^{n+1}} [U_j'^n - U_{j+1}'^n] \right) \\ &+ \frac{1}{h_j^{n+1}} \left[\frac{1}{h_j^{n+1}} \left(\frac{h_j^{n+1}}{2} + f_j^{n+\frac{1}{2}} k^n \right) \iint_{D_{j-1}^n} G(u(x, t)) \, dx \, dt \right. \\ &\left. + \frac{1}{h_j^{n+1}} \left(\frac{h_j^{n+1}}{2} - f_j^{n+\frac{1}{2}} k^n \right) \iint_{D_j^n} G(u(x, t)) \, dx \, dt \right]. \end{aligned} \quad (27)$$

Here, we use the same approximations as before with respect to (27), namely, $f_j^{n+\frac{1}{2}} = \frac{H(U_j^{n+\frac{1}{2}})}{U_j^{n+\frac{1}{2}}}$ and $f_j^n = \frac{H(U_j^n)}{U_j^n} \approx \frac{H(u)}{u}$. Notice that the quantities $\left(\frac{h_j^{n+1}}{2} + f_j^{n+\frac{1}{2}} k^n\right)$ and $\left(\frac{h_j^{n+1}}{2} - f_j^{n+\frac{1}{2}} k^n\right)$ are not the characteristic curves associated to the quasilinear form of the homogeneous counterpart of the balance law but rather they are precisely an approximation of the conservative integral tubes that are naturally extracted from the conservative integral form of the nonlinear balance law given by (21), which in turn dictates the dynamics of the local space-time control volume D_j^n and the position $\sigma_j^n(t)$ to any quadrature rule of the source term $G(u)$ of the RHS of (21). In addition, the balance problem is then solved by forward tracking the boundary of grid cells along the so-called integral tubes. This is a distinct feature of the proposed Lagrangian-Eulerian approach. The similar Eulerian-Lagrangian schemes in [24] are designed to handle trace-back integration related to purely hyperbolic problems rather than balance laws. Several quadrature rules can be used to such aim, based on the above framework [33]. We present a predictor-corrector type of approximation, but midpoint and trapezoidal rules have also been studied in the work [33].

We make use of $U_j^{n+\frac{1}{2}}$ as the known predictor value for $u(x, t)$ at space-time point (x_j, t^n) . Thus, write the source term approximation as,

$$\iint_{D_j^n} G(u(x, t)) \, dx \, dt \approx \iint_{D_j^n} G(U_j^{n+\frac{1}{2}}) \, dx \, dt = G(U_j^{n+\frac{1}{2}}) \iint_{D_j^n} dx \, dt = G(U_j^{n+\frac{1}{2}}) \mathcal{A}(D_j^n),$$

where

$$\mathcal{A}(D_j^n) = \int_{t^n}^{t^{n+1}} \int_{\sigma_j^n(t)}^{\sigma_{j+1}^{n+1}(t)} dx \, dt = \int_{t^n}^{t^{n+1}} (\sigma_{j+1}^{n+1}(t) - \sigma_j^n(t)) \, dt. \quad (28)$$

Since $\sigma_{j+1}^{n+1}(t) - \sigma_j^n(t) = (t - t^n)f_{j+1}^{n+\frac{1}{2}} + x_{j+1}^n - (t - t^n)f_j^{n+\frac{1}{2}} - x_j^n = (t - t^n)(f_{j+1}^{n+\frac{1}{2}} - f_j^{n+\frac{1}{2}}) + h$, we recast (28) as,

$$\mathcal{A}(D_j^n) = k \left[\frac{k}{2}(f_{j+1}^{n+\frac{1}{2}} - f_j^{n+\frac{1}{2}}) + h \right].$$

Now, in view of the balance law $u_t + H_x(u) = G(u)$ we might write $u_t = G(u) - H_x(u)$ and thus reads,

$$G(u_j^{n+\frac{1}{2}}) \approx G(u(x_j^n, t^n) + \frac{k}{2}u_t(x_j^n, t^n)) = G \left[u_j^n + \frac{k}{2}(G(u_j^n) - (H(u))_x)_j^n \right]. \quad (29)$$

Here again the quantity $H_x(u(x, t))_j^n$ denotes the numerical derivative of function $H(u)$ with respect to space variable x evaluated at point (x_j, t^n) , and a family of slope limiters can be used here. Finally, from equations (28) and (29), we might write,

$$\iint_{D_j^n} G(u(x, t)) \, dx \, dt \approx k^n G \left[U_j^n + \frac{k^n}{2}(G(U_j^n) - H_x(u)_j^{n+\frac{1}{2}}) \right] \left[\frac{k^n}{2}(f_{j+1}^{n+\frac{1}{2}} - f_j^{n+\frac{1}{2}}) + h_j^{n+1} \right]. \quad (30)$$

4. Extension to systems of hyperbolic conservation laws and balance laws

We now turn our attention to describing how to extend the scalar Lagrangian-Eulerian procedure to one-dimensional systems of balance laws $u_t + f_x(u) = G(u)$, where now $u(x, t)$ can be viewed as the unknown n -vector of the form $u = (u_1(x, t), u_2(x, t), \dots, u_n(x, t))^T$, and $f(u)$ is the flux vector function such that $f(u) = (f_1(u), f_2(u), \dots, f_n(u))^T$. We will see that the analogue Lagrangian-Eulerian scheme in the case of systems of balance laws is a straightforward application of the scalar framework and that retains all the simplicities of the scalar case. For simplicity of presentation and with no loss of generality, let us consider the following prototype 3×3 system of balance laws.

We consider the system of balance laws

$$Q_t + [F(Q)]_x = G(Q), \quad (31)$$

where $F(Q) = [f_1(Q), f_2(Q), f_3(Q)]$, $Q = [u, v, w]$, $u = u(x, t)$, $v = v(x, t)$ and $w = w(x, t)$, along with $G(Q) = [g_1(Q), g_2(Q), g_3(Q)]$. System (31) can be written in open form as,

$$u_t + [f_1(u, v, w)]_x = g_1(u, v, w), \quad v_t + [f_2(u, v, w)]_x = g_2(u, v, w), \quad w_t + [f_3(u, v, w)]_x = g_3(u, v, w). \quad (32)$$

As before, we consider the space-time control finite volumes for each variable u, v, w as follows, (see Figure 2 for an illustration of the integral tubes and its approximations for systems),

$$D_{s,j}^n = \{(t, x) / t^n \leq t \leq t^{n+1}, \quad \sigma_{s,j}^n(t) \leq x \leq \sigma_{s,j+1}^n(t)\}, \quad s = u, v, w, \quad (33)$$

where $\sigma_{u,j}^n(t)$, $\sigma_{v,j}^n(t)$ and $\sigma_{w,j}^n(t)$ are parametrized curves such that $\sigma_{u,j}^n(t^n) = x_j^n$, $\sigma_{v,j}^n(t^n) = x_j^n$ and $\sigma_{w,j}^n(t^n) = x_j^n$. These curves $\sigma_{s,j}^n(t)$, $s = u, v, w$ define the “lateral boundaries” of integral tubes for each primitive variable u, v, w , that will be used to design a balancing *unbiased* upwinding Riemann-solver-free discretization between the numerical flux functions and the source terms by forward tracking the boundaries along the so-called integral tubes (see left picture in the Figure 2). Formally, the divergence theorem can

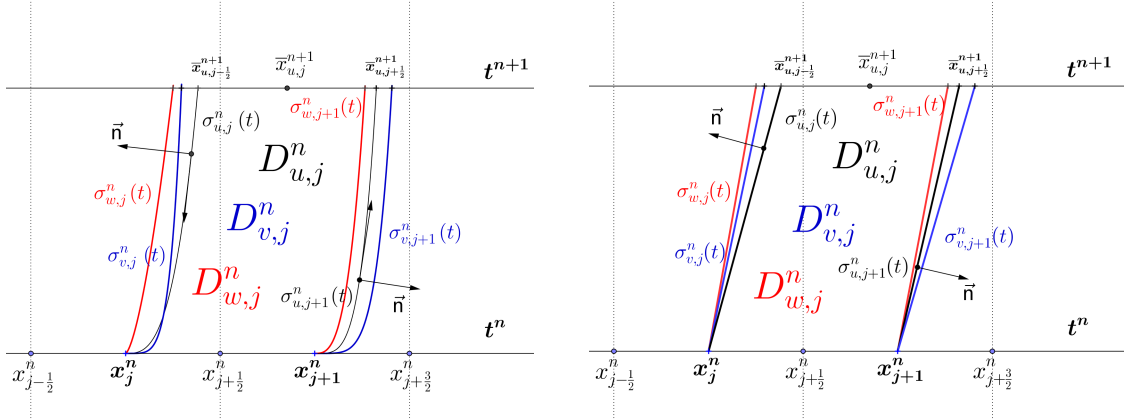


Figure 2: On the left (resp. right) is shown an illustration of the continuous (resp. discrete) local space-time integral tube domains $D_{s,j}^n$, for each $s = u, v, w$.

be used in the (33), the space-time finite volumes $D_{u,j}^n$, $D_{v,j}^n$ and $D_{w,j}^n$. By construction of the algorithm, as before, this implies that curves $\sigma_{s,j}^n(t)$ and $\sigma_{s,j+1}^n(t)$, for $s = u, v, w$ are naturally zero-flux boundaries. Similarly, from this fact the space-time $D_{s,j}^n$, $s = u, v, w$ are then called as “Integral tubes” for $t^n \leq t \leq t^{n+1}$. As a consequence we get, for the normal vectors n_s of each integral curve for each variable $s = u, v, w$, $\left[1, \frac{d\sigma_{s,j}^n(t)}{dt}\right] \perp n_s$ and $\left[1, \frac{d\sigma_{s,j+1}^n(t)}{dt}\right] \perp n_s$ since the slopes $\frac{d\sigma_{s,j}^n(t)}{dt}$ are one-to-one equal to the slope of the vector $[s, f_k(Q)]$, $s = u, v, w$; $k = 1, 2, 3$, respectively, over the parametrized curves $\sigma_{s,j}^n(t)$ and $\sigma_{s,j+1}^n(t)$, $s = u, v, w$, $j \in \mathbb{Z}$. Therefore $\sigma_{s,j}^n(t)$, $s = u, v, w$ are solutions of the set of ODEs,

$$\frac{d\sigma_{s,j}^n(t)}{dt} = \frac{f_k(u, v, w)}{s}, \quad \sigma_{s,j}^n(t^n) = x_j^n, \quad t^n \leq t \leq t^{n+1}, \quad \text{for each } s = u, v, w; k = 1, 2, 3, \quad (34)$$

where $u, v, w \neq 0$. As a consequence of the divergence theorem and the above equations (33)-(34), the integrals over curves $\sigma_{s,j}^n(t)$, $s = u, v, w$ vanish and the line integral over the boundary of the region $\partial D_{s,j}^n$ leads to,

$$\int_{\bar{x}_{j-\frac{1}{2}}^{n+1}}^{\bar{x}_{j+\frac{1}{2}}^{n+1}} s(x, t^{n+1}) dx = \int_{x_j^n}^{x_{j+1}^n} s(x, t^n) dx + \iint_{D_{s,j}^n} g_k(u, v, w) dx dt, \quad (35)$$

where $s = u, v, w$; $k = 1, 2, 3$, respectively, and we can define as before $\bar{x}_{s,j-\frac{1}{2}}^{n+1} = \sigma_{s,j}^n(t^{n+1})$ and $\bar{x}_{s,j+\frac{1}{2}}^{n+1} = \sigma_{s,j+1}^n(t^{n+1})$. Equation (35) is called “locally conservative relation” to the system of balance laws (32).

Thus, the approximations of the variables u, v, w for system are a rather component-wise extension of the scalar framework given by (for $S = U, V, W$ and $s = u, v, w$),

$$S_j^n = \frac{1}{h} \int_{x_{j-\frac{1}{2}}^n}^{x_{j+\frac{1}{2}}^n} s(x, t^n) dx, \quad \text{and} \quad \bar{S}_j^{n+1} = \frac{1}{h_{s,j}^{n+1}} \int_{\bar{x}_{j-\frac{1}{2}}^{n+1}}^{\bar{x}_{j+\frac{1}{2}}^{n+1}} s(x, t^{n+1}) dx \quad j \in \mathbb{Z}, \quad (36)$$

respectively, and the initial condition is $U(x_j^0, t^0) = U_j^0$, $V(x_j^0, t^0) = V_j^0$ and $W(x_j^0, t^0) = W_j^0$ over the local space-time cells $[x_{j-\frac{1}{2}}^0, x_{j+\frac{1}{2}}^0]$, $j \in \mathbb{Z}$. Next, we use (36) into to “locally conservative relation” to get,

$$\bar{S}_j^{n+1} = \frac{1}{h_{s,j}^{n+1}} \int_{\bar{x}_{j-\frac{1}{2}}^{n+1}}^{\bar{x}_{j+\frac{1}{2}}^{n+1}} s(x, t^{n+1}) dx = \frac{1}{h_{s,j}^{n+1}} \left[\int_{x_j^n}^{x_{j+1}^n} s(x, t^n) dx + \iint_{D_{s,j}^n} g_k(u, v, w) dx dt \right]. \quad (37)$$

In (37) $S = (U, V, W)$ and $s = (u, v, w)$ denotes a representation of a component-wise extension of the scalar case to systems of balance laws in compact form (31). Next, the local approximations \bar{S}_j^{n+1} , $j \in \mathbb{Z}$ are projected over the original grid and reads,

$$S_j^{n+1} = \frac{1}{h} \left[c_{s,0j} \bar{S}_{j-1}^{n+1} + c_{s,1j} \bar{S}_j^{n+1} \right]. \quad (38)$$

Here $c_{s,0j} = (\frac{h}{2} + f_{s,j}^{n+\frac{1}{2}} k)$, $c_{s,1j} = h - c_{s,0j} = (\frac{h}{2} - f_{s,j}^{n+\frac{1}{2}} k)$ and we use the approximation $f_{s,j}^{n+\frac{1}{2}} = \frac{f_k(U_j^{n+\frac{1}{2}}, V_j^{n+\frac{1}{2}}, W_j^{n+\frac{1}{2}})}{S_j^{n+\frac{1}{2}}} \approx \frac{f_k(u, v, w)}{s}$, $S = U, V, W$, $s = u, v, w$ and $k = 1, 2, 3$, respectively. Notice that now the curve $\sigma_{s,j}^n(t)$ is a simple straight line for $f_{s,j}^n$ (see right picture in Figure 2), along with $k^n = \Delta t^n = t^{n+1} - t^n$. Finally, combination of equations (37) and (38) form the building-block for the new Lagrangian-Eulerian scheme, which reads as a componentwise extension for equation 27 ($S = U, V, W$, $s = u, v, w$ and $k = 1, 2, 3$, respectively):

$$\begin{aligned} S_j^{n+1} &= \frac{S_{j-1}^n + 2S_j^n + S_{j+1}^n}{4} + \frac{S'_{j-1} - S'_{j+1}}{32} \\ &+ \frac{k^n}{4} \left(\frac{f_{k,j-1}^{n+\frac{1}{2}} + f_{k,j}^{n+\frac{1}{2}}}{h_{j-1}^{n+1}} [S_{j-1}^n + S_j^n] - \frac{f_{k,j}^{n+\frac{1}{2}} + f_{k,j+1}^{n+\frac{1}{2}}}{h_j^{n+1}} [S_j^n + S_{j+1}^n] \right) \\ &+ \frac{k^n}{32} \left(\frac{f_{k,j-1}^{n+\frac{1}{2}} + f_{k,j}^{n+\frac{1}{2}}}{h_{j-1}^{n+1}} [S'_{j-1} - S_j^n] - \frac{f_{k,j}^{n+\frac{1}{2}} + f_{k,j+1}^{n+\frac{1}{2}}}{h_j^{n+1}} [S_j^n + S'_{j+1}] \right) \\ &+ \frac{1}{h_j^{n+1}} \left[\frac{1}{h_j^{n+1}} \left(\frac{h_j^{n+1}}{2} + f_{k,j}^{n+\frac{1}{2}} k^n \right) \iint_{D_{j-1}^n} G_k(s(x, t)) dx dt \right. \\ &\left. + \frac{1}{h_j^{n+1}} \left(\frac{h_j^{n+1}}{2} - f_{k,j}^{n+\frac{1}{2}} k^n \right) \iint_{D_j^n} G_k(s(x, t)) dx dt \right]. \end{aligned} \quad (39)$$

5. Two-dimensional hyperbolic conservation laws

We now turn our attention to introducing a new computational approach for the design of a new class of approximate solutions for two-dimensional hyperbolic conservation laws. This novel scheme is based on the same Lagrangian-Eulerian framework discussed for the one-dimensional scalar problem.

A natural first attempt would be a straightforward extension used in the one-dimensional case, but now applied to three-dimensional variables (x, y and t) as $D_{i,j}^n \subset \mathbb{R}^3$, see Figure 3 (left), where i and j refer to (x_i, y_j) and n refers to time level t^n . The boundary of control volumes $D_{i,j}^n$ will be denoted by $\partial D_{i,j}^n = R_{i,j}^n \cup S_{i,j}^n \cup \bar{R}_{i,j}^{n+1}$ where the control volume $R_{i,j}^n = [x_{i-\frac{1}{2}}^n, x_{i+\frac{1}{2}}^n] \times [y_{j-\frac{1}{2}}^n, y_{j+\frac{1}{2}}^n]$ in \mathbb{R}^2 is the “inflow” of the integral tube, $\bar{R}_{i,j}^{n+1}$ in \mathbb{R}^2 is the “outflow” of the integral tube, while $S_{i,j}^n$, in \mathbb{R}^3 , is the lateral (impervious) surface of the tube. As before, we consider the hyperbolic conservation law in two-dimensional

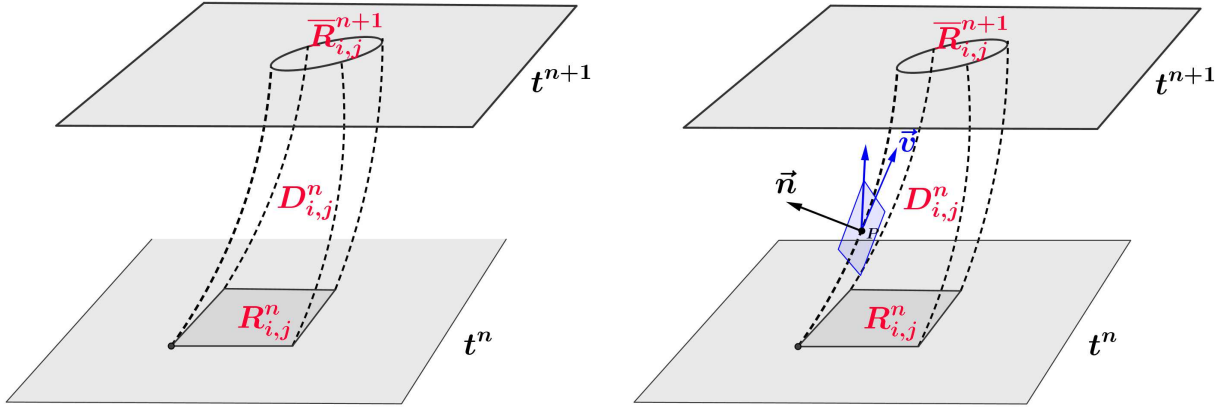


Figure 3: Integral tube in 3D.

variables in divergence form,

$$\frac{\partial u}{\partial t} + \frac{\partial f(u)}{\partial x} + \frac{\partial g(u)}{\partial y} = 0 \quad \Longleftrightarrow \quad \nabla_{t,x,y} \begin{bmatrix} u \\ f(u) \\ g(u) \end{bmatrix} = 0. \quad (40)$$

Again, the integration over the control volume and the application of the divergence theorem gives,

$$\iiint_{D_{i,j}^n} \nabla_{t,x,y} \begin{bmatrix} u \\ f(u) \\ g(u) \end{bmatrix} dV = 0 \quad \Leftrightarrow \quad \int_{\partial D_{i,j}^n} \begin{bmatrix} u \\ f(u) \\ g(u) \end{bmatrix} \cdot \vec{n} d(\partial D_{i,j}^n) = 0. \quad (41)$$

The normal vector with respect to $R_{i,j}^n$ is, in usual convention, $[-1 \ 0 \ 0]^T$ and the vector normal in the outflow $\bar{R}_{i,j}^{n+1}$ is $[1 \ 0 \ 0]$. Then, the right side of (41) can be written as,

$$\int_{R_{i,j}^n} \begin{bmatrix} u \\ f(u) \\ g(u) \end{bmatrix} \cdot [-1 \ 0 \ 0]^T dA + \int_{S_{i,j}^n} \begin{bmatrix} u \\ f(u) \\ g(u) \end{bmatrix} \cdot \vec{n} dS + \int_{\bar{R}_{i,j}^{n+1}} \begin{bmatrix} u \\ f(u) \\ g(u) \end{bmatrix} \cdot [1 \ 0 \ 0]^T dA = 0. \quad (42)$$

We suppose there is not any flow through the surface $S_{i,j}^n$ ($S_{i,j}^n$ is impervious). So, the surface integral of $S_{i,j}^n$ is zero and therefore,

$$-\int_{R_{i,j}^n} u(x, y, t^n) dA + \int_{\bar{R}_{i,j}^{n+1}} u(x, y, t^{n+1}) dA = 0. \quad (43)$$

or

$$\int_{\bar{R}_{i,j}^{n+1}} u(x, y, t^{n+1}) dA = \int_{R_{i,j}^n} u(x, y, t^n) dA, \quad (44)$$

which we call conservation identity. The numerical approximations $U_{i,j}^n$ and $\bar{U}_{i,j}^{n+1}$ can be defined from (44).

The core issue of this approach is to define the normal vector \vec{n} along with the unique definition of the tangent vector \vec{v} to the surface $S_{i,j}^n$ in the point (x_i, y_j, t^n) , see right picture in Figure 3. Notice that at this point there is a tangent plane, then the *integral surfaces* as well as *integral curves* coming from $[u \ f(u) \ g(u)]^T \cdot \vec{n} = 0$ seem to be at first glance not straightforward to construct. One possibility is to define the concepts of *Mean curvature* and *Gaussian curvature* associated with the underlying conservation

law [23] (see also [26]). In this regard, one possibility is to construct naturally a normal curvature and a geodesic curvature from equation (40). They are primarily given by the projection of \vec{v} onto the local normal vector and the local tangent plane, respectively. Thus, it is possible to define a unique curve for each one of the points that appear at the bottom of the integral tube, from time step t^n to t^{n+1} , at least from a theoretical viewpoint. For concreteness, one possible numerical approach is to consider the level set approach introduced in [32] (see also [11]).

The construction of optimal methods based on the approach above needs a novel theory along with feasible numerical algorithms to be pursued later on. On the other hand, we here propose a simple, fast, and also elegant alternative approach. Our procedure is based in writing the two-dimensional scalar conservation law (45) in the form of a coupled set of two balance laws along with initial data. The main idea behind our approach is quite simple. First, consider the two-dimensional nonlinear hyperbolic conservation law with initial data,

$$\begin{cases} \frac{\partial U}{\partial t} + \frac{\partial f(U)}{\partial x} + \frac{\partial g(U)}{\partial y} = 0, \\ U(x, y, t^n) = U^n. \end{cases} \quad (45)$$

The initial data at a time t^n is given by the set U^n of discrete cell average values $U_{i,j}^n$, where i denotes the x -direction and j denotes the y -direction. Consider now the cell-centered finite-volume cells,

$$\begin{aligned} D_{i,j}^n &= \{(t, x, y)/t^n \leq t \leq t^{n+\frac{1}{2}}, y_{j-\frac{1}{2}}^n \leq y \leq y_{j+\frac{1}{2}}^n, \sigma_i^n(t) \leq x \leq \sigma_{i+1}^n(t)\}, \\ D_{i,j}^{n+\frac{1}{2}} &= \{(t, x, y)/t^{n+\frac{1}{2}} \leq t \leq t^{n+1}, x_{i-\frac{1}{2}}^{n+\frac{1}{2}} \leq x \leq x_{i+\frac{1}{2}}^{n+\frac{1}{2}}, \gamma_j^{n+\frac{1}{2}}(t) \leq y \leq \gamma_{j+1}^{n+\frac{1}{2}}(t)\}, \end{aligned}$$

where $\sigma_i^n(t)$ and $\gamma_j^n(t)$ are parameterized curves such that $\sigma_i^n(t^n) = x_i^n$ and $\gamma_j^{n+\frac{1}{2}}(t^{n+\frac{1}{2}}) = y_j^{n+\frac{1}{2}}$. Our approach is based in writing (45) in the form of a coupled set of two balance laws along with initial data,

$$\begin{cases} \frac{\partial U}{\partial t} + \frac{\partial f(U)}{\partial x} = - \left(\frac{\partial g(U)}{\partial y} \right)_j, & \text{in } D_{i,j}^n, \\ U(x, y, t^n) = U^n, \end{cases} \quad (46a)$$

$$\begin{cases} \frac{\partial U}{\partial t} + \frac{\partial g(U)}{\partial y} = - \left(\frac{\partial f(U)}{\partial x} \right)_i, & \text{in } D_{i,j}^{n+\frac{1}{2}}, \\ U(x, y, t^{n+\frac{1}{2}}) = U^{n+\frac{1}{2}}. \end{cases} \quad (46b)$$

where $\left(\frac{\partial g(U)}{\partial y} \right)_j$ and $\left(\frac{\partial f(U)}{\partial x} \right)_i$ are numerical approximations of derivatives respectively. Denote $S_x(t)$ and $S_y(t)$ as approximate solution operators for (46a) and (46b), respectively. Indeed, such approximate solution operators can be given by scheme (27)-(30). but in both directions x or y . Thus, $U_{i,j}^{n+\frac{1}{2}} = S_x(\Delta t/2)U_{i,j}^n$ and $U_{i,j}^{n+1} = S_y(\Delta t/2)U_{i,j}^{n+\frac{1}{2}}$, so that, the full scheme is given by,

$$U_{i,j}^{n+1} = S_y(\Delta t/2)S_x(\Delta t/2)U_{i,j}^n, \quad (47)$$

along with the CFL condition,

$$Mk/h \leq \sqrt{2}/2, \quad (48)$$

with $M = \max\{\max_j\{f'(U_{i,j}^n)\}, \max_j\{\frac{f(U_{i,j}^n)}{U_{i,j}^n}\}, \max_j\{g'(U_{i,j}^n)\}, \max_j\{\frac{g(U_{i,j}^n)}{U_{i,j}^n}\}\}$. The equations appearing in (46a) and (46b) can be viewed as a set of local balance laws in the time step $(t^n, t^{n+1}]$, but coupled via the source terms on the RHS of (46) and thus linked to the full problem (45). Then the procedure to solve (45) is quite simple as follows: in the time step from t^n to $t^{n+\frac{1}{2}}$ the information of the previous time, say, in the y coordinate is accounted through the source term for the balance law in the x coordinate. Similarly, in time step from $t^{n+\frac{1}{2}}$ to t^{n+1} , the information in the x coordinate is also accounted through of the source term for the balance law in the y coordinate. This formulation has allowed us to correctly approximate solutions of two-dimensional hyperbolic conservation law problems from paper [18] as we show in Section 6.

6. Numerical experiment studies with applications

We first present a mesh refinement study in order to give some numerical evidence of convergence for the proposed scheme. Next, computations for scalar conservation laws with convex and non-convex flux functions are presented and discussed. A problem modeling three-phase flow in porous media for one-dimensional problems is presented, illustrating an example of system of conservation laws. We then present two examples of two-dimensional conservation laws. Next, we show examples for scalar balance laws, the numerical well-balancedness property and systems of balance laws modeling shallow water equations.

6.1. Convex and non-convex flux functions for conservation laws

For a first mesh refinement study we test our scheme with a non-convex flux function to the scalar conservation law $u_t + f_x(u) = 0$, for $f(u) = 0.5(e^{-25(u-0.5)^2} + 8(u-0.5)^2)$, along with Riemann initial data $u(x, 0) \equiv \eta(x) = 0.8, x < 0$ and $u(x, 0) \equiv \eta(x) = 0.2, x > 0$. In Figure 4 is shown three different mesh grid cells (128, 256 and 512) against a reference numerical solution with 1024 mesh grid cells at dimensionless time $t = 2.0$.

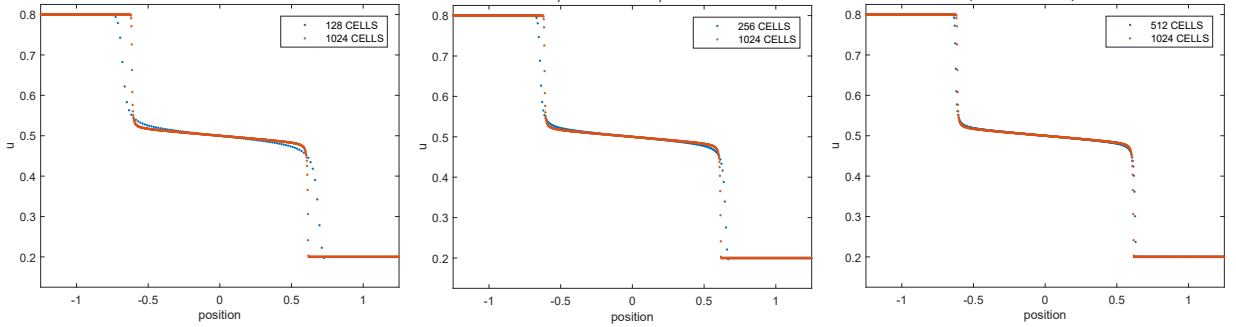


Figure 4: Mesh refinement study for a non-convex flux function. The finest mesh in this case is a solution with 1024 grid cells.

In Figure 5 it is shown numerical solutions for $u_t + \left(\frac{u^2}{2}\right)_x = 0$, along with smooth initial data $u(x, 0) = 0.5 + \sin(x)$. It is well-known that the solution of this problem develops a shock discontinuity at the critical time $T_c = 1$, and then it exhibits pre-shock (resp. post-shock) solution for $T_c < 1$ (resp. $T_c > 1$); on the left it is shown the post-shock solution computed with (17)-(18) at time simulation $t = 2$ for 256 cells. We have also conducted similar numerical experiments to problem $u_t + \left(\frac{u^2}{2}\right)_x = 0$ along with discontinuous initial data $u(x, 0) = 1, x < 0$ & $u(x, 0) = 0, x > 0$ (middle: shock) and $u(x, 0) = -1, x < 0$ & $u(x, 0) = 1, x > 0$ (right: rarefaction). On these frames are shown snapshot graphs at time $t = 2.4$ of simulation, with waves moving from left to right. We get a very nice looking numerical approximate solution with scheme (17)-(18), which in turn seems to be propagating at entirely entropy-correct Rankine-Hugoniot speed (middle). Similar good results are shown to the rarefaction case as well. Indeed, in the terminology of gas dynamics to the rarefaction cases for the inviscid Burgers equation we see that the transonic rarefaction (right frame) is well resolved. That is, as the rarefaction wave is crossed, there is a sign change in the characteristic speed u and thus there is one point at which $u = 0$, the sonic point. So, there is no spurious anomalies around $u = 0$.

We now turn attention to the classical nonlinear one-dimensional Buckley-Leverett two-phase problem [28, 29], which in turn is depicted in left picture in Figure 6. Computed solutions with scheme (17)-(18) at time simulation $t = 2$ are shown to the Riemann Problem (Initial Value Problem with non-convex flux function): $u_t + f_x(u) = 0, f(u) = u^2/(u^2 + a(1 - u)^2), a = 1$, along with Riemann initial data (left) $u(x, 0) \equiv \eta(x) = 1.0, x < 0$ and $u(x, 0) \equiv \eta(x) = 0.0, x > 0$. On physical ground, such initial data corresponds to water flooding of an oil reservoir. The well known solution for this model comprises a leading shock wave (an oil bank) followed by an attached rarefaction wave. The weak solution satisfying the Oleinik entropy condition is in very good agreement along with the scheme (17)-(18) propagating at entirely entropy-correct Rankine-Hugoniot speed and with the precisely post-shock value. We have also considered another

non-convex flux function (see right picture in Figure 6) to the scalar conservation law $u_t + f_x(u) = 0$, with $f(u) = 0.5(e^{-25(u-0.5)^2} + 8(u-0.5)^2)$, along with Riemann initial data (left) $u(x, 0) \equiv \eta(x) = 0.8$, $x < 0$ and $u(x, 0) \equiv \eta(x) = 0.2$, $x > 0$. Again, the numerical solution is in agreement with Oleinik entropy condition, whose approximate left and right shock waves are propagating with correct Rankine-Hugoniot speed and entropy-correct post-shock values.

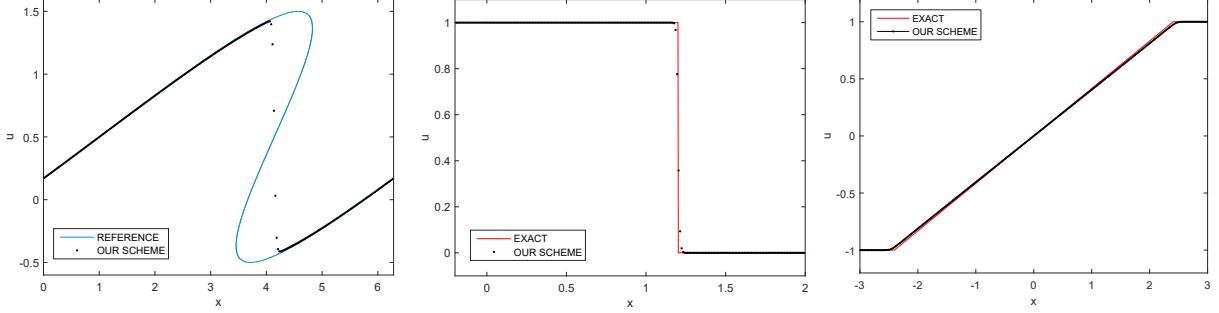


Figure 5: Inviscid nonlinear Burgers' problem: post-shock solution for smooth initial data (left), Riemann problem with shock wave (middle), Riemann problem with rarefaction fan (right).

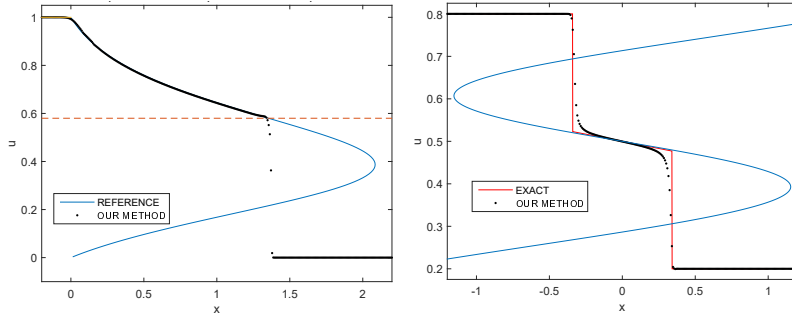


Figure 6: Left: Classical one-dimensional Buckley-Leverett two-phase problem computed by scheme (17)-(18). Right: A non-convex flux function.

6.2. Non-strictly hyperbolic three-phase system of conservation laws in porous media applications

First, let us briefly review a immiscible incompressible three-phase formulation for porous media [2, 31]. In this formulation the governing equations are written in terms of a pressure, expressing Darcy's law of force, coupled to two saturation equations that express the conservation of mass of water, oil and gas. In one dimension the pressure equation implies that the total fluid velocity is independent of position, so we take it to be constant. After nondimensionalizing the time (we suppose the porosity to be a constant) and space variables, fluid viscosities, and capillary pressures in the standard way, one obtains the following system of partial differential equations [31, 2]:

$$\frac{\partial s_w}{\partial t} + \frac{\partial}{\partial x} f_w(s_w, s_g) = \frac{\partial w_w}{\partial x}, \quad (49)$$

$$\frac{\partial s_g}{\partial t} + \frac{\partial}{\partial x} f_g(s_w, s_g) = \frac{\partial w_g}{\partial x}, \quad (50)$$

where

$$w_w = \left(\lambda_w(1 - f_w) \frac{\partial p_{wo}}{\partial s_w} - \lambda_w f_g \frac{\partial p_{go}}{\partial s_w} \right) \frac{\partial s_w}{\partial x} + \left(\lambda_w(1 - f_w) \frac{\partial p_{wo}}{\partial s_g} - \lambda_w f_g \frac{\partial p_{go}}{\partial s_g} \right) \frac{\partial s_g}{\partial x}, \quad (51)$$

and

$$w_g = \left(-\lambda_g f_w \frac{\partial p_{wo}}{\partial s_w} + \lambda_g (1 - f_g) \frac{\partial p_{go}}{\partial s_w} \right) \frac{\partial s_w}{\partial x} + \left(-\lambda_g f_w \frac{\partial p_{wo}}{\partial s_g} + \lambda_g (1 - f_g) \frac{\partial p_{go}}{\partial s_g} \right) \frac{\partial s_g}{\partial x}. \quad (52)$$

Here, λ_i is the relative mobility, $\lambda_i = \frac{k_i(s_w, s_g)}{\mu_i}$, k_i is the relative permeability, μ_i is the fluid viscosity, $\lambda = \sum_i \lambda_i$ is the total mobility and $f_i(s_w, s_g) = \lambda_i / \lambda$ are the fractional flow functions. Here, the constraint $s_w + s_g + s_o = 1$ is imposed. In our model we choose, for convenience, to work with the saturations of water and gas. The diffusive term is represented by the right-hand side of the system (49)-(50) and it incorporates the capillary pressure effects. We neglect the capillary diffusive effect, by just taking $w_w = 0$ and $w_g = 0$ in (49)-(52), but we do know from [2, 31] how the correct structure of the solutions of the non-classical three-phase model under consideration is. However, we point out that for a wave to be truly defined as a “shock wave”, a discontinuity must be the zero-diffusion limit of traveling wave solutions. For such solutions, diffusion balances the convergence of waves caused by hyperbolic nonlinearity. Moreover, the set of non-classical wave solutions obtained in the zero-diffusion (zero-capillarity) limit might depend sensitively on the form of the diffusion matrix and not only on the hyperbolic structure of the equations; see [31, 2] and the references cited therein for further technical details.

We present the results of numerical grid refinement studies for the simulation of two Riemann problems, namely RP_1 and RP_2 , given by:

$$RP_1 : \begin{cases} s_w^L = 0.613 & \text{and} & s_w^R = 0.05, \\ s_g^L = 0.387 & \text{and} & s_g^R = 0.15, \end{cases} \quad RP_2 : \begin{cases} s_w^L = 0.721 & \text{and} & s_w^R = 0.05, \\ s_g^L = 0.279 & \text{and} & s_g^R = 0.15. \end{cases} \quad (53)$$

We use the quadratic model by Corey-Pope, extensively used for phase relative permeabilities,

$$k_w = s_w^2, \quad k_o = s_o^2 \quad \text{and} \quad k_g = s_g^2. \quad (54)$$

As in [2, 31], we consider the following viscosity values $\mu_o = 1.0$, $\mu_w = 0.5$, and $\mu_g = 0.3$. From the analysis discussed in [31], we remark that for the choice of parameters described above, a transitional shock wave is present in the solution of RP_2 , which in turn is not present in the solution of RP_1 .

Since the oil phase saturation can be directly obtained from the other two phase saturations (i.e., $s_o = 1 - s_w - s_g$), we display the oil saturation profile in Figure 8, showing the effect of a grid refinement in the numerical solution of (49)-(50) – $w_w = 0$ and $w_g = 0$ – with Riemann data RP_1 on the left and RP_2 on the right. The computed saturation profiles are shown at dimensionless time 2.50. In each frame we compare numerical solutions obtained on grids having 256, 512 and 1024 cells against a reference numerical solution of 2048 cells. It is clear from the pictures in Figure 8, that as the grid is refined we have some good evidence of numerical convergence of our scheme. We remark that the numerical solutions presented here are in very good agreement with the semi-analytic results reported in [31], yielding a numerical verification of our computations. We now show numerical experiments concerning the three-phase flow problem (49)-(50) – $w_w = 0$ and $w_g = 0$ and with Riemann data RP_1 on top and RP_2 on the bottom – in order to show that our scheme is able to capture analytical properties of the wave structures, as originally introduced in [31]; see also [2] and the references cited therein. For completeness we describe the non-classical solution. Right picture in Figure 7: the slow wave group comprises a strong slow rarefaction fan from left (injection) state to the post-shock value and an adjoining slow front wave from the post-shock value to the first plateau. The fast wave group is a Buckley-Leverett front wave from the second plateau. Between the slow and fast wave groups is a non-classical front wave. For the classical solution, we have only the slow and fast wave groups (Left picture in Figure 7). We point out that in both numerical solutions the plateau are located in the correct heights, with respect to the semi-analytical solutions presented in [31].

6.3. Two-dimensional simulations of nonlinear scalar hyperbolic conservation laws

The first example is taken from [18]. The test consists in considering the simple flux functions

$$f(u) = g(u) = \frac{u^2}{u^2 + 2(1 - u)^2},$$

with the Gaussian initial data $u_0(x, y) = \exp(-10((x + 0.25)^2 + (y + 0.25)^2))$, $x, y \in (-1, 1)$.

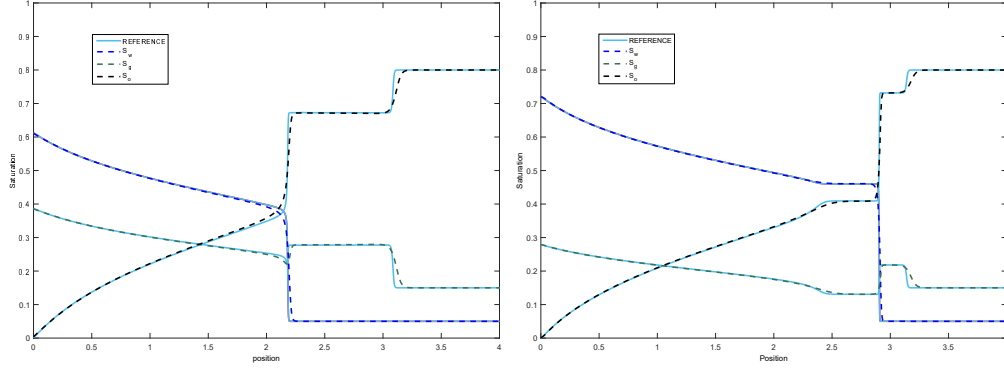


Figure 7: Oil, water and gas saturation profiles are shown as a function of distance. RP_1 on the left and RP_2 on the right.

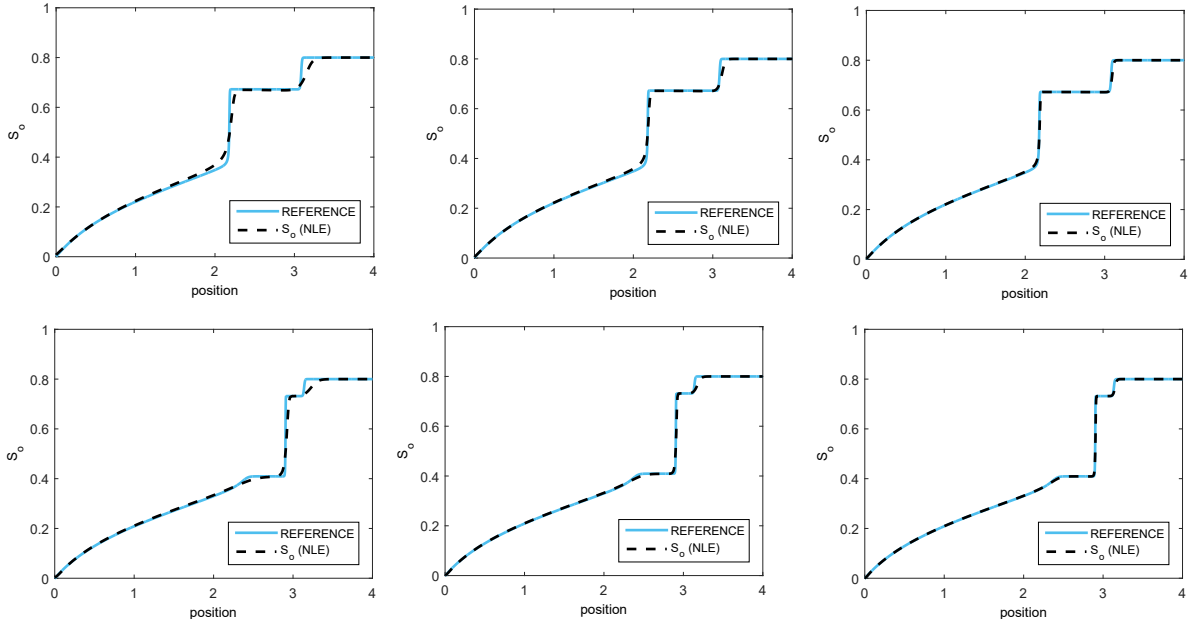


Figure 8: Mesh refinement study for mesh values 256, 512 and 1024 against a reference solution of 2048 mesh points. Oil saturations are shown as a function of distance. RP_1 on the top and RP_2 on the bottom.

Numerical solutions with 512 cells and end time $t = 1.5$ of simulation are shown in Figure 9, left picture is the approximation with our proposed scheme given by (27)-(30) and (46)-(48), middle picture with a Strang splitting approximation along with the well-known high-resolution, non-oscillatory, second order Nessyahu-Tadmor central scheme (see elsewhere, e.g., [28]), used here as reference solution, and finally in right picture it is shown the absolute error between both solutions. The next test is called “fingering test” in [18]. In this test, it is used two different flux functions $f(u) = \frac{u^2}{2}$ and $g(u) = \frac{2u^2}{5}$, along with the initial

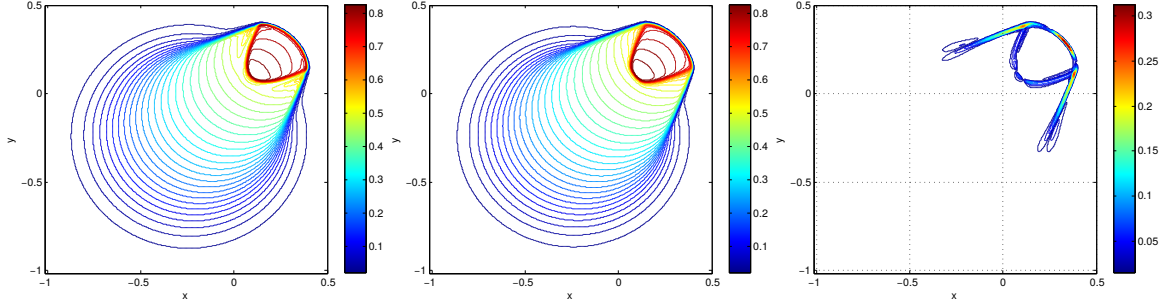


Figure 9: Numerical solutions Buckley-Leveret.

condition $u(x, y, 0) = 1$ in the circle $\{(x, y)/(x + 0.5)^2 + (y + 0.5)^2 \leq 0.16\}$, $u(x, y, 0) = -1$ in the circle $\{(x, y)/(x - 0.5)^2 + (y - 0.5)^2 \leq 0.16\}$ and zero in otherwise, when $(x, y) \in [-1, 1]^2$. The accurate numerical solutions displayed in Figure 10 is arranged as above for Figure 9, but for an end time $t = 2$ of simulation.

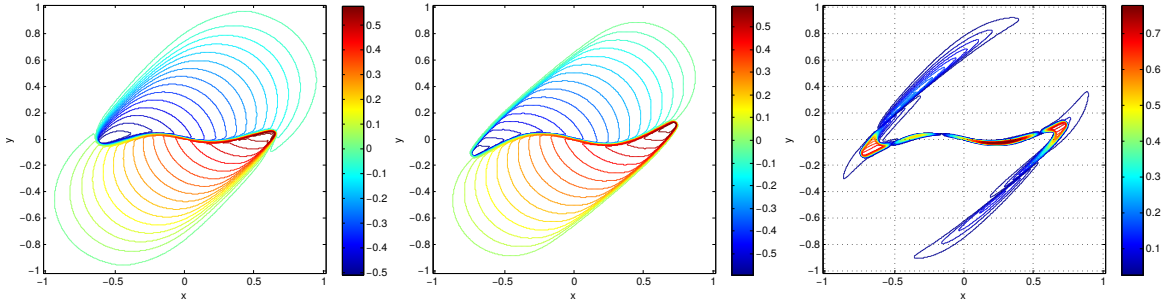


Figure 10: Numerical solutions “fingering test”.

6.4. Source terms $g(x, u) = a'(x)u$ with function discontinuous in space and non-trivial topography

We discuss the hard case of a balance law $u_t + f_x(u) = g(x, u)$ with g discontinuous in x , along with our method as developed in Section 3. In other words, we have not made any special treatment for approximation of the discontinuous source term. In particular, our results (see Figure 11) are in very good agreement with the numerical experiment reported in [36]. This means that our novel approach is able to capture the delicate nonlinear local interaction between the flux and the source within the control volume of the Lagrangian-Eulerian framework. In addition, we mention that the discontinuity of the source term might lead to significant influences on the shock or rarefaction waves generated by the initial Riemann data, and produces some new and interesting phenomena such as the appearance of weak discontinuities and the appearance and absorption of new shocks (see [16] for details). In [36], Shi Jin considered the model,

$$u_t + (f(u))_x = g(x, u) \quad (55)$$

with flux function $f(u) = \frac{u^2}{2}$ and source term $g(x, u) = z'(x)u$ with $z(x) = \cos(\pi x)$, $4.5 \leq x \leq 5.5$ and 0 otherwise with $0 < x < 10$. Note that $z'(x)$ is then a discontinuous function, so that $g(x, u)$ is a discontinuous source term in x . Figure 11 shows approximations with initial data $u(x, 0) = 0$, $x > 0$ and $u(0, t) = 2$, $t > 0$.

In the bottom pictures of Figure 11 it is shown solutions of $u + z = 2$ compared with the exact solution (solid line) at steady state for a continuous topography in a mesh refinement study; from left to right we have numerical solutions (dashed lines): 128, 256 and 512 cells. In the top pictures of Figure 11 it is shown solutions at finite time the steady state counterpart solutions for the same situation. The numerical scheme gives clearly qualitatively correct approximations at $t = 10$ even in numerical coarse grids. A study of the numerical error for the balance law problem with discontinuous source term is shown in Figure 12, along with the observed first-order behavior of accuracy in the computed solutions in several discrete norms.

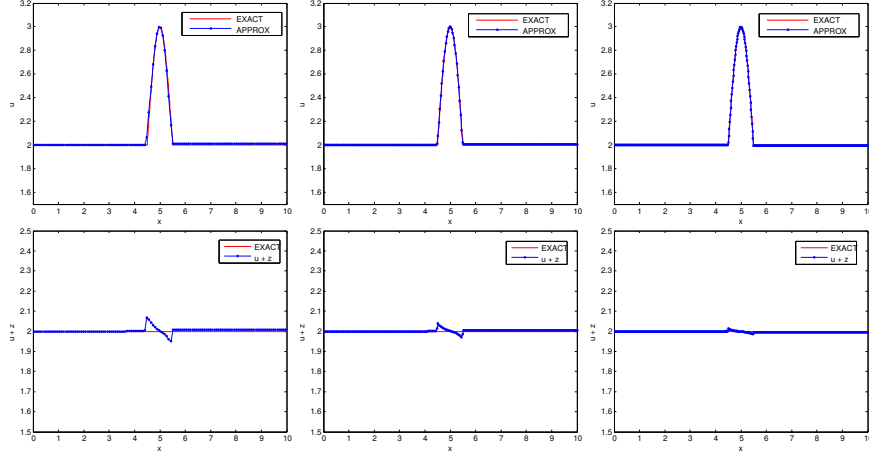


Figure 11: Numerical solutions with discontinuous source term $g(x, u)$.

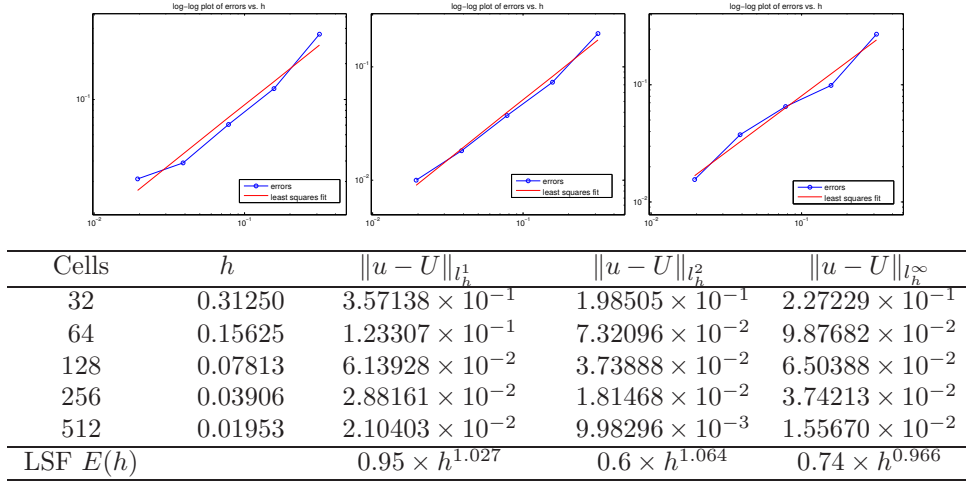


Figure 12: On the top we have log-log plots for norms L^1 (left), L^2 (middle) and L^∞ (right) of the error versus the cell sizes, for the situation with a source term $g(x, u)$ discontinuous in x ; we can see first-order behavior of accuracy in the numerical solutions. On the bottom, we have corresponding errors between the numerical approximations (U) and exact solutions (u).

We now discuss the shallow water equations over non-trivial topography $g(x, u)$ of the seminal work of Greenberg and LeRoux [22] (see also [21]) given by

$$u_t + \left(\frac{u^2}{2} \right)_x = g(x, u),$$

with flux function $f(u) = \frac{u^2}{2}$ and source term $G(u) = a'(x)u$ with $a(x) = 0.9 \cos(\pi(\frac{x-1}{2}))^{30}$, $x \leq 2$ and 0

otherwise. Figure 13 shows a non-stationary shock wave connecting two states that correspond to steady solutions for which $u + a = 1.3$ on the left and $u + a = 1$ on the right. In this numerical test, the initial data is $u(x, 0) = 1 - a(x)$, $x > 0.2$ and $u(x, 0) = 1.3 - a(x)$, $x < 0.2$. The scheme produces a qualitatively correct monotone curve as the mesh grid is refined keeping the total height $u + a$ at $t = 1.5$.

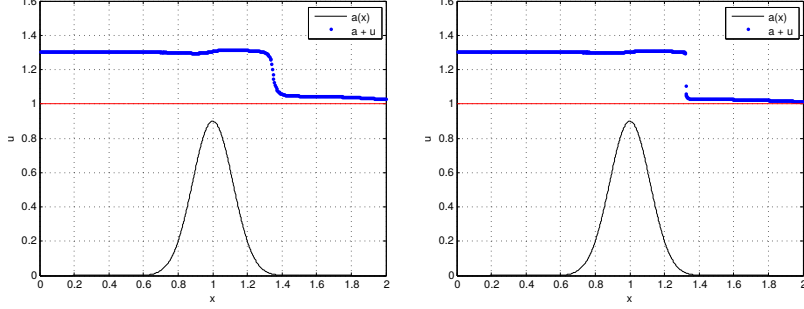


Figure 13: Numerical solutions with source term $g(x, u)$. 512 cells (left), 1024 cells (right).

6.5. A scalar balance law: a hard test case with exponential growth of the source term

The main goal of this example is, as in [17], to emphasize the qualitative difference between time-splitting, (or fractional step methods) and well-balanced numerical schemes when it comes to computing the entropy solution of a simple scalar, yet non-resonant, balance law $\partial_t u + \partial_x(f(u)) = k(x)g(u)$, $0 < k \in L^1 \cap C^0(\mathbb{R})$, f is genuinely non-linear and $g \in C^1(\mathbb{R})$, see [17] for more details. In this particular problem it is considered $f(u) = u^2/2$, $k(x) = 0.2$ and $g(u) = u$ with initial data $u_0(x) = Y(x)$, Y the Heaviside function. This results in the classical “one-half” order of convergence in L^1 , which is known to be optimal for Godunov type [34, 37], denoting the entropy solution u and its numerical approximation by $u^{\Delta t}$; see [37] that states: $\forall t \in [0, T]$, $\|u^{\Delta t}(t, \cdot) - u(t, \cdot)\|_{L^1(\mathbb{R})} \leq C\sqrt{\Delta t}$. The analysis discussed in [38] reveals that the “constant C ” is actually an exponential in time, which results in the more rigorous statement: $\forall t \in [0, T]$, $\|u^{\Delta t}(t, \cdot) - u(t, \cdot)\|_{L^1(\mathbb{R})} \leq C \exp(\max[g'(u)]t)\sqrt{\Delta t}$. This estimate is disastrous from a computational standpoint, because in order to keep the absolute error below a given tolerance, the computational grid’s parameters are meant to decrease exponentially with time (except if $g' \leq 0$, for which $TV(u)(t, \cdot)$ decays exponentially too). Figure 14 shows numerical approximations with 256 and 512 cells.

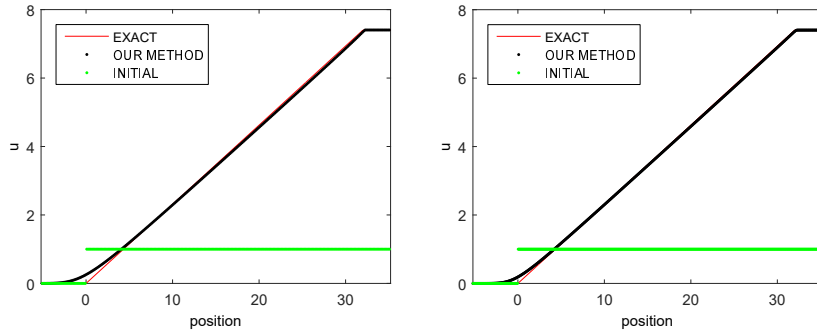


Figure 14: Numerical approximations of the scalar balance law. The solution is shown with 256 cells (left) and 512 cells (right).

6.6. Zero velocity and steady-state solutions

One particular case occurs when $f_j^n = 0$. The integral curves now are vertical lines, so the original grid does not change in time and we obtain the steady-state solution of the simulated problem. To illustrate

such situation, we present in this section an example from [22]:

$$\begin{cases} \frac{\partial u}{\partial t} + \frac{\partial(f(u))}{\partial x} = -u Z_x(x), & t > 0, \quad (x, t) \in \mathbb{R} \times (0, T], \\ u(x, 0) + Z(x) = 1, \end{cases} \quad (56)$$

where $Z(x) = 0.9 \left(\cos(\pi \left(\frac{x-1}{2} \right)) \right)^{30}$ if $0 \leq x \leq 2$ and zero otherwise. With $f(u) = u^2/2$ the steady-state solution of this problem is $u + Z(x) = 1$. Note that the steady-state solution is achieved when the following identity is satisfied:

$$0 = \frac{\partial u}{\partial t} = -\frac{\partial(\frac{u^2}{2})}{\partial x} - u Z_x(x) = -u(u + Z)_x. \quad (57)$$

The control volume is

$$D_j^n = \{(t, x) / t^n \leq t \leq t^{n+1}, x_j^n \leq x \leq x_{j+1}^n\},$$

where the integrals curves are the vertical lines $x = x_j^n$ i.e the original grid does not change in time. Hence, the projection step is not necessary anymore. This is the geometrical interpretation of the tracing forward of the cell dual grid being identical to the original grid. Integrating (57) over D_j^n gives:

$$\int_{t^n}^{t^{n+1}} \int_{x_j^n}^{x_{j+1}^n} \nabla_{t,x} \cdot \begin{bmatrix} u \\ 0 \end{bmatrix} dxdt = \int_{t^n}^{t^{n+1}} \int_{x_j^n}^{x_{j+1}^n} (u_t + [0]_x) dxdt = \int_{t^n}^{t^{n+1}} \int_{x_j^n}^{x_{j+1}^n} (-u(u + Z)_x) dxdt. \quad (58)$$

By the application of the divergence theorem on the left side of (58), we get

$$\oint_{\partial D_j^n} \vec{n} \cdot \begin{bmatrix} u \\ 0 \end{bmatrix} \partial D_j^n = \int_{t^n}^{t^{n+1}} \int_{x_j^n}^{x_{j+1}^n} (-u(u + Z)_x) dxdt. \quad (59)$$

Since the integrals curves $x = x_j^n$ are impervious, the flux is vertical from t^n to t^{n+1} . Dividing by h , we get

$$\frac{1}{h} \int_{x_j^n}^{x_{j+1}^n} u(x, t^{n+1}) dx - \frac{1}{h} \int_{x_j^n}^{x_{j+1}^n} u(x, t^n) dx = \frac{1}{h} \int_{t^n}^{t^{n+1}} \int_{x_j^n}^{x_{j+1}^n} (-u(u + Z)_x) dxdt. \quad (60)$$

Thus

$$U_{j+\frac{1}{2}}^{n+1} - U_{j+\frac{1}{2}}^n = \frac{1}{h} \int_{t^n}^{t^{n+1}} \int_{x_j^n}^{x_{j+1}^n} (-u(u + Z)_x) dxdt. \quad (61)$$

With this, the numerical scheme can be written as follows

$$U_{j+\frac{1}{2}}^{n+1} = U_{j+\frac{1}{2}}^n + \frac{1}{h} \int_{t^n}^{t^{n+1}} \int_{x_j^n}^{x_{j+1}^n} (-u(u + Z)_x) dxdt \approx U_{j+\frac{1}{2}}^n - \frac{1}{h} U_{j+\frac{1}{2}}^n ((u + Z)_x)_{j+\frac{1}{2}}^n \int_{t^n}^{t^{n+1}} \int_{x_j^n}^{x_{j+1}^n} dxdt. \quad (62)$$

Notice that we approximate the derivative $(u + Z)_x$ with the previously discussed slope limiters. We show in Figure 15 the steady-state solution approximated by this numerical scheme. This example exhibits a numerical version of a well-balancedness property for our framework, see Figure 15 (left). We also show an example from [6], see Figure 15 (right), with $Z(x) = 0.4e^{(\sin(x)-1)}$ and the steady-state solution of the simulated problem given by $u + Z = 0.5$.

6.7. Systems of balance laws: The shallow-water problem

Here we consider a numerical approximation of the well known system of balance laws modeling the shallow-water problem. The model under consideration is as follows:

$$\begin{cases} \frac{\partial h}{\partial t} + \frac{\partial(hu)}{\partial x} = 0, \\ \frac{\partial(hu)}{\partial t} + \frac{\partial(hu^2 + \frac{g}{2}h^2)}{\partial x} = -ghZ_x, \end{cases} \quad (63)$$

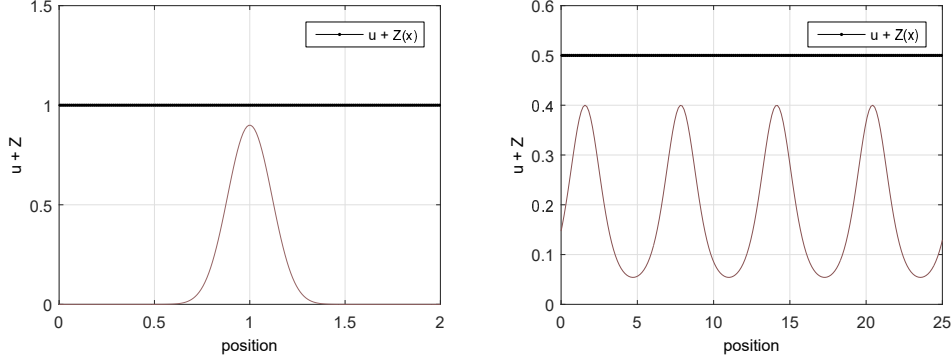


Figure 15: Steady-state solution for the problem modeled by equation 56 with different topographies. The solution for both cases is approximated with 200 mesh grid cells at time $t = 100$.

which we rewrite as

$$\begin{cases} \frac{\partial h}{\partial t} + \frac{\partial(hu)}{\partial x} = 0, \\ \frac{\partial(hu)}{\partial t} + \frac{\partial(hu^2)}{\partial x} = -\frac{\partial}{\partial x} \left(\frac{g}{2} h^2 \right) - gh \frac{\partial Z}{\partial x}, \end{cases} \quad (64)$$

where $h \geq 0$ denotes the water height, $u \in \mathbb{R}$ is the water velocity in the x direction, and $g > 0$ stands for the gravity constant. The function Z denotes the smooth topography.

Applying the Lagrangian-Eulerian method to each equation, we get

$$\begin{cases} \int_{D_{h,j}^n} \left(\frac{\partial h}{\partial t} + \frac{\partial(hu)}{\partial x} \right) dA = 0, \\ \int_{D_{m,j}^n} \left(\frac{\partial(hu)}{\partial t} + \frac{\partial(hu^2)}{\partial x} \right) dA = -g \int_{D_{m,j}^n} h \left(\frac{\partial h}{\partial x} + \frac{\partial Z}{\partial x} \right) dA. \end{cases} \quad (65)$$

The integrals on the left side in (65) were previously discussed. We will focus on how to approximate the integral on the right side. We have

$$I_{m,j}^n = \int_{D_{m,j}^n} h \left(\frac{\partial h}{\partial x} + \frac{\partial Z}{\partial x} \right) dA = \int_{t^n}^{t^{n+1}} \int_{\sigma_j^n(t)}^{\sigma_{j+1}^n(t)} h \frac{\partial(h+Z)}{\partial x} dx dt. \quad (66)$$

Therefore from (66) we get,

$$I_{m,j}^n \approx H_j^n \int_{t^n}^{t^{n+1}} (h(\sigma_{j+1}^n(t), t) + Z(\sigma_{j+1}^n(t)) - (h(\sigma_j^n(t), t) + Z(\sigma_j^n(t)))) dt. \quad (67)$$

The last integral can be approximated using Taylor series expansion of order one, where we use a slope limiter to approximate the derivatives $(H_x)_j$ and $(Z_x)_j$, and the trapezoidal rule for the integral on time. The final approximation gives

$$\begin{aligned} I_{m,j}^n &\approx H_j^n (H_{j+1}^n + Z_{j+1} - (H_j^n + Z_j)) \\ &\quad + 0.5 H_j^n (\Delta t)^2 (f_{h,j+1}^n (H_x)_{j+1}^n + f_{h,j}^n (Z_x)_{j+1} - (f_{h,j}^n (H_x)_j - f_{h,j+1}^n (Z_x)_{j+1})). \end{aligned} \quad (68)$$

The next three test cases come from [20] (see [6, 12, 35] and references therein). The topography is flat with a bump for $x \in [8, 12]$, as follows: $Z(x) = 0.2 - 0.05(x - 10)^2$. The transcritical flow without

shock, transcritical flow with shock and subcritical flow test cases are performed according to the initial and boundary conditions given by [12, 20, 35]. The first test models the transcritical flow without shock [35]. For this case, the initial water height is 0.33 m. A unit discharge of $1.53 \text{ m}^2/\text{s}$ is imposed at the upstream boundary, and open boundary conditions ($\frac{dh}{dx} = 0$, $\frac{du}{dx} = 0$) are applied at the downstream side. The numerical solutions for water height and discharge can be seen in Figure 16 after the steady state has been reached (which happens at time 41.5 sec.). We show in Figure 16 the numerically evaluated water height and discharge with the corresponding analytical solutions, with three levels of refinement (200, 600 and 1000 mesh points). At the end of the bump a constant level is again reached. Discharge shows an underestimation near the bump, reduced on refinement. The second test models the transcritical flow with a shock. The initial water height is also 0.33 m. A unit discharge of $0.18 \text{ m}^2/\text{s}$ is imposed on the upstream boundary and a depth of 0.33 m is imposed on the downstream boundary. The steady state here is reached at 175.5 sec. We show in Figure 17 the analytical and numerical solution for water surface profile and discharge, with three levels of refinement (200, 600 and 1000 mesh points). A local peak in numerical solution for discharge is observed on the jump after the bump (for more details on this behavior see [35] and references therein). The third test models the subcritical flow over a bump without a shock. Subcritical flow conditions are maintained in the same channel as taken in the above two cases. A unit discharge of $4.42 \text{ m}^2/\text{s}$ is imposed on the upstream boundary and a depth of 2.0 m is imposed on the downstream boundary. The steady state is reached at time 85.5 sec. Figure 18 shows the solutions for this case after reaching the steady state, with three levels of refinement (200, 600 and 1000 mesh points). For all the three cases, the Lagrangian-Eulerian scheme produced qualitatively correct results compared to analytical solutions with 200 mesh grid cells.

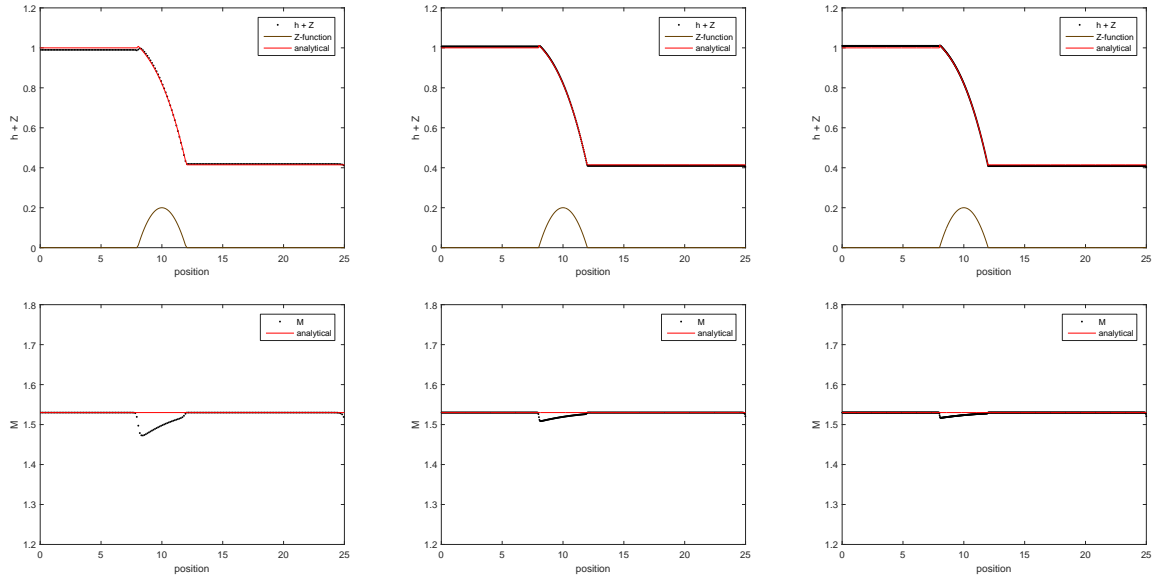


Figure 16: Transcritical without shock test case. The steady-state has been already reached (exhibited time is $t = 600 \text{ sec.}$). Top: $h + Z$ solutions with 200, 600 and 1000 mesh grid points. Bottom: discharge M with 200, 600 and 1000 mesh grid points

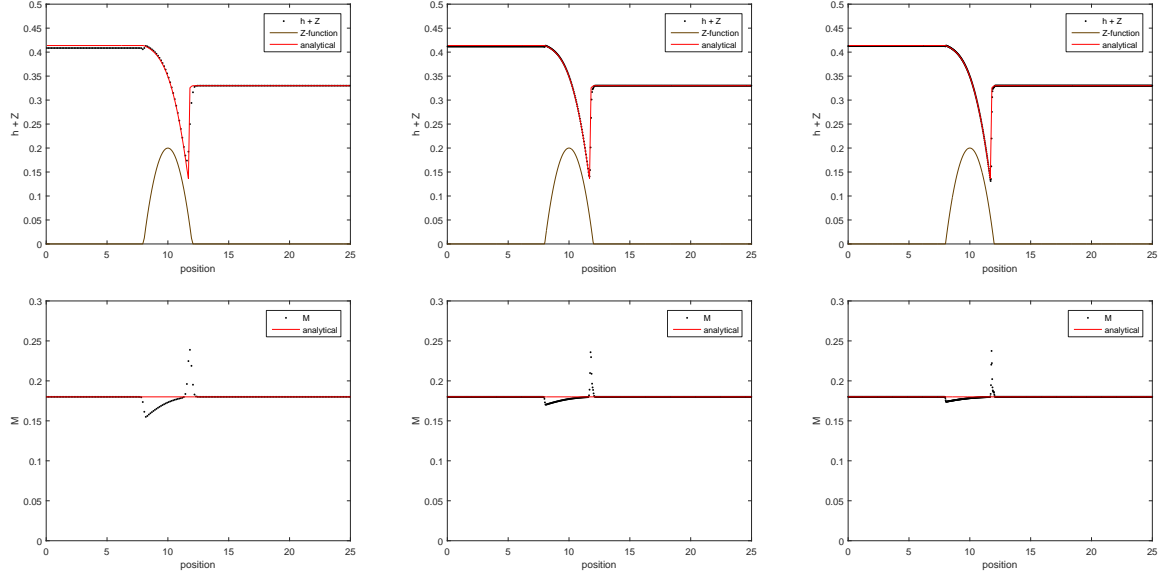


Figure 17: Transcritical with shock test case. The steady-state has been already reached (exhibited time is $t = 600$ sec.). Top: $h + Z$ solutions with 200, 600 and 1000 mesh grid points. Bottom: discharge M with 200, 600 and 1000 mesh grid points

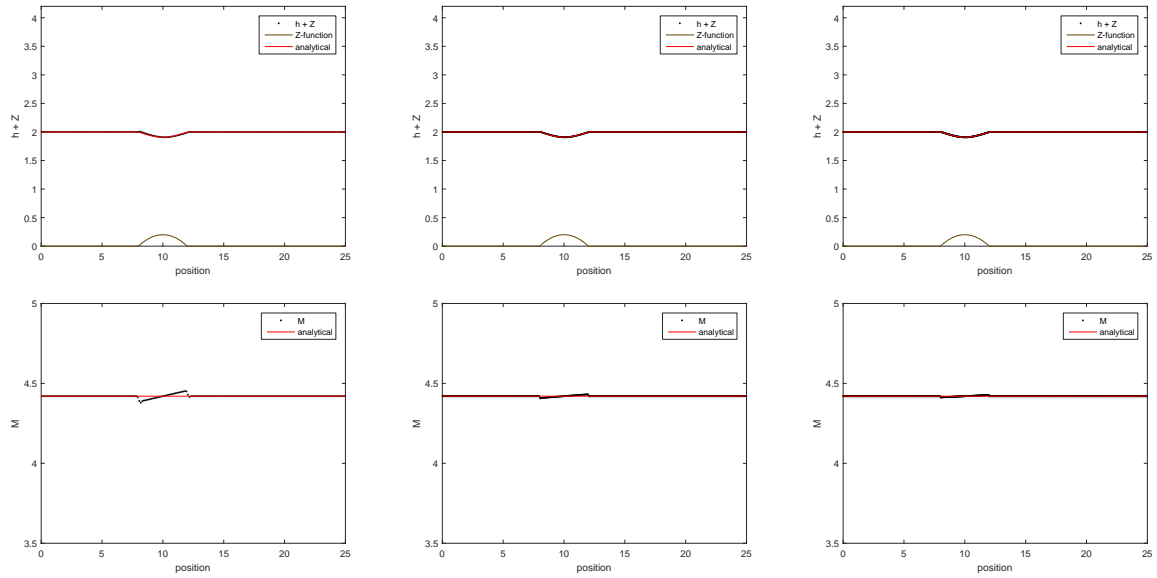


Figure 18: Subcritical test case. The steady-state has been already reached (exhibited time is $t = 600$ sec.). Top: $h + Z$ solutions with 200, 600 and 1000 mesh grid points. Bottom: discharge M with 200, 600 and 1000 mesh grid points

The following results are reproductions of the test cases presented in [10] - Small perturbation of steady flow over a slanted surface. We consider the modified system for shallow water equations presented in the cited paper, with water source term $R(x, t)$ (which for the test cases is identically zero) and a bottom friction term with the classical Manning formulation. In one spatial dimension the equation is reduced to:

$$\begin{cases} \frac{\partial h}{\partial t} + \frac{\partial(hu)}{\partial x} = R(x, t), \\ \frac{\partial(hu)}{\partial t} + \frac{\partial(hu^2 + \frac{g}{2}h^2)}{\partial x} = -ghZ_x - g\frac{n^2}{h^{\frac{4}{3}}}u|u|, \end{cases} \quad (69)$$

We consider the initial data

$$h(x, 0) = h_0 + \begin{cases} 0.2h_0, & 1 \leq x \leq 1.25, \\ 0, & \text{otherwise} \end{cases} \quad q(x, 0) = q_0 \quad (70)$$

The first test is a supercritical case, with $h_0 = 0.09564$, $q_0 = 0.1$, $n = 0.02$ and the (constant) slope of topography $Z_x = -0.01$. We show on Figure 19 the initial state, a snapshot at time $t = 1.0$ sec., where the perturbation propagates to the right and the steady state at time $t = 100$ sec. Next, the subcritical case is presented with $h_0 = 0.02402$, $q_0 = 0.002$, $n = 0.1$ and the slope of topography again as -0.01 . Here, the shape of the propagated solution is different from the previous case. We show on Figure 20 the initial state, a snapshot at time $t = 0.5$ sec. and the steady state solution at time $t = 100$ sec. Then, the last case on Figure 21 shows a magnitude of topography slope larger than the other cases, $Z_x = \frac{1}{\sqrt{3}}$. In this case, the perturbation propagates faster than in previous tests, but the numerical steady state is achieved at large times. These tests are evaluated with 200 grid cells.

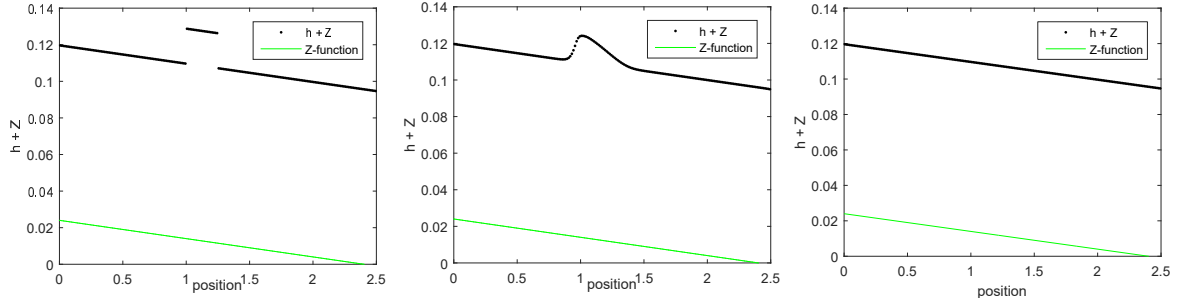


Figure 19: Supercritical test case at initial time (left), $t = 1.0$ sec. (middle), and steady state at $t = 100$ sec. (right).

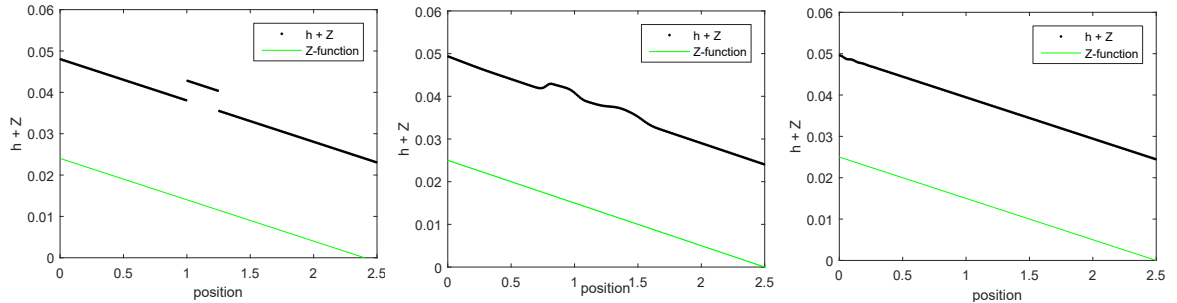


Figure 20: Subcritical test case at initial time (left), $t = 0.5$ sec. (middle), and steady state at $t = 100$ sec. (right).

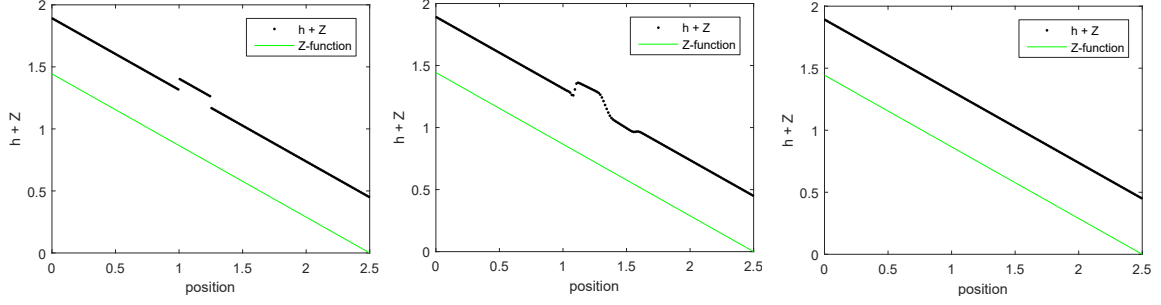


Figure 21: Larger slope topography test case at initial time (left), $t = 0.05$ sec. (middle), and steady state at $t = 100$ sec. (right).

6.8. Error analysis

We present an error analysis study performed for the linear conservation law $u_t + au_x = 0$, with $a = 1.0$ and a smooth initial condition. We observe from information below that our method presents first-order accuracy behavior.

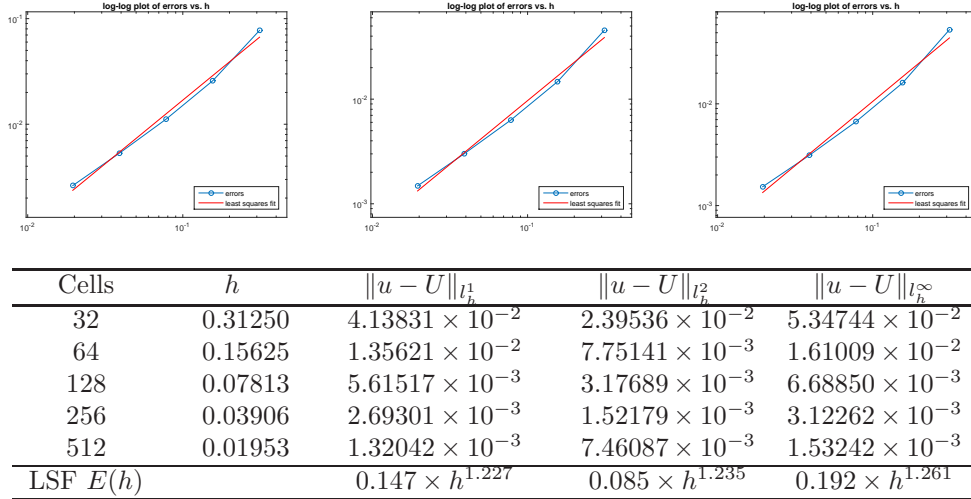


Figure 22: On the top we have log-log plots for norms L^1 (left), L^2 (middle) and L^∞ (right) of the error versus the cell sizes, for the the linear problem $u_t + u_x = 0$ at time $T = 1.0$ with smooth initial condition $u(x, 0) = e^{-x^2}$; we can see first-order behavior of accuracy in the numerical solutions. On the bottom, we have corresponding errors between the numerical approximations (U) and exact solutions (u)

7. Concluding Remarks

In the present work, we constructed an efficient numerical scheme in local conservative form for solving nonlinear hyperbolic conservation and balance law problems – both for the scalar case and for systems of equations – using a novel Lagrangian-Eulerian approach. This method is based on a reformulation of the equation regarding an equivalent locally conservative space-time divergence form problem. We make use of piecewise linear reconstruction ideas along with predictor-corrector type approximations for improvements of the computed numerical solutions. A rigorous mathematical demonstration of such approach is beyond the scope of the present paper, and is to be attempted in future research. We discussed qualitatively correct numerical solutions for problems such as the classical inviscid Burgers equation, two-phase and three-phase

flow problems in porous media and nonlinear shallow water equations, including test cases with bottom friction. In particular we were also able to reproduce qualitatively correct approximations for the situation of balance laws $u_t + f_x(u) = g(u, x)$, with $g(u, x)$ discontinuous in x . This framework is aimed to be independent of a particular structure of the flux function and the stiff source term. Moreover, we also discussed ideas on how to extend the Lagrangian-Eulerian framework for higher dimensions. Indeed, we have also discussed another simple, fast and elegant alternative for extending the novel approach to more than one dimension along with a two-dimensional concrete example. Our procedure is based on writing the two-dimensional scalar conservation law in the form of a coupled set of two balance laws along with initial data. We also discuss the extension of our novel framework to the case of systems of balance laws and for nontrivial test cases that can be found in the recent specialized literature. As announced, a convergence proof is not ready to the moment, but its numerical aspects and their applications were covered in the current work by a very large and representative set of numerical experiments to give convincing evidence that we were able to compute qualitatively correct approximations for several transport models and related applications.

Acknowledgements

E. Abreu thanks for financial support through grants FAPESP No. 2014/03204-9, FAPESP No. 2011/23628-0, CNPq No. 445758/2014-7 and UNICAMP /FAEPEX No. 519.292-0280/2014. J. Perez and A. Santo thanks, respectively, CAPES-IMECC/UNICAMP and CNPq-IMECC/UNICAMP for a graduate fellowship. We also thank anonymous referees for constructive comments and suggestions.

Appendix A. A CFL constrain to the linear advection model $u_t + au_x = 0$, $a \in \mathbb{R}$

We perform a preliminary stability analysis for the numerical scheme, without reconstruction and predictor-corrector ideas. The simplified scheme with constant time step for linear conservation laws is,

$$U_j^{n+1} = \frac{1}{4} [U_{j-1}^n + 2U_j^n + U_{j+1}^n] - \frac{ak}{2h} [U_{j+1}^n - U_{j-1}^n]. \quad (\text{A.1})$$

By means of the Fourier analysis every one-step scheme can be recast in a recurrence relation, given by (from the Fourier inversion formula):

$$\widehat{U}^{n+1} = (g(h\xi))\widehat{U}^n, \quad \text{with} \quad \widehat{U}^n = (g(h\xi))^n \widehat{U}^0, \quad (\text{A.2})$$

where \widehat{U}^n is the Fourier transform of a grid function U^n , defined at grid points $x_j = jh$ for $j = 0, \pm 1, \pm 2, \dots$ and all crucial information about a scheme is embedded in its amplification factor *or characteristic function* $g(h\xi)$ for the scheme at wave number ξ . Therefore, replacing U_j^n by $g^n e^{i\xi jh}$ and plugging this into the Lagrangian-Eulerian scheme (A.1) and matching coefficients reads (with $\omega \equiv h\xi$ for convenience of notation):

$$g(\omega)^{n+1} e^{i\xi jh} = \frac{g(\omega)^n}{4} (e^{i\xi(j-1)h} + 2e^{i\xi jh} + e^{i\xi(j+1)h}) - \frac{ak}{2h} (e^{i\xi(j+1)h} - e^{i\xi(j-1)h}). \quad (\text{A.3})$$

From (A.3) one easily find that,

$$g(\omega) = \frac{1}{4} (e^{-i\xi h} + 2 + e^{i\xi h}) - \frac{ak}{2h} (e^{i\xi h} - e^{-i\xi h}) = \frac{1}{2} (1 + \cos(\xi h)) - v \sin(\xi h), \quad (\text{A.4})$$

where $v = akh^{-1}$ is the Courant number. Thus, the analogue Lagrangian-Eulerian finite difference scheme is stable if there is a positive constant K (independent of ξ , h , k , but h , k are in the stability region) such that, $|g(\omega, k, h)| \leq 1 + Kk$. If amplification factor does not depend of h and k , then $g(\omega, k, h)$ can be replaced with the restricted stability condition $|g(\omega)| \leq 1$. Thus, the amplification factor of the Lagrangian-Eulerian scheme (A.1) is given by,

$$|g(\xi)|^2 = \frac{1}{4} (1 + \cos(\xi h))^2 + v^2 \sin^2(\xi h). \quad (\text{A.5})$$

Notice the restriction $|g(\omega)| \leq 1$ is also true if $v^2 \leq \frac{1}{4}$, and then we get,

$$|v| \leq \frac{1}{2}. \quad (\text{A.6})$$

This now gives a support to what was used in [5]. Additionally, a more detailed analysis of the amplification factor (A.4) shows that the bound in the equation (A.6) can be greater. We consider now the function from (A.5),

$$t(\omega, v) = |g(\omega)|^2 = \frac{1}{4} (1 + \cos(\omega))^2 + v^2 \sin^2(\omega). \quad (\text{A.7})$$

Differentiation of $t(\omega, v)$ with respect to ω and setting $t_\omega(\omega, v) = 0$ reads,

$$\cos(\omega) = \frac{\frac{1}{2}}{2v^2 - \frac{1}{2}}, \quad (\text{A.8})$$

from which we get the following constraint for $v \neq \frac{1}{2}$:

$$\left| \frac{\frac{1}{2}}{2v^2 - \frac{1}{2}} \right| \leq 1. \quad (\text{A.9})$$

Therefore $0 < v < \frac{1}{2}$ or $\frac{\sqrt{2}}{2} < v$. Indeed, this function $t(\omega, v)$ has no critical points on the interval $\frac{1}{2} < v < \frac{\sqrt{2}}{2}$, but $t_\omega(\omega, v) \equiv 0$ in this interval is zero. This implies that function $t(\omega, v)$ is constant there, but the function is still limited by one for $v \in]\frac{1}{2}, \frac{\sqrt{2}}{2}[$. Now, notice that the function $t(\omega, v)$ (A.9) associated to the analogue linear Lagrangian-Eulerian scheme (A.1) is continuous, even smooth with respect to the variable v . Therefore, stability condition for the linear Lagrangian-Eulerian scheme (A.1) is,

$$|v| \leq \frac{\sqrt{2}}{2}, \quad v = \frac{ak}{h}, \quad a \in \mathbb{R}, \quad h, k > 0. \quad (\text{A.10})$$

References

- [1] E. Abreu, A. Bustos, W. Lambert, Non-monotonic traveling wave and computational solutions for gas dynamics Euler equations with stiff relaxation source terms, *Computers and Mathematics with Applications* 70 (2015) 2155-2176.
- [2] E. Abreu, Numerical modelling of three-phase immiscible flow in heterogeneous porous media with gravitational effects, *Mathematics and Computers in Simulation* 97 (2014) 234-259.
- [3] G. Alberti, S. Bianchini, and L. Caravenna, Eulerian, Lagrangian and Broad continuous solutions to a balance law with non-convex flux I, *Journal of Differential Equations* (Available online 7 July 2016).
- [4] D. Amadori, L. Gosse, Error Estimates for Well-Balanced Schemes on Simple Balance Laws (One-Dimensional Position-Dependent Models), *Springer International Publishing (SpringerBriefs in Mathematics)*, 2015.
- [5] J. Aquino, A. Francisco, F. Pereira, T.J. Pereira, H.A. Souto, A Lagrangian strategy for the numerical simulation of radionuclide transport problems, *Progress in Nuclear Energy* 52 (2010) 282-291.
- [6] C. Berthon, M. De Leffe, V. Michel-Dansac, A conservative well-balanced hybrid SPH scheme for the shallow-water model, in: *Finite Volumes for Complex Applications VII-Elliptic, Parabolic and Hyperbolic Problems*, Springer, 2014, pp. 817-825.
- [7] R. Botchorishvili, B. Perthame, A. Vasseur, Equilibrium schemes for scalar conservation laws with stiff sources. *Mathematics of Computation* 72(241) (2003) 131-157.
- [8] F. Bouchut, H. Ounaissa, B. Perthame, Upwinding of the source term at interfaces for Euler equations with high friction, *Comput. Math. Appl.* 53 (2007) 361-375.
- [9] M. J. Castro, P. G. LeFloch, M. L. Muñoz-Ruiz and Carlos Parés. Why many theories of shock waves are necessary: Convergence error in formally path-consistent schemes, *Journal of Computational Physics* 227 (2008) 8107-8129.
- [10] A. Chertock, S. Cui, A. Kurganov, T. Wu, Well-balanced positivity preserving central-upwind scheme for the shallow water system with friction terms, *International Journal for Numerical Methods in Fluids* 78 (2015) 355-383.
- [11] David L. Chopp, J. A. Sethian Flow under Curvature: Singularity Formation, Minimal Surfaces, and Geodesics *Experimental Mathematics* 2(4) (1993) 235-255 (Published online: 03 Apr 2012).
- [12] O. Delestre, C. Lucas, P.A. Ksinant, F. Darboux, C. Laguerre, T.N.T. Vo, F. James, S. Cordier, SWASHES: a compilation of Shallow Water Analytic Solutions for Hydraulic and Environmental Studies, *International Journal for Numerical Methods in Fluids* 72 (2013) 269-300.

- [13] R. Donat, I. Higueras, A. Martinez-Gavara On stability issues for IMEX schemes applied to 1D scalar hyperbolic equations with stiff Reaction terms *Mathematics of computation* 80(276) (2011) 2097-2126.
- [14] J. Douglas Jr, F. Pereira, L.M. Yeh, A locally conservative Eulerian-Lagrangian numerical method and its application to nonlinear transport in porous media, *Computational Geosciences* 4 (2000) 1-40.
- [15] M. Dumbser, C. Enaux, E. F. Toro, Finite volume schemes of very high order of accuracy for stiff hyperbolic balance laws *Journal of Computational Physics* 227 (2008) 3971-4001.
- [16] B. Fang, P. Tang, Y.-G. Wang, The Riemann problem of the Burgers equation with a discontinuous source term, *Journal of Mathematical Analysis and Applications*, 395 (2012) 307-335.
- [17] L. Gosse, Computing qualitatively correct approximations of balance laws, *SIMAI Springer Series* 2 (2013).
- [18] L. Gosse, A two-dimensional version of the Godunov scheme for scalar balance laws. *SIAM Journal on Numerical Analysis*, Society for Industrial and Applied Mathematics, 2014, 52 (2), pp.626-652.
- [19] L. Gosse, G. Toscani, An asymptotic-preserving well-balanced scheme for the hyperbolic heat equations, *Comptes Rendus Mathematique* 334 (2002) 337-342.
- [20] N. Goutal, F. Maurel, Proceedings of the 2nd workshop on dam-break wave simulation, Electricité de France. Direction des études et recherches, 1997.
- [21] J. M. Greenberg, A. Y. Leroux, R. Baraille, and A. Noussair. Analysis and approximation of conservation laws with source terms. *SIAM Journal on Numerical Analysis*, 34(5):1980-2007, 1997.
- [22] J.M. Greenberg, A.Y. Leroux, A well-balanced scheme for the numerical processing of source terms in hyperbolic equations, *SIAM Journal on Numerical Analysis* 33 (1996) 1-16.
- [23] F. Hélein, *Harmonic Maps, Conservation Laws and Moving Frames*, Cambridge University Press, 2002.
- [24] C.S. Huang, T. Arbogast, J. Qiu, An Eulerian-Lagrangian WENO finite volume scheme for advection problems, *Journal of Computational Physics* 231 (2012) 4028-4052
- [25] J. Langseth, A. Tveito, R. Winther, On the convergence of operator splitting applied to conservation laws with source terms, *SIAM journal on numerical analysis* 33 (1996) 843-863.
- [26] D. S. Lee, J. S. Kim, Mean curvature flow by the Allen-Cahn equation, *European Journal of Applied Mathematics*, 26(4) (2015) 535-559.
- [27] R.J. LeVeque, H. C Yee, A study of numerical methods for hyperbolic conservation laws with stiff source terms, *Journal of Computational Physics* 86(1) (1990) 187-210.
- [28] R.J. LeVeque, *Finite volume methods for hyperbolic problems*, volume 31, Cambridge university press, 2002.
- [29] M. Leverett, W. Lewis, et al., Steady flow of gas-oil-water mixtures through unconsolidated sands, *Transactions of the AIME* 142 (1941) 107-116.
- [30] S. F. Liotta, V. Romano, G. Russo, Central schemes for balance laws of relaxation type, *SIAM J. Numer. Anal.* 38 (2000) 1337-1356.
- [31] D. Marchesin, B.J. Plohr, et al., Wave structure in WAG recovery, *SPE Journal* 6 (2001) 209-219.
- [32] S. Osher, J. A. Sethian. Fronts propagating with curvature-dependent speed: Algorithms based on Hamilton-Jacobi formulations. *Journal of Computational Physics*, 79(1) (1988) 12-49.
- [33] J. Perez, *Lagrangian-Eulerian approximate methods for balance laws and hyperbolic conservation law*, Ph.D. thesis, University of Campinas, 2015.
- [34] F. Sabac, The optimal convergence rate of monotone finite difference methods for hyperbolic conservation laws, *SIAM Journal on Numerical Analysis* 34 (1997) 2306-2318.
- [35] J. Singh, M.S. Altinakar, Y. Ding, Two-dimensional numerical modeling of dam-break flows over natural terrain using a central explicit scheme, *Advances in Water Resources* 34 (2011) 1366-1375.
- [36] J. Shi. A steady-state capturing method for hyperbolic systems with geometrical source terms. *ESAIM: Mathematical Modelling and Numerical Analysis* 35(4) (2001) 631-645.
- [37] T. Tang, Z.H. Teng, Error bounds for fractional step methods for conservation laws with source terms, *SIAM Journal on Numerical Analysis* 32 (1995) 110-127.
- [38] T. Tang, Z.H. Teng, The sharpness of Kuznetsov's $O(\sqrt{\Delta x})L^1$ -error estimate for monotone difference schemes, *Mathematics of Computation* 64 (1995) 581-589.

A conservative Lagrangian-Eulerian finite volume approximation method for balance law problems

Eduardo Abreu¹

Institute of Mathematics, Statistics and Scientific Computing IMECC - UNICAMP, Campinas, SP

John Pérez²

Facultad de Ciencias ITM Institución Universitaria, Medellín, Colombia.

Arthur Santo³

Institute of Mathematics, Statistics and Scientific Computing IMECC - UNICAMP, Campinas, SP

Abstract

We present a simple numerical method based on a Lagrangian-Eulerian framework for approximate solutions of nonlinear balance law problems. This framework has been used for numerically solving partial differential equations of several types, such as hyperbolic conservation laws [3, 8], balance laws problems [4]. As in [3, 5] the mass conservation takes place in the space-time volume D_j^n , and this region in the form of [3] is used to define naturally a balance law. This balance law is the central idea to build a efficient numerical method to approximate solution to balance law problems. Verification of the technique is also made by comparison with analytical solutions when they are available.

Keywords. hyperbolic balance laws, Lagrangian-Eulerian, Finite Volume Methods

1 Introduction

We propose a first order high-resolution three point numerical scheme based on a Lagrangian-Eulerian framework for numerically solving nonlinear balance law problems. The Lagrangian-Eulerian approach is a promising tool for numerically solving partial differential equations of several types. Recently, in [2, 3, 8] such ideas were extended to a wide range of nonlinear purely hyperbolic conservation laws and balance laws scalar and systems. Here, we make use of polynomial reconstruction ideas into the Lagrangian-Eulerian novel approach, but keeping the scheme simple, fast and without any strong restriction over the source term other than integrability on the finite volume. As in [2, 3, 8] the hyperbolic part of balance law is written in a space time divergence form so that the inherent conservation properties of the hyperbolic operator are used efficiently to build a numerical method to hyperbolic balance law problems [5]. Such framework presents an interesting property of being rather independent of a particular structure of the source terms. Our

¹eabreu@ime.unicamp.br

²jhonperez@itm.edu.co

³arthurm@ime.unicamp.br

goal on the current work is two-fold: 1) to present the novel high-resolution Lagrangian-Eulerian three point numerical scheme for general balance laws, and 2) the application of the new scheme to a wide range of nonlinear balance laws that appear in transport in porous media problems as well as to the shallow water equations with discontinuous source term. For such problems, we present evidences that we are calculating qualitatively correct approximations with accurate resolution of small perturbations around the stationary solution. Our work shows accurate results computed efficiently with the simple high-resolution Lagrangian-Eulerian numerical scheme for general balance laws.

2 Numerical Method

We consider a novel Lagrangian-Eulerian formulation that can be viewed as an extension of previous works [2, 3, 8] for practical construction of numerical solutions for balance law problems, but following innovative recent ideas introduced in [1] to construct weak asymptotic methods for scalar equations and systems of conservation law equations. For simplicity, we consider the particular scalar equation with $u = u(x, t)$

$$\frac{\partial u}{\partial t} + \frac{\partial(u f(u))}{\partial x} = g(x, u), \quad x \in \mathbb{R}, t > 0; \quad u(x, 0) = u_0(x) \in L^\infty(\mathbb{T}), \quad x \in \mathbb{R}, \quad (1)$$

with f Lipschitz, with Lipschitz coefficient bounded on bounded sets and source term $g(x, u)$ integrable over the finite volume D_j^n . We provide a formal development of the analogue Lagrangian-Eulerian scheme [4, 5, 8] for numerically solving the initial value problem (1). As in the Lagrangian-Eulerian schemes [3–5], a local mass balance equation is obtained by integrating the hyperbolic balance law (1) over the region in the space-time domain. Here we consider the Lagrangian-Eulerian finite-volume cell centers

$$D_j^n = \{(t, x) / t^n \leq t \leq t^{n+1}, \sigma_{j-\frac{1}{2}}^n(t) \leq x \leq \sigma_{j+\frac{1}{2}}^n(t)\}, \quad (2)$$

where $\sigma_{j-\frac{1}{2}}^n(t)$ is the parameterized integral curve such that $\sigma_{j-\frac{1}{2}}^n(t^n) = x_{j-\frac{1}{2}}^n$. These curves are the lateral boundaries of the domain D_j^n in (2) and we define $\bar{x}_{j-\frac{1}{2}}^{n+1} := \sigma_{j-\frac{1}{2}}^n(t^{n+1})$ and $\bar{x}_{j+\frac{1}{2}}^{n+1} := \sigma_{j+\frac{1}{2}}^n(t^{n+1})$ as their endpoints in time t^{n+1} . The numerical scheme is expected to satisfy some type of local mass balance (due to the inherent nature of the problem) from time t^n in the space domain $[x_{j-\frac{1}{2}}^n, x_{j+\frac{1}{2}}^n]$ to time t^{n+1} in the space domain $[\bar{x}_{j-\frac{1}{2}}^{n+1}, \bar{x}_{j+\frac{1}{2}}^{n+1}]$. With this, we must have the flux through curves $\sigma_{j-\frac{1}{2}}^n(t)$ to be zero. From the integration of (1) and the divergence theorem applied on the hyperbolic operator, left side of equation (1), and using the fact that the line integrals over curves $\sigma_j^n(t)$ vanish, we get the local balance mass equation

$$\int_{\bar{x}_{j-\frac{1}{2}}^{n+1}}^{\bar{x}_{j+\frac{1}{2}}^{n+1}} u(x, t^{n+1}) dx = \int_{x_{j-\frac{1}{2}}^n}^{x_{j+\frac{1}{2}}^n} u(x, t^n) dx + \iint_{D_j^n} g(x, u) dx dt. \quad (3)$$

As in [3], the curves $\sigma_{j-1/2}^n(t)$ are not straight lines in general, but rather solutions of the local nonlinear differential equations [2, 4, 8]: $\frac{d\sigma_{j-1/2}^n(t)}{dt} = \frac{uf(u)}{u} = f(u)$, for $t^n < t \leq t^{n+1}$, with initial condition $\sigma_{j-1/2}^n(t^n) = x_{j-1/2}^n$, assuming $u \neq 0$ (for the sake of presentation).

The extension of this construction follows naturally from the finite volume formulation of the linear Lagrangian-Eulerian scheme, as in [2, 3, 8], building block to construct *local* approximations such as $f_{j-1/2}^n = f(U_{j-1/2}^n) \approx f(u(x_{j-1/2}, t^n))$ with the initial condition $\sigma_{j-1/2}^n(t^n) = x_{j-1/2}^n$. Indeed, distinct and high-order approximations are also acceptable for $\frac{d\sigma_{j-1/2}^n(t)}{dt} = f(u)$. As in [3], the piecewise constant numerical data is reconstructed into a piecewise linear approximation (but high-order reconstructions are acceptable), through the use of MUSCL-type interpolants $L_j(x, t) = u_j(t) + (x - x_j)\frac{1}{\Delta x}u'_j$. For the numerical derivative $\frac{1}{\Delta x}u'_j$, there are several choices of slope limiters. A priori choice of such slope limiters is quite hard, but they are chosen upon the underlying model problem under investigation. A possible slope limiter is

$$U'_j = MM \left\{ \alpha \Delta u_{j+\frac{1}{2}}, \frac{1}{2}(u_{j+1} - u_{j-1}), \alpha \Delta u_{j-\frac{1}{2}} \right\}, \quad (4)$$

and this choice allows steeper slopes near discontinuities and retain accuracy in smooth regions. The range of the parameter α is typically guided by the CFL condition. Equation (3) defines a local mass balance between space intervals at time t^n and at time t^{n+1} . We will later address how to project these volumes back to the original mesh. Defining

$$\overline{U}_j^{n+1} := \frac{1}{h_j^{n+1}} \int_{\bar{x}_{j-\frac{1}{2}}^{n+1}}^{\bar{x}_{j+\frac{1}{2}}^{n+1}} u(x, t^{n+1}) dx, \quad \text{and} \quad U_j^n := \frac{1}{h} \int_{x_{j-\frac{1}{2}}^n}^{x_{j+\frac{1}{2}}^n} u(x, t^n) dx,$$

then, equation (3) can be rewritten into

$$\overline{U}_j^{n+1} = \frac{1}{h_j^{n+1}} \left(h U_j^n + \iint_{D_j^n} g(x, u) dx dt \right). \quad (5)$$

Solutions $\sigma_{j-1/2}^n(t)$ of the differential system are obtained using the approximations

$$U_{j-\frac{1}{2}} = \frac{1}{h} \left(\int_{x_{j-1}^n}^{x_{j-\frac{1}{2}}^n} L_{j-1}(x, t) dx + \int_{x_{j-\frac{1}{2}}^n}^{x_j^n} L_j(x, t) dx \right) = \frac{1}{2}(U_{j-1} + U_j) + \frac{1}{8}(U'_j - U'_{j-1}). \quad (6)$$

The above approximation is not necessary in the linear case where $uf(u) = a(x, t)u$. We must notice that the approximation of $f_{j-1/2}^n$ may cause spurious oscillation in Riemann problems, specially in shocks and discontinuity regions. For that, we use a polynomial reconstruction of second degree to smooth out the approximation and also slope limiters approximation of the form (4). The numerical solutions have shown qualitatively correct behavior for nonlinear hyperbolic conservation laws. Convergence order remains unchanged even with the reconstruction, being first-order. In the reconstruction we use the nonlinear Lagrange polynomial in U_{j-1} , U_j and U_{j+1} . Equation (5) reads,

$$\overline{U}_j^{n+1} = \frac{1}{h_j^{n+1}} \int_{x_{j-\frac{1}{2}}^n}^{x_{j+\frac{1}{2}}^n} P_2(x) dx, \quad (7)$$

where $P_2(x) = U_{j-1}^n L_{-1}(x - x_j) + U_j^n L_0(x - x_j) + U_{j+1}^n L_1(x - x_j)$, $L_0(x) = 1 - (\frac{x}{h})^2$ and $L_{\pm 1}(x) = \frac{1}{2} \left[(\frac{x}{h} \pm \frac{1}{2})^2 - \frac{1}{4} \right]$. Next, we obtain the resulting projection formula as follows

$$U_j^{n+1} = \bar{U}_j^{n+1} + \frac{\Delta t^n}{h} \left(f_{j-\frac{1}{2}}^+ \bar{U}_{j-1}^{n+1} - |f_j| \bar{U}_j^{n+1} + f_{j+\frac{1}{2}}^- \bar{U}_{j+1}^{n+1} \right), \quad (8)$$

where $f_{j-\frac{1}{2}}^+ = f^+(U_{j-\frac{1}{2}}^n)$, $f_{j+\frac{1}{2}}^- = f^-(U_{j+\frac{1}{2}}^n)$ and $|f_j| = f_{j-\frac{1}{2}}^+ + f_{j+\frac{1}{2}}^-$. Here Δt^n is obtained under CFL-condition

$$\max_j \left\{ f_{j-\frac{1}{2}}^+, f_{j+\frac{1}{2}}^- \right\} \Delta t^n \leq \frac{h}{2},$$

which is taken by construction of method. We note that in the linear case, when $a(x, t) = a > 0$ (or $a < 0$), the numerical scheme (5)-(8) is a extension of the Upwind scheme to linear balance law, but our scheme can approximate solution in both cases $a > 0$ and $a < 0$, the CFL-condition in this case is $|a \Delta t| \leq h$ as in the Upwind scheme.

3 Numerical Experiments

We present and discuss approximate computations for scalar balance laws and systems of balance laws. The scalar calculations were performed in less that one second with Matlab on a standard laptop with 2.60 GHz Intel Core i7-4510U CPU and 8.0 GB of RAM memory.

The first test is an example of linear advection with a smooth (polynomial) source:

$$u_t + 2u_x = x^3 + 6tx^2, \quad u(x, 0) = 0.$$

The initial data here is zero, but the exact solution of this differential equation is $u(x, t) = tx^3$. In $x = 0$ we have a sonic point accurately captured by our simulations. Figure 1 presents numerical solutions at times $t = 0$, $t = 1.5$ and $t = 3.0$ for a 256 cells mesh. For this case we have a natural and robust generalization for the upwind method for balance laws. The observed convergence rate was studied at time $t = 3.0$ with 32, 64, 128, 256, 512 and 1024 mesh grid cells and second-order convergence was observed (see Figure 2). Here we used the midpoint rule for the source term quadrature, but the linear advection hyperbolic operator is being exactly calculated due to exact CFL condition.

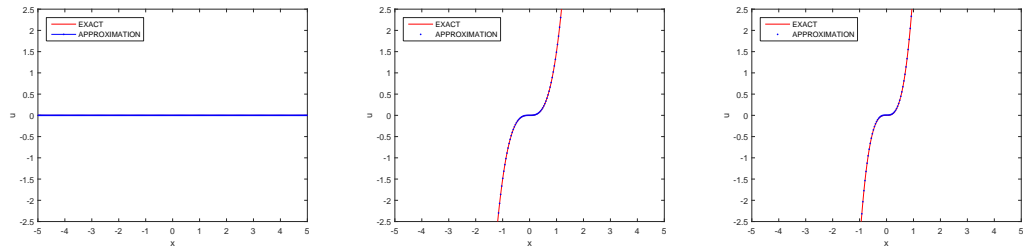


Figure 1: Numerical solutions with smooth source term $g(x, t) = x^3 + 6tx^2$.

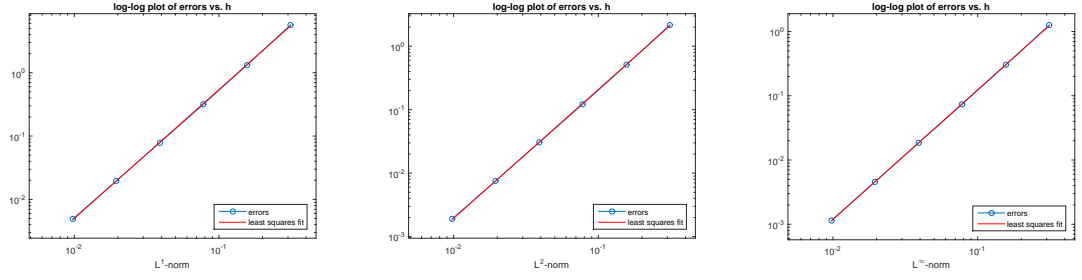


Figure 2: Convergence of error in L^1 , L^2 and L^∞ norms with uniform mesh refinement for the smooth source term test. Second-order convergence is observed in this example.

For the second test, proposed by Shi Jin in [9], the source term is of the discontinuous form $g(x, u) = z'(x)u$.

$$u_t + (u f(u))_x = g(x, u)$$

with flux function $u f(u) = \frac{u^2}{2}$ and $z(x) = \cos(\pi x)$, $4.5 \leq x \leq 5.5$ and 0 otherwise with $0 < x < 10$. Note that $z'(x)$ is a discontinuous function, so that $g(x, u)$ is a discontinuous source term in x . Figure 3 involves approximations with initial data $u(x, 0) = 0$, $x > 0$ and $u(0, t) = 2$, $t > 0$. The steady state solution of this problem is $u + z = 2$. The pictures in Figure 3 show approximations with 128 cells (left), 256 (middle) and 512 cells (right) for u (top pictures) and for steady state $u + z$ (bottom pictures). The numerical results present clearly qualitatively correct approximations at $t = 1$.

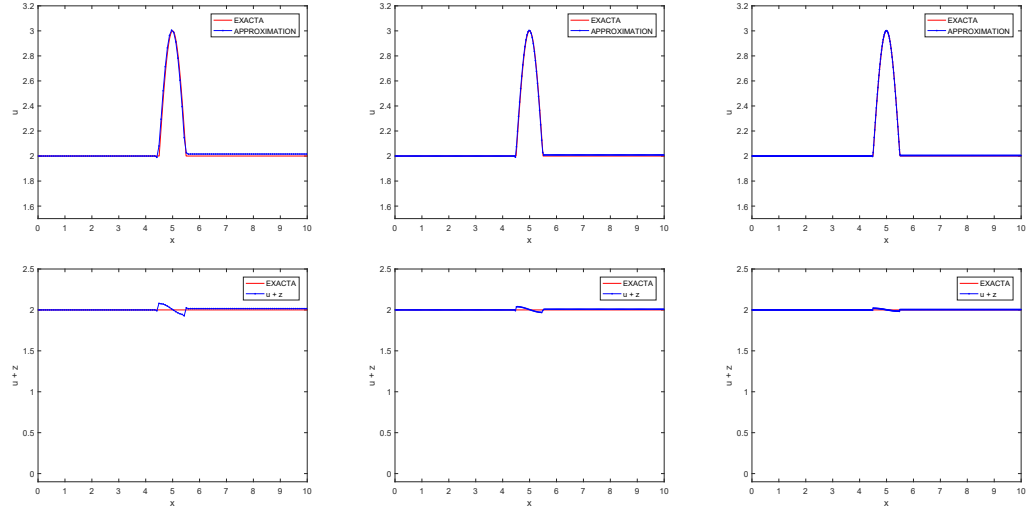


Figure 3: Numerical solutions with discontinuous source term $g(x, u)$.

We also consider, as in [7], a 2×2 nonlinear system of balance laws modeling the flow of water downing in a channel having a rectangular cross section and inclined at a constant angle θ to the horizontal. This is a prototype model for shallow-water flow (see [8]) in an

inclined channel with friction the system may be written as (in dimensionless variables)

$$\begin{cases} \frac{\partial h}{\partial t} + \frac{\partial(hu)}{\partial x} = 0, \\ \frac{\partial(hu)}{\partial t} + \frac{\partial(hu^2 + \frac{1}{2}h^2)}{\partial x} = h - C \frac{1+h}{\tan(\theta)} v^2, \end{cases} \quad (9)$$

where h is the height of the free surface and v is the averaged horizontal velocity. Precisely, as in [7], the friction coefficient C is taken to be 0.1, while the inclination angle $\theta = \frac{\pi}{6}$. On physical grounds, in this model problem it was assumed the hydrostatic balance in the vertical direction and ignored any surface tension. Here, the initial velocity is taken to be $v_0 = 1.699$, while the initial height of the free surface consists of a triangular perturbation of the uniform flow level, $h_0(x) = x + 1.5$, $-0.5 \leq x \leq 0$, $h_0(x) = -x + 1.5$, $0 \leq x \leq 0.5$, and 1 elsewhere. Numerical approximations are shown in Figure 4 with a clearly qualitatively correct approximations at $t = 1$.

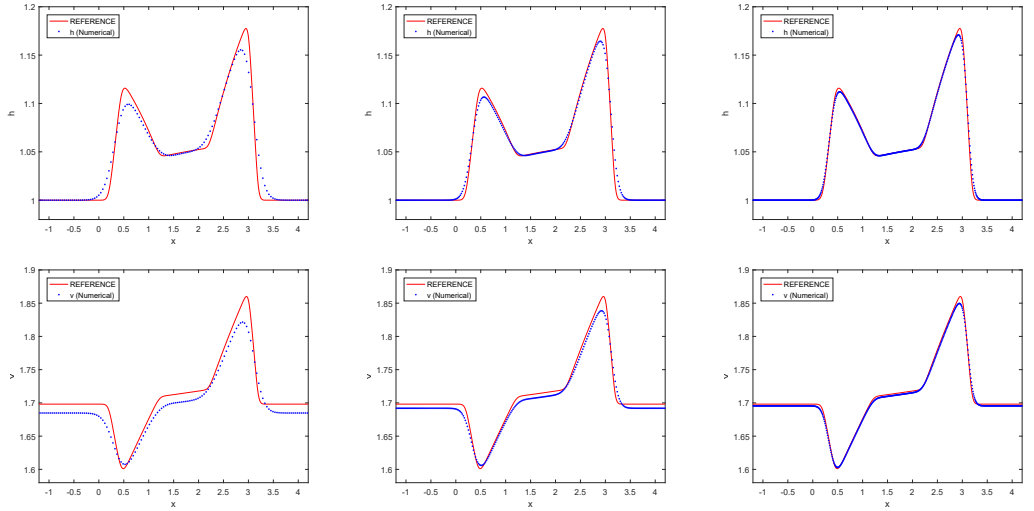


Figure 4: Numerical solutions to shallow water system (9) with 128, 256 and 512 cells (left to right), h (height) in top and v (velocity) bottom .

4 Concluding Remarks

We presented the development of a simple and effective numerical scheme for solving nonlinear scalar balance laws problems with the Lagrangian-Eulerian framework. This method is based on a reformulation of the conservation laws in terms of an equivalent locally conservative space-time problem in divergence form. We make use of piecewise linear and parabolic reconstructions ideas for resolution and accuracy reasons and the resulting method present qualitatively correct numerical approximations. Our method is robust in

a way that no special treatment is needed when the sign of velocity changes over time. We expect to establish a componentwise extension of the scheme in order to perform numerical experiments for systems of conservation and balance laws, as well as multidimensional problems. Our numerical experiments show good evidence of computational convergence and preservation of the well-balanced property of balance laws.

Acknowledgements

E. Abreu thanks financial support through grants FAPESP No. 2014/03204-9, FAPESP No. 2011/23628-0, CNPq No. 445758/2014-7 and UNICAMP /FAEPEX No. 519.292-0280/2014. A. Santo thanks CNPq-IMECC/ UNICAMP for a graduate fellowship.

References

- [1] E. Abreu., M. Colombeau and E. Panov. (2016). Weak asymptotic methods for scalar equations and systems. *Journal of Mathematical Analysis and Applications*, 444(2), 1203-1232.
- [2] E. Abreu, W. Lambert, J. Pérez and A. Santo, A new finite volume approach for transport models and related applications with balancing source terms, *Mathematics and Computers in Simulation* (2017), <http://dx.doi.org/10.1016/j.matcom.2016.12.012>
- [3] E. Abreu, J. Pérez and A. Santo. Solving hyperbolic conservation laws by using Lagrangian-Eulerian approach XXXVI Congresso Nacional de Matemática Aplicada e Computacional (CNMAC), 05 a 09 de setembro de 2016, Gramado - RS.
- [4] J. Aquino, A. S. Francisco, F; Pereira, T. Jordem Pereira, and H. P. Amaral Souto. A lagrangian strategy for the numerical simulation of radionuclide transport problems. *Progress in Nuclear Energy*, 52(3):282–291, 2010.
- [5] J. Douglas Jr, F. Pereira, and L.-M. Yeh. A locally conservative eulerian–lagrangian numerical method and its application to nonlinear transport in porous media. *Computational Geosciences*, 4(1):1–40, 2000.
- [6] G.-S. Jiang and C.-W. Shu. Efficient implementation of weighted eno schemes. Technical report, DTIC Document, 1995.
- [7] J. O. Langseth, A. Tveito, and R. Winther. On the convergence of operator splitting applied to conservation laws with source terms. *SIAM journal on numerical analysis*, 33(3):843863, 1996.
- [8] J. Pérez *Lagrangian-Eulerian approximate methods for balance laws and hyperbolic conservation law*. Tese de Doutorado, University of Campinas, 2015.
- [9] J Shi. “A steady-state capturing method for hyperbolic systems with geometrical source terms.” *ESAIM: Mathematical Modelling and Numerical Analysis* 35.04 (2001): 631-645.

A CONSERVATIVE LAGRANGIAN-EULERIAN FINITE VOLUME APPROXIMATION METHOD FOR BALANCE LAW PROBLEMS

Eduardo Abreu
University of Campinas (Brazil)

John Pérez
ITM-Institución Universitaria (Colombia)
johnaps22@gmail.com

Arthur Santo
University of Campinas (Brazil)

Abstract

We propose a simple and fast numerical method based on a Lagrangian-Eulerian framework for numerically solving nonlinear balance law problems. As in [1, 2, 5] the hyperbolic part of balance law is written in a space-time divergence form (see [4, 5]) so that the inherent conservation properties of the hyperbolic operator are used efficiently to build a numerical method to hyperbolic balance law problems. Such framework presents an interesting property of being rather independent of a particular structure of the flux function as well as of the source terms. Without any strong restriction over the source term other than integrability on the finite volume, the above procedure leads to a first-order three-point numerical scheme. To enhance resolution and accuracy of the approximations, we make use of polynomial reconstruction ideas into the Lagrangian-Eulerian novel approach. Besides, we use the novel technique to a wide range of nonlinear balance laws that appear in transport in porous media problems as well as to the shallow water equations with discontinuous source term. In such problems, we present evidences that we are calculating qualitatively correct approximations with accurate resolution of small perturbations around the stationary solution. Verification of the technique is also made by comparison with analytical solutions when they are available.

Keywords. Conservation laws, Lagrangian-Eulerian, Finite Volume Methods, high order methods.

References

- [1] E. C. Abreu, W. Lambert, J. A. Perez S., and A. M. E. Santo. A lagrangian-eulerian algorithm for solving hyperbolic conservation laws with applications. In *Proceedings of the 6th International Conference on Approximation Methods and Numerical Modelling in Environment and Natural Resources (MAMERN VI)*, pages 599–617, Pau/Granada, 2015.
- [2] E. Abreu, J. Pérez, W. Lambert, and A. Santo., A new finite volume approach for transport models and related applications with balancing source terms, *Mathematics and Computers in Simulation* (accepted).
- [3] E. Abreu, J. Pérez, and A. Santo. Solving hyperbolic conservation laws by using Lagrangian-Eulerian approach. In: XXXVI Congresso Nacional de Matematica Aplicada e Computacional (CNMAC), 2016, Gramado - RS. Proceeding Series of the Brazilian Society of Computational and Applied Mathematics, 2016. p. 1-7.
- [4] J. Douglas Jr, F. Pereira, and L.-M. Yeh. A locally conservative eulerian-lagrangian numerical method and its application to nonlinear transport in porous media. *Computational Geosciences*, 4(1):1–40, 2000.

- [5] J. A. Pérez S., A Lagrangian-Eulerian computational formulation to hyperbolic problems and balance laws, PhD. Thesis, Institute of Mathematics, Statistics and Scientific Computing, University of Campinas (2015).